

# Applications of Gauge/Gravity Duality in Heavy Ion Collisions

by

Di-Lun Yang

Department of Physics  
Duke University

Date: \_\_\_\_\_

Approved:

---

Berndt Müller, Supervisor

---

Steffen Bass

---

Ashutosh Kotwal

---

Jian-Guo Liu

---

Thomas Mehen

Dissertation submitted in partial fulfillment of the requirements for the degree of  
Doctor of Philosophy in the Department of Physics  
in the Graduate School of Duke University  
2014

ABSTRACT

Applications of Gauge/Gravity Duality in Heavy Ion  
Collisions

by

Di-Lun Yang

Department of Physics  
Duke University

Date: \_\_\_\_\_

Approved:

\_\_\_\_\_  
Berndt Müller, Supervisor

\_\_\_\_\_  
Steffen Bass

\_\_\_\_\_  
Ashutosh Kotwal

\_\_\_\_\_  
Jian-Guo Liu

\_\_\_\_\_  
Thomas Mehen

An abstract of a dissertation submitted in partial fulfillment of the requirements for  
the degree of Doctor of Philosophy in the Department of Physics  
in the Graduate School of Duke University  
2014

Copyright © 2014 by Di-Lun Yang  
All rights reserved except the rights granted by the  
Creative Commons Attribution-Noncommercial Licence

# Abstract

In order to analyze the strongly interacting quark gluon plasma in heavy ion collisions, we study different probes by applying the gauge/gravity duality to facilitate our qualitative understandings on such a non-perturbative system. In this dissertation, we utilize a variety of holographic models to tackle many problems in heavy ion physics including the rapid thermalization, jet quenching, photon production, and anomalous effects led by external electromagnetic fields. We employ the AdS-Vaidya metric to study the gravitational collapse corresponding to the thermalization of a strongly coupled gauge theory, where we compute the approximated thermalization time and stopping distances of light probes in such a non-equilibrium medium. We further generalize the study to the case with a nonzero chemical potential. We find that the non-equilibrium effect is more influential for the probes with smaller energy. In the presence of a finite chemical potential, the decrease of thermalization times for both the medium and the light probes is observed.

On the other hand, we also investigate the anisotropic effect on the stopping distance related to jet quenching of light probes and thermal-photon production. The stopping distance and photoemission rate in the anisotropic background depend on the moving directions of probes. The influence from a magnetic field on photoemission is also investigated in the framework of the D3/D7 system, where the contributions from massive quarks are involved. The enhancement of photon production for photons generated perpendicular to the magnetic field is found. Given that the mass

of massive quarks is close to the critical embedding, the meson-photon transition will yield a resonance in the spectrum. We thus evaluate the flow coefficient  $v_2$  of thermal photons in a 2+1 flavor strongly interacting plasma. The magnetic-field induced photoemission results in large  $v_2$  and the resonance from massive quarks gives rise to a mild peak in the spectrum. Moreover, we utilize the Sakai-Sugimoto model to analyze the chiral electric separation effect, where an axial current is generated parallel to the applied electric field in the presence of both the vector and axial chemical potentials. Interestingly, the axial conductivity is approximately proportional to the product of the vector chemical potential and the axial chemical potential for arbitrary magnitudes of the chemical potentials.

# Contents

<b>Abstract</b>	<b>iv</b>
<b>List of Figures</b>	<b>ix</b>
<b>Acknowledgements</b>	<b>xviii</b>
<b>1 An introduction to heavy-ion phenomenology</b>	<b>1</b>
1.1 Overview of relativistic heavy ion collisions . . . . .	1
1.2 Hydrodynamics and Elliptic Flow . . . . .	5
1.3 Jet quenching of hard probes in the medium . . . . .	10
1.4 Strong Electromagnetic Fields in Heavy Ion Collisions . . . . .	16
1.5 Outline of the Dissertation . . . . .	20
<b>2 Review of the gauge/gravity duality</b>	<b>24</b>
2.1 AdS/CFT Correspondence . . . . .	24
2.2 Holography at Finite Temperature . . . . .	32
2.3 Adding Flavors . . . . .	35
<b>3 Jet Quenching and Holographic Thermalization</b>	<b>41</b>
3.1 The Falling Mass Shell in the AdS-Vaidya Spacetime . . . . .	43
3.2 Jet Quenching of Colorless Probes in the Non-equilibrium Plasma . .	47
3.3 Jet Quenching of Virtual Gluons in the Non-Equilibrium Plasma . . .	54
3.4 Thermalization Time with Chemical Potentials . . . . .	61
3.5 Jet Quenching with Chemical Potentials . . . . .	65

3.6	Conclusions and Discussions . . . . .	69
<b>4</b>	<b>Investigating Strongly Coupled Anisotropic Plasmas</b>	<b>74</b>
4.1	The Einstein-Axion-Dilaton System . . . . .	76
4.2	Light Probes in Anisotropic Plasmas . . . . .	79
4.3	Photon Production in an Anisotropic Plasma . . . . .	87
4.4	Photon Spectra from Massive Quarks in an Anisotropic Plasma . . . . .	91
4.5	Concluding Remarks . . . . .	97
<b>5</b>	<b>Photon Production with a Strong Magnetic Field</b>	<b>99</b>
5.1	External Magnetic Fields . . . . .	100
5.2	Photon Production from Magnetic Fields in Anisotropic Plasmas . . . . .	102
5.3	Thermal-Photon $v_2$ Induced by a Constant Magnetic Field . . . . .	110
5.4	Concluding Remarks . . . . .	121
<b>6</b>	<b>Holographic Chiral Electric Separation Effect</b>	<b>123</b>
6.1	Interpretation of Chiral Electric Conductivity . . . . .	124
6.2	Basics of Sakai-Sugimoto model . . . . .	127
6.3	Background-Field Expansion . . . . .	130
6.4	DC and AC Conductivities for Small Chemical Potentials . . . . .	134
6.5	Arbitrary Chemical Potentials . . . . .	140
6.6	Discussions . . . . .	145
<b>7</b>	<b>Conclusions and Outlook</b>	<b>149</b>
<b>A</b>	<b>Appendices for Chapter 3</b>	<b>154</b>
A.1	Perturbative Expansions of the Dilaton Field . . . . .	154
A.2	Quasi-Static Approximation and the Thin-Shell Limit . . . . .	156
A.3	The Redshift Factor and Thermalization times . . . . .	159
A.4	The String Profile in the Quasi-AdS Spacetime . . . . .	164

A.5	The Dangling String and Wave velocity in the Quasi-AdS Spacetime .	165
A.6	Finding the Stopping Distance in Eddington-Finkelstein Coordinates	166
A.7	The Dyonic Black Hole . . . . .	169
<b>B</b>	<b>Appendices for Chapter 4 and Chapter 5</b>	<b>172</b>
B.1	General Expressions for Field Equations . . . . .	172
B.2	Near-Boundary Expansion . . . . .	173
<b>C</b>	<b>Appendices for Chapter 6</b>	<b>176</b>
C.1	Entropy Principle for CESE . . . . .	176
	<b>Bibliography</b>	<b>179</b>
	<b>Biography</b>	<b>190</b>

# List of Figures

1.1	The schematic figure of different stages in heavy ion collisions taken from the presentation by S. Bass. . . . .	2
1.2	The pseudo-rapidity distributions for charged particles for different centralities[1]. . . . .	6
1.3	The schematic figure of azimuthal asymmetry of the medium in position and momentum spaces. In the left panel, the green region represents the cross section of two colliding nuclei in non-central collisions. In the right panel, the orange region represents the corresponding anisotropic momentum distribution. The figure is taken from the lecture of P. Huovinen in Jet Summer School 2012. . . . .	9
1.4	The comparison between hadron $v_2$ obtained from ideal hydrodynamics[2] and those measured in RHIC[3, 4, 5]. The figure is taken from [6]. . .	10
1.5	Pressure anisotropy as a function of proper time with different anisotropic and viscous hydrodynamics approximations corresponding to different color lines. Here $\xi_0$ denotes the initial momentum- space anisotropy and $\eta/S$ denotes the shear viscosity to entropy density ratio. The figure is taken from [7]. . . . .	11
1.6	Two energetic quarks created back-to-back in the medium: one travels mostly in the vacuum and one traverses the plasma. The former radiates few gluons and quickly hadronizes, while the latter loses more energy due to the induced radiation and finally fragments into the quenched jet. The jet quenching is characterized by the transport coefficient $\hat{q}$ , gluon density per rapidity $dN_g/dy$ and temperature T. The figure is taken from [8]. . . . .	12
1.7	The nuclear modification factors for different particles measured in RHIC[9]. . . . .	13
1.8	$v_2$ in minimum bias collisions, using two different reaction plane detectors for (a) $\pi^0$ , (b)inclusive photons, (c)direct photons [10]. . . . .	18

2.1	Schematic representation of the AdS/CFT duality[11]. . . . .	30
2.2	The dimensions of D3/D7 embedding, where 0, 1, 2, 3 denote the four dimensional spacetime on the boundary. . . . .	36
2.3	Schematic representation of different types of embeddings[12]. . . . .	38
2.4	The mass as a function of $\psi_0$ modified from[13]. . . . .	38
3.1	The scenario of a massless particle ejecting from the boundary as the shell starts to fall, where $v_0$ denotes the thickness of the shell and the solid red curves and the dashed red curve represent the surfaces and the center of the shell, respectively. The dashed arrow denotes the massless particle as a hard probe falling from the boundary at $t = 0$ . . . . .	51
3.2	The red, blue, and green curves represent the trajectories of particles falling in the AdS-Schwarzschild spacetime and in the AdS-Vaidya spacetime with $v_0 = 0.2$ and $v_0 = 0.0001$ , respectively. Three curves coincide and cannot be distinguished. Here we take $ \vec{q}  = 0.99\omega_0$ and $z_h = 1$ . . . . .	51
3.3	The energy ratio with respect to the collision point $z_c$ , where $\delta = 0.99$ and $z_h = 1$ . . . . .	53
3.4	A schematic figure for the sting profile in AdS-Vaidya spacetime before colliding with the shell. . . . .	54
3.5	A schematic figure for the sting profile in AdS-Vaidya spacetime after colliding with the shell. . . . .	54
3.6	The blue and red dots represent the stopping distances in AdS-Vaidya and AdS-Schwarzschild spacetimes respectively, where $\hat{x}_s = x_s\pi T$ and $\hat{E} = \pi\alpha'z_h E = \frac{1}{\sqrt{g_{YM}^2 N_c}} \frac{E}{T}$ . Here we fix the initial velocities of probes $v_I = \delta = 0.99$ . . . . .	61
3.7	The blue and red dots represent the stopping distances in AdS-Vaidya and AdS-Schwarzschild spacetimes respectively, where $\gamma$ denote the Lorentz factors encoding the initial velocities of gluons. Here we fix the initial energies of probes $\hat{E} = 50$ . . . . .	61
3.8	The thermalization time $\tau$ with different values of chemical potential in $d = 3$ . . . . .	65
3.9	The thermalization time $\tau$ with different values of chemical potential in $d = 4$ . . . . .	65

3.10	The ratio to the stopping distances with and without chemical potential in the unit of temperature for $d = 3$ , where $\hat{x}_s^1 = x_s^1 T$ . Here we set $M = 1$ , $z_I = 0$ , and $ \vec{q}  = 0.99\omega$ . . . . .	68
3.11	The ratio to the stopping distances with and without chemical potential in the unit of temperature for $d = 4$ , where $\hat{x}_s^1 = x_s^1 T$ . Here we set $M = 1$ , $z_I = 0$ , and $ \vec{q}  = 0.99\omega$ . . . . .	68
3.12	The entropy density with different values of the chemical potential for $d = 3$ . Here we set $M = 1$ . . . . .	68
3.13	The entropy density with different values of the chemical potential for $d = 4$ . Here we set $M = 1$ . . . . .	68
3.14	The red and blue curves represent the trajectories of the massless particles moving in AdS-RN and AdS-RN-Vaidya spacetimes for $d = 3$ and $\chi_3 = 4.47$ , respectively. The red and blue dashed lines denote the first collision point and the position of the future horizon. Here we take $z_I = 0.4$ , $M = 1$ , and $ \vec{q} /\tilde{\omega} = 0.99$ as the initial conditions in both spacetimes. . . . .	70
3.15	The red and blue curves represent the trajectories of the massless particles moving in AdS-RN and AdS-RN-Vaidya spacetimes for $d = 4$ and $\chi_4 = 1.1$ , respectively. The red and blue dashed lines denote the first collision point and the position of the future horizon. Here we take $z_I = 0.4$ , $M = 1$ , and $ \vec{q} /\tilde{\omega} = 0.99$ as the initial conditions in both spacetimes. . . . .	70
3.16	The red and blue points represent the stopping distances with different values of chemical potential in AdS-RN and AdS-RN-Vaidya for $d = 3$ , respectively. Here we set $M = 1$ , $z_I = 0.4$ , and $ \vec{q} /\tilde{\omega} = 0.99$ as the initial conditions in both spacetimes. . . . .	71
3.17	The red and blue points represent the stopping distances with different values of chemical potential in AdS-RN and AdS-RN-Vaidya for $d = 4$ , respectively. Here we set $M = 1$ , $z_I = 0.4$ , and $ \vec{q} /\tilde{\omega} = 0.99$ as the initial conditions in both spacetimes. . . . .	71
3.18	The blue and red points represent the thermalization times scaled by the temperature obtained from our approach and that from analyzing non-local observables, respectively. Here we take $M = 1$ in the both cases. . . . .	73
4.1	The energy and pressures normalized by their isotropic values as functions of $a/T$ [14]. . . . .	79

- 4.2  $R_x = x_{aniso}/x_{iso}$  represents the ratio of the stopping distances in the MT geometry with anisotropy to without anisotropy, where  $x_{aniso} = x_T$  for the red points and  $x_{aniso} = x_L$  for the large blue points. Here we take  $|\vec{q}| = 0.99\omega$  and fix the temperature of media. . . . . 84
- 4.3  $R_x = x_{aniso}/x_{iso}$  represents the ratio of the stopping distances in the MT geometry with anisotropy to without anisotropy, where  $x_{aniso} = x_T$  for the red points and  $x_{aniso} = x_L$  for the large blue points. Here we take  $N_c = 3$ ,  $|\vec{q}| = 0.99\omega$  and fix the energy density of media. . . . 85
- 4.4  $R_x = x_{aniso}/x_{iso}$  represents the ratio of the stopping distances in the MT geometry with anisotropy to without anisotropy, where  $x_{aniso} = x_T$  for the red points and  $x_{aniso} = x_L$  for the large blue points. Here we take  $N_c = 3$ ,  $|\vec{q}| = 0.99\omega$  and fix the entropy density of media. . . . 85
- 4.5 The red and thick blue curves represent the ratios  $R_x = x_{aniso}/x_{iso}$  at mid anisotropy at equal temperature and at equal entropy density, respectively. Here we take  $|\vec{q}| = 0.99\omega$ ,  $u_h = 1$ , and  $a/T \approx 4.4$  or equivalently  $a/s^{1/3} \approx 1.2$  for  $N_c = 3$ . . . . . 86
- 4.6 The red and thick blue curves represent the ratios  $R_x = x_{aniso}/x_{iso}$  at large anisotropy at equal temperature and at equal entropy density, respectively. Here we take  $|\vec{q}| = 0.99\omega$ ,  $u_h = 1$ , and  $a/T \approx 86$  or equivalently  $a/s^{1/3} \approx 17$  for  $N_c = 3$ . . . . . 86
- 4.7 The blue, green, and red curves(from top to bottom) represent the ratios of spectral densities at fixed temperature for  $\epsilon_T = \epsilon_x$  or  $\epsilon_y$  when  $k = (-\omega, 0, 0, \omega)$ , for  $\epsilon_T = \epsilon_y$  and  $\epsilon_T = \epsilon_z$  when  $k = (-\omega, \omega, 0, 0)$ , respectively. Here we take  $u_h = 1$  and  $a/T = 4.4$ . . . . . 92
- 4.8 The red, green, and blue curves(from top to bottom) represent the spectral functions with  $k = (-\omega, 0, 0, \omega)$  for  $\hat{M}_q/(\pi T) = 0.61, 0.89,$  and  $1.31$ .The dashed ones and solid ones correspond to the results with and without anisotropy, respectively. Here we take  $u_h = 1$  and  $a/T = 4.4$ . . . . . 97
- 4.9 The red, green, and blue curves(from top to bottom) represent the spectral functions with  $k = (-\omega, \omega, 0, 0)$  and the  $y$ -polarization for  $\hat{M}_q/(\pi T) = 0.61, 0.89,$  and  $1.31$ . The thin ones correspond to isotropic results. The thick ones and dashed ones correspond to the anisotropic results with  $\epsilon_y$  and  $\epsilon_z$ , respectively. Here we take  $u_h = 1$  and  $a/T = 4.4$ . 97

- 5.1 The blue and red solid curves(from top to bottom) represent the quark mass scaled by temperature without and with magnetic field  $B_z$ , respectively. The blue, green, and red dashed curves(from top to bottom) correspond to the anisotropic case without magnetic field, with  $B_y$ , and with  $B_z$ , respectively. Here we set  $u_h = 1$ ,  $B_y = B_z = 2(\pi T)^2$ , and  $a/T = 4.4$ . . . . . 102
- 5.2 The red, green, and blue curves(from top to bottom) represent the spectral functions with  $k = (-\omega, 0, 0, \omega)$  for  $\hat{M}_q/(\pi T) = 0.45, 0.65,$  and  $0.86$ , respectively. The solid, dashed, and dot-dashed correspond to  $(a/T, B_z/(\pi T)^2) = (0, 0), (0, 2),$  and  $(4.4, 2)$ , respectively. . . . . 102
- 5.3 The red, green, and blue curves(from top to bottom) represent the spectral functions with  $k = (-\omega, \omega, 0, 0)$  and  $\epsilon_T = \epsilon_y$  for  $\hat{M}_q/(\pi T) = 0.45, 0.65,$  and  $0.86$ , respectively. The solid, dashed, and dot-dashed correspond to  $(a/T, B_z/(\pi T)^2) = (0, 0), (0, 2),$  and  $(4.4, 2)$ , respectively. 106
- 5.4 The red, green, and blue curves(from top to bottom) represent the spectral functions with  $k = (-\omega, \omega, 0, 0)$  and  $\epsilon_T = \epsilon_z$  for  $\hat{M}_q/(\pi T) = 0.45, 0.65,$  and  $0.86$ , respectively. The solid, dashed, and dot-dashed correspond to  $(a/T, B_z/(\pi T)^2) = (0, 0), (0, 2),$  and  $(4.4, 2)$ , respectively. 106
- 5.5 The ratios of DC conductivity with  $\epsilon_T = \epsilon_y$  versus quark mass. The red(triangle), green(circle), and blue(square) dots correspond to the cases with  $(a/T, B_z/(\pi T)^2) = (4.4, 0), (0, 2),$  and  $(4.4, 2)$ , respectively. . 107
- 5.6 The ratios of DC conductivity with  $\epsilon_T = \epsilon_z$  versus quark mass. The red(triangle), green(circle), and blue(square) dots correspond to the cases with  $(a/T, B_z/(\pi T)^2) = (4.4, 0), (0, 2),$  and  $(4.4, 2)$ , respectively. . 107
- 5.7 The red and blue (upper and lower at  $\omega/(\pi T) = 1$ ) curves represent the differential emission rate per unit volume with  $k = (-\omega, \omega, 0, 0)$  for  $\hat{M}_q/(\pi T) = 0.45$  and  $0.86$ . The solid, dashed, and dot-dashed ones correspond to  $(\epsilon_T, B_z/(\pi T)^2) = (\epsilon_{z(y)}, 0), (\epsilon_z, 2),$  and  $(\epsilon_y, 2)$ , respectively. 108
- 5.8 The spectral functions with  $k = (-\omega, \omega, 0, 0)$  and  $\epsilon_T = \epsilon_z$ . The solid and dashed curves correspond to  $(a/T, B_y/(\pi T)^2) = (0, 2)$  and  $(4.4, 2)$ , respectively. . . . . 110
- 5.9 The spectral functions with  $k = (-\omega, \omega, 0, 0)$  and  $\epsilon_T = \epsilon_y$ . The solid and dashed curves correspond to  $(a/T, B_y/(\pi T)^2) = (0, 2)$  and  $(4.4, 2)$ , respectively. . . . . 110

5.10	The spectral functions with $k = (-\omega, 0, 0, \omega)$ and $\epsilon_T = \epsilon_x$ . The solid and dashed curves correspond to $(a/T, B_y/(\pi T)^2) = (0, 2)$ and $(4.4, 2)$ , respectively. . . . .	111
5.11	The spectral functions with $k = (-\omega, 0, 0, \omega)$ and $\epsilon_T = \epsilon_y$ . The solid and dashed curves correspond to $(a/T, B_y/(\pi T)^2) = (0, 2)$ and $(4.4, 2)$ , respectively. . . . .	111
5.12	The spectral functions with $k = (-\omega, 0, \omega, 0)$ and $\epsilon_T = \epsilon_x$ . The solid and dashed curves correspond to $(a/T, B_y/(\pi T)^2) = (0, 2)$ and $(4.4, 2)$ , respectively. . . . .	112
5.13	The spectral functions with $k = (-\omega, 0, \omega, 0)$ and $\epsilon_T = \epsilon_z$ . The solid and dashed curves correspond to $(a/T, B_y/(\pi T)^2) = (0, 2)$ and $(4.4, 2)$ , respectively. . . . .	112
5.14	The coordinates of the system, where the magnetic field points along the z axis and the x axis is parallel to the beam direction. The $k$ denotes the momentum of emitted photons and $\theta$ denotes the angle between the momentum and the x-y plane as the reaction plane; $\epsilon^{out}$ and $\epsilon^{in}$ represent the out-plane and in-plane polarizations, respectively.	114
5.15	The red(dot-dashed) and blue(dashed) curves correspond to the $v_2$ of the photons with in-plane and out-plane polarizations, respectively. The black(solid) curve correspond to the one from the averaged emission rate of two types of polarizations. Here we consider the contribution from massless quarks at $B_z = 1(\pi T)^2$ . . . . .	117
5.16	The colors correspond to the same cases as in Fig.5.15. Here we consider the contributions from solely the massive quarks with $m = 1.143$ at $B_z = 1(\pi T)^2$ . . . . .	117
5.17	The colors correspond to the same cases as in Fig.5.15. Here we consider the contributions from both massless quarks and massive quarks with $m = 1.143$ at $B_z = 1(\pi T)^2$ . . . . .	118
5.18	The colors correspond to the same cases as in Fig.5.15. Here we consider the contributions from both massless quarks and massive quarks with $m = 1.307$ at $B_z = 0.1(\pi T)^2$ . . . . .	120
5.19	The colors correspond to the same cases as in Fig.5.15. Here we consider the contributions from both massless quarks and massive quarks with $m = 1.3$ at $B_z = 0.2(\pi T)^2$ . . . . .	121
6.1	The schematic description of the embeddings in the SS model[15]. . .	128

6.2	D8-brane embeddings in the Sakai-Sugimoto model[16]:(a)chiral symmetry breaking in vacuum (b)chiral symmetry breaking in the plasma (c)chiral symmetry restored in the plasma. Here the black circles on top represent the compactified $x^4$ on $S^1$ and the red curves represent the $D8$ branes and $\overline{D8}$ branes in the bulk. . . . .	128
6.3	The DC conductivities in the $L/R$ bases versus the chemical potentials scaled by temperature. . . . .	138
6.4	The blue and red(dashed) curves correspond to the normal DC conductivity and the axial one with $\mu_V = T$ , respectively. . . . .	141
6.5	The blue and red(dashed) curves correspond to the normal DC conductivity and the axial one with $\mu_A = 0.5T$ , respectively. . . . .	141
6.6	Power-counting estimation in (6.9) with $\mu_A = 0.01T$ . . . . .	141
6.7	Power-counting estimation in (6.9) with $\mu_V = 0.2T$ . . . . .	141
6.8	The red, blue(dashed), and black(dot-dashed) curves correspond to the cases with $\mu_V = T, 0.6T$ , and $0, 3T$ . Here $\hat{\mu}_{V/A} = \mu_{V/A}/T$ . . . . .	142
6.9	The red(solid), blue(dashed), and green(dotted) curves correspond to the real part of the normal AC conductivity with $\mu_A = 0.2T, 0.5T$ , and $0.9T$ , respectively. Here $\mu_V = T$ . . . . .	142
6.10	The red(solid), blue(dashed), and green(dotted) curves correspond to the real part of the axial AC conductivity with $\mu_A = 0.2T, 0.5T$ , and $0.9T$ , respectively. Here $\mu_V = T$ . . . . .	143
6.11	The red(solid), blue(dashed), and green(dotted) curves correspond to the imaginary part of the axial AC conductivity with $\mu_A = 0.2T, 0.5T$ , and $0.9T$ , respectively. Here $\mu_V = T$ . . . . .	143
6.12	The DC conductivities in the $L/R$ bases versus the chemical potentials scaled by temperature. The dashed red curve and solid blue curve correspond to the result from the background-field expansion and from solving the full DBI action, respectively. . . . .	144
6.13	The blue and red(dashed) curves correspond to the normal DC conductivity and the axial one with $\mu_V = 4T$ , respectively. . . . .	145
6.14	The blue and red(dashed) curves correspond to the normal DC conductivity and the axial one with $\mu_A = 3T$ , respectively. . . . .	145

6.15	The red, blue(dashed), black(dot-dashed), and green(long-dashed) curves correspond to the cases with $\mu_V = 10T, 8T, 4T$ , and $T$ . Here $\hat{\mu}_{V/A} = \mu_{V/A}/T$ . . . . .	146
6.16	The Green(solid), red(long-dashed), and black(dot-dashed) curves correspond to the real part of the normal AC conductivity with $(\mu_V, \mu_A) = (4T, 3T), (4T, T)$ and $(T, 0.9T)$ . The blue(dashed) curve corresponds to the one with $(\mu_V, \mu_A) = (T, 0.9T)$ from the background-field expansions. . . . .	146
6.17	The real part of the axial AC conductivity with the colors corresponding to the same cases as Fig.6.16. . . . .	147
6.18	The imaginary part of the axial AC conductivity with the colors corresponding to the same cases as Fig.6.16. . . . .	147
A.1	The comparison between the leading-order mass function to $\mathcal{O}(\epsilon^2)$ and the next leading-order one to $\mathcal{O}(\epsilon^4)$ in terms of $v$ . Two results coincide and cannot be distinguished in the figure. . . . .	156
A.2	The red curve and blue curve illustrate the $\phi(z = 0.99, v)$ up to $\mathcal{O}(\epsilon)$ and $\mathcal{O}(\epsilon^3)$ , respectively. When $v \approx 3v_0$ , the contribution from the higher order terms starts to increase, while its amplitude is rather small as $v$ is still within $(-3v_0, 3v_0)$ . . . . .	156
A.3	The solid red, orange, and blue curves represent the position of the center of the shell using the linear approximation for $(v_0, \epsilon) = (0.1, 0.02306), (0.2, 0.06523)$ , and $(0.4, 0.18451)$ , respectively. The dashed curves are the result of numerically computing $v(t, z)$ . . . . .	158
A.4	Same plot as in Fig.A.3, but zooming onto late time evolution. . . . .	158
A.5	The full numerical computation for $m(v)$ at $v_0 = 0.1$ and $\epsilon = 0.02306$ . . . . .	159
A.6	The red and blue curves represent the leading order mass function to $\mathcal{O}(\epsilon^2)$ for $v_0 = 0.1$ and $\epsilon = 0.02306$ at $z_0 = 0.99$ and $z_0 = 0.3$ , respectively. . . . .	159
A.7	The red curve represents the redshift factor $c(z_0)$ as a function of the position of the shell, while the blue curve represents $F(z_0)$ , where the future horizon is at $z_h = 1$ . . . . .	160
A.8	The blue and red curves represent the positions of the shell obtained from (3.18) and (A.8), respectively. Here the blue dashed line denotes the future horizon at $z_h = 1$ . . . . .	160

- A.9 The scenario of a massless particle ejecting from the boundary as the shell starts to fall, where  $v_0$  denotes the thickness of the shell and the solid red curves and the dashed red curve represent the surfaces and the center of the shell, respectively. Here the blue dashed line represents the massless particle ejected from  $z_I$ . . . . . 169
  
- A.10 The green points represent the stopping distances in AdS-RN-Vaidya spacetime in EF coordinates, which match those derived in Poincare coordinates as shown by the blue points. Here the initial conditions are the same as those in Fig.3.17 and we take  $v_0 = 0.0001$ . . . . . 169

# Acknowledgements

First, I would like to thank my supervisor Berndt Müller for his guidance and supervision. He has been always supportive and encouraging to cultivate my independent thinking in scientific research. Without his help, the accomplishment of this dissertation will not be possible.

Moreover, I am deeply grateful to my collaborators Elena Caceres, Arnab Kundu, and Diana Vaman. Most of the early work of this dissertation is in collaboration with them. As experienced string theorists, they have taught me essential knowledge and techniques in the AdS/CFT correspondence. Also, I appreciate their hospitality during my visits in U.T. Austin and in University of Virginia.

I would also like to thank my friends in Taiwan, Shi Pu and Shang-Yu Wu, as my collaborators contributing a big part of my research in this dissertation. The discussions with them are always fruitful and enlightening, which allow me to explore heavy ion physics from broader perspectives in holography. Besides direct collaboration, I deeply acknowledge numerous engaging conversations with Peter Arnold, Jinfeng Liao, Juan Pedraza, Andreas Schäfer, Michael Strickland, Bo-Wen Xiao, and Hongbao Zhang.

On the other hand, it is as well important to mention many people I met in Duke. Among the senior members, my special acknowledgment goes to Steffen Bass and Thomas Mehen from whom I have learned a lot in heavy ion physics and the effective field theory. Particularly, I thanks Tom for his supervision on my research in my early

graduate years. I also thank my colleagues Shanshan Cao, Christopher Coleman-Smith, and Guang-You Qin for useful discussions in academics. I am fortunate to have Jui-an Chao, Ching-Yun Cheng, Chung-Ting Ke, Leo Fang, Hung-Ming Tsai, and Chi-Ho Wang for sharing great experiences in daily life and helping me to pass the suffering moments in my graduate study.

I most humbly acknowledge the contribution of my parents whom this thesis is dedicated to. Without their sacrifice, unconditional support and love none of these would be possible.

# An introduction to heavy-ion phenomenology

## 1.1 Overview of relativistic heavy ion collisions

The high-energy experiments in the Relativistic heavy ion collider (RHIC) and Large Hadron Collider (LHC) collide two ultra-relativistic nuclei to produce the so called quark gluon plasma (QGP) as a deconfined phase of quarks and gluons. In RHIC, the Au+Au collisions can reach  $\sqrt{s} = 200$  GeV, where  $\sqrt{s}$  represents the energy per nucleon in the center of mass frame. At the LHC, the maximum collision energy for Pb+Pb collisions can further reach  $\sqrt{s} = 2.76$  TeV. The ultrahigh energy collisions provide high resolution to probe the internal structure of nucleons with the strong interaction governed by quantum chromodynamics (QCD). The collision of two colliding nuclei will form QGP as a thermal medium. Based on hydrodynamic properties of QGP, it is now generally believed that QGP is strongly coupled. The investigation of heavy-ion phenomenology thus provides profound information on the strongly coupled QCD. Moreover, the experiments could be regarded as a "small Bang", which may simulate the formation of early universe. Therefore, the studies of QGP may as well facilitate our understandings from the cosmological perspective.

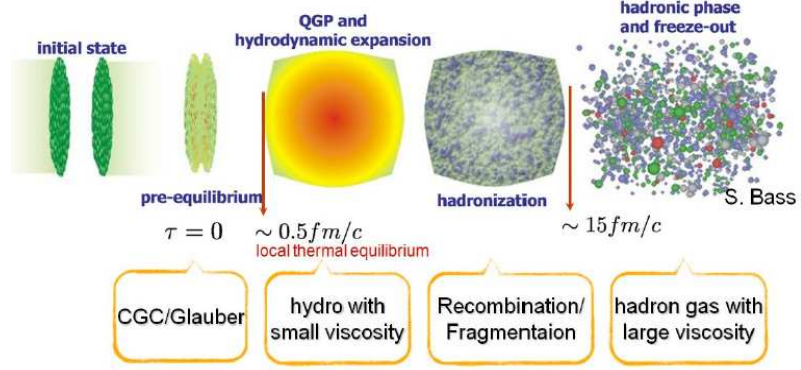


FIGURE 1.1: The schematic figure of different stages in heavy ion collisions taken from the presentation by S. Bass.

The medium formed in heavy-ion collisions undergoes different stages, which are schematically illustrated in Fig.1.1. The smashed nuclei firstly break the confinement via large kinetic energy, while it takes short but finite time for the deconfined medium to reach a thermal state with the temperature greater than the deconfined temperature of QCD. Whether such a pre-equilibrium state is weakly coupled or strongly coupled is still under debate. Given the large  $Q_s$  (energy transfer) in deep inelastic collisions, where  $Q_s \gg \Lambda_{\text{QCD}}$ , the QCD coupling here should be rather small according to the asymptotic freedom [17, 18]. Based on the weakly coupled QCD, a phenomenological model approximates the thermalization time as  $\tau \sim \alpha_s^{-13/5} Q_s^{-1}$  [19], where  $g_s = \sqrt{4\pi\alpha_s}$  represents the QCD coupling. This approximated thermalization time is much larger than the small thermalization and isotropization times for  $t_{\text{th(iso)}} < 1 \text{ fm}/c$  extracted from the initial conditions of hydrodynamics applied to simulate the later phase [2, 20, 21, 22]. However, the small thermalization and isotropization times are found in string-theory-based models in the infinitely strong coupling limit [23, 24, 25, 26, 27, 28, 29], which may support the strongly coupled scenario in the pre-equilibrium state. After the rapid thermalization, the thermalized medium forms QGP, which undergoes hydrodynamic expansion. By fitting the experimental

data with hydrodynamic simulations, it has been shown that QGP has a small shear viscosity to entropy density ratio, which is close to  $1/(4\pi)$ , which is the lowest bound for universal quantum systems proposed by Kovtun, Son, and Starinets(KSS)[30] in string theory. The small ratio hence suggests that QGP is a nearly perfect fluid. In Section II, we will further introduce the elliptic flow  $v_2$  as an important quantity measured by experiments to characterize the collective behavior of QGP. While the low-energy partons as soft probes in QGP are governed by hydrodynamics, the energetic partons as hard probes like jets or heavy quarks may behave differently. These hard probes are mostly generated in early times due to their high energies. There exists an interesting phenomenon called "jet quenching" as suppression of these hard probes observed in heavy ion collisions, which will be further discussed in Section III. In the end of the hydrodynamic evolution, the color objects have to hadronize to form the color singlets. The hadronization of QGP are dictated by the QCD fragmentation[31, 32, 33] and recombination effect[34, 35, 36, 37], where the latter generally originates from co-moving quarks with total kinetic energy and quantum numbers equal to those of moving hadrons. Finally, the interactions between hadrons become rather weak and all hadrons move freely toward detectors; such a last phase is called freeze-out.

In theory, non-perturbative approaches are required in order to study the strongly coupled QGP(sQGP) phase. Hydrodynamics as a long-wave length effective theory successfully describes most of experimental observables, but the microscopic mechanisms behind the input parameters such as the transport coefficients, thermalization time, and initial conditions are unknown. Although lattice QCD can provide static properties of strongly coupled QCD, the computations of dynamical observables are challenging[38, 39, 40]. Furthermore, there exists a sign problem for lattice QCD at finite density. The gauge/gravity duality or the so called anti-de Sitter space/conformal field theory(AdS/CFT) correspondence as a duality between a

strongly coupled gauge theory living in a lower-dimensional spacetime and the string theory in a higher-dimensional spacetime may be a useful tool to analyze qualitative features of sQGP[41, 42, 43, 44, 45]. Since the gauge theory here can be regarded as a hologram of the string theory, the AdS/CFT correspondence is sometimes abbreviated as holography. Despite the fact that the AdS/CFT correspondence as a conjecture has not been proved and the corresponding gauge theory,  $\mathcal{N} = 4$  super Yang-Mills theory originally proposed in the conjecture, is distinct from QCD, many studies such as thermodynamic properties and the shear viscosity to entropy density ratio in holography suggest that such a gauge theory and QCD have similar features at the finite temperature of RHIC and LHC[46, 47, 30, 48]. Based on this "evidence", the AdS/CFT correspondence has been widely applied to investigate many observables in heavy ion collisions, while the direct comparisons with experimental measurements are still challenging. On the other hand, the understanding of the pre-equilibrium state before the QGP phase is as well insufficient in theory. In the weakly coupled scenario, the color glass condensate (CGC)[49, 50, 51, 52] based on the gluon saturation at the small Bjorken scaling  $Q_s^2/s$  approximates the gluons by classical gauge fields. This effective theory is employed to provide the initial conditions for the pre-equilibrium state[53, 54, 55]. Although CGC may provide a more realistic initial conditions for heavy ion collisions based on QCD, which can further incorporate initial-state fluctuations[56, 57, 58], CGC itself can not explain the rapid thermalization. As a counter part in the strongly coupled scenario, holographic models are proposed to simulate the collisions and thermalization of the medium[23, 24, 59, 60, 61, 62, 63, 64, 65, 66, 25, 26, 27, 28, 67].

In the following sections, we will elaborate in more about the strongly coupled features of QGP and introduce the relevant observables in experiments. On the other hand, we will also review the theoretical approaches proposed to address the experimental measurements, while more emphasis will be put on the related works

in holography.

## 1.2 Hydrodynamics and Elliptic Flow

Hydrodynamics is a low-energy effective theory based on local conservation of charges and energy-momentum,

$$\partial_\mu T^{\mu\nu}(x) = 0, \quad \partial_\mu N^\mu(x) = 0, \quad (1.1)$$

where  $T^{\mu\nu}$  and  $N^\mu$  here denote the energy-momentum tensor and the current of the baryon number(or electric charge), respectively. The hydrodynamic evolution depends on initial conditions, equations of state, and the transport coefficients characterizing viscous effects. In most of cases, only numerical solutions can be attained, while one can obtain analytical solutions with certain approximations. The Bjorken expansion can be taken as a simplest initial condition for the longitudinal expansion[68], which approximates boost-invariant particle production along the beam axis. As shown in Fig.1.2, it turns out that the Bjorken expansion is valid in the mid-rapidity regime in high-energy collisions. To be more concrete, we will perform simple calculations to solve the conservation equations in (1.1) in an ideal fluid with the Bjorken expansion. For clarity, we should mention that the pseudo rapidity  $\eta$  is defined as

$$\eta = -\ln\left(\tan\frac{\Theta}{2}\right), \quad (1.2)$$

where  $\Theta$  is the angle between the momentum of the produced particle  $\vec{p}$  and the beam axis  $\hat{z}$ . At high energy, it is equal to the momentum rapidity defined as

$$\tilde{y} = \frac{1}{2}\ln\left(\frac{E+p_z}{E-p_z}\right) \approx \frac{1}{2}\ln\left(\frac{1+\cos\Theta}{1-\cos\Theta}\right) = \eta. \quad (1.3)$$

We will hereafter use the momentum rapidity as the rapidity throughout this dissertation.

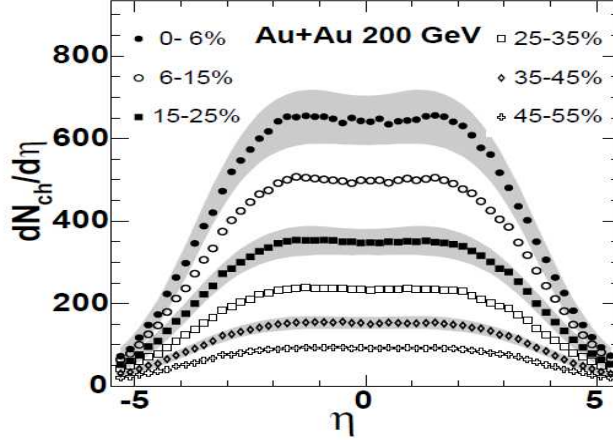


FIGURE 1.2: The pseudo-rapidity distributions for charged particles for different centralities[1].

Now the energy-momentum tensor and the particle-number current can be written as

$$T^{\mu\nu} = (\epsilon + P)u^\mu u^\nu - P g^{\mu\nu} + \Pi^{\mu\nu}, \quad N^\mu = n u^\mu, \quad (1.4)$$

where  $P$ ,  $\epsilon$ , and  $n$  are the pressure, energy, and number densities, respectively. Here  $u^\mu = dx^\mu/d\tau$  denotes the local velocity of the fluid and  $g_{\mu\nu}$  represents the spacetime metric, where  $\tau$  denotes the proper time and we have  $u^\mu u_\mu = -1$ . The last term  $\Pi^{\mu\nu}$  in the energy-momentum tensor is the viscous stress tensor that includes the shear and bulk viscosities stemming from dissipation. Considering ideal hydrodynamics for a perfect fluid, we will take  $\Pi^{\mu\nu} = 0$ . By contracting the conservation of energy-stress tensor in (1.1) with  $u^\nu$  and using the expressions in (1.4), one obtains

$$\begin{aligned} u^\mu \partial_\mu \epsilon + (\epsilon + P) \partial_\mu u^\mu &= 0, \\ u^\mu \partial_\mu n + n \partial_\mu u^\mu &= 0. \end{aligned} \quad (1.5)$$

Next, we should consider the boost invariant setup. In the simplest case, we assume that the transverse distribution of particle number and that of the energy are homogeneous, which corresponds to the so-called (0 + 1)d model. The medium only

expands along the  $z$  axis as the beam direction. By making the coordinate transformations,

$$t = \tau \cosh \tilde{y}, \quad z = \tau \sinh \tilde{y}, \quad (1.6)$$

one then derives

$$\begin{aligned} u^\mu &= (\cosh \tilde{y}, 0, 0, \sinh \tilde{y}), \\ u^\mu \partial_\mu &= \partial_\tau, \quad \partial_\mu u^\mu = \tau^{-1}. \end{aligned} \quad (1.7)$$

By inserting the relations in (1.7) into (1.5), we find

$$\begin{aligned} \partial_\tau \epsilon + \frac{1}{\tau}(\epsilon + P) &= 0 \\ \partial_\tau n + \frac{n}{\tau} &= 0. \end{aligned} \quad (1.8)$$

The second equation in (1.8) yields

$$n(\tau) = n_0 \frac{\tau_0}{\tau}, \quad (1.9)$$

where  $n_0$  and  $\tau_0$  represent the initial number density and the initial(thermalization) time. Such a relation directly indicates that  $dN/d\tilde{y} = 0$ , which is consistent with the experimental measurements shown in Fig.1.2 at central rapidity. One may further assume the ideal-gas equation of state,  $P = \epsilon/3$  and  $\epsilon \propto T^4$ , which gives rise to the time-evolution of the energy density and temperature as

$$\begin{aligned} \epsilon(\tau) &= \epsilon_0 \left( \frac{\tau_0}{\tau} \right)^{\frac{4}{3}}, \\ T(\tau) &= T_0 \left( \frac{\tau_0}{\tau} \right)^{\frac{1}{3}}, \end{aligned} \quad (1.10)$$

where  $\epsilon_0$  and  $T_0$  denote the initial energy density and the initial temperature. The first equation in (1.8) is utilized to derive the above relations.

In reality, even at the central rapidity, the  $(0 + 1)$ d model is too coarse. In the  $(2 + 1)$ d hydrodynamic simulations, the transverse expansion is considered. For transverse directions, distinct initial conditions such as the Glauber model[69, 70] and Kharzeev-Levin-Nardi(KLN) model[53, 71, 72, 54, 73, 57] are applied. The Glauber model is basically a geometrical constraint on the distributions, where the initial energy or entropy density profile is taken to be proportional to the profile of nucleon-nucleon collisions. On the contrary, the KLN model approximates the entropy density distribution proportional to the distribution of gluons produced in primary collisions in the framework of CGC. Also, the equation of state is nowadays obtained by lattice QCD. Moreover, the ideal hydrodynamics assumes local thermal equilibrium and that the system is non-dissipative. When the system is slightly away from thermal equilibrium, one can perform the derivative expansion of the energy-momentum tensor, which leads to the stress viscous tensor. The transport coefficients of the derivative terms such as the shear and bulk viscosities are attributed to the dissipative effect. These transport coefficients are usually determined by fitting experimental data. It turns out that the transport coefficients results in significant effects upon many observables, see the review[74] and references therein. Although the transport coefficients can not be directly derived from hydrodynamics itself, they may be computed in the strongly coupled systems analogous to the QGP via the AdS/CFT correspondence. For example, the renowned lower bound for the shear viscosity to entropy density ratio is derived from a strongly coupled  $\mathcal{N} = 4$  SYM plasma at large  $N_c$  limit through holography[46, 30], where the result is rather close to the values extracted from RHIC data.

In experiments, one of the most important observables supporting the fluid behavior of the QGP is the so-called elliptic flow. In the central-rapidity region of non-central collisions as illustrated in Fig.1.3, the position-space anisotropy of the medium results in large pressure gradient parallel(or anti-parallel) to  $x$  axis.

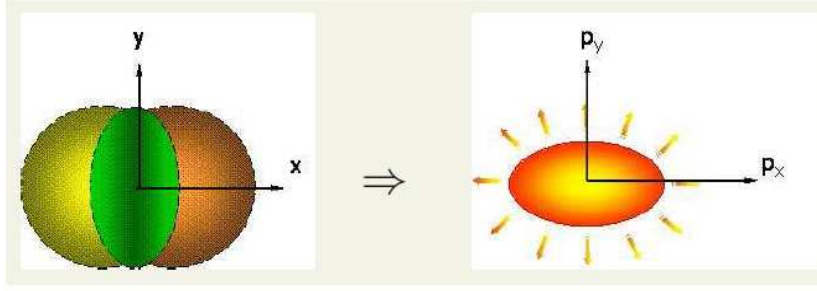


FIGURE 1.3: The schematic figure of azimuthal asymmetry of the medium in position and momentum spaces. In the left panel, the green region represents the cross section of two colliding nuclei in non-central collisions. In the right panel, the orange region represents the corresponding anisotropic momentum distribution. The figure is taken from the lecture of P. Huovinen in Jet Summer School 2012.

Therefore, particles receive greater momenta along  $\pm\hat{x}$  directions, which convert the position-space anisotropy into the momentum-space anisotropy. Such azimuthal asymmetry in transverse directions can be characterized by the elliptic flow,

$$v_2(p_T, \tilde{y}) = \frac{\int_0^{2\pi} d\theta \cos(2\theta) \frac{dN}{d^2p_T d\tilde{y}}}{\int_0^{2\pi} d\theta \frac{dN}{d^2p_T d\tilde{y}}}, \quad (1.11)$$

where  $\theta$  denotes the angle between the transverse momentum  $\vec{p}_T$  and the reaction plane and  $N$  represents the particle yield. From the definition, large  $v_2$  as well implies the enhanced particle production along the  $\pm\hat{x}$  directions relative to that along the  $\pm\hat{y}$  directions. Large  $v_2$  of charged particles as a fluid-like signal were observed in RHIC and LHC[3, 4, 5, 75]. As shown in Fig.1.4, the RHIC data match the hydrodynamic simulations for hadron  $v_2$  with small transverse momenta.

Although ideal hydrodynamics was first applied to analyze the data, where it stems from the local thermal equilibrium and pressure isotropy, the recent development of viscous hydrodynamics[76, 77, 78, 79, 58, 80] and anisotropic hydrodynamics[81,

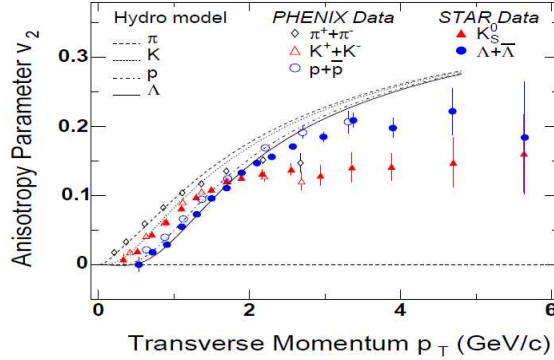


FIGURE 1.4: The comparison between hadron  $v_2$  obtained from ideal hydrodynamics[2] and those measured in RHIC[3, 4, 5]. The figure is taken from [6].

82, 83, 84, 85, 86, 7] reveals a large pressure difference between the longitudinal (beam) and transverse directions. As shown in Fig.1.5, the pressure anisotropy may exist even at very late time near the freeze-out at  $\tau \sim 7 - 10$  fm. When the shear viscosity to entropy density ratio increases, the pressure anisotropy will be increased. More recent comparisons of the hydrodynamic simulations and experimental data also suggest that QGP has small but nonzero shear viscosity. In addition, the pressure anisotropy is also found in the studies of thermalization via the AdS/CFT correspondence. As shown in [27, 28], the longitudinal pressure is smaller than the transverse one even after the thermalization. Due to the rising evidence, the influence of pressure anisotropy and viscous effects on various probes in heavy ion collisions has been widely studied, see the review[87] and references therein.

### 1.3 Jet quenching of hard probes in the medium

From the high-energy scatterings in the collisions, the back-to-back jets comprising energetic partons are engendered in both proton-proton(p+p) collisions and heavy ion collisions. In heavy ion collisions, most of the hard partons form energetic pions as lightest mesons after the freeze-out. On the other hand, heavy quarks are generated

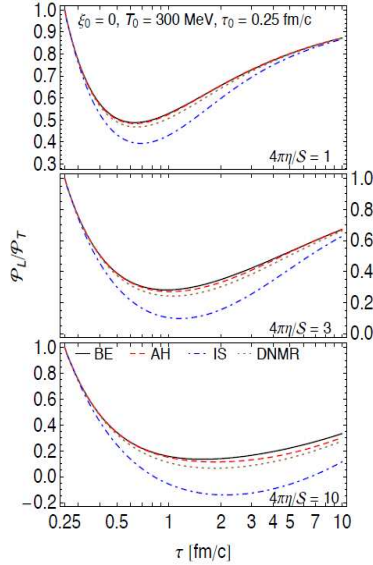


FIGURE 1.5: Pressure anisotropy as a function of proper time with different anisotropic and viscous hydrodynamics approximations corresponding to different color lines. Here  $\xi_0$  denotes the initial momentum- space anisotropy and  $\eta/S$  denotes the shear viscosity to entropy density ratio. The figure is taken from [7].

from hard scatterings as well due to their large mass above the temperature of QGP. The hard probes such as energetic partons and heavy quarks may not inherit the bulk properties and collectively evolve with the medium. However, due to the interaction with the medium, the behaviors of hard probes traveling through QGP in heavy ion collisions are distinct from that through vacuum in p+p collisions. As depicted in Fig.1.6, one of the hard probes created as a pair traversing further in the medium scatters with the medium more extensively and loses more energy in the end. The yield of such a hard probe is thus suppressed, which is called jet quenching in heavy ion physics and is one of the signals supporting the existence of QGP.

In experiments, the jet quenching is characterized by the nuclear modification factor as a function of transverse momenta of hadrons and rapidity,

$$R_{AB}^h(p_T, \tilde{y}) = \frac{\frac{dN^{AB \rightarrow h}}{dp_T d\tilde{y}}}{\langle N_{AB} \rangle \frac{dN^{pp \rightarrow h}}{dp_T d\tilde{y}}}, \quad (1.12)$$

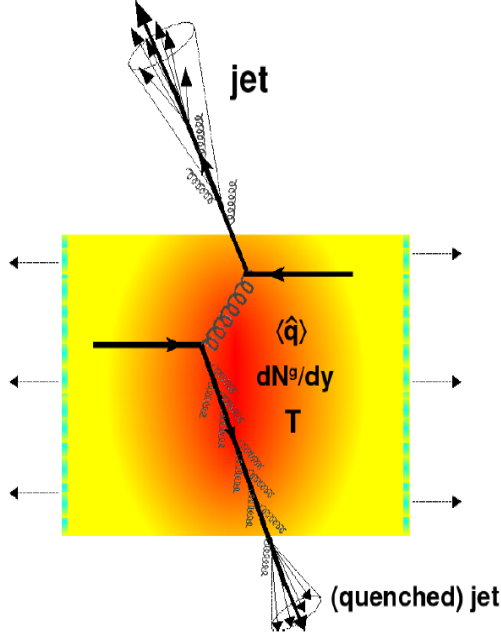


FIGURE 1.6: Two energetic quarks created back-to-back in the medium: one travels mostly in the vacuum and one traverses the plasma. The former radiates few gluons and quickly hadronizes, while the latter loses more energy due to the induced radiation and finally fragments into the quenched jet. The jet quenching is characterized by the transport coefficient  $\hat{q}$ , gluon density per rapidity  $dN_g/dy$  and temperature  $T$ . The figure is taken from [8].

where  $N^{AB \rightarrow h}$  denotes the number of hadrons produced from the collisions of nucleus A and nucleus B and  $N^{pp \rightarrow h}$  denotes the number of hadrons produced from p+p collisions. Here  $\langle N_{AB} \rangle$  corresponds to the average number of the nucleon-nucleon collisions in A+B collisions, which is introduced to compare the A+B collisions with p+p collisions on equal footing. Given that  $R_{AB}^h < 1$ , one can conclude that jet quenching does exist. From RHIC data as shown in Fig.1.7, the strong suppression for pion-production is observed. Notice that  $R_{AA}^h$  as well depends on the centrality of collisions. In more central collisions, the hard probes may travel a longer distance in the medium. The  $R_{AA}^h$  thus is smaller in such cases[88]. On the other hand, in order to disentangle the influences from initial conditions (early state) and from medium (final state) effects, we may refer to the  $R_{dA}^h$  for d-Au(deuteron-gold) collisions[89, 90],

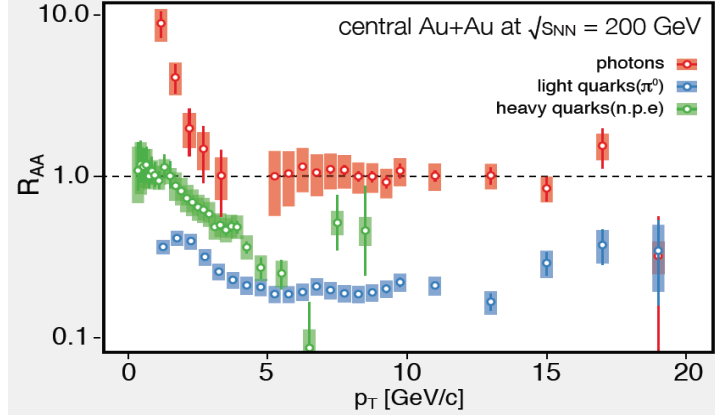


FIGURE 1.7: The nuclear modification factors for different particles measured in RHIC[9].

where  $R_{dA}^h \approx 1$  for the arbitrary transverse momentum and rapidity. It turns out that the jet quenching is less affected by the early state due to the absence of a thermal medium formed in d+A collisions. In addition, electromagnetic probes such as high-energy photons are approximately unaffected by the thermal medium after they have been produced due to weak electromagnetic couplings. As long as the initial conditions for photoemission are similar in p+p collisions and in A+A collisions, we should expect no suppression in the latter case. Thus, the dominance of the medium effect upon jet quenching is as well supported by  $R_{AA}^\gamma \approx 1$  for the high-energy photon production in A+A collisions as presented in Fig.1.7.

In theory, according to the experimental observations, one may assume that the modification of the spectra of hard probes in the medium compared with those in vacuum arises from parton energy loss[91, 92, 93, 94, 95, 96]. Upon this assumption, the modified partonic cross sections in the medium can be written as

$$d\sigma_{\text{med}}^{AB \rightarrow h + \text{rest}} = \sum_f d\sigma_{\text{vac}}^{AB \rightarrow f + X} \otimes P_f \otimes D_{f \rightarrow h}^{\text{vac}}, \quad (1.13)$$

where  $\sigma_{\text{vac}}^{AB \rightarrow f + X}$  denote the cross sections of p+p collisions augmented by the nuclear distribution functions. Here  $D_{f \rightarrow h}^{\text{vac}}$  denotes the fragmentation function from the

intermediate parton  $f$  to the final hadron  $h$ . All information of the energy loss  $\Delta E$  is encoded in the function  $P_f$ . The nuclear modification factor can be as well written as

$$R_{AB}^h(p_T, \tilde{y}) = \frac{\frac{d\sigma^{AB \rightarrow h + \text{rest}}}{dp_T d\tilde{y}}}{\langle N_{AB} \rangle \frac{d\sigma^{pp \rightarrow h+X}}{dp_T d\tilde{y}}}. \quad (1.14)$$

In general, the mechanisms of energy loss for hard probes in QGP mainly arise from medium-induced radiation and collisions. One of the parameters that characterizes the interaction between hard probes and the medium is the jet quenching parameter  $\hat{q}$ , which is roughly defined as

$$\hat{q} = \frac{\langle p_t^2 \rangle}{\Delta L}, \quad (1.15)$$

where  $\langle p_t^2 \rangle$  represents the momentum broadening and  $\Delta L$  denotes the distance traversed by the hard probes. Here  $p_t$  corresponds to the momentum transverse to the moving direction of hard probes, which is distinct from  $p_T$  as the momentum transverse to the beam direction. In the central rapidity regime,  $p_t$  is approximately perpendicular to  $p_T$ . From pQCD, the average medium-induced energy loss is given by

$$\Delta E = \frac{\Delta L^2}{8} \alpha_s C_R \hat{q}, \quad (1.16)$$

where  $g_s = \sqrt{4\pi\alpha_s}$  is the QCD coupling and  $C_R$  is the Casimir operator. Since  $\hat{q}$  is non-perturbative, it can only be extracted from experimental data or evaluated via strongly coupled approaches.

In the AdS/CFT correspondence, the jet quenching parameter of heavy quarks can be computed from a light-cone Wilson loop in a thermalized background[97, 98]. The result reads

$$\hat{q}_{\text{SYM}} = \frac{\pi^{3/2} \Gamma(\frac{3}{4})}{\Gamma(\frac{5}{4})} \sqrt{\lambda} T^3 \quad (1.17)$$

for  $\mathcal{N} = 4$  SYM plasma, where  $\lambda = g_{YM}^2 N_c$  denotes the t'Hooft coupling. Here  $N_c$  is the number of colors and  $g_{YM} = \sqrt{4\pi\alpha_{YM}}$  is the coupling of SYM plasma. Taking  $N_c = 3$  and  $\alpha_s = 1/2$  as an analog of the condition in sQGP, one finds  $\hat{q} = 4.5, 10.6,$  and  $20.7 \text{ GeV}^2/\text{fm}$  for  $T = 300, 400,$  and  $500 \text{ MeV}$ [97]. Recent analysis of the measurements in RHIC suggests that  $\hat{q} = 2 - 10 \text{ GeV}^2/\text{fm}$ [9], which approximately agrees with the AdS/CFT result for  $T = 300 - 400 \text{ MeV}$  as the RHIC initial temperature. Nonetheless, the computation for  $\hat{q}$  in [98, 97] only involves the collisional energy loss. On the contrary, the radiation energy loss in the strongly coupled scenario is characterized by a trailing string[99, 100]. In this setup, the end of the string moving on the boundary, where the strongly coupled gauge theory lives, mimics a heavy quark traversing the medium. By assuming that the energy loss is due to the drag force exerted on the string, the radiation energy loss in this scenario is given by

$$\frac{dE}{dt} = -\frac{\pi}{2}\sqrt{\lambda}T^2\gamma v^2, \quad (1.18)$$

where  $\gamma$  is the Lorentz factor and  $v$  is the velocity of the quark. Nevertheless, the trailing-string scenario results in over-suppression of the nuclear modification factors for heavy quarks in comparison with the experimental measurements[101].

On the other hand, one may speculate that the hard probes, especially for light probes such as light quarks or gluons, may not travel all the way through the medium. They may gradually lose energy and diffuse (stop) in the medium. Such a notion leads to the analysis of a different quantity related to jet quenching, which is the so-called stopping distances. In holography, the scenario is characterized by falling strings[102, 103] or the supergravity excitation viewed as a point particle falling into the black hole[104, 105]. From these approaches, it is found that

$$x_s^{\text{max}} \propto E^{\frac{1}{3}}, \quad (1.19)$$

where  $x_s^{\max}$  is the possible maximum stopping distance. This energy-dependent stopping distance can be further implemented in phenomenological models to evaluate  $R_{AA}$  for light probes[106].

#### 1.4 Strong Electromagnetic Fields in Heavy Ion Collisions

In non-central collisions, strong electromagnetic fields can be produced by the fast-moving nuclei. In the region near the origin of the coordinates shown in Fig.1.3 where the QGP is firstly formed, one may expect a strong magnetic field pointing along the  $y$  direction. However, by symmetry, the average electric field in such a region will be approximately zero. By assuming the colliding nuclei moving along the  $\pm z$  directions with the same speed  $v$  and the nuclear charge  $Ze$  to be distributed uniformly within the nuclear radius  $R$ , the magnetic field in such a region can be approximated as

$$\mathbf{B}(t) \approx \frac{Ze\gamma vb}{4\pi (R^2 + \gamma^2 v^2 t^2)^{3/2}} \hat{y}, \quad (1.20)$$

where  $b$  is the impact parameter and  $\gamma$  is the Lorentz factor. Considering non-central Au+Au collisions with  $\sqrt{s} = 200$  GeV per nucleon and  $b \approx R$ , we have  $Z = 79$ ,  $R \approx 7$  fm,  $v \approx 1$ , and  $\gamma \approx 100$ . At  $t = 0$ , the magnitude of the magnetic field is about

$$|e\mathbf{B}(0)| = eB_y(0) \approx 4.56 \times 10^{-2} \text{GeV}^2 \approx 2m_\pi^2, \quad (1.21)$$

which is  $10^5$  times larger than the critical magnetic field of electrons  $|e\mathbf{B}_c| = m_e^2 = 2.5 \times 10^{-7} \text{GeV}^2$  with  $m_\pi$  and  $m_e$  being the pion and electron masses. When  $|e\mathbf{B}| \gg |e\mathbf{B}_c|$ , the classical electrodynamics may breakdown and nonlinear quantum electrodynamics(QED) effects become pronounced[107]. On the other hand, the QGP approximately behaves as an chiral system due to  $T \gg m_q$  with  $m_q$  being the masses of light quarks. In the presence of topological charge fluctuations

pertinent to the axial anomaly in QCD, which results in nonzero vector and axial chemical potentials in QGP, accompanied by the electromagnetic anomaly, a mechanism called chiral magnetic effect(CME) was proposed[108, 109, 110, 111]. From CME, the magnetic field will induce a vector current parallel to it via

$$\mathbf{J}_\mathbf{v} = \frac{N_c e}{2\pi^2} \mu_A \mathbf{B}, \quad (1.22)$$

where  $\mu_A$  represents the axial chemical potential,  $N_c$  is the degree of freedom for fermions,  $\mathbf{B}$  is the external magnetic field, and  $e$  is the electric charge. Along with CME, the magnetic field can also trigger an axial current parallel to the applied field in the presence of nonzero charge density via

$$\mathbf{J}_\mathbf{a} = \frac{N_c e}{2\pi^2} \mu_V \mathbf{B}, \quad (1.23)$$

where  $\mu_V$  represents a vector chemical potential. This effect is called chiral separation effect(CSE)[112]. Based on these two effects, the fluctuations of both  $\mu_A$  and  $\mu_V$  result in a propagating wave as the chiral magnetic wave(CMW)[110]. As shown in [113], the CMW could generate a chiral dipole and charge quadrupole in QGP, which may contribute to the charge asymmetry of elliptic flow  $v_2$  measured in RHIC[114, 115].

Also, the strong magnetic field may enhance the photon production in heavy ion collisions[116, 117, 118, 119, 120], which serves as one of the possible mechanisms to cause large photon  $v_2$  recently measured in RHIC[10] and in LHC[121]. Unlike the hadronic flow, the large flow of direct photons (i.e. not originating from the hadronic decays) is unexpected since the high-energy photons are presumed to be generated in early times, where the initial flow should be relatively small compared to the flow built up by hydrodynamics. In general, the photons with  $p_T > 1$  GeV are categorized as direct photons. The direct photons mainly incorporate prompt photons created

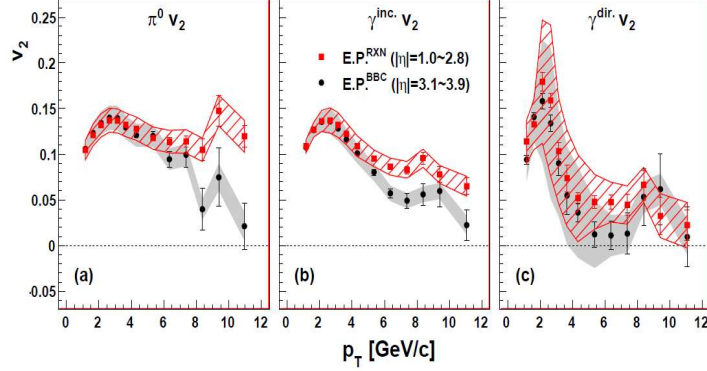


FIGURE 1.8:  $v_2$  in minimum bias collisions, using two different reaction plane detectors for (a) $\pi^0$ , (b)inclusive photons, (c)direct photons [10].

in the pre-equilibrium state and thermal photons generated in QGP. Surprisingly, as shown in Fig.1.8, the direct-photon  $v_2$  is comparable to pion  $v_2$  in RHIC. Similar observations were found in LHC as well[121].

In addition to the strong magnetic field, a strong electric field could be produced in heavy ion collisions as well. In general, the magnitude of the average electric field is much smaller than that of the average magnetic field by symmetry as mentioned in the previous context. Nonetheless, based on the fluctuations of colliding nuclei, it has been shown that the magnitude of the electric field can be comparable to that of the magnetic field[122]. Moreover, in the asymmetric collisions such as Cu + Au collisions for two colliding nuclei having different numbers of charge, there exists a strong electric field directing from the Au nucleus to the Cu nucleus[123]. Accordingly, a novel phenomenon called chiral electric separation effect(CESE) was proposed in Ref.[124]. In the presence of both vector and axial chemical potentials, an axial current can be induced by an electric field  $\mathbf{E}$  through

$$\mathbf{J}_a = \sigma_5 \mathbf{E} = \chi_e \mu_V \mu_A \mathbf{E}, \quad (1.24)$$

where  $\sigma_5$  denotes the anomalous conductivity which is proportional to the product of  $\mu_V$  and  $\mu_A$  for small chemical potentials compared to the temperature ( $\mu_{V/A} \ll T$ )

and  $\chi_e$  is a function of  $T$  in that case. Unlike CME and CSE, the CESE does not originate from the electromagnetic anomaly, but naturally comes from the interactions of chiral fermions. In fact, the normal conductivity also receives the correction proportional to  $\mu_V^2 + \mu_A^2$  in the system. Combining CESE with CME, the authors in Ref.[124] further indicated that a charge quadrupole could be formed in the asymmetric collisions, which may give rise to nontrivial charge azimuthal asymmetry as a signal for CESE in experiments.

Although the initial magnetic field is rather strong in heavy ion collisions, according to (1.20), it decreases rapidly with respect to time as  $|e\mathbf{B}(t)| \sim |e\mathbf{B}(0)|t^{-3}$  in vacuum. Nevertheless, the thermal quarks in QGP may have nonzero electrical conductivity  $\sigma_e$ , which could extend the lifetime of the magnetic field. Such an electrical conductivity can not be directly measured by experiments, but it can be computed by lattice QCD. As reported in Ref.[125], the result reads

$$\sigma_e = (5.8 \pm 2.9) \frac{T}{T_c} \text{MeV}, \quad (1.25)$$

where  $T$  is plasma temperature and  $T_c$  is critical temperature. By taking an approximation based on the diffusion equation of magnetic fields, it has been shown that the magnetic field with the nonzero electrical conductivity above depletes much slower than that in vacuum[126]. Nevertheless, there exist caveats for making such an approximation. The electric conductivity here is extracted from the zero-frequency mode of the spectral function. When having electromagnetic fields varying rapidly with time, the higher-frequency modes should become dominant. Also, as pointed out in [127], the diffusion equation relies on an unrealistic condition, where the electric conductivity is much larger than the inverse of the characteristic time scale of the magnetic field. Although the precise lifetime of magnetic fields generated in heavy ion collisions is undetermined, it is generally believed that the magnetic field drops rapidly after the collisions.

## 1.5 Outline of the Dissertation

In this dissertation, we will utilize the AdS/CFT correspondence to investigate the properties of strongly coupled plasmas and their influence on different probes, which may facilitate our understanding of analogous scenarios in heavy ion collisions. For jet quenching, most of the previous studies in holography have been focused on the hard probes traveling in a thermalized and isotropic medium. We thus generalize the studies for light probes to the cases of out-of-equilibrium conditions with and without a chemical potential or in a thermal plasma with pressure anisotropy. On the other hand, we also investigate the influence of pressure anisotropy upon thermal photons. Motivated by the anomalous flow of direct photons observed by experiments, we further analyze the thermal-photon production in both isotropic and anisotropic backgrounds in the presence of a constant magnetic field. Moreover, by considering a chiral plasma with an electric field, we investigate CESE in the strongly coupled scenario. This dissertation emphasizes three significant effects on various probes in heavy ion collisions: 1) thermalization effects, 2) pressure anisotropy, and 3) external electromagnetic fields.

In addition to the review on the gauge/gravity duality in Chapter 2, the bulk of this dissertation is based on my works with my collaborators, presented in Chs. 3-7[128, 129, 130, 131, 132, 133]. The dissertation is organized in the following order. In Chapter 2, we make a brief review of the gauge/gravity duality and some essential techniques in holography, which will be applied or generalized in the following chapters.

In Chapter 3, we present our studies related to holographic thermalization and jet quenching in out-of-equilibrium conditions. We utilize the AdS-Vaidya metric describing a falling mass shell to investigate the thermalization of the strongly-coupled plasma. By studying the gravitational redshift in Poincare coordinates, we may ap-

proximate the thermalization time of the medium in the thin-shell limit. In addition, we compute the stopping distance of a massless particle traveling through the AdS-Vaidya spacetime in the Wentzel-Kramers-Brillouin (WKB) approximation, which characterizes the jet quenching of a light probe in the non-equilibrium plasma. However, for an energetic probe carrying infinite energy, its stopping distance would not be affected by the thermalization of the medium. In contrast, we study the stopping distance of a softer gluon described by the falling string. We find its stopping distance in the thermalizing plasma is larger than that in the thermalized plasma, which suggests that the jet quenching of a softer probe with the energy not infinitely larger than the thermalization temperature should be suppressed by the thermalization process of the medium. Also, the enhancement of stopping distances is more substantial for relativistic probes. Then we generalize our studies to the case with a nonzero chemical potential by analyzing a falling shell with charge characterized by the AdS-Reissner-Nordström-Vaidya (AdS-RN-Vaidya) geometry. We find that the stopping distance decreases when the chemical potential is increased in both AdS-RN and AdS-RN-Vaidya spacetimes, which correspond to the thermalized and thermalizing media respectively. Moreover, we find that the soft gluon with an energy comparable to the thermalization temperature and chemical potential in the medium travels further in the non-equilibrium plasma. The thermalization time obtained here by tracking a falling charged shell does not exhibit, generically, the same qualitative features as the one obtained studying non-local observables. This indicates that –holographically– the definition of thermalization time is observer dependent and there is no unambiguous definition.

In Chapter 4, we employ the gauge/gravity duality to study the jet quenching of light probes traversing a static yet anisotropic strongly coupled  $\mathcal{N} = 4$  SYM plasma. We compute the stopping distance of an image jet induced by a massless source field, which is characterized by a massless particle falling along the null geodesic in the

WKB approximation, in an anisotropic dual geometry introduced by Mateos and Trancanelli(MT). At mid and large anisotropic regimes, the stopping distances of a probe traveling in the anisotropic plasma along various orientations are suppressed compared to those in an isotropic plasma especially along the longitudinal direction at equal temperature. However, when fixing the entropy density, the anisotropic values of stopping distances near the transverse directions slightly surpass the isotropic values. In general, the jet quenching of light probes is increased by the anisotropic effect in a strongly coupled and equilibrium plasma.

Next, we consider the thermal-photon production in the same anisotropic background. In order to include the effects from massive quarks, we work in the black hole embeddings in the D3/D7 system. We find that the photon spectra with different quark mass are enhanced at large frequency when the photons are emitted parallel to the anisotropic direction with larger pressure. However, for photons emitted perpendicular to the anisotropic direction, the spectra approximately saturate isotropic results.

In Chapter 5, we further investigate the influence of a constant magnetic field on the thermal-photon production in the MT geometry. The photoemission rate is increased for photons moving perpendicular to the magnetic field. Moreover, a resonance emerges at moderate frequency for the photon spectrum with heavy quarks when the photons move along that direction. The resonance is more robust when the photons are polarized along the magnetic field. On the contrary, in the presence of pressure anisotropy, the resonance will be suppressed. There exist competing effects of magnetic field and pressure anisotropy on meson melting in the strongly coupled SYM plasma, while we argue that the suppression led by anisotropy may not apply to the quark gluon plasma. Motivated by the enhancement led by magnetic field, we compute the elliptic flow  $v_2$  of thermal photons in the cases of a 2+1 flavor SYM plasma analogous to the photon production in QGP, we obtain the thermal-photon

$v_2$ , which is qualitatively consistent with the direct-photon  $v_2$  measured in RHIC at intermediate energy. However, due to the simplified setup, the thermal-photon  $v_2$  in our model should be regarded as an upper bound for the  $v_2$  generated solely by a magnetic field in the strongly coupled scenario.

In Chapter 6, we investigate the chiral electric separation effect, where an axial current is induced by an electric field in the presence of both vector and axial chemical potentials, in a strongly coupled plasma via the Sakai-Sugimoto model with an  $U(1)_R \times U(1)_L$  symmetry. By introducing different chemical potentials in  $U(1)_R$  and  $U(1)_L$  sectors, we compute the axial direct current (DC) conductivity stemming from the chiral current and the normal DC conductivity. We find that the axial conductivity is approximately proportional to the product of the axial and vector chemical potentials for arbitrary magnitudes of the chemical potentials. We also evaluate the axial alternating current (AC) conductivity induced by a frequency-dependent electric field, where the oscillatory behavior with respect to the frequency is observed.

The last chapter will summarize the main results of the dissertation and discuss some of the on-going efforts and future directions to improve our approaches and shed more light on heavy ion physics via holography.

## Review of the gauge/gravity duality

### 2.1 AdS/CFT Correspondence

The gauge/gravity duality or the so called AdS/CFT correspondence generally refers to a duality between an  $d$  dimensional strongly coupled gauge theory and an  $d + 1$  dimensional gravity theory in the curved spacetime. However, to be more precise, it is based on a conjecture proposed by Maldacena that the  $\mathcal{N} = 4$   $SU(N)$  supersymmetric Yang-Mills theory (SYM) in the large  $N$  limit is dual to the string theory in a curved background with the  $AdS_5 \times S^5$  geometry[41], where the  $S^5$  could be reduced when the  $\mathcal{R}$  symmetry is unbroken. The further studies have been carried out in [42, 43, 44, 45]. More relevant works can be found in the review articles[45, 48, 134, 12, 135] and the references therein.

Before beginning the discussion of the conjecture, we may briefly explain some of the terminologies above. In the gauge theory side, the supersymmetric transformation in  $\mathcal{N} = 4$   $SU(N)$  SYM theory is dictated by 32 supercharges encoded in four sets of complex Majorana fermions, where the  $\mathcal{N}$  denotes the number of such sets. Also, the  $\mathcal{N} = 4$   $SU(N)$  SYM theory as a conformal field theory (CFT) contains

one gauge field, four Majorana fermions, and six real scalars in the adjoint representation. In the gravity side, the  $AdS_{d+1}$  background represents an  $d + 1$  dimensional anti-de sitter space. Such a geometry can be described by a hyperboloid in the  $d + 2$  dimensional space,

$$X_0^2 + X_{d+1}^2 - \sum_{i=1}^d X_i^2 = L^2, \quad (2.1)$$

with the metric,

$$ds^2 = -dX_0^2 - dX_{d+1}^2 + \sum_{i=1}^d dX_i^2. \quad (2.2)$$

The metric now has a  $SO(2, d)$  isometry. By performing the proper coordinate transformation:

$$\begin{aligned} X_0 &= \frac{1}{2r} \left( 1 + z^2 \left( L^2 + \sum_{i=1}^{d-1} (x^i)^2 - t^2 \right) \right), & X_{d+1} &= Lrt, \\ X^i &= Lrx^i, & X^d &= \frac{1}{2r} \left( 1 - r^2 \left( L^2 - \sum_{i=1}^{d-1} (x^i)^2 + t^2 \right) \right), \end{aligned} \quad (2.3)$$

the metric can be rewritten as

$$ds^2 = L^2 \left( \frac{dr^2}{r^2} + r^2 (-dt^2 + \sum_{i=1}^{d-1} (dx^i)^2) \right), \quad (2.4)$$

which are the so-called Poincare coordinates. For simplicity, we will henceforth replace  $\sum_{i=1}^{d-1} (dx^i)^2$  by  $(dx^i)^2$ .

To understand the origin of such a conjecture, we should introduce the concept of  $D_p$  branes. We will then discuss the properties of  $D_p$  branes from two perspectives. Loosely speaking, we firstly analyze  $D_p$  branes from the gauge-theory side and then from gravity side. Based on similar features from two perspectives, we conjecture the

duality of the corresponding gauge theory and gravity theory for  $D_p$  branes. In string theory,  $D_p$  branes are  $p+1$  dimensional hypersurfaces that are the endpoints of open strings. The open string endpoints should obey Dirichlet boundary conditions along  $n - p - 1$  dimensions for  $n$  being the number of dimensions of the full spacetime, while the endpoints are allowed to move along the  $p + 1$  dimensions on the world-volume of  $D_p$  branes. In the presence of  $N$  coincident  $D_p$  branes, the endpoints of an open string can locate on different  $D_p$  branes, which results in an  $N \times N$  matrix corresponding to the adjoint representation of  $U(N)$  symmetry. Essentially, we can choose to decouple the  $U(1)$  gauge group from the  $SU(N)$  gauge theory in the full  $U(N)$  symmetry. We may regard the ground states of these open strings as the excitations of massless fields coupled to the  $D_p$  branes. More explicitly, the  $D_p$  branes are described by the so-called Dirac-Born-Infeld(DBI) action which is a generalization of the Nambu-Goto (NG) action,

$$S_{D_p} = T_{D_p} \int d^{p+1}x \sqrt{-\det(G_{\mu\nu} + 2\pi l_s^2 F_{\mu\nu})}, \quad (2.5)$$

where  $T_{D_p}$  denotes the tension and  $G_{\mu\nu}$  denotes the induced metric of  $D_p$  branes. Here  $F_{\mu\nu}$  represents the world-volume field strength coming from the gauge-field excitation on the  $D_p$  branes and  $l_s = \alpha'^{1/2}$  corresponds to the typical string length. In addition to the gauge-field, the  $D_p$  branes can also fluctuate along bulk directions, which contributes to  $n - p - 1$  scalar fields. Considering supersymmetry, there also exist fermionic excitations to balance the bosonic degrees of freedom. In the low energy limit, we may neglect the excitations of massive fields. Therefore, we have one gauge field,  $n - p - 1$  scalars, and corresponding massless fermions living on the  $D_p$  branes. Here we are particularly interested in the  $p = 3$  case. In the type II superstring theories with 10 dimensional spacetime, the low-energy effective theory of open strings living on  $D_3$  branes should incorporate one gauge field, four Majorana fermions, and six real scalars, which corresponds to an  $\mathcal{N} = 4$  SYM theory with

$SU(N)$  symmetry in the four dimensional spacetime.

On the other hand, there exist closed strings such as gravitons represented by the fluctuations of the spacetime metric, which are not constrained to  $D_p$  branes and free to propagate in the bulk. In general, the full action should be written as

$$S_f = S_{\text{branes}} + S_{\text{bulk}} + S_{\text{int}}, \quad (2.6)$$

where  $S_{\text{int}}$  contains the interaction between the open strings on the branes and the closed strings in the bulk. We can expand the bulk action in powers of the gravitational constant  $\kappa \sim g_s l_s^4$ , with  $g_s$  being the string coupling, as

$$S_{\text{bulk}} \sim \frac{1}{2\kappa^2} \int d^{10}x \sqrt{g} R \sim \int d^{10}x [(\partial h)^2 + \kappa h (\partial h)^2], \quad (2.7)$$

where  $g = \det(g_{\mu\nu})$  and we expand the spacetime metric as  $g_{\mu\nu} = \eta_{\mu\nu} + \kappa h_{\mu\nu}$ . Although we only consider the graviton encoded by the spacetime metric here, other terms including different fields should be expanded in the similar fashion. As shown in (2.5), the interaction terms are encoded in the DBI action. For example, the interaction between the spacetime metric and the world-volume gauge field on the  $D_3$  branes in the  $\kappa$  expansion reads

$$S_{\text{int}} \sim \int d^4x \sqrt{-g} \text{Tr}[F^2] + \dots \sim \kappa \int d^4x h_{\mu\nu} \text{Tr} \left[ F^\mu{}_\rho F^{\nu\rho} - \frac{\delta^{\mu\nu} F^2}{4} \right] + \dots \quad (2.8)$$

Actually, the spacetime metric  $g_{\mu\nu}$  in (2.8) should be replaced by the induced metric  $G_{\mu\nu}$  on the  $D_3$  branes, while the expansion usually reduces to the same form. When we fix energy and take  $l_s \rightarrow 0$ , which corresponds to  $\kappa \rightarrow 0$ , we find that the interaction terms vanish. Therefore, the open strings and closed strings become decoupled in such a limit. The bulk action ends up with free supergravity(i.e. gravitons propagate in the flat spacetime), whereas the  $D_3$ -brane action incorporates the  $\mathcal{N} = 4$  SYM theory living in the flat geometry with four spacetime dimensions.

Next, we may study the same system from a different point of view. The  $D_p$  branes can carry charge and act as sources of bulk fields. In type II supergravity, the semi-classical solution of  $D_3$  branes is given by [136]

$$ds^2 = H^{-1/2}(-dt^2 + d^2x^i) + H^{1/2}(dr^2 + r^2 d\Omega_5^2), \quad C_{0123} = 1 - H^{-1}, \quad (2.9)$$

where

$$H = 1 + \frac{L^4}{r^4}, \quad L^4 = 4\pi g_s l_s^4 N_c. \quad (2.10)$$

Here  $i = 1, 2, 3$  denote the spatial dimensions on  $D_3$  branes,  $r$  represents the radial coordinate transverse to the  $D_3$  branes, and  $C_{0123}$  is a four-form field coupled to  $D_3$  branes. The string coupling  $g_s$  is now characterized by the ratio of a dimensionful constant  $L$  and the typical string length  $l_s$ . The metric component of  $-dt^2$  is regarded as a redshift factor since there exists a horizon at  $r = 0$ . For an observer on the boundary at  $r \rightarrow \infty$ , the energy in the bulk reads

$$E = H^{-1/4} E_r = \left(1 + \frac{L^4}{r^4}\right)^{-1/4} E_r, \quad (2.11)$$

where  $E_r$  is the energy measured by an observer at the bulk  $r$ . Due to the redshift factor, the energy of an object measured by an observer at infinity becomes smaller as it approaches the horizon (bottom of the throat) at  $r \rightarrow 0$ . As a result, there exist two types of low energy excitations measured by an observer at infinity. One corresponds to massless fields propagating in the bulk with large wavelengths. Another type results from the near-horizon excitations with arbitrary sizes. In the low energy limit, these two types of excitations are decoupled. As shown in [137], the low energy absorption cross section of the massless scalar field is given by

$$\sigma_{\text{abs}} = \frac{\pi^4}{8} \omega^3 L^8, \quad (2.12)$$

where  $\omega$  is the energy of the scalar field. The cross section vanishes as  $\omega L \ll 1$ , which is the case for the field with a wavelength much larger than  $L$ . From (2.9), we see that the redshift factor  $H \rightarrow 1$  of the spacetime metric in the bulk for  $r \gg L$ . Thus, we have free supergravity in the bulk region. In the near-horizon region for  $r \rightarrow 0$ , the spacetime metric reduces to

$$ds^2 = \frac{r^2}{L^2}(-dt^2 + (dx^i)^2) + \frac{L^2}{r^2}(dr^2 + r^2 d\Omega_5^2). \quad (2.13)$$

It is then more convenient to work in the coordinates with a finite boundary by making the coordinate transformation  $z = L^2/r$ . The spacetime metric in (2.13) becomes

$$ds^2 = \frac{L^2}{z^2}(-dt^2 + (dx^i)^2 + dz^2) + L^2 d\Omega_5^2, \quad (2.14)$$

which is the  $AdS_5 \times S^5$  geometry. Here  $L$  governs the radius of  $S^5$ , which is usually called the AdS radius.

By comparing the  $D_3$ -brane system from two points of view as discussed above, we find that the bulk is governed by free supergravity in the low energy limit from both perspectives. The remained parts are the  $SU(N)$   $\mathcal{N} = 4$  SYM theory on the  $D_3$  branes and the low energy excitations in the  $AdS_5 \times S^5$  geometry. It is then natural to conjecture the correspondence between  $SU(N)$   $\mathcal{N} = 4$  SYM theory in four dimensional spacetime and the supergravity in the  $AdS_5 \times S^5$  background geometry. A schematic representation of the AdS/CFT correspondence is shown in Fig. 2.1. Although the spacetime is warped by the  $D_3$  branes located in the IR regime at the horizon, we can further introduce the  $D_3$  probe branes on the boundary characterizing the  $SU(N_c)$   $\mathcal{N} = 4$  SYM theory in the UV scale. In fact, the UV behaviors of operators in the gauge theory side will be our primary concern. Moreover, the correspondence can be further supported by the symmetries. The  $\mathcal{N} = 4$  SYM theory

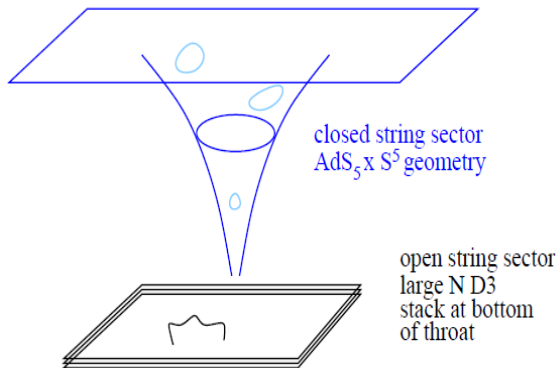


FIGURE 2.1: Schematic representation of the AdS/CFT duality[11].

is a conformal theory, which preserves a  $SO(2,4)$  symmetry from the combination of the conformal symmetry and Lorentz symmetry. In addition, the  $\mathcal{R}$  symmetry for the  $\mathcal{N} = 4$  supercharge yields an additional  $SU(4) \sim SO(6)$  symmetry. From (2.14), we see that the  $AdS_5$  and  $S^5$  backgrounds as well possess  $SO(2,4)$  and  $SO(6)$  isometries, respectively. The consistency of the symmetry of the SYM theory and the isometry of the curved background further supports the correspondence. In general, the  $S^5$  can be further reduced. The AdS/CFT correspondence sometimes may simply refer to the duality between the SYM theory in the four-dimensional spacetime and the gravity in an  $AdS_5$  background with restrictions to a certain subsector of the SYM theory. Subsequently, we should briefly discuss the regime of validity for this correspondence. As mentioned in the  $\kappa$  expansion below (2.8), the decoupling limit is reached by taking the typical string length  $l_s \rightarrow 0$ . From the gravity point of view as shown in (2.11), the low energy limit with respect to the observer on the boundary corresponds to  $L \gg r$ . Now the only relevant scale in the system is the typical string length. Such a limit for  $r \sim l_s \ll L$  as well implies the small string length. From (2.10), we see that the ratio  $L^4/l_s^4$  is proportional to  $g_s N_c$ . On the other hand, the string coupling can be related to the YM coupling thorough[138],

$$\lambda = g_{\text{YM}}^2 N = 4\pi g_s N, \quad (2.15)$$

where  $\lambda$  is the so-called t'Hooft coupling. The correspondence working in the low energy limit or equivalently the decoupling limit hence requires

$$\frac{L^4}{l_s^4} \sim 4\pi g_s N \sim g_{\text{YM}}^2 N \gg 1, \quad (2.16)$$

which suggests that the t'Hooft coupling for the  $SU(N)$  SYM theory has to be rather strong. However, in order to approximate the superstring theory by supergravity, we further entail the weak string coupling  $g_s \rightarrow 0$ . To satisfy both constraints, we have to take  $N \rightarrow \infty$ . As a result, the AdS/CFT correspondence is valid for the strongly coupled  $\mathcal{N} = 4$   $SU(N)$  SYM theory in the large  $N$  limit.

Technically, the AdS/CFT suggests an useful duality of bulk fields in gravity and boundary operators in the field theory. The boundary value of a bulk field corresponds to the source of a gauge-invariant operator. Schematically, the correspondence is written as

$$\mathcal{Z}_{\text{SYM}}[\phi_0] = \left\langle \int d^4x \mathcal{O} \phi_0 \right\rangle = \mathcal{Z}_{\text{AdS}_5}[\phi \rightarrow \phi_0], \quad (2.17)$$

where  $\mathcal{Z}_{\text{SYM}}$  and  $\mathcal{Z}_{\text{AdS}_5}$  represent the generating functionals of the  $\mathcal{N} = 4$  SYM theory in the four dimensional spacetime and the gravity theory in the  $\text{AdS}_5$  background, respectively. The bulk field  $\phi(z)$  acts as the source of an operator  $\mathcal{O}$  on the boundary, where  $\phi(0) = \phi_0$ . Generally, the contribution from  $S^5$  is encoded in the overall coefficient of the gravity action. The duality is nowadays generalized to arbitrary dimensions, where a  $d$  dimensional strongly coupled gauge theory is dual to a  $d + 1$  dimensional gravity theory. Furthermore, the mass of the bulk fields are connected to the conformal dimensions of the field-theory operators. The relations depend on

the types of bulk fields. Here we list two of them[43, 139]:

$$\begin{aligned} \text{scalar} : \Delta &= \frac{1}{2}(d + \sqrt{d^2 + 4m^2}), \\ \text{vector} : \Delta &= \frac{1}{2}(d + \sqrt{(d-2)^2 + 4m^2}), \end{aligned} \tag{2.18}$$

where  $\Delta$  denote the conformal dimensions of the dual operators and  $m$  represents the mass of corresponding bulk fields. It is usually stated in the AdS/CFT context that the gauge theory lives on the  $D_3$  branes on the boundary according to the operators/bulk fields duality. Rigorously speaking, these  $D_3$  branes should correspond to the  $D_3$  probe branes mentioned previously instead of the  $D_3$  branes in the horizon as the source of the warped geometry in the gravity dual since the correspondence between the open strings on the  $D_3$  branes and the near-horizon excitations is actually found in the IR regime.

## 2.2 Holography at Finite Temperature

To study sQGP in thermal equilibrium, we have to introduce a finite temperature in holography. In the gravity dual, the temperature and thermodynamics can be obtained from Hawking radiation of a black hole as prescribed by Witten[44]. In analogy to finite temperature field theory, we have to work with the Euclidean signature by making Wick rotation for the time coordinate,  $-it = t_E$ . Then the temperature is encoded in the periodic boundary condition for the Euclidean time via

$$t_E = t_E + \frac{1}{T}. \tag{2.19}$$

As mentioned in the previous section, the  $S^5$  is usually reduced. We thus focus on the five dimensional gravity action,

$$S = \frac{1}{16\pi G_5} \int d^5x (\mathcal{L}_{\text{grav}} + \mathcal{L}_{\text{matter}}), \tag{2.20}$$

where the volume of  $S^5$  is encoded in  $G_5$  as the five dimensional Newton constant. The gravity action consists of two parts. The gravitational part of the Lagrangian density reads

$$\mathcal{L}_{\text{grav}} = \sqrt{-g} \left( R + \frac{12}{L^2} \right), \quad (2.21)$$

where  $g = \det(g_{\mu\nu})$  for  $g_{\mu\nu}$  being the five dimensional spacetime metric. The matter part of  $\mathcal{L}_{\text{matter}}$  consists of matter fields. In general, the spacetime metric should be obtained from the extremization of the full gravity action, while the matter fields can be treated as perturbations and their backreaction to the metric can be discarded in some cases. By solving only the gravitational part in (2.21) without matter fields, we find that the  $AdS_5$  geometry is one of the isotropic and homogeneous solutions. Nonetheless, there also exists the solution with a black hole(brane) in the bulk, called the AdS-Schwarzschild geometry. The scenario is rather similar to a black hole in asymptotically flat spacetime.

In  $AdS_5$ , the presence of a black hole should modify the spacetime metric in the bulk and impose an IR cutoff since all objects inside the event horizon are causally disconnected from the outer regime. Before dealing with the AdS-Schwarzschild geometry, we may firstly show the derivation of temperature in a more general case via Witten's prescription. We may assume the modified metric takes the form,

$$ds^2 = g(z)(f(z)dt_E^2 + (dx^i)^2) + \frac{L^2}{z^2 h(z)} dz^2, \quad (2.22)$$

with the conservation of four-momentum. In most of cases,  $f(z) = h(z)$  denotes the so-called blackening function, which determines the position of the event horizon at  $z = z_h$  with  $f(z_h) = 0$ . Given that  $g(z)$  is well-defined at  $z_h$ , the near-horizon metric reads

$$ds^2|_{z \rightarrow z_h} = g(z_h)(-f'(z_h)(z_h - z)dt_E^2 + (dx^i)^2) - \frac{L^2}{z_h^2 f'(z_h)(z_h - z)} dz^2, \quad (2.23)$$

where the primes represent the derivatives with respect to  $z$ . By making the coordinate transformation,

$$\rho = \frac{2L}{z_h} \sqrt{\frac{(z_h - z)}{-f'(z_h)}}, \quad \tau = -\frac{t_E}{2L} z_h \sqrt{g(z_h)} f'(z_h), \quad (2.24)$$

we can rewrite the asymptotic metric as

$$ds^2|_{z \rightarrow z_h} = d\rho^2 + \rho^2 d\tau^2 + g(z_h) (dx^i)^2. \quad (2.25)$$

We see that the metric in (2.25) now has a conical singularity at  $\rho = 0$ . To avoid the cone singularity, one should impose a periodic boundary condition as

$$\tau = \tau + 2\pi. \quad (2.26)$$

Combined with the period boundary condition for the Euclidean time in (2.19), the temperature is now given by

$$T = -\frac{z_h f'(z_h)}{4\pi L} \sqrt{g(z_h)}. \quad (2.27)$$

We may now consider the AdS-Schwarzschild geometry, which is dual to the isotropic and homogeneous  $\mathcal{N} = 4$   $SU(N_c)$  SYM on the boundary. In  $d = 4$ , the AdS-Schwarzschild geometry is given by

$$ds^2 = \frac{L^2}{z^2} \left( -f(z) dt^2 + (dx^i)^2 + \frac{dz^2}{f(z)} \right), \quad (2.28)$$

where

$$f(z) = 1 - Mz^4 = 1 - \frac{z^4}{z_h^4}, \quad (2.29)$$

with  $M = z_h^{-4}$  being the mass of the black hole. Compared to (2.22), one easily recognizes that here  $g(z) = L^2/z^2$ . Without losing generality, we will set  $L = 1$  as

the unit to measure all scales in our system. From (2.27), we derive the temperature,

$$T = \frac{1}{\pi z_h}. \quad (2.30)$$

In addition, the entropy is determined by the area of the horizon. The area element at  $t = \text{constant}$  and  $z = z_h$  hypersurface is

$$dA_H = \frac{1}{z_h^3} dx^1 dx^2 dx^3. \quad (2.31)$$

The entropy density now reads

$$s = \frac{A_H}{4\pi V_3} = \pi^2 N_c^2 T^3, \quad (2.32)$$

where we use  $G_5 = \pi^2/(2N_c^2)$ . We can further derive the energy and pressure densities by utilizing thermodynamic relations:

$$s = \frac{\partial P}{\partial T}, \quad \epsilon = -P + Ts. \quad (2.33)$$

The energy and pressure densities in the AdS-Schwarzschild spacetime then become

$$P = \frac{1}{8\pi^2} N_c^2 T^4, \quad \epsilon = \frac{3}{8\pi^2} N_c^2 T^4. \quad (2.34)$$

Notice that the conformal symmetry is preserved here from  $\epsilon = 3P$ . One can show that both  $P$  and  $\epsilon$  in (2.34) are 3/4 times of the free  $\mathcal{N} = 4$  SYM gas, which agree with the lattice data near the temperature in RHIC and LHC[38].

### 2.3 Adding Flavors

In analogy to QCD, the  $SU(N)$  gauge symmetry in the  $\mathcal{N} = 4$  SYM theory may correspond to the  $SU(N_c)$  color symmetry. Nonetheless, since all fields in the SYM theory are in the adjoint representation, the SYM theory may only characterize

0	1	2	3	4	5	6	7	8	9
<i>D3</i>	X	X	X	X					
<i>D7</i>	X	X	X	X	X	X	X	X	X

FIGURE 2.2: The dimensions of D3/D7 embedding, where 0, 1, 2, 3 denote the four dimensional spacetime on the boundary.

the gluon degrees of freedom in QCD. In order to incorporate the quark degrees of freedom, we have to further introduce matters in the fundamental representation. In this section, we will briefly introduce the inclusion of matters in the fundamental representation in the deconfined phase of the  $\mathcal{N} = 4$  SYM plasma in AdS/CFT.

From the top-down approach based on string theory, the inclusion of fundamental matters can be realized by embedding flavor branes[140, 141]. Consider an open string with one end fixed on the original  $D_3$  brane and one on the flavor brane, the string hence possesses both the color and flavor in the fundamental representation. Moreover, the separation between two branes on the boundary then lead to the mass proportional to the tension of the string for such a fundamental matter. We will henceforth call these fundamental matters quarks in the context. There are different types of embeddings in string theory, while we will focus on the D3/D7 system[142, 143, 144] in the thesis. In such a system,  $N_f$   $D_7$  branes are introduced, which share the same spacetime dimensions as the  $N_c$   $D_3$  branes on the boundary. The  $D_7$  branes further wrap an  $S^3$  in the  $S^5$  and extend along the bulk direction. The embedded dimensions in the D3/D7 system are simply shown in Fig.2.2. Now,

the radius of the  $S^3$  is denoted by

$$\tilde{r}^2 = (x^4)^2 + \dots + (x^7)^2, \quad (2.35)$$

which will shrink to zero at the endpoint of  $D_7$  branes in the bulk. Since the bulk direction is  $r^2 = \tilde{r}^2 + (x^8)^2 + (x^9)^2$ , the separation between the  $D_3$  branes and the  $D_7$  branes on the boundary reaches a maximum as  $\tilde{r} \rightarrow 0$  on the boundary, which gives a rise to infinite mass for a quark via the relation  $m_q \sim \sqrt{(x^8)^2 + (x^9)^2}|_{r \rightarrow \infty}$ . Therefore, as the  $D_7$  branes end in the deeper part of the bulk, the quark mass becomes smaller. For the case with the  $D_7$  branes extending all the way to  $r = 0$ , the corresponding quarks will be massless, which is dubbed as the trivial embedding.

In the presence of a black hole, the situation will become more sophisticated. There exist three types of embeddings as schematically depicted in Fig.2.3. As in the case of the so-called Minkowski embedding, the  $D_7$  branes end above the horizon in the bulk. The corresponding quark mass will be greater than the critical mass  $m_c$  (or equivalently the critical temperature  $T_c$ ) and the embedding hence characterizes the confined phase. For the black hole (BH) embedding, the  $D_7$  branes then terminate below the horizon, which corresponds to the deconfined phase with  $m_q < m_c$ . The part inside the black hole will be causally disconnected from the region outside. When the endpoint of  $D_7$  branes approximately coincides with the horizon as the critical embedding, the first order phase transition occurs [145]. It has been shown in [145] that the free energy around this region is degenerate and the critical embedding is thus unstable. In this thesis, we will present the computations of the thermal-photon production in various backgrounds. Since sQGP is in the deconfined phase, we will only emphasize the BH embedding. In general, the embedding of flavor branes should lead to backreaction to the background geometry which complicates the computations. Therefore, the probe brane approximation based on the assumption that  $N_f \ll N_c$  is usually taken to discard the backreaction.

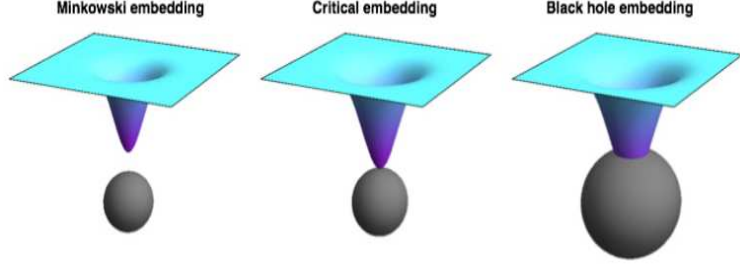


FIGURE 2.3: Schematic representation of different types of embeddings[12].

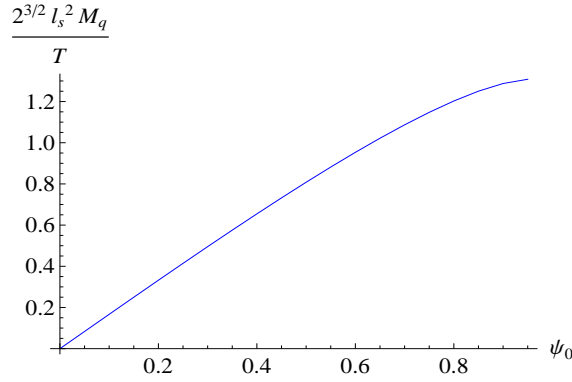


FIGURE 2.4: The mass as a function of  $\psi_0$  modified from[13].

We may now make a concrete example by considering the BH embedding in the D3/D7 system with the AdS-Schwarzschild background[143, 145, 144]. As mentioned above, The flavor D7 brane extended into the bulk shares the same spacetime dimensions with the D3 brane on the boundary and wraps an  $S^3$  inside the  $S^5$ ,

$$d\Omega_5^2 = d\theta^2 + \sin^2 \theta d\Omega_3^2 + \cos^2 \theta d\eta^2, \quad (2.36)$$

where  $\theta$  and  $\eta$  represent the polar coordinates of the  $x^8$  and  $x^9$  directions. The flavor D7 brane is characterized by the Dirac-Born-Infeld (DBI) action,

$$S = -N_f T_{D7} \int_{D7} d^8 x \sqrt{-\det(G)}, \quad (2.37)$$

where  $G$  is the induced metric on the D7 branes and  $T_{D7} = (2\pi l_s)^{-7} (g_s l_s)^{-1}$  is the

D7-brane string tension. For the nontrivial embedding, the radius of the  $S^3$  denoted by  $\sin \theta$  is a function of the bulk direction. Here we use  $u$  to replace  $z$  as the bulk direction, where  $u = 0$  corresponds to the boundary. In Chapter.4 and Chapter.5, we will generalize the computations in this section to the case with an anisotropic background, where  $z$  will be assigned to the anisotropic direction. Therefore, we will set  $u$  as the bulk direction in this section and in Chapter.4 and Chapter.5. The induced metric now is given by

$$ds_{D7}^2 = \frac{1}{u^2} (-f(u)dt^2 + dx^2 + dy^2 + dz^2) + \frac{1 - \psi(u)^2 + u^2 f(u) \psi(u)'^2}{u^2 f(u) (1 - \psi(u)^2)} du^2 + (1 - \psi(u)^2) d\Omega_3^2, \quad (2.38)$$

where  $\sqrt{1 - \psi(u)^2} = \sin \theta$  represents the radius of the internal  $S^3$  wrapped by the D7 branes. The DBI action in (4.30) can be explicitly written as

$$S = -K_{D7} \int dt d^3 \vec{x} du \frac{(1 - \psi^2)}{u^5} \sqrt{(1 - \psi^2 + u^2 f \psi'^2)}, \quad (2.39)$$

where the prefactor  $K_{D7}$  includes the integration over the internal space  $\Omega_3$  wrapped by the D7 branes. The embedding function  $\psi$  can be solved by extremizing the DBI action, which give a rise to the equation of motion as

$$\psi'' + \left( \frac{f'}{f} - \frac{3}{u} \right) \psi' - \frac{4uf}{(1 - \psi^2)} \left( 1 - \frac{uf'}{8f} \right) \psi'(u)^3 + \frac{3}{u^2 f (1 - \psi^2)} \left( 1 + \frac{4\psi' u^2 f}{3} \right) \psi - \frac{3}{u^2 f (1 - \psi^2)} \psi^3 = 0. \quad (2.40)$$

Since the equation in (2.40) is nonlinear, we can only solve it numerically. However, by taking the near-boundary expansion, one can show that

$$\psi(u)|_{u \rightarrow 0} = m \frac{u}{2^{1/2} u_h} + c \frac{u^3}{2^{3/2} u_h^3} + \dots, \quad (2.41)$$

where the dimensionless coefficients  $m$  and  $c$  are related to the magnitudes of quark mass and condensate through [143, 145]

$$\begin{aligned}
M_q &= \frac{m}{2^{3/2}\pi l_s^2 u_h} = \frac{\sqrt{\lambda}m}{2\pi u_h}, \\
\langle \mathcal{O} \rangle &= -2^{3/2}\pi^3 l_s^2 N_f T_{D7} u_h^{-3} c = -\frac{\sqrt{\lambda}N_c N_f}{8\pi^3 u_h^3} c.
\end{aligned}
\tag{2.42}$$

In the black-hole embeddings, the values of  $m$  and  $c$  depend on the boundary conditions of the embedding functions on the horizon, where we take  $\psi(u_h) = \psi_0$  and  $\psi'(u_h) = (-3u^{-2}\psi/f')|_{u=u_h}$  [143, 144]. The  $\psi'(u_h)$  here is directly obtained from the equation of motion in (2.40) near the horizon. As shown in Fig.2.4, the quark mass increases as  $\psi_0$  is increased, while the increase ceases as  $\psi_0 = \psi_c$  as the critical value of  $\psi_0$  near the critical embedding at  $\psi_0 = 1$ . The corresponding mass  $M_c$  for  $\psi_0 = \psi_c$  could be approximated as the critical mass for which the phase transition occurs. More rigorous investigation of the first order transition near the critical embedding is presented in [145], where the condensates and free energy become degenerate with respect to the quark mass. In the following chapters, we will further generalize the D3/D7 system to an anisotropic background and incorporate an external magnetic field.

## Jet Quenching and Holographic Thermalization

The work in this chapter was first published in [128, 129]. As discussed in Section 1.3, the thermal plasma in the gravity side is characterized by an asymptotic  $AdS_5$  geometry induced by a black hole. Therefore, the thermalization process of the strongly coupled  $\mathcal{N} = 4$  SYM theory may be characterized by the formation of a black hole in the gravity dual in the AdS/CFT correspondence. In [25, 26], the scenario of the gravitational collapse is characterized by the AdS-Vaidya metric at the thin-shell limit, which describes an infinitesimally thin shell falling in the  $AdS_5$  background. It is shown in [63] that the AdS-Vaidya metric comes from the leading order perturbation led by a time-dependent and weak dilaton field on the boundary. Eventually, the shell approximately forms an event horizon and the exterior of the shell, which characterize the medium of the plasma, then reaches thermal equilibrium. To find the thermalization time of the medium, the authors in [25, 26] compute different non-local operators in Eddington-Finkelstein(EF) coordinates to probe the backreaction of the shell to the spacetime. The approach is generalized to the study of a non-equilibrium plasma with nonzero chemical potential by introducing a charged

shell in [146].

In this chapter, our primary goal is to estimate the influence led by the thermalization of the medium on the light probe. We proceed by investigating the null geodesic of a massless particle falling in the AdS-Vaidya spacetime, as a means of getting the stopping distance for the probe traversing a non-equilibrium and strongly coupled plasma. On the other hand, we track the falling shell to approximate the thermalization time defined as the time when the shell roughly reach the future horizon. This is an alternative approach to measure the thermalization time of the medium compared to the thermalization time extracted from the thermalization of non-local operators with a length scale about the inverse of the thermalized temperature.

This chapter is organized as follows. In Section 3.1, we firstly present the derivation of an analytical expression of the AdS-Vaidya metric in Poincare coordinates in the thin-shell limit. By tracking the position of the shell, we are able to monitor the thermalization of the medium. In Section 3.2, we study the jet quenching of a colorless probe (e.g. a virtual photon) in the field theory. For such a probe, its stopping distance is determined by its 4-virtuality. According to AdS/CFT correspondence these jets are sourced by some supergravity fluctuation. For a highly energetic jet with a small 4-virtuality, the supergravity fluctuation/wave packet can be treated in a WKB approximation and approximated as a massless particle falling from the boundary following a null geodesic. We track the falling shell and the massless particle moving along the null geodesic in the AdS-Vaidya spacetime and compute the stopping distance of this light probe. In Section 3.3, we will carry out the same approach to compute the stopping distance of soft gluons characterized by falling strings in the AdS-Vaidya spacetime. In Section 3.4, we will generalize our study to the non-equilibrium background with a chemical potential and evaluate the thermalization time by tracking a falling charged shell. In Section 3.5, we further investigate the jet quenching for virtual gluons in the both thermalized and thermal-

izing backgrounds with chemical potentials. Finally, we conclude and discuss about the thermalization time with chemical potentials in the last section.

### 3.1 The Falling Mass Shell in the AdS-Vaidya Spacetime

In [63], the AdS-Vaidya metric is generated by a time-dependent and weak dilaton field in EF coordinates. However, in this section, we will convert the AdS-Vaidya metric with a step-like mass function of the shell into Poincare coordinates in the thin-shell limit in the  $AdS_{d+1}$  background. We will not solve the dilaton profile which generates certain mass function here in the  $AdS_5$ , while we leave the complete analysis in the case of the  $AdS_4$  in the appendix, where more discussion about the validity of the AdS-Vaidya metric can be found. We assume that the major features should not depend on the dimensionality of the spacetime.

The mass function of the shell should characterize the gravitational collapse; thus, it should behave as a step function in the thin-shell limit. Here we take the mass function proposed in [25, 26],

$$m(v) = \frac{M}{2} \left( 1 + \tanh \left( \frac{v}{v_0} \right) \right), \quad (3.1)$$

where  $v$  is the EF time coordinate as a function of  $t$  and  $z$  in the Poincare coordinates for  $z$  being the fifth dimension. Here  $M$  denotes the full mass of the shell, which determines the position of the future horizon by  $z_h = M^{-1/4}$ , and  $v_0$  denotes the thickness of the shell. The thermalization temperature is also encoded by the position of the future horizon via  $T = (\pi z_h)^{-1}$ . At the thin-shell limit  $v_0 \rightarrow 0$ , the spacetime will be separated into two regions, the exterior of the shell for  $v > v_0$  and the interior of the shell for  $v < v_0$ , where the two regions are governed by different spacetime geometries. To further simplify the computation, we apply a quasi-static approximation by chopping the spacetime into different time slices. At each time

slice, we study the  $z$  dependence of the metric and then glue all slices together by tracking the position of the center of the falling shell as a function of time. Given the position of the shell, we are able to approximate the thermalization time of the medium.

We should begin with the AdS-Vaidya metric in  $\text{AdS}_{d+1}$  background in terms of EF coordinates,

$$ds^2 = \frac{1}{z^2} (-f(v, z)dv^2 - 2dv dz + dx_i^2), \quad (3.2)$$

in which  $f(v, z) = 1 - m(v)z^d$  and  $x_i$  represent the  $d$  dimensional spacetime coordinates by setting the AdS curvature radius  $L = 1$ . Later we will take  $d = 4$  as an example, but here we leave  $d$  undefined for generality. By rewriting the EF time coordinate  $v$  in terms of  $t$  and  $z$  in Poincare coordinates

$$dv = g(t, z)dt - \frac{1}{f(v, z)}dz, \quad (3.3)$$

(3.2) becomes

$$ds^2 = \frac{1}{z^2} \left( -f(v, z)g(t, z)^2 dt^2 + \frac{dz^2}{f(v, z)} + dx_i^2 \right). \quad (3.4)$$

Here  $g(t, z)$  is an unknown function expressing the redshift factor of the nonzero gravitational potential inside the shell for an observer on the boundary. From (3.3), when  $v(t, z) = v_c = \text{const}$  for  $v_c$  representing the center of the shell, the  $t$  coordinate will be a function of  $z$  even though the function  $g(t, z)$  is unknown; hence the  $t$  coordinate can be written as a function of the position of the center of the shell in the  $z$  coordinate, denoted by  $z_0$ . More explicitly, we have

$$\left( \frac{\partial z_0}{\partial t} \right)_{v=v_c} = g(t, z_0) f(v_c, z_0). \quad (3.5)$$

For an arbitrary  $z_0$ ,  $v(t(z_0), z = z_0) = v_c$  must be satisfied and fixing  $z_0$  is equivalent to fixing  $t$ . At the thin-shell limit, we may set  $v_c = v_0 = 0$ . By revisiting (3.3) at fixed  $z_0$  (fixed  $t$ ), we can write down the differential equation encoding the  $z$  dependence of  $v(t, z)$ ,

$$\left(\frac{\partial v(t(z_0), z)}{\partial z}\right)_{z_0} = -\frac{1}{f(v, z)}, \quad (3.6)$$

where we use the center of the shell to represent the position of the shell. The above differential equation with the boundary condition,  $v(t(z_0), z = z_0) = v_c = 0$ , can be solved numerically without making further approximations and the  $v$  coordinate can thus be expressed in terms of  $z$  at fixed  $t$ . However, to derive the full solution of  $v$  with the varying  $t(z_0)$ , we have to solve  $g(t, z)$ . Since the mixed derivatives of  $v$  with respect to  $t$  and  $z$  should commute, we have

$$\left(\frac{\partial g(t, z)}{\partial z}\right)_t = \left(\frac{\partial f(v, z)}{\partial t}\right)_z \frac{1}{f(v, z)^2} = \left(\frac{\partial f(v, z)}{\partial v}\right)_z \frac{g(t, z)}{f(v, z)^2}, \quad (3.7)$$

where we use the chain rule  $\left(\frac{\partial f(v, z)}{\partial t}\right)_z = \left(\frac{\partial f(v, z)}{\partial v}\right)_z \left(\frac{\partial v(t, z)}{\partial t}\right)_z = \left(\frac{\partial f(v, z)}{\partial v}\right)_z g(t, z)$  to derive the second equality. We may rewrite (3.7) into integral form by taking the integration from the boundary to the position  $z_p$  at fixed  $t(z_0)$ ,

$$g(t(z_0), z_p) = g_0(z_0) \exp \left[ \int_0^{z_p} \frac{dz}{f(v(t(z_0), z), z)^2} \left(\frac{\partial f(v, z)}{\partial v}\right)_z \right], \quad (3.8)$$

where  $g_0(z_0) = g(t(z_0), 0)$  represents the redshift factor on the boundary. This integral can be computed by inserting the solution of  $v(t(z_0), z)$  at fixed  $t(z_0)$  in (3.6). For the region outside the shell, the spacetime is governed by the AdS-Schwarzschild metric, which imposes  $g_0(z_0) = 1$ . By setting  $f(v, z) = 1 - m(v)z^4$  at  $d = 4$ , (3.8) can be written as

$$g(t(z_0), z_p) = \exp \left[ - \int_0^{z_p} \frac{dz z^4}{(1 - m(v)z^4)^2} \frac{dm(v)}{dv} \right]. \quad (3.9)$$

In the thin-shell limit, the derivative of  $m(v)$  with respect to  $v$  in (3.9) is highly localized at  $z_0$ ; thus we find  $g(t(z_0), z_p) = 1$  for  $z_p < z_0$  as expected. For  $z_p > z_0$ ,  $g(t(z_0), z_p)$  is a constant, which can be derived from (3.5) by assuming two surfaces of the shell fall with the same velocity. Since  $g(t, z) = 1$  for  $z < z_0$  plus  $m(v) = M$  and  $m(v) = 0$  for  $z < z_0$  and  $z > z_0$ , respectively, we find that  $g(t, z) = 1 - Mz_0^4$  for  $z > z_0$  in the thin-shell limit. More generally, the integral in (3.8) can be computed by inserting the solution of  $v(t(z_0), z)$  at fixed  $t(z_0)$  into (3.6), which yields

$$g(t(z_0), z_p) = g_0(z_0) \exp \left[ - \int_{f(v,0)}^{f(v,z_p)} \frac{df(v, z)}{f(v, z)} \right]. \quad (3.10)$$

In the thin-shell limit, since the blackening function inside the shell reduces to one, the redshift factor inside the shell only depends on the blackening function outside the shell. The AdS-Vaidya metric in Poincare coordinates is then given by

$$ds^2 = \begin{cases} \frac{1}{z^2} \left( -F(z) dt^2 + \frac{dz^2}{F(z)} + dx^2 \right) & \text{if } v > 0 (z < z_0), \\ \frac{1}{z^2} (-F(z_0)^2 dt^2 + dz^2 + dx^2) & \text{if } v < 0 (z > z_0), \end{cases} \quad (3.11)$$

where  $F(z) = 1 - z^4/z_h^4$ . The bulk is separated into two regimes; the exterior of the shell for  $z < z_0$  is governed by the AdS-Schwarzschild geometry and the interior for  $z > z_0$  is characterized by the quasi-AdS spacetime. More discussions about the computation of the redshift factor  $g(t(z_0), z_p)$  are presented in Appendix A.3.

By using (3.5), the position of the shell is characterized by

$$t_0 = \int_0^{z_0} dz_s \frac{1}{F(z_s)} = \frac{z_h}{2} \left[ \tan^{-1} \left( \frac{z_0}{z_h} \right) + \tanh^{-1} \left( \frac{z_0}{z_h} \right) \right]. \quad (3.12)$$

Due to the gravitational redshift, it takes infinite time for the shell to exactly coincide with the horizon. The trajectory of the falling shell can be found in Fig.A.8 by taking  $z_h = 1$ . We may define the thermalization time as  $t_{th} = t_0|_{z_0=0.99z_h}$ . By using (3.18),

we find the thermalization time in the unit of temperature  $t_{th}T = 0.55$ . In [26],  $t_{th}T \approx 0.5$  when the length scale of the non-local operator for probing the thermalization of the medium is about the inverse of the thermalization temperature; the value is approximately consistent with the result we obtain. In [27], it is found that the viscous hydrodynamics applies for  $t_{th}T \geq 0.6 - 0.7$ , which leads to the thermalization time close to our result despite the different definition of the thermalization in their approach. It is generally believed that the thermalization time should be within 0.1 fm/c to 1 fm/c at the RHIC energy. By taking  $T \approx 300$  MeV about the temperature at RHIC, the possible range of the thermalization time in the unit of temperature is given by  $0.15 \leq t_{th}T \leq 1.52$ , which basically covers all above results obtained from different holographic models.

### 3.2 Jet Quenching of Colorless Probes in the Non-equilibrium Plasma

To investigate the influence of the thermalization process of the medium on the jet quenching of light probes, we are interested in the stopping distance in the AdS-Vaidya geometry. We apply the approach in [105], where a localized R-charge current generates high momentum wave packet of a massless field propagating from the boundary to the bulk. When the wave function of the massless field penetrates the horizon, the induced jet on the boundary dissipates and reaches thermal equilibrium in the medium. The jet is the holographic image on the AdS boundary of the wave packet propagating in the bulk [147]. By applying the WKB approximation, the wave function of the bulk field is approximated as a massless particle falling along a null geodesic. As showed in [105], the trajectory of the massless particle in the thermalized medium governed by the AdS-Schwarzschild geometry can be written as

$$x^1(z_p) = \int_0^{z_p} \frac{dz}{\left(\frac{\omega^2}{|\vec{q}|^2} - F(z)\right)^{1/2}} = \int_0^{z_p} \frac{dz}{\left(\frac{z^4}{z_h^4} - \frac{q^2}{|\vec{q}|^2}\right)^{1/2}}, \quad (3.13)$$

where the particle carries the four-momentum  $q_i = (-\omega, |\vec{q}|, 0, 0)$  and  $q^2 = -\omega^2 + |\vec{q}|^2$  represents its virtuality. The stopping distance is thus given by  $x^1(z_h)$ .

In the previous section, we have derived the AdS-Vaidya metric in Poincare coordinates in the thin-shell limit. Nevertheless, in the thin-shell limit, the massless particle just travels outside the shell when the particle is ejected from the boundary after the injection of the shell. The falling shell may characterize the top-down scenario of the thermalization starting from the ultraviolet scale to the infrared scale of the medium. In this case, the trajectory of the particle moving in the AdS-Vaidya spacetime should be the same as that in the AdS-Schwarzschild spacetime. Even though we may assume the energetic probe is created slightly before the thermalization of the medium, the redshift effect is negligible near the boundary and thus the probe should feel like moving in the pure AdS geometry at the early time. Since the shell falls with the speed of light, the particle will then travel most of time outside the shell and behave as in the thermalized medium.

However, when the shell has finite thickness, the same expectation is not obvious although we will find that the result turns out to be the same. To track the null geodesic of the massless particle amid the shell in Poincare coordinates is technically difficult, because the trajectory of the particle is continuously deflected by interactions with the shell. Despite the information about the thermalization time of the probe, it is easier to compute the stopping distance of the probe in EF coordinates. By using the metric in (3.2) at  $d = 4$ , the geodesic equations are given by

$$\begin{aligned}
\frac{d^2 v}{d\lambda^2} + \Gamma_{vv}^v \left( \frac{dv}{d\lambda} \right)^2 + \Gamma_{11}^v \left( \frac{dx^1}{d\lambda} \right)^2 &= 0 \\
\frac{d^2 z}{d\lambda^2} + \Gamma_{vv}^z \left( \frac{dv}{d\lambda} \right)^2 + 2\Gamma_{vz}^z \left( \frac{dv}{d\lambda} \right) \left( \frac{dz}{d\lambda} \right) + \Gamma_{11}^z \left( \frac{dx^1}{d\lambda} \right)^2 + \Gamma_{zz}^z \left( \frac{dz}{d\lambda} \right)^2 &= 0, \\
\frac{d^2 x^1}{d\lambda^2} + 2\Gamma_{z1}^1 \left( \frac{dz}{d\lambda} \right) \left( \frac{dx^1}{d\lambda} \right) &= 0,
\end{aligned} \tag{3.14}$$

where

$$\begin{aligned}
\Gamma_{vv}^v &= \frac{1}{z}(1 + m(v)z^4), \quad \Gamma_{11}^v = -\frac{1}{z}, \\
\Gamma_{vv}^z &= -\frac{1}{z} \left( 1 - m(v)^2 z^8 + \frac{1}{2} z^5 \frac{dm(v)}{dv} \right), \\
\Gamma_{vz}^z &= -\frac{1}{z}(1 + m(v)z^4), \quad \Gamma_{zz}^z = -\frac{2}{z}, \\
\Gamma_{11}^z &= \frac{1}{z}(1 - m(v)z^4), \quad \Gamma_{z1}^1 = -\frac{1}{z}.
\end{aligned}$$

and  $\lambda$  is the affine parameter. Also, the mass function is defined as

$$m(v) = \frac{M}{2} \left( 1 + \tanh \left( \frac{v}{v_0} - \frac{1}{2} \right) \right), \quad (3.15)$$

where the shift in the hyperbolic-tangent function is to fit the setup shown in Fig.3.1 and the future horizon is determined by  $z_h = M^{-1/4}$ . We notice that only the momentum  $q_1$  along the  $x^1$  direction is conserved in EF coordinates, where we set the momenta along the  $x^2$  and  $x^3$  directions to be zero. We define the conserved momentum as  $q_1 = |\vec{q}| = z^{-2} \frac{dx^1}{d\lambda}$ . Next, we can rewrite the geodesic equations in terms of the derivative with respect to  $x^1$ ,

$$\begin{aligned}
\frac{dx^\mu}{d\lambda} &= \frac{dx^\mu}{dx^1} \frac{dx^1}{d\lambda} = z^2 |\vec{q}| x'^\mu, \\
\frac{d^2 x^\mu}{d\lambda^2} &= |\vec{q}|^2 z^2 (x''^\mu z^2 + 2zz' x'^\mu),
\end{aligned} \quad (3.16)$$

where the prime denotes a derivative with respect to  $x^1$ . By inserting (A.24) into the geodesic equations, we find that the last equation in (A.20) is automatically satisfied due to the conservation of the momentum along the  $x^1$ . To solve other two geodesic equations in (A.20), we have to introduce the proper initial conditions. Even though the energy of the particle is not conserved in the AdS-Vaidya spacetime, the

gravitational effect caused by the falling shell is negligible at early times. Therefore, we may write down the initial conditions under the pure AdS metric. For a particle ejected from the boundary, we have

$$\begin{aligned}
z|_{x^1=0} &= v|_{x^1=0} = t|_{x^1=0} = 0, \\
v'|_{x^1=0} &= (t' - z')|_{x^1=0} = \frac{\omega_0}{|\vec{q}|} - \frac{\sqrt{\omega_0^2 - |\vec{q}|^2}}{|\vec{q}|}, \\
z'|_{x^1=0} &= \frac{\sqrt{\omega_0^2 - |\vec{q}|^2}}{|\vec{q}|},
\end{aligned} \tag{3.17}$$

where we use the four-momentum defined in Poincare coordinates  $q_i = g_{ij} \frac{dx^j}{d\lambda} = (-\omega_0, |\vec{q}|, 0, 0)$ . We will further assume that the particle has small virtuality, which implies  $|\vec{q}| \approx \omega_0$  as required for the WKB approximation. The trajectory of the massless particle traveling in the AdS-Vaidya spacetime with a thick shell and that in the thin-shell limit are shown in Fig.3.2. It turns out that the two results match closely and are indistinguishable on the plot, which shows that the thermalization of the hard probe is not influenced by the detail structure of the non-equilibrium medium. In addition, the two trajectories also coincide with that in AdS-Schwarzschild spacetime. Because the energy of the massless particle in the WKB approximation is much larger than any other scale in this scenario, its stopping distance is unaffected by the thermalization process.

When the thickness of the shell becomes comparatively large with respect to the inverse of the temperature ( $v_0 \approx z_h = (\pi T)^{-1}$ ), the null geodesic in the AdS-Vaidya spacetime may receive a slight correction compared to that in the AdS-Schwarzschild spacetime. Nonetheless, such a thick shell would jeopardize the validity of the AdS-Vaidya metric as mentioned in Appendix 3.1. The thickness of the shell is a typical time scale for the injection of energy from the boundary. In the analogue of QGP produced in heavy ion collisions, the thickness of the shell may be characterized by

the inverse of the parton saturation scale  $Q_s$  in the colliding nuclei, which should be much greater than the temperature of the medium. Although the analogue here is coarse, it may support the small thickness of the shell from a physical point of view.

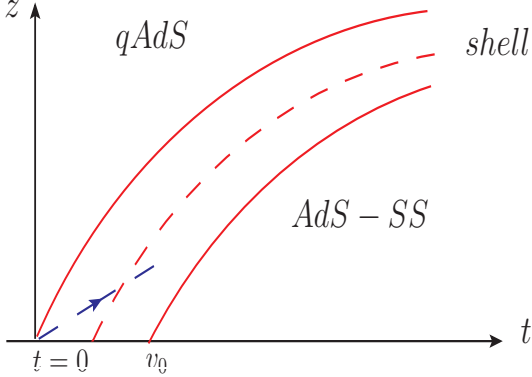


FIGURE 3.1: The scenario of a massless particle ejecting from the boundary as the shell starts to fall, where  $v_0$  denotes the thickness of the shell and the solid red curves and the dashed red curve represent the surfaces and the center of the shell, respectively. The dashed arrow denotes the massless particle as a hard probe falling from the boundary at  $t = 0$ .

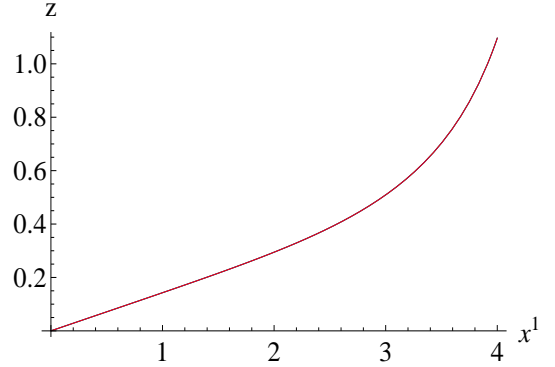


FIGURE 3.2: The red, blue, and green curves represent the trajectories of particles falling in the AdS-Schwarzschild spacetime and in the AdS-Vaidya spacetime with  $v_0 = 0.2$  and  $v_0 = 0.0001$ , respectively. Three curves coincide and cannot be distinguished. Here we take  $|\vec{q}| = 0.99\omega_0$  and  $z_h = 1$ .

Although we have found the trajectory of the massless particle falling in the AdS-Vaidya spacetime in EF coordinates, it is interesting to further analyze the interaction between the shell and the massless particle, which will also be useful when studying stopping distances of soft gluons in the following section. For simplicity, we consider the AdS-Vaidya geometry in Poincare coordinates in the thin-shell limit. In (3.44), we may define a new time coordinate  $d\tilde{t} = F(z_0)dt$  inside the shell. Then the metric inside the shell reduces to the pure AdS geometry. By extending (3.13), the trajectory of the massless particle in the AdS-Vaidya spacetime will be given by

$$x^1(z_p) = \int_0^{z_c} \frac{dz}{\left(\frac{\tilde{\omega}^2}{|\vec{q}|^2} - 1\right)^{1/2}} + \int_{z_c}^{z_p} \frac{dz}{\left(\frac{\omega^2}{|\vec{q}|^2} - F(z)\right)^{1/2}}, \quad (3.18)$$

if we eject the massless particle prior to the presence of the falling shell. Here  $z_c$  is the collision point where the particle crosses the shell. For the massless particle in the quasi-AdS spacetime inside the shell, we define its four-momentum in terms of the  $\tilde{t}$  coordinate as  $\tilde{p}_\mu = (-\tilde{\omega}, |\vec{q}|, 0, 0)$  and thus  $\tilde{p}_z = \sqrt{\tilde{\omega}^2 - |\vec{q}|^2}$ . We may convert them into  $t$  and  $z$  coordinates,  $p_\mu = (F(z_0)\tilde{p}_0, \tilde{p}_1, 0, 0)$  and  $p_z = \sqrt{\tilde{p}_0^2 F(z_0)^{-2} - \tilde{p}_1^2}$ . While for the massless particle in the AdS-Schwarzschild spacetime outside the shell, we define  $q_\mu = (-\omega, |\vec{q}|, 0, 0)$  and thus  $q_z(z) = F(z)^{-1} \sqrt{\omega^2 - F(z)|\vec{q}|^2}$ . Since the three-dimensional spatial momentum is always conserved, we only have to focus on the matching between the momentum along the  $t$  and  $z$  coordinates. In this scenario, the particle firstly moves in the quasi-AdS geometry for a short period and then transitions into the AdS-Schwarzschild spacetime. Since the shell is homogeneous along the spatial direction, the particle may only exchange the energy with the shell in the collision.

To find the energy change of the particle in the collision, we have to construct a matching condition, in analogy of Snell's law, to relate  $\tilde{\omega}$  and  $\omega$ . In the WKB approximation, the wave function of the massless field is given by

$$\Psi_{\text{WKB}} = \exp\left(i \int q_\mu dx^\mu\right). \quad (3.19)$$

By assuming the continuity of the wave function at the collision point and using the conservation of the spatial momentum, we have

$$(-\omega dt + q_z dz)|_{z_c^-} = (-\tilde{\omega} d\tilde{t} + \tilde{p}_z d\tilde{z})|_{z_c^+}, \quad (3.20)$$

where  $q_z$  and  $\tilde{p}_z$  are the momenta along the fifth dimension defined in the exterior and the interior of the shell, respectively. By doing some algebra, (3.20) can be further written as

$$-\omega + F(z_c)q_z|_{z_c} = F(z_c)(-\tilde{\omega} + \tilde{p}_z|_{z_c}). \quad (3.21)$$

This equation serves as the matching condition encoding the energy change of the massless particle penetrating the thin shell. Since  $\tilde{\omega}$  remains constant in the quasi-AdS spacetime, it represents the initial energy  $\omega_0$  of the massless particle. Thus, from (3.21), the energy change should be characterized by the ratio

$$\frac{\omega}{\tilde{\omega}} = \frac{1}{2(1 - \sqrt{1 - \delta^2})} [2F(z_c)(1 - \sqrt{1 - \delta^2}) + \delta^2(1 - F(z_c))], \quad (3.22)$$

where  $\delta = |\vec{q}|/\tilde{\omega}$ . As shown in Fig.3.3, the ratio decreases when the collision point is away from the boundary. When the massless particle crosses the shell, it loses a certain amount of its energy. In the thermalization process, the virtuality of the massless particle is reduced and it may travel further than in a thermalized medium. This scenario should become robust only when the massless particle is ejected long before the presence of the shell due to the small virtuality of the probe. Physically, we thus expect the thermalization will lead to suppressed radiation of the light probe. Nonetheless, when the light probe carries small virtuality, the effect would be negligible. This scenario will then be different when we introduce a soft probe as shown in the next section.

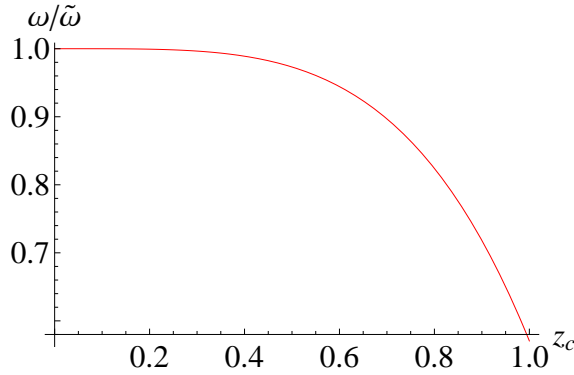


FIGURE 3.3: The energy ratio with respect to the collision point  $z_c$ , where  $\delta = 0.99$  and  $z_h = 1$ .

### 3.3 Jet Quenching of Virtual Gluons in the Non-Equilibrium Plasma

In the gravity dual, a suitable candidate for a color probe would be the double string with two ends fixed on the D-branes far below the future horizon, which corresponds to an energetic gluon [103]. In this setup, the tip of the double string comes out of the future horizon and encodes the initial energy of the virtual gluon. The tip of the string should finally fall into the future horizon within the thermalized medium, in which the gluon loses all its energy in the plasma. By tracking the trajectory of the tip, we are able to investigate the stopping distance of the gluon before it thermalizes. We will assume that the tip of the string travels along the null geodesic, which leads to the maximum stopping distance.

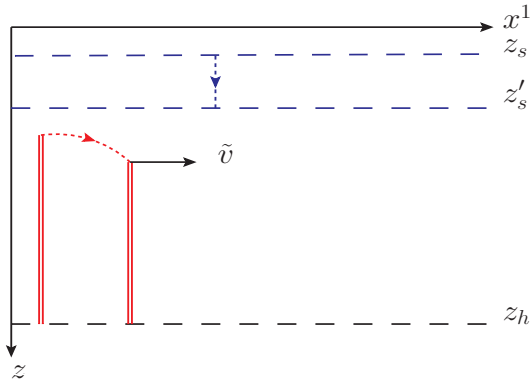


FIGURE 3.4: A schematic figure for the sting profile in AdS-Vaidya spacetime before colliding with the shell.

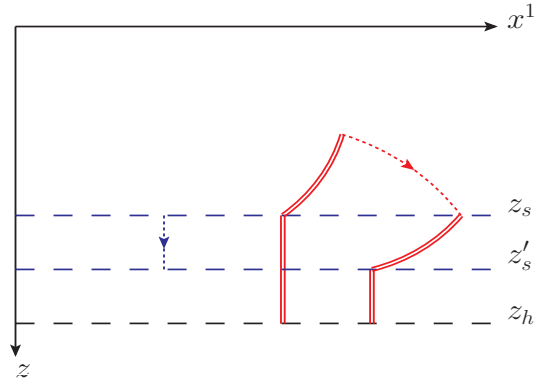


FIGURE 3.5: A schematic figure for the sting profile in AdS-Vaidya spacetime after colliding with the shell.

In this section, we will follow the approach in [103] to compute the maximum stopping distance led by the falling massless particle characterizing the tip of the string in the AdS-Vaidya spacetime in the thin-shell limit.

Before tracking the trajectory of the massless particle and computing the stopping distance by employing the null geodesic equations in (3.18), we have to specify the initial values for the four-momentum of the massless particle. As shown in [103], these initial values are determined by the initial profile of the falling string. Since

the gluon represented by the string is created in the pre-thermalized state governed by the quasi-AdS metric in the gravity dual, the string profile is different from that in the thermalized medium. By using the appropriate time coordinate  $d\tilde{t} = F(z_0)dt$  for the metric inside the shell, we find that the initial profile of the string is a straight string. We thus set  $x^1 = \tilde{v}\tilde{t}$  and choose  $\sigma^\alpha = (\tilde{t}, z)$  as the world sheet coordinates. Then the Nambu-Goto action is given by

$$S = \frac{-1}{2\pi\alpha'} \int d\tilde{t}dz\sqrt{-h} = \frac{-1}{2\pi\alpha'} \int d\tilde{t}dz \frac{\sqrt{1-\tilde{v}^2}}{z^2}, \quad \text{where } h_{\alpha\beta} = g_{\mu\nu}\partial_\alpha X^\mu\partial_\beta X^\nu \quad (3.23)$$

Here  $h_{\alpha\beta}$  represents the worldsheet metric and  $\alpha, \beta$  represent the worldsheet directions. This action yields the following momentum density and momentum of the string

$$\begin{aligned} \pi_\mu^0 &= \frac{\partial\mathcal{L}}{\partial\dot{x}^\mu} = (\pi_{\tilde{t}}^0, \pi_{x^1}^0, \pi_{x^2}^0, \pi_{x^3}^0, \pi_z^0) = \frac{-1}{2\pi\alpha'z^2\sqrt{1-\tilde{v}^2}}(1, -\tilde{v}, 0, 0, 0), \\ p_\mu &= 2 \int_{z_I}^{z_h} dz \pi_\mu^0 = \frac{1 - z_I/z_h}{\pi\alpha'z_I\sqrt{1-\tilde{v}^2}}(-1, \tilde{v}, 0, 0, 0), \end{aligned} \quad (3.24)$$

where  $\dot{x}^\mu = (dx^\mu/d\tilde{t})$  and  $z_I$  represents the initial position of the tip of the string. In the second equation, the factor of two in front of the integral comes from the double string and we set an infrared cutoff at the future horizon.

Since the endpoints of the string are located at infinity, the string should be approximately straight when the falling velocity of the tip is not too large. In this case, all pieces of the string except for the part at the infinity approximately fall parallelly as a null string. Therefore, the four-momentum of the massless particle is proportional to the four-momentum of the string. We then have

$$\frac{\tilde{q}_i}{\tilde{q}_0} = \frac{p_i}{p_0} = -\tilde{v}, \quad (3.25)$$

and the string should remain straight for an observer inside the shell as illustrated in Fig.3.4. Although it is indicated in [102, 103] that the determinant of the worldsheet

metric should vanish for a null string, the trailing string solution would match the falling string only when  $\tilde{v} = 1$ . We may choose  $\tilde{v} \approx 1$ , for which the trailing string solution approximates the null string solution, while the Lorentz factor  $\gamma = 1/\sqrt{1 - \tilde{v}^2}$  stays finite. In this limit, the massless particle has small virtuality and falls slowly along the  $z$ -direction, which satisfies our previous assumption that the falling velocity cannot be too large. We will discuss more about this scenario in Appendix A.4. After the tip of the string collides with the falling shell and partially enters the AdS-Schwarzschild spacetime, the tip of the string may still move along the null geodesic, whereas the rest part in the medium would be trailed by the backreaction of the spacetime metric led by the shell. Despite the profile of the string outside the shell being sophisticated, the rest part inside the shell should remain unchanged because the wave velocity of the string in the quasi-AdS spacetime is slower than the velocity of the falling shell, which falls with the speed of light. The calculation of the wave velocity by studying the perturbation of the straight string can be found in Appendix A.5. As a result, the string inside the shell is causally disconnected to the disturbances outside. The schematic profile of the falling string after the collision is depicted in Fig.3.5.

After pinning down the initial conditions of the massless particle representing the tip of the string, we may implement the geodesic equation in (3.18) to track the trajectory of the falling particle. Similar to the scenario of the falling wave packet in the WKB approximation, we have to set up the matching condition to connect the  $\tilde{\omega}$  and  $\omega$  defined in two spacetimes at the collision point where the particle crosses the falling shell, while the approach here should be independent of the matching of wave functions.

In the thin-shell limit,  $H(t, z) = z - z_0(t) = 0$  denoting the position of the shell is a hyper-surface. When the massless particle crosses the surface, we may use the conservation of the momentum tangent to the surface, which results in the matching

condition. We now write down the normal vector of the shell,

$$U_\mu = \partial_\mu H(t, z) = (-dz_0/dt, 1) = (-F(z_0), 1) , \quad (3.26)$$

where  $\mu = 0, 1$  denote the  $t$  and  $z$  directions. By taking  $V^\mu U_\mu = 0$  for  $V^\mu$  being the tangent vector, we subsequently obtain

$$V^\mu = (1, F(z_0)) . \quad (3.27)$$

We then use  $q_\mu$  and  $p_\mu$  introduced in the previous context to denote the four-momenta of the particle outside and inside the shell, respectively. By using the matching condition that  $q_\mu V^\mu = p_\mu V^\mu$  at the collision point  $z_c$ , we obtain

$$q_0 + q_z(z_c)F(z_c) = p_0 + p_z F(z_c) = \tilde{p}_0 F(z_c) + \tilde{p}_z F(z_c) . \quad (3.28)$$

By writing it in terms of  $\omega$  and  $\tilde{\omega}$ , we have

$$-\omega + q_z(z_c)F(z_c) = -\tilde{\omega}F(z_c) + \tilde{p}_z F(z_c) , \quad (3.29)$$

which matches (3.21) and leads to the same energy ratio in (3.22). When the shell is null, the derivation is equivalent to the matching of propagating bulk fields in [148] except for the difference in redshift factors.

There is a caveat here: the energy loss of the massless particle representing the tip of the string as a function of the collision point does not correspond to the total energy loss of the string. Only in the case of the null string, the energy loss of the massless particle and that of the falling string would be equivalent since all pieces of the string can be approximated as massless particles moving along the null geodesics coherently. In fact, for an observer on the boundary in the  $t$  coordinate, the string actually decelerates and thus loses energy in the quasi-AdS spacetime when the shell falls. In general, to analyze the instantaneous energy loss entails the understanding of the full string profile, which could not be easily solved when the string crosses the shell; therefore we will not address this issue in the dissertation.

After setting the matching condition and deriving the energy ratio at the collision point, we may track the trajectory of the massless particle traveling in the AdS-Vaidya spacetime. By ejecting a particle at the same time as the injection of the shell from the boundary, which characterizes a virtual gluon generated in the early time when the medium begins to thermalize, the massless particle travels in the quasi-AdS spacetime and then collides with the shell at the first collision point  $z_c$ . Since the shell always falls with the speed of light, the particle will be surpassed by the shell and then moves in the AdS-Schwarzschild spacetime. Finally, it takes infinite time for the particle to collide with the shell at the second collision point  $z_b$  close to the future horizon. At the second collision, the massless particle will attach to the shell and dissipate in the thermalized medium. The stopping distance is thus defined as the traveling distance of the massless particle along the  $x^1$  direction from the ejecting point to  $z_b \approx z_h$ .

We firstly track the trajectory of the massless particle and the position of the shell simultaneously in the quasi-AdS spacetime, where we may use the position of the shell to characterize the time coordinate. From [105], we have

$$\int_0^{\tilde{t}_p} d\tilde{t} = \frac{z_p - z_I}{\left(1 - \frac{|\vec{q}|^2}{\tilde{\omega}^2}\right)^{1/2}}, \quad (3.30)$$

where  $z_p$  denotes the position of the particle at  $\tilde{t}_p$ . On the other hand, the position of the shell is recorded by (3.18) and  $z_I$  is the initial position of the tip of the string. In the  $\tilde{t}$  coordinate, the shell actually falls with the speed of light. Therefore, we may rewrite the position of the massless particle in the interior of the shell in terms of the position of the shell as

$$z_p(z_0) = z_I + \left(1 - \frac{|\vec{q}|^2}{\tilde{\omega}^2}\right)^{1/2} z_0, \quad (3.31)$$

where the values of  $z_I$ ,  $|\vec{q}|$ , and  $\tilde{\omega}$  are determined by the initial conditions. Now,

the  $z_c$  can be obtained by solving (3.31) at  $z_p = z_0 = z_c$ . After the first collision, the trajectory of the particle moving in the AdS-Schwarzschild spacetime can also be found from [105],

$$t_p = t_c + \int_{z_c}^{z_p} \frac{dz}{F(z) \left(1 - F(z) \frac{|\bar{q}|^2}{\omega^2}\right)^{1/2}}, \quad (3.32)$$

while the position of the shell is still governed by (3.18)

$$t_0 = t_c + \int_{z_c}^{z_0} \frac{dz_s}{F(z_s)}. \quad (3.33)$$

Finally,  $z_b$  can be found by solving  $t_p = t_0$  via (3.32) and (3.33) at  $z_p = z_0 = z_b$ , while we may take  $z_b \approx z_h$  for simplicity and the deviation is in fact negligible. By using (3.18), the stopping distance of the massless particle traveling in AdS-Vaidya spacetime is

$$x_s^1 = \int_{z_I}^{z_c} \frac{dz}{\left(\frac{\bar{\omega}^2}{|\bar{q}|^2} - 1\right)^{1/2}} + \int_{z_c}^{z_b} \frac{dz}{\left(\frac{\omega^2}{|\bar{q}|^2} - F(z)\right)^{1/2}}. \quad (3.34)$$

As discussed in the previous section, the stopping distance of a string with  $z_I = 0$  as a gluon with infinite energy is unaffected by the thermalization process. On the contrary, when  $z_I$  is below the boundary, the string may characterize a soft gluon. Although the energies of gluons depend on the string profiles in dual geometries, the string profiles do not affect the maximum stopping distances. In order to make the comparison, we could choose straight strings for the initial profiles in both AdS-Schwarzschild and AdS-Vaidya spacetimes and thus the gluons traveling in the thermalized and non-thermalized media will carry the same initial energy and momentum. The initial four-momentum of a gluon as a straight string in the dual geometry is given in (3.24).

In Fig. 3.6, we illustrate the stopping distances scaled by temperature when fixing the initial velocities of gluons with distinct initial energies scaled by temperature and the t'Hooft coupling in both equilibrium and non-equilibrium media. For soft probes, we find the larger stopping distances in the non-equilibrium case. Since the thermalization of the medium in the top-down scenario described by the falling shell starts from the ultraviolet scale, soft probes generated in the infrared scale travel in the vacuum in the early time and hence result in larger stopping distances compared to the probes initially created in the thermalized medium. On the other hand, as shown in Fig. 3.7, the thermalization of the medium is more influential for light probes compared to heavy probes with the same energy. For highly offshell gluons, the energy loss may stem from their intrinsic radiation, which suppresses the induced radiation due to the collision effect amid the medium. Notice that the gluons traveling in early times actually decelerate even in the vacuum due to the redshift effect led by a falling shell which thus loss energy from the radiation in vacuum. In this scenario, the increase of velocities, which correspond to the decrease of virtualities, leads to the increase of stopping distances. This scenario should be less affected by the thermalization of media, which can be observed from Fig.3.7, where the stopping distances in the equilibrium and non-equilibrium media coincide at small  $\gamma$ . On the contrary, for nearly onshell gluons, the energy loss should be attributed to the induced radiation when traversing the media. This scenario is also indicated in [149] for heavy probes, where the trailing string can be separated by a critical point into two parts in the bulk. The part above the point could be interpreted as dressed color field and the part below the point would be causally disconnected and be regarded as radiation. When the velocities of gluons increase, the induced radiation becomes more robust and cause the decrease of stopping distances, which can be observed in Fig. 3.7 for large  $\gamma$ . Therefore, the induced radiation of gluons traveling in the non-equilibrium medium should be suppressed compared to the

case in the thermalized medium in the ultra-relativistic limit. The intrinsic radiation and induced radiation may compete with each other and give rise to maximum stopping distances for gluons with certain velocities. In general, the stopping distances of the probe gluons are enhanced by the thermalizing process of the medium.

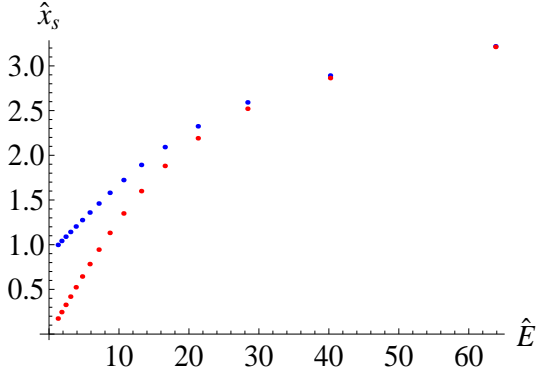


FIGURE 3.6: The blue and red dots represent the stopping distances in AdS-Vaidya and AdS-Schwarzschild spacetimes respectively, where  $\hat{x}_s = x_s \pi T$  and  $\hat{E} = \pi \alpha' z_h E = \frac{1}{\sqrt{g_{YM}^2 N_c}} \frac{E}{T}$ . Here we fix the initial velocities of probes  $v_I = \delta = 0.99$ .

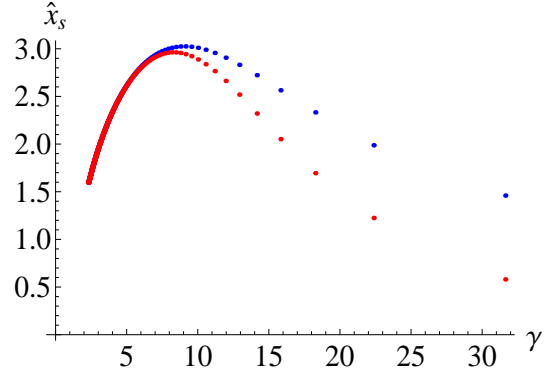


FIGURE 3.7: The blue and red dots represent the stopping distances in AdS-Vaidya and AdS-Schwarzschild spacetimes respectively, where  $\gamma$  denote the Lorentz factors encoding the initial velocities of gluons. Here we fix the initial energies of probes  $\hat{E} = 50$ .

### 3.4 Thermalization Time with Chemical Potentials

In this section, we will extract the thermalization time of the non-equilibrium plasma with a non-zero chemical potential by tracking the position of the falling shell in Poincare patch of AdS-RN-Vaidya geometry. The approach is different from studying non-local operators in Eddington-Finkelstein (EF) coordinates as carried out in [146, 150]. Since we can define thermalization time to be the time when the shell almost coincides with the future horizon, it is independent of the length of the operators. We will observe that with increasing chemical potential, this thermalization time decreases.

We begin with the AdS-RN-Vaidya<sup>1</sup> metrics in EF coordinates with  $d = 3$  and  $d = 4$ , respectively. For  $d = 3$ , we have

$$ds^2 = \frac{1}{z^2} \left( -f(v, z)dv^2 - 2dv dz + dx_i^2 \right) , \quad A_v = q(v)(z_h - z) , \quad (3.35)$$

where  $f(v, z) = 1 - m(v)z^3 + \frac{1}{2}q(v)^2z^4$ . For  $d = 4$ , we have

$$ds^2 = \frac{1}{z^2} \left( -f(v, z)dv^2 - 2dv dz + dx_i^2 \right) , \quad A_v = q(v)(z_h^2 - z^2) , \quad (3.36)$$

where  $f(v, z) = 1 - m(v)z^4 + \frac{2}{3}q(v)^2z^6$ . Here we have set the AdS curvature radius  $L = 1$ . The coordinates  $x_i$  represent the  $d$ -dimensional spatial directions. Also,  $v$  denotes the EF time coordinate and  $z$  denotes the radial direction. The boundary is located at  $z = 0$  and  $z_h$  denotes the future horizon. In the equations above,  $m(v)$  and  $q(v)$  represent the mass and electric charge of the shell. The charge is related to the time component of the vector potential, which generates an R-charge chemical potential in the gauge theory side *via*

$$\mu = \lim_{z \rightarrow 0} A_v(v, z) . \quad (3.37)$$

For simplicity, we are interested in the thin-shell limit of the interpolating mass function

$$m(v) = \frac{M}{2} \left( 1 + \tanh \left( \frac{v}{v_0} \right) \right) \quad (3.38)$$

with  $v_0 \rightarrow 0$ . We can make the same *choices* as [146] by taking  $q(v)^2 = Q^2 m(v)^{4/3}$  and  $q(v)^2 = Q^2 m(v)^{3/2}$  for  $d = 3$  and  $d = 4$ , respectively. The values of  $z_h$  are

<sup>1</sup> For  $d = 3$ , the Hodge dual of the bulk electro-magnetic field is another two-form. Thus we can also introduce a magnetic charge in the AdS-Vaidya type background: such a background should be dubbed as AdS-dyon-Vaidya background. By adjusting the values of the electric and magnetic charge in the system, the final temperature of the medium can be fine-tuned to zero, which corresponds to an electro-magnetic quench phenomenon. More discussion on the dyonic background can be found in Appendix A.7.

determined by

$$f(v > v_0, z_h) = 1 - Mz_h^3 + \frac{1}{2}M^{4/3}Q^2z_h^4 = 0, \quad \text{for } d = 3, \quad (3.39)$$

$$f(v > v_0, z_h) = 1 - Mz_h^4 + \frac{2}{3}M^{3/2}Q^2z_h^6 = 0, \quad \text{for } d = 4. \quad (3.40)$$

We assume the shell falls from the boundary at  $t = 0$  and thus  $\mu$  is a constant since  $v = t \geq 0$  on the boundary. On the other hand, the thermalization temperature is given by

$$T = -\frac{1}{4\pi} \frac{d}{dz} f(v > v_0, z)|_{z_h}. \quad (3.41)$$

The entropy can be determined by the area of the black hole,

$$S = \frac{A_h}{4\pi G}, \quad (3.42)$$

where  $A_h$  represents the area of the black hole and  $G$  denotes the Newtonian constant.

Before proceeding further, a few comments are in order. Since the underlying theory is conformal, the only relevant parameter is the ratio  $T/\mu$ . Thus we define

$$\chi_d = \frac{1}{4\pi} \left( \frac{\mu}{T} \right), \quad (3.43)$$

which we will consider throughout the chapter. By using (3.10), one can attain the AdS-RN-Vaidya geometry in Poincare coordinates in the thin-shell limit as

$$ds^2 = \begin{cases} \frac{1}{z^2} \left( -F(z) dt^2 + \frac{dz^2}{F(z)} + dx^2 \right) & \text{if } v > 0 (z < z_0), \\ \frac{1}{z^2} \left( -F(z_0)^2 dt^2 + dz^2 + dx^2 \right) & \text{if } v < 0 (z > z_0), \end{cases} \quad (3.44)$$

where

$$F(z) = \begin{cases} 1 - Mz^3 + (1/2)M^{4/3}Q^2z^4 & \text{for } d = 3, \\ 1 - Mz^4 + (2/3)M^{3/2}Q^2z^6 & \text{for } d = 4. \end{cases} \quad (3.45)$$

Since the falling velocities of the upper and lower surfaces are the same in the thin-shell limit, the position of the falling shell is given by

$$t(z_0) = \int_0^{z_0} dz_s \frac{1}{F(z_s)}. \quad (3.46)$$

Given that the shell never coincides with the future horizon exactly in the Poincare coordinates, we approximate the thermalization time as  $\tau = t(z_0)|_{z_0=0.99z_h}$ , which is shown in Fig. 3.8 and Fig. 3.9 with different values of chemical potential measured in the unit of temperature for  $d = 3$  and  $d = 4$ , respectively. When increasing the chemical potential, the thermalization time decreases. We should comment here that the specific choice of  $z_0 = 0.99z_h$  does not affect the qualitative feature as far as the thermalization time is concerned, any other choice yields a similar behavior. Also, for very large value of  $\chi_d$  the thermalization time vanishes asymptotically.

The qualitative behaviors here are distinct from those found by studying non-local operators in the AdS-RN-Vaidya metric[146]. However, we should notice that the definitions of the thermalization time in these two approaches are different. For example, if we introduce a spacelike geodesic with two ends fixed on the boundary, the thermalization time can be defined as the time when the shell grazes the bottom of the geodesic in the bulk. After that, the whole geodesic will reside in the AdS-RN spacetime, which matches the result derived in the thermalized medium. Therefore, in this situation, the thermalization time of non-local operators are recorded by the position of the falling shell. Nevertheless, when the separation on the boundary of the spacelike geodesic is too large such that the bottom of it penetrates the future horizon, the geodesic can never fully reside in the AdS-RN spacetime even when the shell asymptotically reaches the future horizon. In other words, the maximum thermalization time in Poincare coordinates should be the time when the shell almost reaches the future horizon. For the non-local operators with much larger lengths can never thermalize in Poincare coordinates or the definition of the thermalization

time in such a case should be modified. Thus, thermalization times extracted from two approaches can only be compared when the length scale of non-local operators introduced in EF coordinates is about the size of the future horizon.

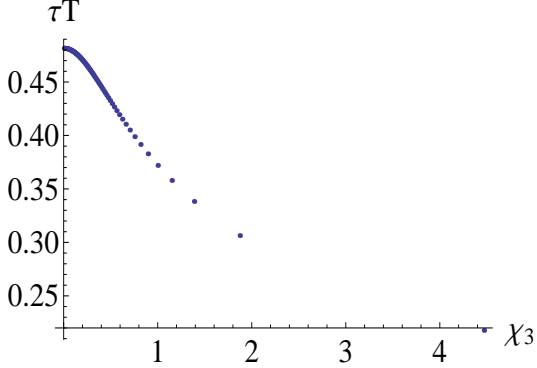


FIGURE 3.8: The thermalization time  $\tau$  with different values of chemical potential in  $d = 3$ .

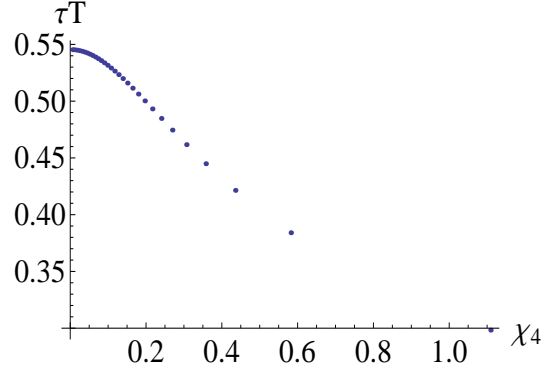


FIGURE 3.9: The thermalization time  $\tau$  with different values of chemical potential in  $d = 4$ .

### 3.5 Jet Quenching with Chemical Potentials

In this section, we will study the stopping distances of light probes in the thermalizing background with chemical potentials. Since the computations are basically the same as those previously shown in the case with zero chemical potentials, we will mainly present the results in this section. Before proceeding with the non-equilibrium medium, we may begin by investigating the thermal medium with a non-zero chemical potential, which is described by the AdS-RN geometry. We will take the physical interpretation in Ref.[103] to consider the stopping distance for a virtual gluon. As shown in Section 3.3, The stopping distance is given by

$$x_s^1 = \int_{z_I}^{z_h} \frac{dz}{\left(\frac{\omega^2}{|\vec{q}|^2} - F(z)\right)^{1/2}}, \quad (3.47)$$

which only depends on the ratio  $|\vec{q}|/\omega$  and the initial position of the tip of the string  $z_I$ . The ratio  $|\vec{q}|/\omega$  roughly represents the ratio to the spatial momentum and energy

of the virtual gluon and  $z_I$  can be associated with its initial energy. Even though determining the ratio of  $|\vec{q}|$  to  $\omega$  entails the initial string profile close to the tip, which could depend on the geometry of the thermalized medium, we may choose the straight string as the simplest setup. As shown in [99, 100], the profile of a moving string obtained from extremizing the Nambu-Goto action in the AdS geometry is a straight string. Although the physical solution in the AdS-Schwarzschild geometry corresponds to a trailing profile, where the profile in the presence of a chemical potential could be more complicated, we will make the same straight-string setup in the thermalized case for comparison. This assures that the gluons traveling in the thermalized medium with different values of chemical potential carry the same initial energy and momentum and as well the same ratio to  $|\vec{q}|$  and  $\omega$ . The ratio of the stopping distance with a non-zero chemical potential to that with zero chemical potential at the same temperature is shown in Fig. 3.10 and Fig. 3.11 for both  $d = 3$  and  $d = 4$ . It turns out that the stopping distance of the light probe decreases when the chemical potential increases, which has the same qualitative feature compared to the thermalization of the medium.

Physically, by increasing the chemical potential, we actually increase the number of states. From (3.42), the entropy density of the plasma in  $d+1$  dimension is given by  $4Gs = z_h^{-(d-1)}$ . As illustrated in Fig. 3.12 and Fig. 3.13, the entropy density increases when the chemical potential is increased. The medium thus becomes denser, which results in the enhanced scattering for the light probe and a smaller stopping distance. On the other hand, the medium also thermalizes faster because of the same effect. Although the holographic correspondence of the falling shell in the gauge theory side is unknown, the falling shell could be characterized by the collective motion of massless particles with large virtuality in the gravity dual since a null shell is homogeneous along spatial directions and it falls along a null geodesic. Each particle

as a component of the shell may as well be influenced by the backreaction to the spacetime metric caused by the falling shell; hence it should qualitatively behave in the same manner as the light probe traversing the medium. Since the component particles of the shell carry large virtuality, the enhanced scattering led by increasing chemical potential would be more pronounced, which reduces the thermalization time of the medium. By comparing Fig. 3.12 with Fig. 3.13, the entropy density for  $d = 4$  increases more rapidly than that for  $d = 3$ , which also manifests the steeper drop of the thermalization time of both the probe and the medium for  $d = 4$  when increasing the chemical potential by comparing Fig. 3.8 with Fig. 3.9 and Fig. 3.10 with Fig. 3.11.

To avoid a naked singularity in the AdS-RN spacetime, there exists a maximum value of  $Q$  such that the position of the horizon is given by  $F(z) = 0$ . By taking  $M = 1$ , the maximum values are  $Q_{\max} = (27/32)^{1/6}$  and  $Q_{\max} = 3^{-1/4}$  for  $d = 3$  and  $d = 4$ , respectively. Given that the derivative of  $F(z)$  vanishes at the horizon, the temperature of the medium then vanishes. The corresponding zero temperature black hole is known as the extremal black hole. However, this does not correspond to the vacuum since it carries a non-zero entropy given by a non-vanishing area of the extremal black hole horizon. In this situation, we see that the dimensionless parameter  $\chi_{4(3)}$  diverges. Also, the stopping distances with a non-zero chemical potential in the unit of temperature,  $\hat{x}_s^1(T, \mu)$  shown in Fig. 3.10 and Fig. 3.11, become zero; we hence lose the ability to make a comparison between the observables in the media with and without a chemical potential in this particular situation. Now, we may follow the approach in the previous sections to evaluate the stopping distances in the AdS-RN-Vaidya geometry. We can compute the stopping distance by either employing Eq.(3.18) by replacing the blackening function  $F(z)$  or directly invoking null geodesic equations as shown in Appendix A.6. Similar to the study in the AdS-Vaidya spacetime, the stopping distance of the massless particle falling

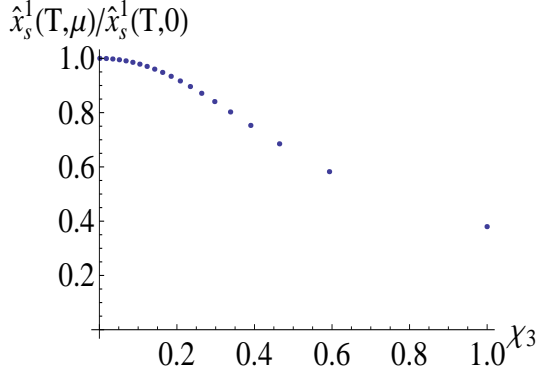


FIGURE 3.10: The ratio to the stopping distances with and without chemical potential in the unit of temperature for  $d = 3$ , where  $\hat{x}_s^1 = x_s^1 T$ . Here we set  $M = 1$ ,  $z_I = 0$ , and  $|\vec{q}| = 0.99\omega$ .

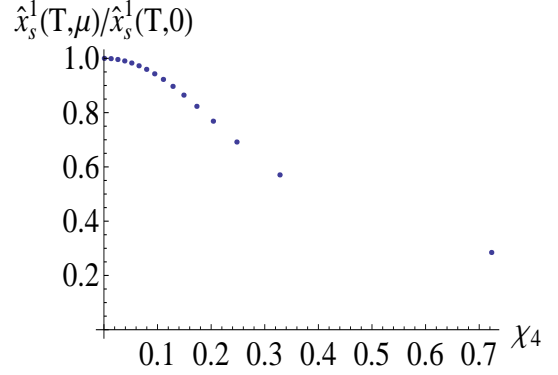


FIGURE 3.11: The ratio to the stopping distances with and without chemical potential in the unit of temperature for  $d = 4$ , where  $\hat{x}_s^1 = x_s^1 T$ . Here we set  $M = 1$ ,  $z_I = 0$ , and  $|\vec{q}| = 0.99\omega$ .

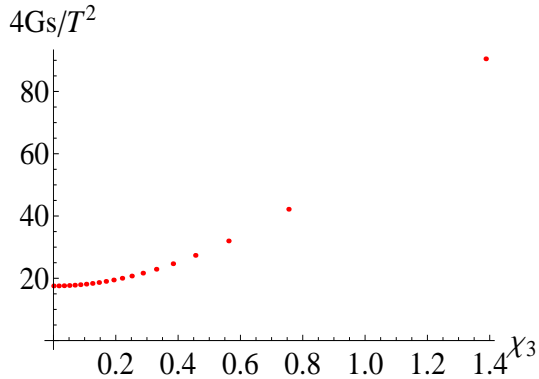


FIGURE 3.12: The entropy density with different values of the chemical potential for  $d = 3$ . Here we set  $M = 1$ .

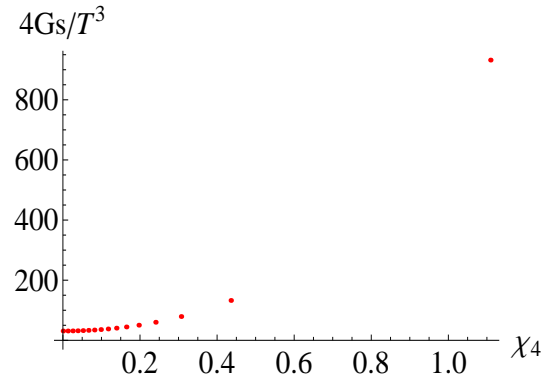


FIGURE 3.13: The entropy density with different values of the chemical potential for  $d = 4$ . Here we set  $M = 1$ .

from the boundary is not affected by the gravitational collapse in the AdS-RN-Vaidya geometry. In our setup, when we set the initial position of the tip of the string on the boundary, the corresponding virtual gluon on the gauge theory side carries infinite energy as shown in (3.24). As indicated previously, when the hard probe has the energy much larger than any other scale such as the thermalization temperature or the chemical potential of the system, the thermalization of the probe would be insensitive to the thermalization of the medium. However, for the soft

probe carrying energy comparable to other scales of the system, we may envision an influence of the thermalization process on the jet quenching phenomenon. This scenario is shown in Fig. 3.14 and Fig. 3.15, where we eject the massless particle below the boundary, which corresponds to the soft gluon with a finite energy. As a result of thermalization, stopping distance of light probes increases.

Finally, we illustrate this behaviour for different values of chemical potential in AdS-RN and AdS-RN-Vaidya spacetimes in Fig. 3.16 and Fig. 3.17. The results can be reproduced by solving geodesic equations directly in EF coordinates, which are presented in Appendix A.6; the latter approach can be further applied beyond the thin-shell limit. As shown in Fig.3.16 and Fig.3.17, the stopping distances scaled by the thermalization temperature in both the AdS-RN-Vaidya and AdS-RN geometries decrease when the values of  $\chi_d$  are increased and will drop to zero when the values of  $\chi_d$  reach infinity.

In general, we find that the probe gluon travels further in the non-equilibrium plasma with a non-zero chemical potential compared to the thermal background. Increasing the magnitude of the chemical potential decreases the stopping distances in both equilibrium and non-equilibrium plasmas.

### 3.6 Conclusions and Discussions

In this chapter, we have investigated the influence of the thermalization of the strongly-coupled plasma on light probes by studying the gravitational collapse in the AdS-Vaidya spacetime. In the thin-shell limit, we write down the analytic expression of the AdS-Vaidya metric in Poincare coordinates. By using the derived red shift factor, we track the position of the falling shell in the bulk. In this scenario, the thermalization time of the medium can be extracted when the shell asymptotically reaches the future horizon. We find  $t_{th}T \approx 0.55$ , which is approximately consistent with the thermalization time obtained in other holographic models, which as

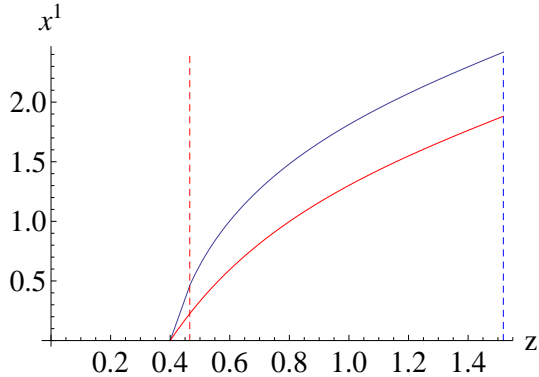


FIGURE 3.14: The red and blue curves represent the trajectories of the massless particles moving in AdS-RN and AdS-RN-Vaidya spacetimes for  $d = 3$  and  $\chi_3 = 4.47$ , respectively. The red and blue dashed lines denote the first collision point and the position of the future horizon. Here we take  $z_I = 0.4$ ,  $M = 1$ , and  $|\vec{q}|/\tilde{\omega} = 0.99$  as the initial conditions in both spacetimes.

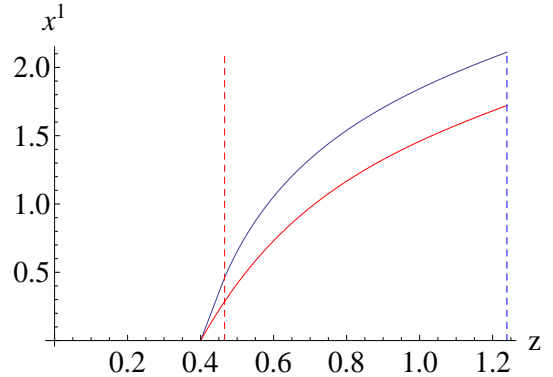


FIGURE 3.15: The red and blue curves represent the trajectories of the massless particles moving in AdS-RN and AdS-RN-Vaidya spacetimes for  $d = 4$  and  $\chi_4 = 1.1$ , respectively. The red and blue dashed lines denote the first collision point and the position of the future horizon. Here we take  $z_I = 0.4$ ,  $M = 1$ , and  $|\vec{q}|/\tilde{\omega} = 0.99$  as the initial conditions in both spacetimes.

well resides in the range of the thermalization time at RHIC based on the viscous hydrodynamics.

Also, we have computed the stopping distance of the light probe traversing the non-equilibrium plasma by solving the null geodesic of a massless particle falling in the AdS-Vaidya geometry. We find the stopping distance of a hard probe is equal to that in the thermalized medium governed by the AdS-Schwarzschild spacetime even when the shell has finite thickness. In the thermalization process, the decrease of the virtualities of hard probes in principle result in larger stopping distances, while this effect is negligible. However, for the soft and relativistic probes, they travel longer in the pre-equilibrium state. The suppression of induced radiation result in larger stopping distances. Therefore, the thermalization of the medium may reduce the jet quenching of soft and relativistic probes.

Moreover, we have analyzed thermalization of a non-equilibrium plasma with a

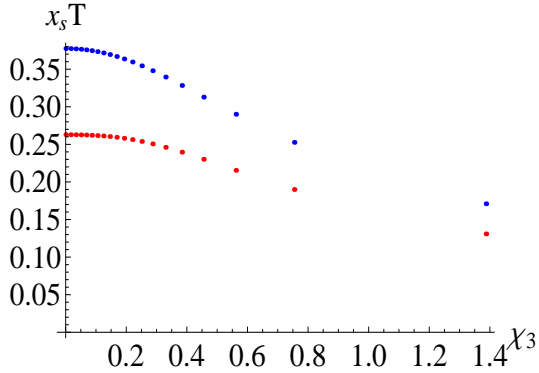


FIGURE 3.16: The red and blue points represent the stopping distances with different values of chemical potential in AdS-RN and AdS-RN-Vaidya for  $d = 3$ , respectively. Here we set  $M = 1$ ,  $z_I = 0.4$ , and  $|\bar{q}|/\tilde{\omega} = 0.99$  as the initial conditions in both spacetimes.

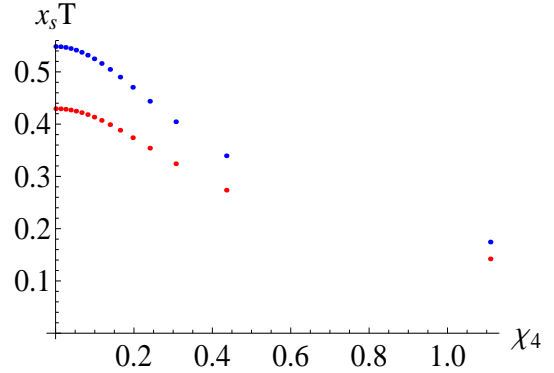


FIGURE 3.17: The red and blue points represent the stopping distances with different values of chemical potential in AdS-RN and AdS-RN-Vaidya for  $d = 4$ , respectively. Here we set  $M = 1$ ,  $z_I = 0.4$ , and  $|\bar{q}|/\tilde{\omega} = 0.99$  as the initial conditions in both spacetimes.

non-zero chemical potential by tracking a thin shell falling in the AdS-RN-Vaidya spacetime. We found the thermalization time of the medium decreases when the chemical potential is increased. We have also studied the jet quenching of a virtual gluon traversing such a medium by computing the stopping distance of a falling string, in which the tip of the string falls along a null geodesic. In both the thermalized or thermalizing medium with a non-zero chemical potential, the stopping distance of the probe gluon decreases when the chemical potential is increased. On the other hand, for a soft gluon with finite energy comparable to the thermalization temperature of the medium, its stopping distance in the thermalizing medium is larger than that in the thermalized case.

In section II, we briefly discussed the difference between the thermalization time obtained from our approach by tracking the falling shell in Poincare coordinates and that derived in Ref.[146] by analyzing non-local operators; we will further elaborate on this here. When the medium carries no chemical potential, the position of the horizon is about the inverse of the temperature. As mentioned in the end of Sec-

tion 3.1, the thermalization times obtained from two approaches in the AdS-Vaidya geometry approximately match when the length scale of the nonlocal operators is about the inverse of the temperature. However, for the medium with a non-zero chemical potential, the temperature does not linearly depend on  $z_h^{-1}$ . To compare the thermalization times obtained from two approaches, we have to investigate the thermalization time for a nonlocal operator with the length scale about the size of the horizon in the AdS-RN-Vaidya spacetime. As shown in Fig.3.18, thermalization time obtained by analyzing non-local observables with a length-scale  $l_s = 1.71z_h$ [146] do exhibit similar qualitative feature as the one we have encountered here. Note that the number  $l_s/z_h$  bears no possible physical significance other than being an order one number where we have found a visibly pleasant matching. As far as the thermalization time of the medium is concerned, we conclude that our approach by tracking the falling shell close to the horizon seems consistent with that by probing the thermalizing medium with nonlocal operators, when the length scale of the operators approximately equals the size of the horizon. In addition, the thermalization times from both approaches starts to drop more rapidly when  $\mu \gtrsim T$ .

For the light probe traversing the medium with a non-zero chemical potential, the decrease of the stopping distance when increasing the chemical potential is expected due to the enhanced scattering with the increasing density of the medium. In [151, 152], it is found that the jet quenching parameter and the drag force of a trailing string in the charged SYM plasma both increase when the chemical potential is increased, which is again consistent with our general observations here.

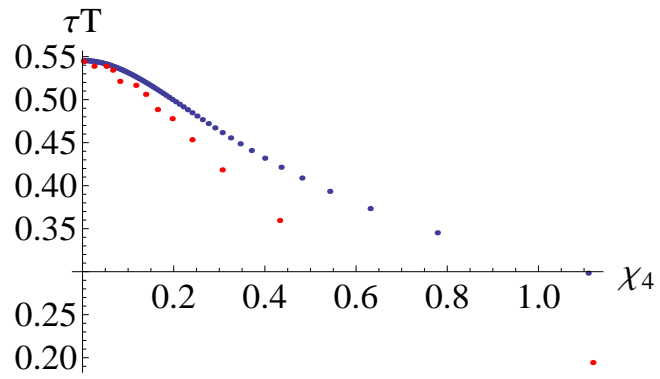


FIGURE 3.18: The blue and red points represent the thermalization times scaled by the temperature obtained from our approach and that from analyzing non-local observables, respectively. Here we take  $M = 1$  in the both cases.

## Investigating Strongly Coupled Anisotropic Plasmas

The work in this chapter was first published in [130, 131]. As discussed in Section 1.2, in heavy ion collisions, the medium may have large pressure anisotropy even after reaching thermal equilibrium. The influence of pressure anisotropy on different probes thus become important. In general, the pressure anisotropy decreases with respect to time during the expansion according to viscous and anisotropic hydrodynamics. As a result, in AdS/CFT correspondence, it is more realistic to study time-dependent backgrounds such as [23, 24, 153, 27, 28, 29, 67]. However, since to solve these time-dependent geometries is more numerically involved, it is rather challenging to introduce external probes in the time-dependent backgrounds. On the other hand, the static yet anisotropic backgrounds may be useful toy models to investigate anisotropic effects on different probes.

In [154] and [155, 14], the dual geometries of such a strongly coupled and static plasma with pressure anisotropy are derived. The former originates from solely the anisotropic stress energy tensor, while the spacetime metric has a naked singularity. The latter is generated from a five-dimensional Einstein action with a dilaton and an

axion field linearly depending on an anisotropic factor, which results in an anisotropic and thermal background regular in the bulk.

The energy loss of hard probes in such strongly-coupled anisotropic plasmas described by holographic models has been investigated recently. The jet quenching parameter, drag force as well as the heavy quark potential are computed in holographic duals [156, 157, 158, 159]. In addition, the energy loss of orbiting quarks and quarkonium dissociation in an anisotropic holographic dual also have been explored in [160] and [161], respectively. It is found in [156, 159] that the drag force in the anisotropic plasma can be smaller or larger than the isotropic case depending on different velocities and orientations of the probes. On the other hand, the anisotropic value of the jet quenching parameter may be enhanced or reduced when comparing to the isotropic value at equal temperature or at equal entropy density [158, 157]. These studies focus on the jet quenching of heavy probes in the gravity dual, whereas the anisotropic effect on light probes has not yet been investigated. Therefore, we will investigate the jet quenching of light quarks by computing their stopping distances in an anisotropic plasma in the following section. Also, although the thermal-photon production in an anisotropic background has been studied in [162], the effect from massive quarks was considered therein. We will hence generalize the study in [162] to incorporate the effect from massive quarks and further include that from a constant magnetic field in Chapter.5 for photon production.

This chapter is organized in the following order. In Section 4.1, we give a brief introduction to the anisotropic and thermalized dual geometry proposed by Mateos and Trancanelli(MT)[155, 14]. In Section 4.2, we compute the stopping distance of light quarks in such a background. In Section 4.3, we investigate the photon production by including the anisotropic background in D3/D7 system with trivial embeddings. In Section 4.4, we further generalize the setup in Section 4.3 to the black hole embedding to incorporate massive quarks. The photon spectra with massive

quarks will then be computed. Finally, we make concluding remarks in the last section.

## 4.1 The Einstein-Axion-Dilaton System

In this section, we will introduce the anisotropic dual geometry led by a five-dimensional dilaton-axion gravity action [155, 14]. In the Einstein frame, the action takes the form,

$$S_E = \frac{1}{2\kappa^2} \int d^5x \sqrt{-g} \left( R + 12 - \frac{1}{2}(\partial\phi)^2 - \frac{1}{2}e^{2\phi}(\partial\chi)^2 \right) + \frac{1}{2\kappa^2} \int d^4x \sqrt{-\gamma} 2K, \quad (4.1)$$

where  $\phi$  and  $\chi$  denote the dilaton and axion, respectively. The second term in (4.1) is the Gibbons-Hawking-York boundary term and  $2\kappa^2 = 16\pi G = 8\pi^2/N_c^2$  is the five dimensional gravitational coupling. To simplify the computations, we have set  $L = 1$ , where  $L = (4\pi g_s N_c l_s^2)^{1/4}$  denotes the radius of  $S^5$  in the ten-dimensional spacetime. The solution of the dual metric in the Einstein frame is given by

$$ds_E^2 = \frac{e^{-\frac{\phi(u)}{2}}}{u^2} \left( -\mathcal{F}(u)\mathcal{B}(u)dt^2 + dx^2 + dy^2 + \mathcal{H}(u)dz^2 + \frac{du^2}{\mathcal{F}(u)} \right) \quad (4.2)$$

for  $\chi = az$ , where  $\mathcal{F}(u)$ ,  $\mathcal{B}(u)$ , and  $\mathcal{H}(u) = e^{-\phi(u)}$  depend on  $\phi(u)$  and the anisotropic factor  $a$ , which corresponds to the density of D7 branes embedded along the anisotropic direction  $z$ . These D7 branes dissolve in the bulk and contribute to the pressure anisotropy of the medium. Note that the D7 branes here are different from the D7 flavor branes mentioned in Chapter.2. Also, hereafter  $u$  will denote the bulk direction through the dissertation. The blackening function  $\mathcal{F}(u)$  vanishes at the event horizon  $u = u_h$ , which results in the temperature and entropy density of the plasma.

From [155, 14], the temperature and entropy density of the MT geometry read

$$\begin{aligned}
T &= -\frac{\partial_u \mathcal{F} \sqrt{\mathcal{B}}|_{u=u_h}}{4\pi} = \sqrt{\mathcal{B}(u_h)} \frac{e^{\frac{1}{2}(\tilde{\phi}_b - \tilde{\phi}_h)}}{16\pi u_h} (16 + u_h^2 e^{\frac{7}{2}\tilde{\phi}_h}), \\
s &= \frac{N_c^2 a^{\frac{5}{7}} e^{-\frac{5}{4}\tilde{\phi}_h}}{2\pi u_h^3},
\end{aligned} \tag{4.3}$$

where  $\tilde{\phi}(z) = \phi(z) + \log a^{4/7}$ ,  $\tilde{\phi}_b = \tilde{\phi}(0)$  and  $\tilde{\phi}_h = \tilde{\phi}(u_h)$ . All metric components are in fact functions of the dilaton field as the solution from a nonlinear field equation of the effective action in (4.1). Due to nonlinearity, this field equation can only be solved numerically, while the analytic result can be found for small anisotropy such that ( $T \gg a$ ). We will then present the small-anisotropy result for future references. In the high-temperature or the small-anisotropy regime ( $T \gg a$ ), the pressure anisotropy is small. In this regime, the anisotropic factor  $a$  in the strongly coupled scenario can be related to a parameter  $\xi$  introduced in the weakly coupled approach [81, 163], which is define as

$$\xi = \frac{\langle p_T^2 \rangle}{2\langle p_L^2 \rangle} - 1, \tag{4.4}$$

where  $p_T$  and  $p_L$  denote the magnitudes of momenta along the transverse and longitudinal directions, respectively. In heavy ion collisions, the longitudinal direction is the beam direction. The parameter  $\xi$  characterizes the momentum anisotropy in a weakly coupled and anisotropic plasma. It was found in [156] that

$$\xi \approx \frac{5a^2}{8\pi^2 T^2} \text{ for } 0 < \xi \ll 1 \tag{4.5}$$

by comparing the pressure differences in both weakly coupled and strongly coupled approaches. When  $T \gg a$ , the analytic expression of the metric up to the leading

order is given by

$$\begin{aligned}
\mathcal{F}(u) &= 1 - \frac{u^4}{u_h^4} + a^2 \mathcal{F}_2(u) + \mathcal{O}(a^4), \\
\mathcal{B}(u) &= 1 + a^2 \mathcal{B}_2(u) + \mathcal{O}(a^4), \\
\mathcal{H}(u) &= e^{-\phi(u)}, \phi(u) = a^2 \phi_2(u) + \mathcal{O}(a^4).
\end{aligned} \tag{4.6}$$

From (B.7), the MT metric in (4.2) will reduce to the AdS-Schwarzschild metric when  $a \rightarrow 0$ . The explicit expression of the leading-order anisotropic terms are

$$\begin{aligned}
\mathcal{F}_2(u) &= \frac{1}{24u_h^2} \left[ 8u^2(u_h^2 - u^2) - 10z^4 \log 2 + (3u_h^4 + 7u^4) \log \left( 1 + \frac{u^2}{u_h^2} \right) \right], \\
\mathcal{B}_2(u) &= -\frac{u_h^2}{24} \left[ \frac{10}{u_h^2 + u^2} + \log \left( 1 + \frac{u^2}{u_h^2} \right) \right], \\
\phi_2(u) &= -\frac{u_h^2}{4} \log \left( 1 + \frac{u^2}{u_h^2} \right).
\end{aligned} \tag{4.7}$$

The temperature at the leading order is thus defined as

$$T = \frac{1}{\pi u_h} + a^2 u_h \frac{5 \log 2 - 2}{48\pi} + \mathcal{O}(a^4). \tag{4.8}$$

Conversely, the horizon can be written as

$$u_h = \frac{1}{\pi T} + a^2 \frac{5 \log 2 - 2}{48\pi^3 T^3} + \mathcal{O}(a^4). \tag{4.9}$$

In fact, the pressure anisotropy in the small-anisotropy regime and that in mid-anisotropy regime have distinct behaviors. As shown in Fig.4.1, the longitudinal pressure is slightly smaller than the transverse pressure for  $a/T \leq 3.4$ , while the longitudinal pressure surpasses the transverse pressure for  $a/T \geq 3.4$ . At large  $a$ , the pressure ratio diverges.

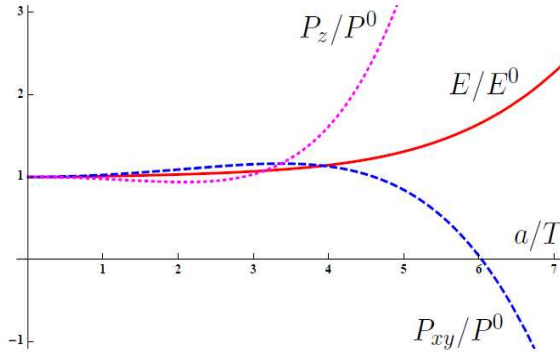


FIGURE 4.1: The energy and pressures normalized by their isotropic values as functions of  $a/T$ [14].

## 4.2 Light Probes in Anisotropic Plasmas

Now, we may study the jet quenching of a light probe in the anisotropic plasma by computing the stopping distance of a massless particle moving along the null geodesic in the MT metric. We will follow the approach introduced in Chapter.3, where an R-charged current is generated by a massless gauge field in the gravity dual. The induced current may be regarded as an energetic jet traversing the medium. When the wave packet of the massless field falls into the horizon of the dual geometry, the image jet on the boundary dissipates and thermalizes in the medium. The stopping distance is thus define as the distance for a jet traversing the medium before it thermalizes. In the WKB approximation, we assume that the wave packet of the gauge field in the gravity dual highly localized in the momentum space. We thus factorize the wave function of the gauge field as

$$A_j(t, u) = \exp \left[ \frac{i}{\hbar} \left( q_k x^k + \int du q_u \right) \right] \tilde{A}_j(t, u), \quad (4.10)$$

where  $q_u$  denotes the momentum along the bulk direction and  $j, k = 0, 1, 2, 3$  represent four-dimensional spacetime coordinates and  $q_k$  denotes the four-momentum, which is conserved as the metric preserves the translational symmetry along the four-

dimensional spacetime. Here  $\tilde{A}_i(t, u)$  is slow-varying with respect to  $t$  and  $u$ . In the classical limit ( $\hbar \rightarrow 0$ ), the equation of motion of the wave packet will reduce to a null geodesic in the dual geometry, which takes the form [105],

$$\frac{dx^i}{du} = \sqrt{g_{uu}} \frac{g^{ij} q_j}{(-q_k q_l g^{kl})^{1/2}}. \quad (4.11)$$

Thus, the wave packet can be approximated as a massless particle and the null geodesic will lead to a maximum stopping distance for an image jet on the boundary in the classical limit. We will take the interpretation in [102] for light quarks, where the bulk governed by the AdS-Schwarzschild geometry is filled with a flavor D7 brane and the backreaction of the flavor D7 brane to the bulk geometry is ignored. A string falling in the bulk then induces a flavor-current on the boundary, which can be regarded as a light quark traversing the medium. Note that the flavor D7 brane here is different from the D7 brane in MT model as the source of anisotropy. When the tip of the string falls into the horizon, the flavor current fully diffuses on the boundary, which corresponds to the thermalization of a light quark in the medium. In this scenario, a null geodesic will result in the maximum stopping distance for the light quark, which is similar to the previous setup for an R-charged current.

By employing (4.2) and (4.11), we can compute the stopping distances of the probes traveling along the transverse direction perpendicular to the  $z$  axis and the longitudinal direction parallel to the  $z$  axis in the anisotropic medium,

$$x_T = \int_0^{u_h} \frac{du}{\left(\frac{1}{B} \frac{\omega^2}{|\bar{q}|^2} - \mathcal{F}\right)^{1/2}}, \quad (4.12)$$

$$x_L = \int_0^{u_h} \frac{du}{\mathcal{H} \left(\frac{1}{B} \frac{\omega^2}{|\bar{q}|^2} - \frac{\mathcal{F}}{\mathcal{H}}\right)^{1/2}}, \quad (4.13)$$

where we assume that the particle carries the spatial momentum solely along one of the transverse direction in (4.12) and solely along the longitudinal direction in (4.13).

In this computation, the null geodesic in (4.11) remains unchanged even when we use the Einstein frame.

To compare the stopping distance in the media with and without the anisotropic effect, we have to fix a proper physical parameter. In the following computation, we will fix the temperature, energy density, and entropy density, respectively. The recent lattice simulation for the  $SU(N_c)$  plasma at finite temperature within the range of RHIC and LHC has shown that the equilibrium thermodynamic properties have mild dependence of  $N_c$  [164], which supports the validity of the study of QCD based on large  $N_c$  models. In general, only when a particular observable obtained from the lattice calculation matches that found by AdS/CFT, then the lattice findings can be used for the extrapolation to the small- $N_c$  limit. However, for an observable which does not depend on  $N_c$  explicitly, such as the ratio of stopping distances that we are concerned with in this paper, the results in the large- $N_c$  and in the small- $N_c$  limits may share same features qualitatively. When fixing the energy density and entropy density, we will always take  $N_c = 3$  in analogy to QCD, while the choice of  $N_c$  will not affect our qualitative results in this paper. From (4.12) and (4.13), we see that the parameter-dependence of the stopping distance is encoded by the position of the horizon in terms of the physical parameter we fix. By inserting (4.9) into (4.12) and (4.13), we can compute the stopping distance by fixing the temperature of the medium. The stopping distances for different values of the anisotropy factor  $a$  in units of temperature are illustrated in Fig.4.2. In [14], the energy density and entropy density up to leading order in  $a^2$  are given by

$$\begin{aligned}\epsilon &= \frac{3N_c^2\pi^2T^4}{8} + a^2\frac{N_c^2T^2}{32} + \mathcal{O}(a^4), \\ s &= \frac{N_c^2\pi^2T^3}{2} + a^2\frac{N_c^2T}{16} + \mathcal{O}(a^4).\end{aligned}\tag{4.14}$$

Combining (4.9) and (4.14), we rewrite the position of the horizon in terms of the

energy density or the entropy density,

$$\begin{aligned}
u_h &= \left(\frac{3N_c^2}{8\pi^2}\right)^{1/4} \epsilon^{-1/4} + a^2 \frac{5 \log 2 - 1}{128\pi^2} \left(\frac{8\pi^2}{3N_c^2}\right)^{1/4} N_c^2 \epsilon^{-3/4} + \mathcal{O}(a^4), \\
u_h &= \left(\frac{\pi^2 N_c^2}{2}\right)^{1/3} \frac{s^{-1/3}}{\pi} + a^2 \frac{5 \log 2}{96\pi} N_c^2 s^{-1} + \mathcal{O}(a^4).
\end{aligned} \tag{4.15}$$

By utilizing (4.12), (4.13), and (4.15), we are now able to compute the stopping distances for fixed energy density or fixed entropy density. The results are shown in Fig.4.3 and Fig.4.4. We find that the nonzero anisotropic factor leads to smaller stopping distances in both the transverse direction and the longitudinal direction, which indicates stronger jet quenching of light probes traveling through the anisotropic medium. The quenching is more pronounced along the longitudinal direction. Although this effect is rather small, it is not surprising since the momentum anisotropy for  $a \leq T$  is rather small as shown in [156]. In contrast to light probes, the jet quenching of heavy probes is also weakly enhanced at small anisotropy or at high temperature. As shown in [156], only slightly greater jet quenching parameters and drag forces of heavy probes moving beyond the critical velocity are found in the MT geometry at  $a/T = 0.3$ .

We now analyze the relation between the energy density and the stopping distance in the anisotropic plasma in more detail. In the AdS-Schwarzschild spacetime, the energy density is characterized by the temperature,  $\epsilon = 3\pi^2 N_c^2 T^4/8$ . By using (3.13), the stopping distance can be rewritten as

$$x_s = \epsilon^{-1/4} \left(\frac{3N_c^2}{8\pi^2}\right) \int_0^1 \frac{d\tilde{r}}{\left(-\frac{q^2}{|\vec{q}|^2} + r^4\right)^{1/2}} = \epsilon^{-1/4} A_0(N_c, \omega, |\vec{q}|), \tag{4.16}$$

where  $\tilde{r} = u/u_H$  and  $q^2 = -\omega^2 + |\vec{q}|^2$  in the integral and  $A_0(N_c, \omega, |\vec{q}|)$  is a dimensionless factor. We see that the stopping distance of the hard probe decreases when the

energy density is increased. This is analogous to the weakly-coupled plasma where the jet quenching is enhanced for increasing energy density [165]. When including the anisotropic effect, the transverse stopping distance to the order  $a^2$  becomes

$$\begin{aligned}
x_T &= \int_0^1 dr \frac{u_h^0}{\left(-\frac{q^2}{|\vec{q}|^2} + \tilde{r}^4\right)^{1/2}} \left[ 1 + \frac{a^2}{2\left(-\frac{q^2}{|\vec{q}|^2} + \tilde{r}^4\right)} \left( \mathcal{B}_2 \frac{\omega^2}{|\vec{q}|^2} + \mathcal{F}_2 \right) + a^2 \delta u_h^0 \right] \\
&= \epsilon_a^{-1/4} A_0(N_c, \omega, |\vec{q}|) + a^2 \epsilon_a^{-3/4} A_1^T(N_c, \omega, |\vec{q}|), \tag{4.17}
\end{aligned}$$

where  $u_h^0$  and  $\delta u_h^0$  can be read off from (4.15). Here  $\epsilon_a$  is the energy density shown in (4.14) and we may take  $\epsilon_a = \epsilon$  for comparison. For the hard probe with small virtuality, the dimensionless factor  $A_1^T(N_c, \omega, |\vec{q}|)$  is negative; hence the suppression of the stopping distance led by the first-order anisotropic correction is reduced when the energy density is increased. The longitudinal stopping distance  $x_L$  can be written in the same form as  $x_T$  by substituting  $A_1^T(N_c, \omega, |\vec{q}|)$  with a different numerical factor  $A_1^L(N_c, \omega, |\vec{q}|)$ , where  $A_1^L(N_c, \omega, |\vec{q}|)$  is also negative at small virtuality. The similar scenario for fixed entropy density could be found by following the same approach.

In general, in the high-temperature or small-anisotropy limit, the anisotropic values of stopping distances are slightly smaller than the isotropic values by fixing one of physical parameters such as temperature, energy density, or entropy density. The jet quenching along the longitudinal direction is particularly enhanced, although the enhancement is rather small.

In the mid-anisotropy or the large-anisotropy regimes, the longitudinal pressure surpasses the transverse pressure and the pressure inequality becomes substantial [14], which may not be similar to the feature of QGP. In anisotropic hydrodynamics, the pressure difference can be considerably large in early times [82, 84]. However, the longitudinal pressure should be always suppressed by the transverse pressure, which is qualitatively opposite to the scenario described by the MT model beyond small

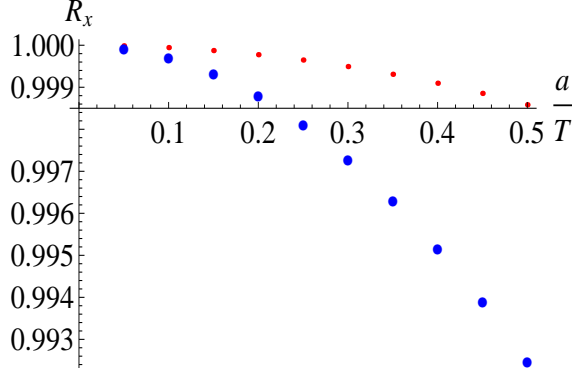


FIGURE 4.2:  $R_x = x_{aniso}/x_{iso}$  represents the ratio of the stopping distances in the MT geometry with anisotropy to without anisotropy, where  $x_{aniso} = x_T$  for the red points and  $x_{aniso} = x_L$  for the large blue points. Here we take  $|\vec{q}| = 0.99\omega$  and fix the temperature of media.

anisotropy. Despite the unrealistic directions of anisotropy, it may be heuristic to investigate the effect of the medium with strong anisotropy on jet quenching of light probes. To study the jet quenching in the mid-anisotropy or the large-anisotropy regimes, we have to employ the numerical solution of the MT metric. Due to the rotational symmetry in the transverse directions, we may set the four-momentum of the massless particle as  $q_i = (-\omega, |\vec{q}| \sin \psi, 0, |\vec{q}| \cos \psi)$ , where  $\psi$  denotes the polar angle in the  $x^1 - x^3(x - z)$  plane with respect to the longitudinal direction  $x^3(z)$ . The probe thus travels along the longitudinal and transverse directions for  $\psi = 0$  and  $\psi = \pi/2$ , respectively. Now the stopping distance acquired from (4.11) is given by  $x_{aniso} = \sqrt{x_{Ts}^2 + x_{Ls}^2}$ , where

$$\begin{aligned}
 x_{Ts} &= \int_0^{u_h} du \frac{\sin \psi}{\left(\frac{1}{B} \frac{\omega^2}{|\vec{q}|^2} - \frac{\mathcal{F}}{\mathcal{H}} (\cos^2 \psi + \mathcal{H} \sin^2 \psi)\right)^{1/2}}, \\
 x_{Ls} &= \int_0^{u_h} du \frac{\cos \psi}{\mathcal{H} \left(\frac{1}{B} \frac{\omega^2}{|\vec{q}|^2} - \frac{\mathcal{F}}{\mathcal{H}} (\cos^2 \psi + \mathcal{H} \sin^2 \psi)\right)^{1/2}}. \tag{4.18}
 \end{aligned}$$

By inserting the numerical solutions of the spacetime metric into the equation above

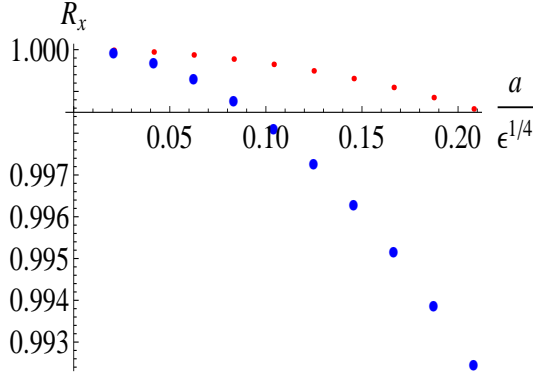


FIGURE 4.3:  $R_x = x_{aniso}/x_{iso}$  represents the ratio of the stopping distances in the MT geometry with anisotropy to without anisotropy, where  $x_{aniso} = x_T$  for the red points and  $x_{aniso} = x_L$  for the large blue points. Here we take  $N_c = 3$ ,  $|\vec{q}| = 0.99\omega$  and fix the energy density of media.

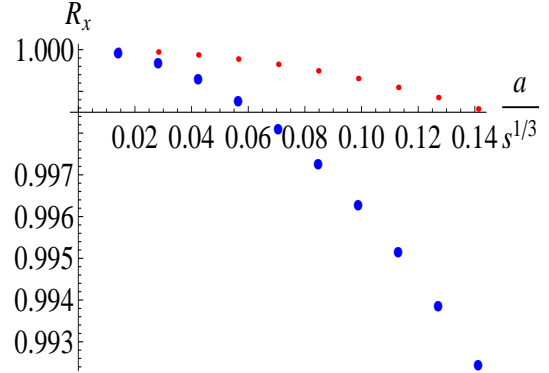


FIGURE 4.4:  $R_x = x_{aniso}/x_{iso}$  represents the ratio of the stopping distances in the MT geometry with anisotropy to without anisotropy, where  $x_{aniso} = x_T$  for the red points and  $x_{aniso} = x_L$  for the large blue points. Here we take  $N_c = 3$ ,  $|\vec{q}| = 0.99\omega$  and fix the entropy density of media.

and carrying out the integrations, the stopping distances at mid and large anisotropy in comparison with those in the isotropic case are shown in Fig.4.5 and Fig.4.6. When fixing the temperature, the stopping distances in both mid and large anisotropy are smaller compared to the isotropic results. As shown in both figures, when  $\psi$  decreases, the suppression of the stopping distance becomes more robust, which suggests stronger jet quenching along the longitudinal direction. In contrast, at equal entropy density, the enhanced jet quenching in the anisotropic medium becomes less prominent and the stopping distances of probes moving close to the transverse directions even exceed the stopping distances in the isotropic case. Overall, the jet quenching of light probes is enhanced when turning up the anisotropic effect except for the probe moving along the transverse direction.

After finding the results at mid and large anisotropy, we may make a comparison with the influence of the anisotropic effect on the jet quenching of heavy probes. In the studies of the drag force in MT metric [156, 159], the longitudinal drag is as well

enhanced by anisotropy at equal temperature or at equal entropy density. Also, at mid or large anisotropy, the enhancement of the drag force for the probe traveling more parallel to the transverse direction diminishes. When the magnitude of the probe velocity is smaller than a critical value, the transverse drag could be smaller than the isotropic drag at equal temperature or equal entropy density. Despite the velocity dependence, the angular dependence of the anisotropic drag is qualitatively analogous to the scenario of the anisotropic stopping distance we find. For the jet quenching parameter computed from lightcone Wilson loops, the enhancement or the suppression due to anisotropy are more subtle, which depends on both the direction of moving quarks and the direction of momentum broadening [158, 157]. Nevertheless, since the momentum broadening is attributed to collisions between the heavy quark and thermal partons in the medium, this effect should be suppressed compared to the radiation energy loss in the case of light probes. As a result, we may not anticipate that the anisotropy effect on stopping distances of light probes shares the same features with the jet quenching parameters.

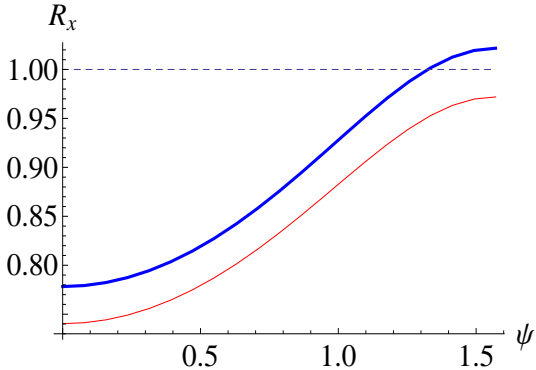


FIGURE 4.5: The red and thick blue curves represent the ratios  $R_x = x_{aniso}/x_{iso}$  at mid anisotropy at equal temperature and at equal entropy density, respectively. Here we take  $|\vec{q}| = 0.99\omega$ ,  $u_h = 1$ , and  $a/T \approx 4.4$  or equivalently  $a/s^{1/3} \approx 1.2$  for  $N_c = 3$ .

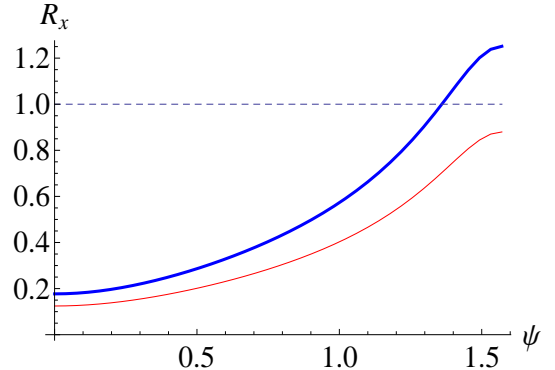


FIGURE 4.6: The red and thick blue curves represent the ratios  $R_x = x_{aniso}/x_{iso}$  at large anisotropy at equal temperature and at equal entropy density, respectively. Here we take  $|\vec{q}| = 0.99\omega$ ,  $u_h = 1$ , and  $a/T \approx 86$  or equivalently  $a/s^{1/3} \approx 17$  for  $N_c = 3$ .

### 4.3 Photon Production in an Anisotropic Plasma

To investigate the spectra of photons and dileptons, we will follow the approaches in [166] by introducing  $U(1)$  gauge fields in the gravity dual as sources of electromagnetic currents on the boundary, where the gauge fields here are regarded as external probes and their back-reaction to the dual geometry is neglected. The effective action for the external gauge fields can be written as

$$S_{\text{ext}} = \frac{-1}{8\kappa^2} \int d^5x \sqrt{-g} F_{MN} F^{MN}, \quad (4.19)$$

which leads to field equations  $\nabla_M F^{MN} = 0$ , where the Latin indices denote the directions of five-dimensional spacetime,  $M, N = t, x, y, z, u$ . We will then choose the gauge  $A_u = 0$ . Based on the translational invariance along  $t, x, y, z$  directions, we can write down the Fourier transform of gauge fields as

$$A_\mu(u, t, \vec{x}) = \int \frac{d^4k}{(2\pi)^4} e^{ik_0t + i\vec{k}\cdot\vec{x}} A_\mu(u, k), \quad (4.20)$$

where the Greek indices denote the directions of four dimensional spacetime,  $\mu = t, x, y, z$ . Since now the dual geometry is anisotropic along the  $z$  direction and rotational symmetry is only preserved on the  $x - y$  plane, we will study two particular cases for  $k = (-\omega, 0, 0, q)$  and  $k = (-\omega, q, 0, 0)$ , where the induced currents move parallel and perpendicular to the anisotropic direction, respectively.

We firstly consider the case for  $k = (-\omega, 0, 0, q)$ ; the field equations are

$$\begin{aligned}
A''_{\perp} &+ \left( \frac{\mathcal{F}'}{\mathcal{F}} - \frac{1}{u} + \frac{\mathcal{B}'}{2\mathcal{B}} + \frac{\mathcal{H}'}{2\mathcal{H}} - \frac{\phi'}{4} \right) A'_{\perp} + \frac{1}{\mathcal{F}^2} \left( \frac{\omega^2}{\mathcal{B}} - \frac{q^2\mathcal{F}}{\mathcal{H}} \right) A_{\perp} = 0, \\
A''_t &- \left( \frac{1}{u} + \frac{\mathcal{B}'}{2\mathcal{B}} - \frac{\mathcal{H}'}{2\mathcal{H}} + \frac{\phi'}{4} \right) A'_t - \frac{q}{\mathcal{F}\mathcal{H}} (qA_t + \omega A_z) = 0, \\
A''_z &+ \left( \frac{\mathcal{F}'}{\mathcal{F}} - \frac{1}{u} + \frac{\mathcal{B}'}{2\mathcal{B}} - \frac{\mathcal{H}'}{2\mathcal{H}} - \frac{\phi'}{4} \right) A'_z + \frac{\omega}{\mathcal{F}^2\mathcal{B}} (\omega A_z + qA_t) = 0, \\
A'_t &= -\frac{q\mathcal{B}\mathcal{F}}{\omega\mathcal{H}} A'_z,
\end{aligned} \tag{4.21}$$

where  $A_{\mu} = A_{\mu}(u, k)$  and primes denote the derivatives with respect to  $u$ . The first equation in (4.21) for  $\perp = x, y$  is the field equation for transverse polarizations perpendicular to the spatial momentum. The rest three equations govern the longitudinal modes, where the last one is in fact redundant, which can be obtained from the linear combination of the other two equations. By defining  $E_{\perp} = \omega A_{\perp}$  and  $E_z = qA_t + \omega A_z$ , we can rewrite the field equations into gauge invariant forms,

$$\begin{aligned}
E''_{\perp} &+ \left( \frac{\mathcal{F}'}{\mathcal{F}} - \frac{1}{u} + \frac{\mathcal{B}'}{2\mathcal{B}} + \frac{\mathcal{H}'}{2\mathcal{H}} - \frac{\phi'}{4} \right) E'_{\perp} + \frac{1}{\mathcal{F}^2} \left( \frac{\omega^2}{\mathcal{B}} - \frac{q^2\mathcal{F}}{\mathcal{H}} \right) E_{\perp} = 0, \\
E''_z &+ \left( \frac{\omega^2\mathcal{H}\mathcal{F}'}{\mathcal{F}} + \left( \frac{\mathcal{B}'}{2\mathcal{B}} - \frac{\mathcal{H}'}{2\mathcal{H}} \right) (\omega^2\mathcal{H} + q^2\mathcal{B}\mathcal{F}) \right) \frac{E'_z}{\omega^2\mathcal{H} - q^2\mathcal{B}\mathcal{F}} - \left( \frac{1}{u} + \frac{\phi'}{4} \right) E'_z \\
&+ \frac{1}{\mathcal{F}^2} \left( \frac{\omega^2}{\mathcal{B}} - \frac{q^2\mathcal{F}}{\mathcal{H}} \right) E_z = 0,
\end{aligned} \tag{4.22}$$

for  $k = (-\omega, 0, 0, q)$ . Similarly, we have

$$\begin{aligned}
E_y'' + \left( \frac{\mathcal{F}'}{\mathcal{F}} - \frac{1}{u} + \frac{\mathcal{B}'}{2\mathcal{B}} + \frac{\mathcal{H}'}{2\mathcal{H}} - \frac{\phi'}{4} \right) E_y' + \frac{1}{\mathcal{F}^2} \left( \frac{\omega^2}{\mathcal{B}} - q^2 \mathcal{F} \right) E_y &= 0, \\
E_z'' + \left( \frac{\mathcal{F}'}{\mathcal{F}} - \frac{1}{u} + \frac{\mathcal{B}'}{2\mathcal{B}} - \frac{\mathcal{H}'}{2\mathcal{H}} - \frac{\phi'}{4} \right) E_z' + \frac{1}{\mathcal{F}^2} \left( \frac{\omega^2}{\mathcal{B}} - q^2 \mathcal{F} \right) E_z &= 0, \\
E_x'' + \left( \frac{\omega^2 \mathcal{F}'}{\mathcal{F}} + \frac{\mathcal{B}'}{2\mathcal{B}} (\omega^2 + q^2 \mathcal{B} \mathcal{F}) \right) \frac{E_x'}{\omega^2 - q^2 \mathcal{B} \mathcal{F}} - \left( \frac{1}{u} + \frac{\phi'}{4} - \frac{\mathcal{H}'}{2\mathcal{H}} \right) E_x' \\
+ \frac{1}{\mathcal{F}^2} \left( \frac{\omega^2}{\mathcal{B}} - q^2 \mathcal{F} \right) E_x &= 0, \tag{4.23}
\end{aligned}$$

for  $k = (-\omega, q, 0, 0)$ , where  $E_{y,z} = \omega A_{y,z}$  and  $E_x = qA_t + \omega A_x$ . Notice that the equation for  $E_y$  here is slightly different from that for  $E_z$  due to anisotropy of the metric along the  $z$  direction. By using the field equations (4.22) and (4.23), we then write down the boundary terms of the effective action in (4.19),

$$S_\epsilon = \frac{-1}{4\kappa^2} \int \frac{d^4 k}{(2\pi)^4} \frac{Q}{u} \left( \frac{1}{\omega^2} E_\perp^* E'_\perp + \frac{1}{\omega^2 \mathcal{H} - q^2 \mathcal{B} \mathcal{F}} E_z^* E'_z \right)$$

for  $k = (-\omega, 0, 0, q)$ , and

$$S_\epsilon = \frac{-1}{4\kappa^2} \int \frac{d^4 k}{(2\pi)^4} \frac{Q}{u} \left( \frac{1}{\omega^2} (E_y^* E'_y + \mathcal{H}^{-1} E_z^* E'_z) + \frac{1}{\omega^2 - q^2 \mathcal{B} \mathcal{F}} E_x^* E'_x \right) \tag{4.24}$$

for  $k = (-\omega, q, 0, 0)$ , where  $E_\mu^* = E(u, -k)$  and  $Q = \mathcal{F} \sqrt{\mathcal{B}} e^{-\frac{3}{4}\phi}$ . Notice that  $\phi \rightarrow 0$  and  $\mathcal{F}, \mathcal{B}, \mathcal{H} \rightarrow 1$  near the boundary. Although the dual geometry asymptotically reduces to the pure AdS spacetime near the boundary, the boundary value of  $E_y$  and of  $E_z$  will differ due to the breaking of rotational symmetry in the bulk.

In thermal equilibrium, the differential photon emission rate per unit volume can be written as

$$d\Gamma_\gamma = \frac{d^3 k}{2(2\pi)^3} \frac{\chi(k)}{\omega(e^{\beta\omega} - 1)}, \quad \chi(k) = -2\text{Im} \left[ \sum_{s=1}^n \epsilon_s^\mu \epsilon_s^{*\nu} C_{\nu\mu}(k) \right], \tag{4.25}$$

where  $n = 2$  denotes the number of polarizations of photons and  $\chi(k)$  represents the trace of the spectral density, which is related to the retarded current-current correlator  $C_{\mu\nu}(k)$ . When photons are linearly polarized along a particular polarization  $\epsilon_T$ , we should take

$$d\Gamma_\gamma(\epsilon_T) = \frac{d^3k}{2(2\pi)^3} \frac{\chi_{\epsilon_T}(k_0)}{\omega(e^{\beta\omega} - 1)}, \quad \chi_{\epsilon_T}(k_0) = -4\text{Im}[\epsilon_T^\mu \epsilon_T^{*\nu} C_{\nu\mu}(k)]. \quad (4.26)$$

By these definitions, we retrieve  $\chi_{\epsilon_T}(k_0) = \chi(k)$  in the isotropy case. Following the AdS/CFT prescription[167, 168, 166], the retarded correlators can be evaluated by taking the functional derivatives of the boundary action with respect to the gauge fields, which further results in

$$\chi(k) = \mathcal{Z}\text{Im} \lim_{u \rightarrow 0} \frac{QE'_\perp(u, k)}{uE_\perp(u, k)}, \quad \chi_{\epsilon_T}(k_0) = \mathcal{Z}\text{Im} \lim_{u \rightarrow 0} \frac{QE'_{\epsilon_T}(u, k)}{uE_{\epsilon_T}(u, k)}, \quad (4.27)$$

where  $\mathcal{Z}$  is an overall constant. Also, the zero-frequency limit of the spectral function contributes to the DC conductivity as

$$\sigma = \frac{e^2}{4} \lim_{\omega \rightarrow 0} \frac{1}{\omega} \chi(k)|_{|\vec{k}|=\omega}, \quad \sigma(\epsilon_T) = \frac{e^2}{4} \lim_{\omega \rightarrow 0} \frac{1}{\omega} \chi_{\epsilon_T}(k_0)|_{|\vec{k}|=\omega}. \quad (4.28)$$

In thermal equilibrium, only the incoming-wave solutions near the horizon have to be considered. In the isotropic case, the lightlike solution( $q = \omega$ ) takes the form [166],

$$E_{in}^T(\omega, u) = \left(1 - \frac{u^2}{u_h^2}\right)^{-\frac{i\hat{\omega}}{4}} \left(1 + \frac{u^2}{u_h^2}\right)^{-\frac{\hat{\omega}}{4}} \times {}_2F_1\left(1 - \frac{1+i}{4}\hat{\omega}, -\frac{1+i}{4}\hat{\omega}; 1 - i\frac{\hat{\omega}}{2}; \frac{(1-u^2/u_h^2)}{2}\right),$$

where  $u_h = (\pi T)^{-1}$  in the isotropic geometry and  $\hat{\omega} = \omega/(\pi T)$ . However, the anisotropic solutions can only be solved numerically. We thus solve  $E_\perp$  in (4.22)

and  $E_y, E_z$  in (4.23) for  $q = \omega$  by imposing incoming-wave boundary conditions via analysis of the near-horizon expansion of field equations. In the first case, by solving  $E_\perp$  and implementing (4.27), we can derive the spectral density for photons propagating along the anisotropic direction  $z$ . In the second case, the solutions of  $E_y$  and  $E_z$  then contribute to the spectra for photons moving perpendicular to the anisotropic direction.

To compare the results with those found in isotropic case, we have to fix certain physical scales such as temperature or entropy density of the media. In the rest of the paper, we will solely focus on the cases with fixed temperature. Due to the rotational symmetry on the  $x - y$  plane, the computation of the spectral density for  $k = (-\omega, 0, 0, \omega)$  is straightforward. We define the ratio  $\chi_r = \chi_{\epsilon_T \text{ aniso}}/\chi_{\text{iso}}$  to compare the anisotropic and isotropic cases. Nonetheless, as indicated in the previous context, the field equations for  $E_y$  and  $E_z$  are slightly different in (4.23) for  $k = (-\omega, \omega, 0, 0)$ , which bring about different retarded correlators <sup>1</sup>. The results at mid anisotropy for fixed temperature are shown in Fig.4.7, which match those found by fluctuating a flavor probe brane in MT geometry in the massless-quark limit [162]<sup>2</sup>. The matching is expected since only the leading-order contribution of the gauge fields coupled to the flavor brane in the DBI action is considered in [162].

#### 4.4 Photon Spectra from Massive Quarks in an Anisotropic Plasma

To incorporate the flavor degrees of freedom, we will consider the embeddings of flavor D7 branes in the anisotropic background geometry [155, 14]. In addition, we take the quenched approximation by assuming  $N_f \ll N_c$ , where  $N_f$  denotes the number of flavors. With such an approximation, the modification of flavor probe

---

<sup>1</sup> Here  $\chi_r$  is equivalent to  $2\chi_{(1,2)}/\chi_{\text{iso}}(T)$  defined in [162]. Also,  $k = (-\omega, 0, 0, \omega)$  and  $k = (-\omega, \omega, 0, 0)$  correspond to  $\theta = 0$  and  $\theta = \pi/2$  therein.

<sup>2</sup> Following the convention therein,  $\chi_{\epsilon_T} = 2\chi_{(1(2))}$ .

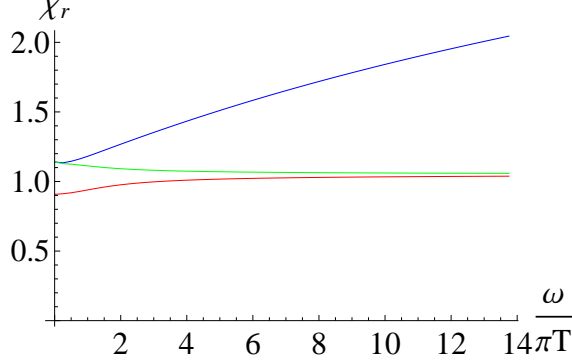


FIGURE 4.7: The blue, green, and red curves (from top to bottom) represent the ratios of spectral densities at fixed temperature for  $\epsilon_T = \epsilon_x$  or  $\epsilon_y$  when  $k = (-\omega, 0, 0, \omega)$ , for  $\epsilon_T = \epsilon_y$  and  $\epsilon_T = \epsilon_z$  when  $k = (-\omega, \omega, 0, 0)$ , respectively. Here we take  $u_h = 1$  and  $a/T = 4.4$ .

branes to the background geometry is  $\mathcal{O}(N_f/N_c)$  suppressed, which will be neglected in this paper. The flavor D7 brane extended into the bulk shares the same spacetime dimensions with the D3 brane on the boundary and wraps an  $S^3$  inside the  $S^5$ ,

$$d\Omega_5^2 = d\theta^2 + \sin^2 \theta d\Omega_3^2 + \cos^2 \theta d\eta^2. \quad (4.29)$$

For convenience, we hereafter work in the string frame. The flavor D7 brane is characterized by the Dirac-Born-Infeld (DBI) action,

$$S = -N_f T_{D7} \int_{D7} d^8 x e^{-\phi} \sqrt{-\det(G + 2\pi l_s^2 F)}, \quad (4.30)$$

where  $G$  is the induced metric on the D7 branes,  $F = dA$  is the U(1) field strength for the massless gauge fields coupled to the brane, and  $T_{D7} = (2\pi l_s)^{-7} (g_s l_s)^{-1}$  is the D7-brane string tension. The induced metric in the string frame led by the embedding of the flavor branes in the MT geometry reads [162]

$$ds_{D7}^2 = \frac{1}{u^2} (-\mathcal{F}(u)\mathcal{B}(u)dt^2 + dx^2 + dy^2 + \mathcal{H}(u)dz^2) + \frac{1 - \psi(u)^2 + u^2 \mathcal{F}(u) e^{\frac{1}{2}\phi(u)} \psi(u)^2}{u^2 \mathcal{F}(u) (1 - \psi(u)^2)} du^2 + e^{\frac{1}{2}\phi(u)} (1 - \psi(u)^2) d\Omega_3^2, \quad (4.31)$$

where  $\sqrt{1 - \psi(u)^2} = \sin \theta$  represents the radius of the internal  $S^3$  wrapped by the D7 branes. To compute the leading-order contribution of photon spectra, we could preserve the quadratic order in the field strength for the D7-brane action,

$$S = -N_f T_{D7} \int_{D7} d^8 x e^{-\phi} \sqrt{-\det(G)} \left( 1 + \frac{(2\pi l_s)^2}{4} F^2 \right). \quad (4.32)$$

By treating the expansion of the field strength in the DBI action perturbatively, we could neglect the back-reaction of gauge fields to the induced metric. The D7-brane action now reads

$$S = -K_{D7} \int dt d^3 \vec{x} du F^2 \frac{(1 - \psi^2) e^{-\frac{3\phi}{4}}}{u^5} \sqrt{\mathcal{B}(1 - \psi^2 + u^2 \mathcal{F} e^{\frac{1}{2}\phi} \psi'^2)}, \quad (4.33)$$

where the prefactor  $K_{D7}$  includes the integration over the internal space  $\Omega_3$  wrapped by the D7 branes. By following the standard AdS/CFT prescription as shown in the previous section, the spectral functions of electromagnetic probes can be obtained. In the case of trivial embedding  $\psi = 0$ , which corresponds to the massless-quark case, the spectra reduce to the results we acquired in the previous section except for the difference in the prefactors.

To incorporate massive quarks, we have to consider nontrivial embeddings  $\psi \neq 0$ . In the absence of the gauge fields, we derive the field equation of  $\psi$  by minimizing

the action in (4.32),

$$\begin{aligned}
\psi''(u) + \mathcal{C}_1\psi'(u) + \mathcal{C}_2\psi'(u)^3 + \mathcal{C}_3\psi(u) + \mathcal{C}_4\psi(u)^3 &= 0, \\
\mathcal{C}_1 &= \frac{\mathcal{B}'}{2\mathcal{B}} + \frac{\mathcal{F}'}{\mathcal{F}} + \frac{\mathcal{H}'}{2\mathcal{H}} - \frac{3}{u} + \frac{\phi'}{4}, \\
\mathcal{C}_2 &= -\frac{4e^{\frac{\phi}{2}}\mathcal{F}u}{(1-\psi^2)} + \frac{e^{\frac{\phi}{2}}\mathcal{F}u^2}{2(1-\psi^2)} \left( \frac{\mathcal{F}'}{\mathcal{F}} + \frac{\mathcal{B}'}{\mathcal{B}} + \frac{\mathcal{H}'}{\mathcal{H}} \right), \\
\mathcal{C}_3 &= \frac{3e^{-\frac{\phi}{2}}}{u^2\mathcal{F}(1-\psi^2)} + \frac{4\psi'^2}{(1-\psi^2)}, \\
\mathcal{C}_4 &= -\frac{3e^{-\frac{\phi}{2}}}{u^2\mathcal{F}(1-\psi^2)}. \tag{4.34}
\end{aligned}$$

The field equation in (4.34) can be solved by imposing proper boundary conditions near the horizon [143, 144], where we take

$$\psi(u_h) = \psi_0, \quad \psi'(u_h) = (-3u^{-2}e^{-\phi/2}\psi/\mathcal{F}')|_{u=u_h}. \tag{4.35}$$

Here we only consider the black hole embedding as a deconfined phase of the plasma, which corresponds to the choice of  $0 \leq \psi_0 < 1$  [143]. At nonzero anisotropy, the asymptotic solution will contain extra logarithmic terms in comparison with the isotropic case shown in (2.41),

$$\psi(u) = m\frac{u}{2^{1/2}u_h} + c\frac{u^3}{2^{3/2}u_h^3} + a^2\rho_3\frac{u^3}{u_h^3}\log(u/u_h)\dots, \tag{4.36}$$

which come from the anisotropy. The numerical computations of  $c$  may become technically difficult due to the presence of the leading logarithmic term, while the extraction of  $m$  is straightforward. Further discussions of black hole embeddings in the MT geometry can be found in Appendix B.2. In Fig.5.1, the quark mass scaled by temperature with respect to  $\psi_0$  for the black hole embeddings with anisotropy is represented by the dashed blue curve, while the solid blue curve corresponds to

the isotropic case. The critical mass at  $\psi_0 \rightarrow 1$  now is increased by anisotropy or equivalently the dissociation temperature is reduced. In fact, as shown in [145], the black hole embedding near  $\psi_0 = 1$  could be metastable or unstable and the phase transition occurs within this region in the isotropic case. To manifest the phase transition near  $\psi_0 = 1$  in the anisotropic case requires further investigation on the thermodynamics of the flavor brane in Minkowski embeddings, which is beyond the scope of this dissertation.

After solving the induced metric of the flavor probe brane, we can now compute photon spectra. By taking the Fourier transform of gauge fields as (4.33), the action near the boundary becomes

$$S_\epsilon = -2K_{D7} \int \frac{d^4k}{(2\pi)^4} \frac{Q_{D7}}{u} \left( -\frac{1}{\mathcal{F}\mathcal{B}} A_t^* A'_t + A_\perp^* A'_\perp + \frac{1}{\mathcal{H}} A_z^* A'_z \right), \quad (4.37)$$

$$Q_{D7} = \frac{(1 - \psi^2)^2 \sqrt{\mathcal{B}\mathcal{F}} e^{-\frac{3\phi}{4}}}{\sqrt{1 - \psi^2 + u^2 \mathcal{F} e^{\frac{1}{2}\phi} \psi'^2}},$$

where the gauge fields have to obey the field equations

$$\partial_\mu (M G^{\mu\alpha} G^{\nu\beta} F_{\alpha\beta}) = 0, \quad M = \frac{(1 - \psi^2) e^{-\frac{3\phi}{4}}}{u^5} \sqrt{\mathcal{B}(1 - \psi^2 + u^2 \mathcal{F} e^{\frac{1}{2}\phi} \psi'^2)}. \quad (4.38)$$

Recall that  $G_{\mu\nu}$  here is the induced metric of D7 branes. To convert (4.37) and (4.38) into gauge-invariant forms, we may follow the general derivation presented in Appendix B.1. From (B.6) and  $\mathcal{H} \rightarrow 1$  near the boundary, we have the photon spectral density

$$\chi_{\epsilon_j}(\omega) = 8K_{D7} \text{Im} \lim_{u \rightarrow 0} \frac{Q_{D7} E'_j(u, \omega)}{u E_j(u, \omega)}, \quad (4.39)$$

where  $E_j(u, \omega) = \omega A_j(u, k)|_{k_0 = -\omega}$  for  $j$  being the transverse polarization. As discussed in the previous section, the gauge field with  $k = (-\omega, 0, 0, \omega)$  and the transverse polarization preserves rotational symmetry on the  $x-y$  plane, which is governed

by just one equation of motion, whereas for the field with  $k = (-\omega, \omega, 0, 0)$ , the two types of transverse polarizations  $A_y$  and  $A_z$  should obey different field equations due to the presence of anisotropy along the  $z$  direction. The computations of solving the field equations can be carried out numerically by imposing the incoming-wave boundary conditions. At mid-anisotropy for  $a/T = 4.4$  or equivalently  $a/s^{1/3} = 1.2$ , the medium forms a prolate in the momentum space with the ratio of pressures  $P_z/P_{x,y} \approx 1.5$ . In the rest of the dissertation, we will focus on the mid-anisotropy region when considering the anisotropic effect on photon production.

To compare the anisotropic spectral densities with isotropic ones, we have to fix the quark mass and temperature of the media. Here we define the rescaled mass  $\hat{M}_Q = 2\pi M_q/\sqrt{\lambda}$ . The spectral functions for photons moving along the anisotropic direction are shown in Fig.4.8, while the results for photons moving perpendicular to the anisotropic direction are illustrated in Fig.4.9, where the spectral functions are in units of  $\pi T$ . At small  $\hat{\omega} = \omega/(\pi T)$ , the spectral functions contributed from the quarks with different mass possess distinct features, while the qualitative structures of isotropic and anisotropic spectra are similar. At large  $\hat{\omega} = \omega/(\pi T)$ , the effect from the difference of quark mass are suppressed by the energy of photons; the spectra hence converge to the same amplitudes. Nevertheless, as shown in Fig.4.8, the anisotropic spectra for photons moving along the anisotropic direction receive overall enhancement in amplitudes. For the photons moving perpendicular to the anisotropic direction, the amplitudes of anisotropic spectra can be smaller or larger than the isotropic ones depending on the quark mass and the polarization as illustrated in Fig.4.9. At large  $\hat{\omega}$ , the anisotropic spectra for photons moving perpendicular to the anisotropic direction saturate the isotropic ones.

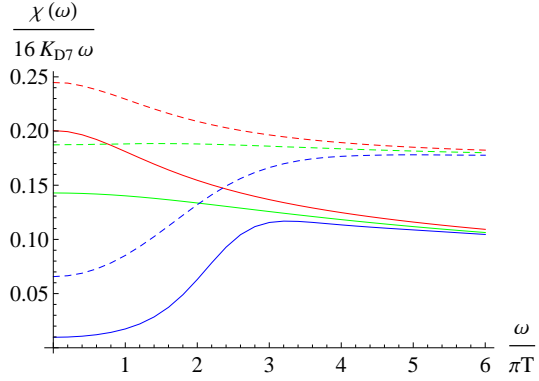


FIGURE 4.8: The red, green, and blue curves (from top to bottom) represent the spectral functions with  $k = (-\omega, 0, 0, \omega)$  for  $\hat{M}_q/(\pi T) = 0.61, 0.89,$  and  $1.31$ . The dashed ones and solid ones correspond to the results with and without anisotropy, respectively. Here we take  $u_h = 1$  and  $a/T = 4.4$ .

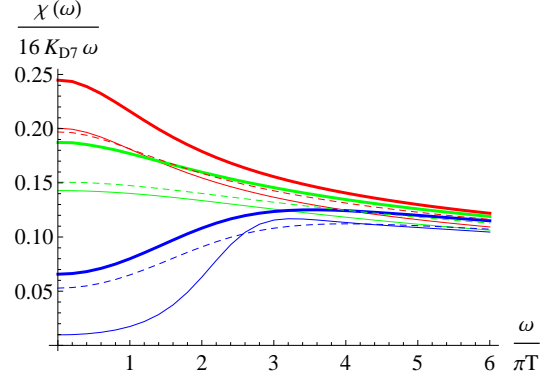


FIGURE 4.9: The red, green, and blue curves (from top to bottom) represent the spectral functions with  $k = (-\omega, \omega, 0, 0)$  and the  $y$ -polarization for  $\hat{M}_q/(\pi T) = 0.61, 0.89,$  and  $1.31$ . The thin ones correspond to isotropic results. The thick ones and dashed ones correspond to the anisotropic results with  $\epsilon_y$  and  $\epsilon_z$ , respectively. Here we take  $u_h = 1$  and  $a/T = 4.4$ .

## 4.5 Concluding Remarks

In this chapter, we have calculated the maximum stopping distance of an energetic jet traveling in a strongly coupled anisotropic plasma by analyzing the null geodesic of a massless particle falling in the dual geometry. We carried out the investigation from low anisotropy to large anisotropy. At small anisotropy, the stopping distances slightly decrease in comparison with the isotropic case for fixed temperature, energy density, and entropy density, respectively. At mid or large anisotropy, we found that the anisotropic stopping distances are generally smaller than the isotropic ones at equal temperature or equal entropy density especially along the longitudinal direction. However, along the transverse direction, the suppression of the stopping distance becomes less prominent at equal temperature. When fixing the entropy density, the transverse stopping distance is even larger than the isotropic one. In

addition, we have computed the thermal-photon production in the anisotropic background. The massive quarks are involved in the anisotropic background through the black hole embedding in the D3-D7 system. The spectra for photons moving along the anisotropy direction are enhanced, while the ones moving perpendicular to the anisotropic direction receive no enhancement compared to the isotropic results at large frequency.

## Photon Production with a Strong Magnetic Field

The work in this chapter was first published in [131, 132]. As discussed in Section 1.4, the photon production led by the magnetic field in heavy ion collisions may be an important effect to generate large  $v_2$  of direct photons. In the weakly coupled scenario, the photon production with magnetic field has been studied in a variety of approaches[116, 117, 118, 119, 120]. In the strongly coupled scenario, the thermal photon production with constant magnetic field in holography have been studied [169, 170, 171]. In [170], it is shown that the photon production perpendicular to the magnetic field in D3/D7 and D4/D6 embeddings with massless quarks is enhanced. In [171], the photon  $v_2$  is computed in the framework of Sakai-Sugimoto model[15]. In this chapter, we will consider the thermal-photon production with a constant magnetic field in the D3/D7 system. In Section 5.1, we firstly introduce a constant magnetic field through the world-volume field strength coupled to D7 branes. In Section 5.2, we subsequently compute the photon production led by the magnetic field in the anisotropic plasma. In Section 5.3, we evaluate the thermal-photon  $v_2$  caused by the magnetic field in an isotropic plasma with  $2 + 1$  flavors. Eventually,

we make concluding remarks in Section 5.4.

## 5.1 External Magnetic Fields

In order to incorporate a constant magnetic field, we may turn on the world-volume field strength on D7 branes as shown in (2.5). The DBI action for the D7 branes now reads

$$S_{D7} = T_{D7} \int d^8x \sqrt{-\det(G_{\mu\nu} + 2\pi l_s^2 F_{\mu\nu})}. \quad (5.1)$$

By setting  $2\pi l_s A_y = B_z x$ , we have a constant magnetic field  $B_z$ <sup>1</sup> along the  $z$  axis. We may start from the AdS-Schwarzschild background, where the DBI action can be explicitly written as

$$S = -K_{D7} \int dt d^3\vec{x} du \frac{(1 - \psi^2)}{u^5} (1 + B_z^2 u^4)^{1/2} \times (1 - \psi^2 + u^2 f \psi'^2)^{1/2},$$

where  $T_{D7} = (2\pi l_s)^{-7} (g_s l_s)^{-1}$  is the D7-brane string tension for  $K_{D7} = N_f T_{D7} (\pi l_s)^2 \Omega_3$ .

The field equation for  $\psi$  is then given by

$$\begin{aligned} \psi'' - \left( \frac{3 + B_z^2 u^4}{u + B_z^2 u^5} - \frac{f'}{f} \right) \psi' + \left( \frac{u(4(2 + B_z^2 u^4)f - u(1 + B_z^2 u^4)f')}{2(1 + B_z^2 u^4)(-1 + \psi^2)} \right) \psi \\ + \left( \frac{3 + 4u^2 f \psi'^2}{u^2 f (-1 + \psi^2)^2} \right) \psi - \frac{2(3 + 2u^2 f \psi'^2)}{u^2 f (-1 + \psi^2)^2} \psi^3 = 0. \end{aligned} \quad (5.2)$$

Although the field equation for  $\psi$  now becomes more complicated, the contribution from the magnetic field vanishes on the boundary. Thus, the near boundary solution for  $\psi$  is not modified compared to the case in the absence of a magnetic field, which reads

$$\psi(u)|_{u \rightarrow 0} = m \frac{u}{2^{1/2} u_h} + c \frac{u^3}{2^{3/2} u_h^3} + \dots, \quad (5.3)$$

---

<sup>1</sup> Notice that the  $B_z$  here is the reparametrized magnetic field. The magnitude of the real magnetic field should be written as  $eB = B_z / (2\pi l_s^2) = B_z \pi^{-1} \sqrt{\lambda/2}$  for  $L = 1$ , which depends on the t'Hooft coupling.

while the relation between  $m$  and  $c$  will be altered by the equation of motion in the bulk. It is shown in [172] that  $c \neq 0$  for  $m = 0$  when the magnetic field exceeds a critical value. In such a condition, the chiral symmetry is always broken. This result qualitatively agrees with the so called magnetic catalysis in QCD, where the presence of a strong magnetic field favors the chiral symmetry breaking. The  $\psi$  in the field equation can be solved numerically with the same manner as in the cases with zero magnetic field. By analyzing the near-horizon expansions of  $\psi$ , one finds that the relation between  $\psi_0$  and  $\psi'_0$  is not altered by the inclusion of magnetic field.

We may now proceed to the black hole embedding with the anisotropic background. Here we consider the presence of constant magnetic field by turning on the worldvolume U(1) gauge field  $2\pi l_s^2 A_y = B_z x$  and  $2\pi l_s^2 A_x = B_y z$  in (4.30), which generate the magnetic field  $B_z$  and  $B_y$  along the  $z$  and  $y$  directions, respectively. To simplify the computations, we will include the magnetic field in one of the directions alone. In the isotropic case, these two setups should degenerate, while the degeneracy will be broken when we further incorporate the pressure anisotropy. The explicit forms of the DBI actions now become

$$\begin{aligned}
S &= -N_f T_{D7} \int d^8 x \frac{(1 - \psi^2) e^{-\frac{3\phi}{4}}}{u^5} \sqrt{\mathcal{B}(1 + B_z^2 u^4)(1 - \psi^2 + u^2 \mathcal{F} e^{\frac{1}{2}\phi} \psi'^2)}, \text{ and} \\
S &= -N_f T_{D7} \int d^8 x \frac{(1 - \psi^2) e^{-\frac{\phi}{4}}}{u^5} \sqrt{\mathcal{B}(\mathcal{H} + B_y^2 u^4)(1 - \psi^2 + u^2 \mathcal{F} e^{\frac{1}{2}\phi} \psi'^2)}, \quad (5.4)
\end{aligned}$$

which lead to same field equations as (4.34) with the following substitutions,

$$\begin{aligned}
C_1 &\rightarrow C_1|_{B_z=0} + \frac{2B_z^2 u^3}{1 + B_z^2 u^4}, & C_2 &\rightarrow C_2|_{B_z=0} + \frac{2B_z^2 e^{\frac{\phi}{2}} u^5 \mathcal{F}}{(1 + B_z^2 u^4)(1 - \psi^2)}, \text{ and} \\
C_1 &\rightarrow C_1|_{B_y=0} + \frac{B_y^2 u^3 (4\mathcal{H} - u\mathcal{H}')}{2\mathcal{H}(B_y^2 u^4 + \mathcal{H})}, & C_2 &\rightarrow C_2|_{B_y=0} + \frac{B_y^2 e^{\frac{\phi}{2}} u^5 \mathcal{F} (4\mathcal{H} - u\mathcal{H}')}{2\mathcal{H}(B_y^2 u^4 + \mathcal{H})(1 - \psi^2)}.
\end{aligned}$$

The  $\psi$  in the field equation can be solved numerically with the same manner as in the cases with zero magnetic field. Different values of quark mass obtained by

varying  $\psi_0$  for black hole embeddings in the presence of magnetic field or anisotropy are illustrated in Fig.5.1. It is found that the magnetic field reduces the critical mass or increases the dissociation temperature, which results in an opposite effect to the pressure anisotropy. Recall that the critical mass refers to the mass of quarks obtained from the black hole embedding near the critical embedding at  $\psi_0 \rightarrow 1$ . The suppression of critical mass by magnetic field has been found in [172] as well.

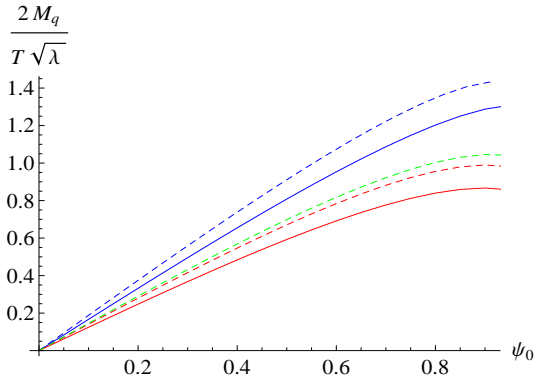


FIGURE 5.1: The blue and red solid curves(from top to bottom) represent the quark mass scaled by temperature without and with magnetic field  $B_z$ , respectively. The blue, green, and red dashed curves(from top to bottom) correspond to the anisotropic case without magnetic field, with  $B_y$ , and with  $B_z$ , respectively. Here we set  $u_h = 1$ ,  $B_y = B_z = 2(\pi T)^2$ , and  $a/T = 4.4$ .

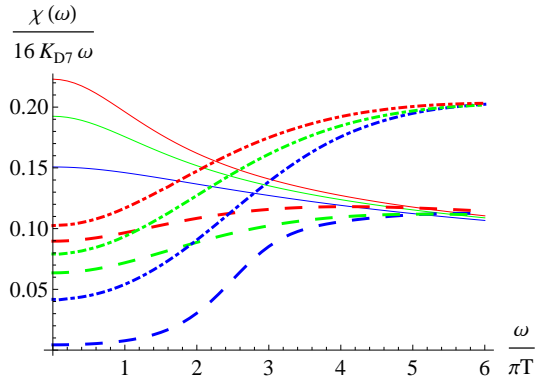


FIGURE 5.2: The red, green, and blue curves(from top to bottom) represent the spectral functions with  $k = (-\omega, 0, 0, \omega)$  for  $\hat{M}_q/(\pi T) = 0.45, 0.65,$  and  $0.86$ , respectively. The solid, dashed, and dot-dashed correspond to  $(a/T, B_z/(\pi T)^2) = (0, 0), (0, 2),$  and  $(4.4, 2)$ , respectively.

## 5.2 Photon Production from Magnetic Fields in Anisotropic Plasmas

To generate the electromagnetic currents on the boundary, we should further introduce the perturbation of gauge fields in the presence of a magnetic field. To the quadratic order in the field strength, the D7-brane action is

$$S = -N_f T_{D7} \int_{D7} d^8 x e^{-\phi} \sqrt{-\det(G_{\mu\nu})} \left( 1 + \frac{(2\pi l_s)^2}{4} F^2 \right), \quad (5.5)$$

where  $G_{\mu\nu}$  is now the induced metric of the D7 branes incorporating the magnetic field. The diagonal elements of  $G_{\mu\nu}$  are the same as those in the absence of magnetic fields, while the off-diagonal terms  $G_{xy}(G_{xz}) = -G_{yx}(G_{zx}) = B_z(-B_y)$  receive the contributions from nonzero magnetic fields. By taking Fourier transform of the gauge fields, the near boundary actions can be written as

$$\begin{aligned}
S_\epsilon &= -2K_{D7} \int \frac{d^4k}{(2\pi)^4} \frac{Q_{B_z}}{u} \left( -\frac{1}{\mathcal{F}\mathcal{B}} A_t^* A_t' + \frac{A_x^* A_x' + A_y^* A_y'}{1 + B_z^2 u^4} + \frac{1}{\mathcal{H}} A_z^* A_z' \right), \\
S_\epsilon &= -2K_{D7} \int \frac{d^4k}{(2\pi)^4} \frac{Q_{B_y}}{u} \left( -\frac{1}{\mathcal{F}\mathcal{B}} A_t^* A_t' + A_x^* A_x' + \frac{A_y^* A_y' + A_z^* A_z'}{\mathcal{H} + B_y^2 u^4} \right), \quad (5.6)
\end{aligned}$$

where

$$\begin{aligned}
Q_{B_z} &= \frac{(1 - \psi^2)^2 \mathcal{F} \sqrt{\mathcal{B}(1 + B_z^2 u^4)} e^{-\frac{3\phi}{4}}}{\sqrt{1 - \psi^2 + u^2 \mathcal{F} e^{\frac{1}{2}\phi} \psi'^2}}, \\
Q_{B_y} &= \frac{(1 - \psi^2)^2 \mathcal{F} \sqrt{\mathcal{B}(\mathcal{H} + B_z^2 u^4)} e^{-\frac{\phi}{4}}}{\sqrt{1 - \psi^2 + u^2 \mathcal{F} e^{\frac{1}{2}\phi} \psi'^2}}. \quad (5.7)
\end{aligned}$$

The field equations of the gauge fields here also take the Maxwell form,

$$\partial_\mu (\sqrt{-\det G_{\mu\nu}} e^{-\phi} G^{\mu\alpha} G^{\nu\beta} F_{\alpha\beta}) = 0. \quad (5.8)$$

The equations above can be converted into gauge-invariant forms from the general expressions in Appendix B.1. Here we list the diagonal terms of the induced metric pertinent to the computations,

$$\begin{aligned}
G^{tt} &= -\frac{u^2}{\mathcal{F}\mathcal{B}}, \quad G^{xx} = G^{yy} = \frac{u^2}{1 + B_z^2 u^4}, \\
G^{zz} &= \frac{u^2}{\mathcal{H}}, \quad G^{uu} = \frac{u^2 \mathcal{F} (1 - \psi^2)}{1 - \psi^2 + u^2 \mathcal{F} e^{\frac{\phi}{2}} \psi'^2} \quad (5.9)
\end{aligned}$$

for  $B_z \neq 0$  and

$$\begin{aligned}
G^{tt} &= -\frac{u^2}{\mathcal{F}\mathcal{B}}, & G^{xx} &= \mathcal{H}G^{zz} = \frac{u^2\mathcal{H}}{\mathcal{H} + B_y^2 u^4}, \\
G^{yy} &= u^2, & G^{uu} &= \frac{u^2\mathcal{F}(1 - \psi^2)}{1 - \psi^2 + u^2\mathcal{F}e^{\frac{\sigma}{2}}\psi'^2}
\end{aligned} \tag{5.10}$$

for  $B_y \neq 0$ . After solving the field equations, we can follow the same procedure as introduced in the previous chapter to compute the spectral functions of photons. To compare the results in the presence of the magnetic field and anisotropy, we have to fix the temperature and quark mass in different setups. We firstly consider the situation when the magnetic field points along the anisotropic direction for which the results are shown in Fig.5.2, Fig.5.3, and Fig.5.4, where the spectral functions are in the unit of  $\pi T$ . As shown in Fig.5.2, the spectra for photons emitted parallel to the magnetic field are suppressed at small  $\hat{\omega}$ , while they saturate the isotropic spectra in the absence of magnetic field at large  $\hat{\omega}$ . When further incorporating the pressure anisotropy, the spectra for photons emitted parallel to the anisotropic direction are enhanced, which is similar to the scenario in the absence of magnetic field as shown in the previous chapter; their amplitudes surpass the isotropic ones with zero magnetic fields at large  $\hat{\omega}$ .

For the photons emitted perpendicular to the magnetic field, as shown in Fig.5.3 and Fig.5.4, their spectra are enhanced at large  $\hat{\omega}$ . Also, the anisotropic effect makes no drastic modifications to the spectra at large  $\hat{\omega}$ . However, at moderate  $\hat{\omega}$ , a resonance emerges in the spectrum led by heavy quarks for photons moving perpendicular to the magnetic field. The resonance is more prominent when the photons are polarized parallel to the magnetic field as illustrated by the dashed blue curve in Fig.5.4. When further incorporating the pressure anisotropy, the resonance is smoothed out.

In the zero-frequency limit, we can also evaluate the DC conductivity by em-

ploying (4.28), where the results are shown in Fig.5.5 and Fig.5.6. As illustrated in Fig.5.5, compared to the isotropic case in the absence of magnetic field, we find that the conductivity for photons with the polarization perpendicular to the anisotropic direction is enhanced in particular for the embedding with heavy quarks. On the contrary, the conductivity for the polarization perpendicular to the magnetic field is suppressed. When the quark mass is increased, the suppression becomes more robust. In contrast, as illustrated in Fig.5.6, for photons with the polarization along the anisotropic direction, the conductivity is almost unchanged compared to the isotropic one except for the embedding with heavy quarks. However, the conductivity for the photons with the polarization parallel to the magnetic field is larger than the isotropic one for the embedding with light quarks. When the quark mass is increased, the enhancement monotonically decreases and even turns into suppression when approaching the critical mass.

When the magnetic field and anisotropy coexist and point perpendicular to each other, the rotational symmetry is fully broken. The photons moving in distinct directions with different polarizations will lead to a variety of spectra, but the general features are not particularly altered from what we have discussed in the paragraph above. The spectra for photons moving parallel to the anisotropic direction and perpendicular to the magnetic field receive the maximum enhancement at large frequency. When the photons are emitted perpendicular to the magnetic field in the isotropic medium, the resonance appears for the spectra with heavy quarks at moderate frequency. The presence of anisotropy then smooths out the resonance regardless of the moving directions of photons. We merely present the results in Fig.5.8-5.13 for reference, where the correspondences between the colors of curves and different values of quark mass are the same as those in Fig.5.2.

The enhancements of the photon spectra with massive quarks at large frequency led by anisotropy and magnetic fields are somewhat expected since the enhancements

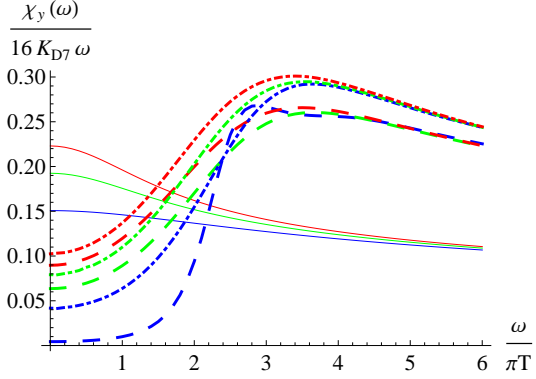


FIGURE 5.3: The red, green, and blue curves (from top to bottom) represent the spectral functions with  $k = (-\omega, \omega, 0, 0)$  and  $\epsilon_T = \epsilon_y$  for  $\hat{M}_q/(\pi T) = 0.45, 0.65,$  and  $0.86,$  respectively. The solid, dashed, and dot-dashed correspond to  $(a/T, B_z/(\pi T)^2) = (0, 0), (0, 2),$  and  $(4.4, 2),$  respectively.

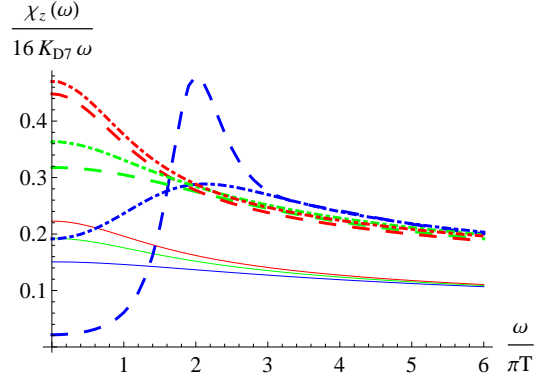


FIGURE 5.4: The red, green, and blue curves (from top to bottom) represent the spectral functions with  $k = (-\omega, \omega, 0, 0)$  and  $\epsilon_T = \epsilon_z$  for  $\hat{M}_q/(\pi T) = 0.45, 0.65,$  and  $0.86,$  respectively. The solid, dashed, and dot-dashed correspond to  $(a/T, B_z/(\pi T)^2) = (0, 0), (0, 2),$  and  $(4.4, 2),$  respectively.

have been found in the limit of massless quarks [162, 170]. When the energy of photons dominates the quark mass, the contributions from massive and massless quarks should degenerate. The enhancements will persist for  $\hat{\omega} \rightarrow \infty$ . In the coexistence of both effects, the enhancement of the spectra could be further amplified. As illustrated in Fig.5.10 and Fig.5.11, for which the magnetic field is perpendicular to the anisotropy direction, the spectra at large frequency in the presence of the magnetic field can be further enhanced by anisotropy. When the photons move along the anisotropic direction in the above situation, their amplitudes of the spectra can be maximally enhanced. Such a scenario may be in analogy to the photon production in relativistic heavy ion collisions. In the peripheral collisions in experiments, the orientation of the averaged magnetic field generated by two colliding nuclei should be perpendicular to the reaction plane. The initial geometry of the medium will lead to pressure anisotropy, in which the largest pressure is perpendicular to the

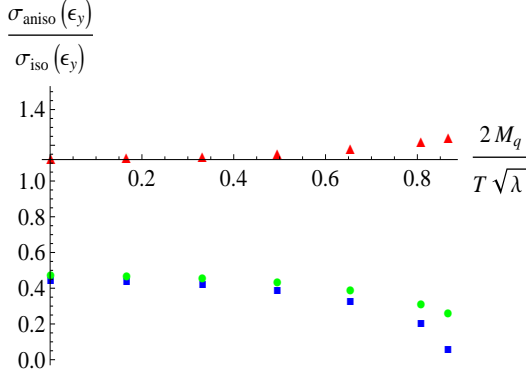


FIGURE 5.5: The ratios of DC conductivity with  $\epsilon_T = \epsilon_y$  versus quark mass. The red(triangle), green(circle), and blue(square) dots correspond to the cases with  $(a/T, B_z/(\pi T)^2) = (4.4, 0)$ ,  $(0, 2)$ , and  $(4.4, 2)$ , respectively.

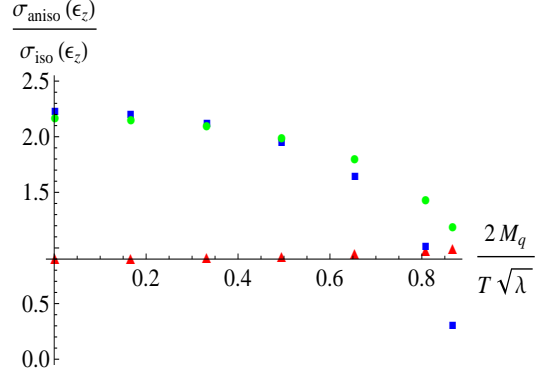


FIGURE 5.6: The ratios of DC conductivity with  $\epsilon_T = \epsilon_z$  versus quark mass. The red(triangle), green(circle), and blue(square) dots correspond to the cases with  $(a/T, B_z/(\pi T)^2) = (4.4, 0)$ ,  $(0, 2)$ , and  $(4.4, 2)$ , respectively.

averaged magnetic field and to the beam direction<sup>2</sup>. At mid rapidity, the observation of large elliptic flow of direct photons corresponds to the excessive production of photons along the orientation with largest pressure. In our model, the maximum enhancement of the thermal photons produced along the anisotropic direction and perpendicular to the magnetic field may qualitatively suggest the cause of such large flow of direct photons.

Nonetheless, there exist caveats when making the comparison above beyond the difference in the SYM theory and QCD. Firstly, the pressure anisotropy in the MT model is distinct from the one in QGP in directions. In the MT model, the rotational symmetry is still preserved on the plane perpendicular to the anisotropic direction with larger pressure, which is drastically distinct from the QGP that the rotational symmetry should be fully broken. Second, the medium will gradually expand and thus the temperature of QGP could be spacetime dependent. Furthermore, the

---

<sup>2</sup> Here we simply refer the pressure to the energy stress tensor in the lab frame. In anisotropic hydrodynamics, the pressure on the transverse plane perpendicular to the beam direction should be isotropic in the co-moving frame, while the pressure gradient along the reaction plane is greater than that perpendicular to the reaction plane.

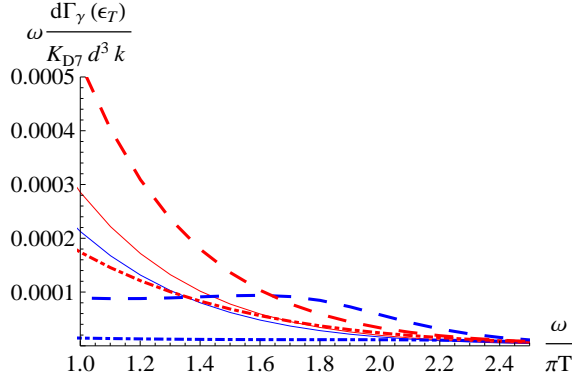


FIGURE 5.7: The red and blue (upper and lower at  $\omega/(\pi T) = 1$ ) curves represent the differential emission rate per unit volume with  $k = (-\omega, \omega, 0, 0)$  for  $\hat{M}_q/(\pi T) = 0.45$  and 0.86. The solid, dashed, and dot-dashed ones correspond to  $(\epsilon_T, B_z/(\pi T)^2) = (\epsilon_{z(y)}, 0)$ ,  $(\epsilon_z, 2)$ , and  $(\epsilon_y, 2)$ , respectively.

magnetic field generated by the colliding nuclei should decay rapidly with time. The lifetime modified by the presence of matter (thermal quarks) is controversial, where the different estimates can be found in [126, 173] and [127]. Despite the distinction between our model and QGP in reality, the results from such a toy model still provide us qualitative understandings of the influence of pressure anisotropy and magnetic fields on the photon production in the strongly coupled scenario.

At moderate frequency, the spectra with heavy quarks in the presence of magnetic fields and anisotropy are rather intriguing. As indicated in [174], the resonance appearing in photon spectra may implies the decay of heavy mesons to on-shell photons. In the previous study of photon spectra with massive quarks in the absence of magnetic fields in an isotropic medium [13], it has been shown that the resonance starts to emerge when the quark mass approaches the critical mass. Since the presence of a magnetic field reduces the critical mass, the resonance appears for the spectrum with smaller quark mass, which suggests that the decay from lighter mesons to on-shell photons will be accessible with the aid of the magnetic field. Moreover, the dependence on orientation and polarization with respect to the magnetic field makes the

resonance distinguishable from the isotropic one triggered by the increase of quark mass in the absence of magnetic fields [13].

Here we plot the differential emission rate per unit volume in the unit of  $(\pi T)^2$  in Fig.5.7 around moderate frequency, where the resonance from heavy quarks could be comparable to the spectrum with lighter quarks in this regime. In the presence of a magnetic field, the impact of the resonance on the shape of the spectrum at moderate frequency is even more pronounced than the enhancement at large frequency, which could generate a mild peak of  $v_2$  at moderate frequency. Despite the over-simplification of our model, the orientation-dependence resonance could give a rise to the mild peak of  $v_2$  in the intermediate energy. On the other hand, it is also indicated in [171] that the photons with out-plane polarizations, which correspond to the photons polarized along the magnetic field when moving perpendicular to the field in our setup, will account for the primary contributions beyond small frequency. The polarization dependence of the enhanced spectra of direct photons could be substantial to clarify the cause of large  $v_2$  in future experiments.

On the contrary, the further inclusion of pressure anisotropy increases the critical mass and thus reduces the resonance in our model, which favors the meson melting in the plasma. Our findings are consistent with [156, 161, 175], in which the increase of anisotropy results in the decrease of the screening length of the quark-antiquark potential in the MT geometry at fixed temperature. At first glance, it is surprising that the qualitative features of heavy-meson suppression led by pressure anisotropy found in the MT geometry are contradictory to those obtained in weakly coupled approaches [176, 177] and anisotropic hydrodynamics [178, 179, 180] for anisotropic QCD plasmas, where the anisotropic media result in less suppression for heavy mesons in comparison with the isotropic ones. Nonetheless, one should recall the difference between the setup in the MT model and in those approaches more analogous to QGP in reality. In the MT model, the ratio of shear viscosity

to entropy density is decreased by the increase of pressure anisotropy [181]. This is drastically different from the approaches related to QGP, in which the pressure anisotropy makes the plasma more viscous. As a result, the anisotropic effect in the MT model facilitates the deconfinement based on the suppression of the shear viscosity to entropy density ratio while the anisotropy in the viscous QGP favors the confinement of heavy mesons. We thus conclude that the resonance stemming from the presence of magnetic field may not be suppressed by pressure anisotropy in QGP.

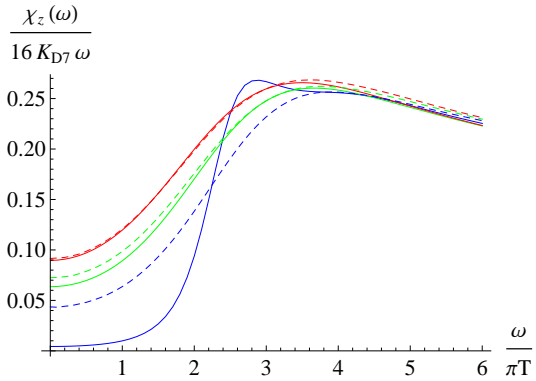


FIGURE 5.8: The spectral functions with  $k = (-\omega, \omega, 0, 0)$  and  $\epsilon_T = \epsilon_z$ . The solid and dashed curves correspond to  $(a/T, B_y/(\pi T)^2) = (0, 2)$  and  $(4.4, 2)$ , respectively.

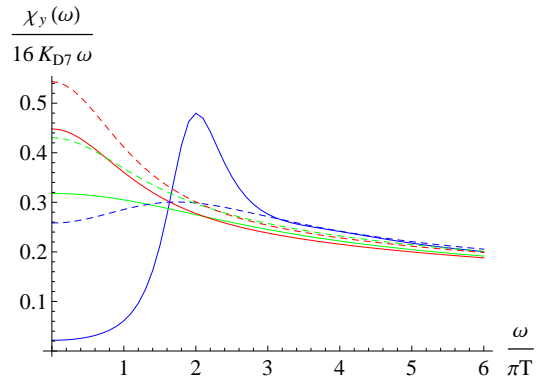


FIGURE 5.9: The spectral functions with  $k = (-\omega, \omega, 0, 0)$  and  $\epsilon_T = \epsilon_y$ . The solid and dashed curves correspond to  $(a/T, B_y/(\pi T)^2) = (0, 2)$  and  $(4.4, 2)$ , respectively.

### 5.3 Thermal-Photon $v_2$ Induced by a Constant Magnetic Field

As discussed in the previous section, the MT geometry may not characterize the anisotropic QGP created in heavy ion collisions. We thus only focus on the effect from magnetic fields on the  $v_2$  of thermal photons. In such a case, we will only apply the isotropic and thermalized background corresponding to the AdS-Schwarzschild geometry. We will then compute the  $v_2$  contributed by two massless quarks and one massive quark with the mass close to the critical mass. Our setup is illustrated in Fig.5.14, where the magnetic field is along the  $z$  direction and two types of po-

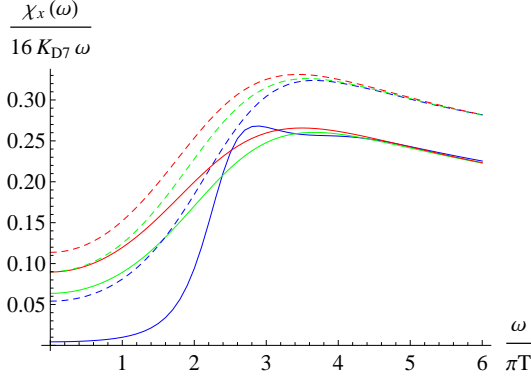


FIGURE 5.10: The spectral functions with  $k = (-\omega, 0, 0, \omega)$  and  $\epsilon_T = \epsilon_x$ . The solid and dashed curves correspond to  $(a/T, B_y/(\pi T)^2) = (0, 2)$  and  $(4.4, 2)$ , respectively.

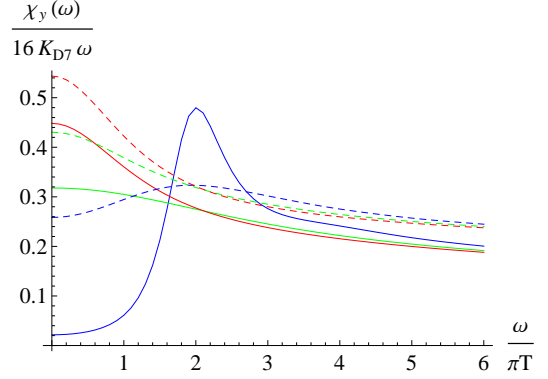


FIGURE 5.11: The spectral functions with  $k = (-\omega, 0, 0, \omega)$  and  $\epsilon_T = \epsilon_y$ . The solid and dashed curves correspond to  $(a/T, B_y/(\pi T)^2) = (0, 2)$  and  $(4.4, 2)$ , respectively.

larizations  $\epsilon^{\text{in}}$  and  $\epsilon^{\text{out}}$  are considered. The four momentum of photons is written as  $k = (-\omega, 0, q_y, q_z)$ , where  $q_y = \omega \cos \theta$  and  $q_z = \omega \sin \theta$ . We will generalize the computations in the isotropic case of [131] to the photon production with an arbitrary angle  $\theta$ . Recall that we will take the quenched approximation by assuming  $N_f \ll N_c$ , where  $N_f$  denotes the number of flavors, and neglect the modification of flavor probe branes to the background geometry. In our convention, we set the AdS radius  $L = (4\pi g_s N_c l_s^4)^{1/4} = 1$ . The temperature of the medium is determined by  $\pi T = u_h^{-1}$ . For convenience, we will further set  $u_h = 1$  in computations. We then turn on the worldvolume U(1) gauge field  $2\pi l_s^2 A_y = u_h^2 B_z x$  coupled to the D7 branes, which generates a constant magnetic field  $eB = u_h^2 B_z / (2\pi l_s^2) = B_z \pi^{-1} \sqrt{\lambda/2}$  along the  $z$  direction. By further perturbing the DBI action in (5.2) with gauge fields, we have the relevant action,

$$S = -K_{D7} \int dt d^3 \vec{x} du F^2 \frac{(1 - \psi^2)}{u^5} (1 + B_z^2 u^4)^{1/2} \times (1 - \psi^2 + u^2 f \psi'^2)^{1/2},$$

where  $F = dA$  is the worldvolume field strength from perturbation.

In the presence of gauge fields in the background of the AdS-Schwarzschild ge-

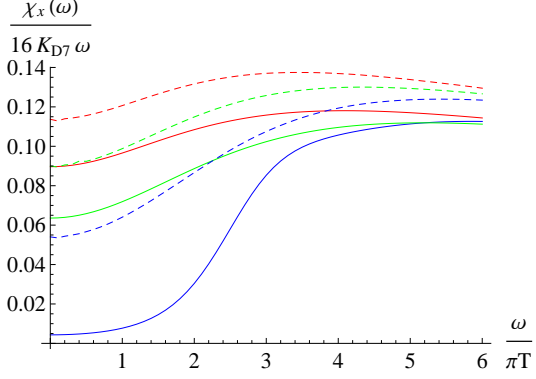


FIGURE 5.12: The spectral functions with  $k = (-\omega, 0, \omega, 0)$  and  $\epsilon_T = \epsilon_x$ . The solid and dashed curves correspond to  $(a/T, B_y/(\pi T)^2) = (0, 2)$  and  $(4.4, 2)$ , respectively.

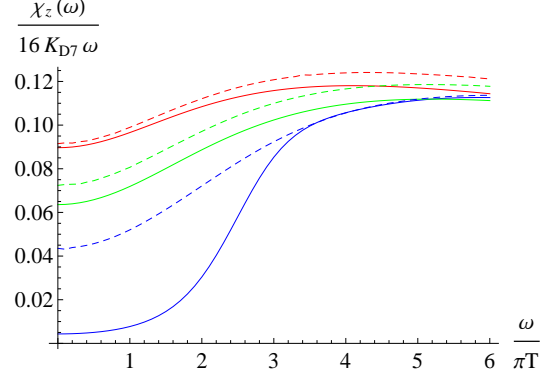


FIGURE 5.13: The spectral functions with  $k = (-\omega, 0, \omega, 0)$  and  $\epsilon_T = \epsilon_z$ . The solid and dashed curves correspond to  $(a/T, B_y/(\pi T)^2) = (0, 2)$  and  $(4.4, 2)$ , respectively.

ometry, the DBI action then gives rise to Maxwell equations

$$\partial_\mu(\sqrt{-\det(G_{\mu\nu})}G^{\mu\alpha}G^{\nu\beta}F_{\alpha\beta}) = 0, \quad (5.11)$$

where the diagonal terms of the induced metric read

$$\begin{aligned} G^{tt} &= -\frac{u^2}{f(u)}, & G^{xx} &= G^{yy} = \frac{u^2}{1 + B_z^2 u^4}, \\ G^{zz} &= u^2, & G^{uu} &= \frac{u^2 f(u)(1 - \psi^2)}{1 - \psi^2 + u^2 f(u) \psi'^2}. \end{aligned} \quad (5.12)$$

To compute the spectral functions, it is more convenient to convert the field equations into gauge invariant forms. For the in-plane polarization  $\epsilon_T = \epsilon^{in} = \epsilon_x$ , the computation is straightforward. By taking  $E_x = \omega A_x$  in momentum space, we have to solve only one field equation,

$$E_x'' + (\log(\sqrt{-G}G^{uu}G^{xx}))' E_x' - \frac{\bar{k}^2}{G^{uu}} E_x = 0, \quad (5.13)$$

where  $G = \det(G_{\mu\nu})$  and  $\bar{k}^2 = G^{tt}w^2 + G^{yy}q_y^2 + G^{zz}q_z^2$ . For the out-plane polarization  $\epsilon_T = \epsilon^{out}$ , we have to consider coupled equations. By implementing the relation

$q_y A_y + q_z A_z = 0$  as shown in Fig.5.14, the field equations can be written into the gauge-invariant forms as

$$\begin{aligned}
E_z'' &+ \left[ (\log(\sqrt{-G}G^{uu}G^{zz}))' + \frac{G^{zz}q_z^2}{\bar{k}^2} \left( \log \left( \frac{G^{tt}}{G^{zz}} \right) \right)' \right] E_z' \\
&+ \frac{q_y q_z G^{yy}}{\bar{k}^2} \left( \log \left( \frac{G^{tt}}{G^{zz}} \right) \right)' E_y' - \frac{\bar{k}^2}{G^{uu}} E_z = 0, \\
E_y'' &+ \left[ (\log(\sqrt{-G}G^{uu}G^{yy}))' + \frac{G^{yy}q_y^2}{\bar{k}^2} \left( \log \left( \frac{G^{tt}}{G^{yy}} \right) \right)' \right] E_y' \\
&+ \frac{q_y q_z G^{zz}}{\bar{k}^2} \left( \log \left( \frac{G^{tt}}{G^{yy}} \right) \right)' E_z' - \frac{\bar{k}^2}{G^{uu}} E_y = 0,
\end{aligned} \tag{5.14}$$

where  $E_{z(y)} = q_{z(y)} A_t + \omega A_{z(y)}$ . The Maxwell equations in (5.13) and (5.14) can be solved numerically by imposing incoming-wave boundary conditions near the horizon[166], where  $\vec{E}(u) \sim (1 - u^2/u_h^2)^{-\frac{i\omega}{4\pi T}}$ .

Since  $\bar{k}^2 \approx -u^6 \omega^2 (1 + B_z^2 \cos^2 \theta)$  near the boundary, eq.(5.14) reduces to

$$(G^{yy} q_y E_y' + G^{zz} q_z E_z')_{u \rightarrow 0} = 0. \tag{5.15}$$

By utilizing the relation above, the near-boundary action can be simplified as

$$\frac{-S_\epsilon}{2K_{D7}} = \int \frac{d^4 k}{(2\pi)^4} \frac{\sqrt{-G}G^{uu}}{\omega^2} G^{jj} E_j^* E_j', \tag{5.16}$$

where  $j = x, y, z$ . We then evaluate the spectral density with the polarization  $\epsilon_T$  via

$$\begin{aligned}
\chi_{\epsilon_T}(k_0) &= -4\text{Im}[\epsilon_T^\mu \epsilon_T^\nu C_{\mu\nu}^R(k)] \\
&= -4\text{Im} \left[ \lim_{u \rightarrow 0} \left( \omega^2 \epsilon_{T\mu} \epsilon_{T\nu} \frac{\delta^2 S_\epsilon}{\delta E_\mu^* E_\nu} \right) \right],
\end{aligned} \tag{5.17}$$

where  $C_{\mu\nu}^R$  denotes the retarded correlator. For the in-plane polarization, we have

$$\begin{aligned}
\frac{\chi_{\epsilon^{in}}}{8K_{D7}} &= \frac{-1}{2K_{D7}} \text{Im}(C_R^{xx}) \\
&= \text{Im} \left[ \lim_{u \rightarrow 0} \left( \sqrt{-G}G^{uu} G^{xx} \frac{E_x'}{E_x} \right) \right].
\end{aligned} \tag{5.18}$$

For the out-plane polarization, we have

$$\begin{aligned}
\frac{\chi_{\epsilon^{out}}}{8K_{D7}} &= \frac{-1}{2K_{D7}} \text{Im} \left[ \sin^2 \theta C_R^{yy} + \cos^2 \theta C_R^{zz} \right. \\
&\quad \left. - \cos \theta \sin \theta (C_R^{yz} + C_R^{zy}) \right] \\
&= \text{Im} \left[ \lim_{u \rightarrow 0} \left( \sqrt{-G} G^{uu} \left( G^{yy} \frac{E'_y}{E_y} + G^{zz} \frac{E'_z}{E_z} \right) \right) \right],
\end{aligned} \tag{5.19}$$

where we utilize (5.15) to derive the second equality above. Solving the  $E_z$  and  $E_y$  for the out-plane polarization is more involved with the coupled equations, for which we discuss the technical details in the following. The procedure is similar to the computations in [162].

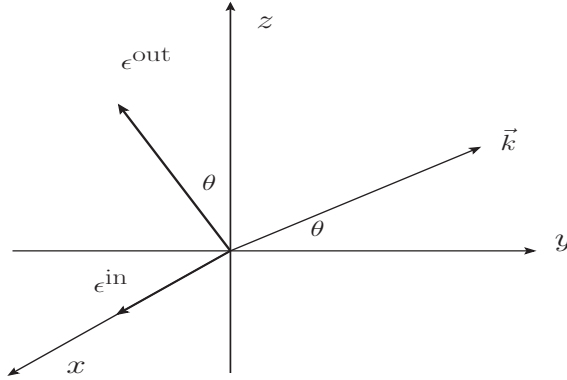


FIGURE 5.14: The coordinates of the system, where the magnetic field points along the  $z$  axis and the  $x$  axis is parallel to the beam direction. The  $\vec{k}$  denotes the momentum of emitted photons and  $\theta$  denotes the angle between the momentum and the  $x$ - $y$  plane as the reaction plane;  $\epsilon^{out}$  and  $\epsilon^{in}$  represent the out-plane and in-plane polarizations, respectively.

Given that the out-plane solution is written in terms of the relevant bases as

$$\vec{E}^{out}(u) = \vec{E}^1(u) + \vec{E}^2(u), \tag{5.20}$$

where  $\vec{E}^1(u) = E_y^1 \hat{y}(u) + E_z^1 \hat{z}(u)$  and  $\vec{E}^2(u) = E_y^2 \hat{y}(u) + E_z^2 \hat{z}(u)$ , such bases should reduce to  $\vec{E}^1(0) = E_y^1(0) \hat{y}$  and  $\vec{E}^2(0) = E_z^2(0) \hat{z}$  on the boundary, which correspond

to  $E_y$  and  $E_z$  in (5.19). Since  $A_t(0) = 0$  on the boundary, the bases follow the constraint  $E_y^1(0)/E_z^2(0) = -\tan\theta$ . The task will be to find these relevant bases.

Presuming that  $\vec{E}^a(u) = E_y^a(u)\hat{y} + E_z^a(u)\hat{z}$  and  $\vec{E}^b(u) = E_y^b(u)\hat{y} + E_z^b(u)\hat{z}$  are two sets of incoming-wave solutions, the relevant bases should be formed by linear combinations of the them. We thus define

$$\begin{aligned}\vec{E}^1(u) &= a_1\vec{E}^a(u) + b_1\vec{E}^b(u), \\ \vec{E}^2(u) &= a_2\vec{E}^a(u) + b_2\vec{E}^b(u).\end{aligned}\tag{5.21}$$

The bases on the boundary then read

$$\begin{aligned}\vec{E}^1(0) &= a_1\vec{E}^a(0) + b_1\vec{E}^b(0) = -E_0 \sin\theta\hat{y}, \\ \vec{E}^2(0) &= a_2\vec{E}^a(0) + b_2\vec{E}^b(0) = E_0 \cos\theta\hat{z},\end{aligned}\tag{5.22}$$

where  $E_0 = |\vec{E}^{out}(0)|$ . By solving the coupled equations above, we find

$$\begin{aligned}(a_1, b_1) &= \frac{(-E_z^b(0) \sin\theta, E_z^a(0) \sin\theta)}{E_y^a(0)E_z^b(0) - E_y^b(0)E_z^a(0)}, \\ (a_2, b_2) &= \frac{(-E_y^b(0) \cos\theta, E_y^a(0) \cos\theta)}{E_y^a(0)E_z^b(0) - E_y^b(0)E_z^a(0)},\end{aligned}\tag{5.23}$$

where we set  $E_0 = 1$  since the retarded correlators are invariant for an arbitrary  $E_0$ . In practice, we could solve for two arbitrary incoming waves  $\vec{E}^{a(b)}(u)$ . Then by employing the coefficients shown in (5.23) to recombine these two solutions, we are able to derive  $E_y(u)$  and  $E_z(u)$  for the out-plane polarization.

Finally, we may compute the elliptic flow  $v_2$  for photon production. In the lab frame of heavy ion collisions, the four-momenta of photons can be parametrized as

$$k_\mu = (-k_T \cosh\tilde{y}, k_T \sinh\tilde{y}, k_T \cos\theta, k_T \sin\theta),\tag{5.24}$$

where  $\tilde{y}$  denotes the rapidity and  $k_T$  denotes the transverse momentum perpendicular to the beam direction  $\hat{x}$ . Notice that  $\omega = k_T \cosh\tilde{y} \approx k_T$  at central rapidity ( $\tilde{y} \approx 0$ ),

which reduces to our setup illustrated in Fig.5.14. The elliptic flow  $v_2$  is defined as

$$v_2^\gamma(k_T, \tilde{y}) = \frac{\int_0^{2\pi} d\theta \cos(2\theta) \frac{dN_\gamma}{d^2k_T d\tilde{y}}}{\int_0^{2\pi} d\theta \frac{dN_\gamma}{d^2k_T d\tilde{y}}}, \quad (5.25)$$

where  $N_\gamma$  is the total yield of the emitted photons. In thermal equilibrium, the differential emission rate per unit volume is given by

$$\omega \frac{d\Gamma_\gamma(\epsilon_T)}{d^3k} = \frac{d\Gamma_\gamma(\epsilon_T)}{d^2k_T d\tilde{y}} = \frac{1}{16\pi^3} \frac{\chi_{\epsilon_T}(k_0)}{(e^{\beta\omega} - 1)}. \quad (5.26)$$

In general, we have to take four dimensional spacetime integral of the emission rate to obtain the yield of photons. In our setup, where the medium is static, the spacetime integral leads to a constant volume, which is irrelevant for  $v_2$  here. The elliptic flow at central rapidity hence becomes

$$v_2^\gamma(\omega, 0) = \frac{\int_0^{2\pi} d\theta \cos(2\theta) \chi_{\epsilon_T}(k_0)}{\int_0^{2\pi} d\theta \chi_{\epsilon_T}(k_0)}. \quad (5.27)$$

All physical observables now will be scaled by temperature of the medium. We set  $B_z = 1(\pi T)^2$ , which corresponds to  $eB = 0.39 \text{ GeV}^2$  in the regular scheme for  $\lambda = 6\pi$  and the average temperature of the SYM plasma  $T = T_{\text{QGP}} = 200 \text{ MeV}$ . In an alternative scheme[182],  $eB = 0.12 \text{ GeV}^2$  for  $\lambda = 5.5$  and  $T = 3^{-1/4} T_{\text{QGP}} \approx 150 \text{ MeV}$ , where the temperature of SYM plasma is lower than that of QGP at fixed energy density. In heavy ion collisions, the approximate magnitude of the magnetic field is about the hadronic scale,  $eB \approx m_\pi^2 \approx 0.02 \text{ GeV}^2$ [126]. It turns out that the magnitude of magnetic field in the alternative scheme is close to the approximate value at RHIC. Even in the regular scheme, the magnitude of the magnetic field in our model is not far from the approximate value. Hereafter we will make comparisons to QGP in the alternative scheme.

We firstly consider the elliptic flow contributed from massless quarks, which corresponds to the trivial embedding( $\psi' = 0$ ). As shown in Fig.5.15, the presence of

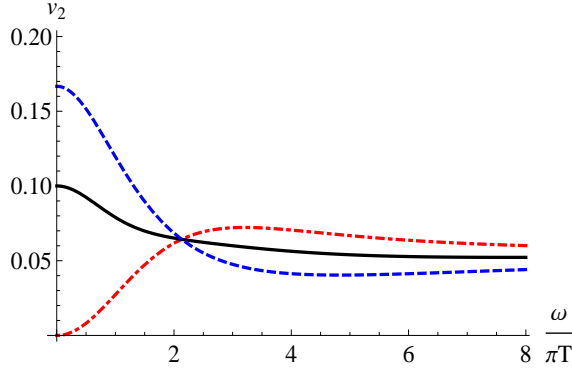


FIGURE 5.15: The red(dot-dashed) and blue(dashed) curves correspond to the  $v_2$  of the photons with in-plane and out-plane polarizations, respectively. The black(solid) curve correspond to the one from the averaged emission rate of two types of polarizations. Here we consider the contribution from massless quarks at  $B_z = 1(\pi T)^2$ .

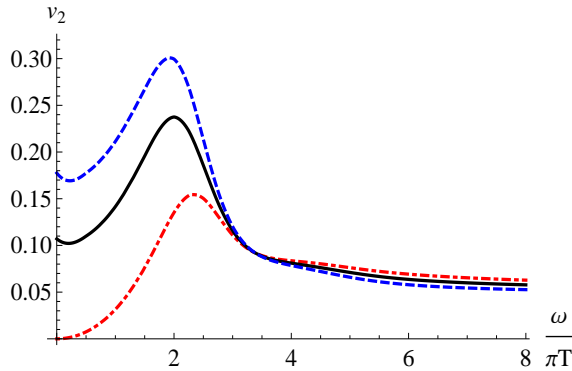


FIGURE 5.16: The colors correspond to the same cases as in Fig.5.15. Here we consider the contributions from solely the massive quarks with  $m = 1.143$  at  $B_z = 1(\pi T)^2$ .

a magnetic field results in nonzero  $v_2$ , while the  $v_2$  remain featureless(without resonances). Here the averaged  $v_2$  is obtained from the averaged emission rate of both the in-plane and out-plane polarizations. Whereas quarks may receive mass correction at finite temperature, we should consider the contributions from massive quarks as well. In addition, at intermediate energy, the photon spectra from the massive quarks may lead to resonances coming from the decays of heavy mesons to light-like photons[13, 174], which makes a considerable contribution to the spectra. As

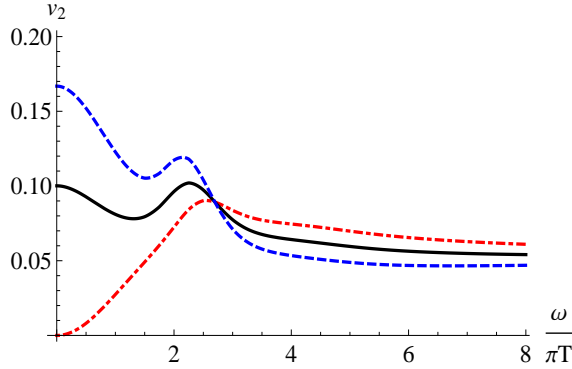


FIGURE 5.17: The colors correspond to the same cases as in Fig.5.15. Here we consider the contributions from both massless quarks and massive quarks with  $m = 1.143$  at  $B_z = 1(\pi T)^2$ .

indicated in the previous section, the resonances in the presence of a magnetic field depend on the moving directions of produced photons, which may generate prominent peaks in  $v_2$ . To incorporate the massive quarks, we choose  $\psi_0 \approx 0.95$ , which is close to the critical embedding ( $\psi_0 \rightarrow 1$ ). In fact, by further tuning  $\psi_0$  up to one, the black hole embeddings may become unstable and multiple resonances will emerge in photon spectra similar to the scenarios in the absence of magnetic field[13]. From (2.41), we find  $m = 1.143$  for the solution of the massive quarks, which corresponds to the bare quark mass  $M_q = 204$  MeV at the average RHIC temperature  $T_{\text{QGP}} = 200$  MeV in the alternative scheme. Due to the presence of the magnetic field and the choice of the alternative scheme, the bare quark mass for the massive quark here is smaller than that in [13, 174] to generate the resonance. As shown in Fig.5.16, a mild peak emerges at intermediate energy for the photon  $v_2$  contributed from solely the massive quarks.

In analogy to the thermal photon production in QGP, we may consider scenarios in the 2+1 flavor SYM plasma. We sum over the photon emission rates from two massless quarks and that from the massive quark with  $M_q = 204$  MeV to compute the  $v_2$ . The results are shown in Fig.5.17, where the resonances of  $v_2$  are milder.

In QGP, the regime in which the thermal photons make substantial contributions is around  $p_T \approx 1 \sim 4$  GeV at central rapidity, where  $p_T \approx \omega$  denotes the transverse momentum of direct photons. By rescaling  $p_T$  with  $\pi T_{\text{QGP}}$ , such a regime corresponds to  $\omega/(\pi T) \approx 1.5 \sim 6$  in Fig.5.17 at  $T_{\text{QGP}} = 200$  MeV. It turns out that the  $v_2$  in our holographic model resemble the RHIC data for the flow of direct photons at intermediate  $p_T$ [10]. Although the mass of the massive quark in our setup does not match that of the strange quark, the mass we introduce is not far from the scale of strange mesons. The resonances in our setup may suggest the transitions of strange mesons to photons in QGP in the presence of a magnetic field. On the other hand, the resonance of  $v_2$  coming from meson-photon transitions may not be subject to the strongly coupled scenario. In the weakly coupled approach such as [118], where the finite-temperature corrections to the intermediate meson in the effective coupling is not considered, the photon production perpendicular to the magnetic field can be possibly enhanced provided that the thermal dispersion relation of the intermediate meson becomes lightlike.

Finally, we mention the caveats when making comparisons between our holographic model and heavy ion collisions in reality except for the intrinsic difference between SYM theory and QCD. Firstly, the QGP undergoes time-dependent expansion, while the medium in our model is static in thermal equilibrium. Second, the magnetic field produced by colliding nuclei is time-dependent, which decay rapidly in early times. Although the influence of thermal quarks on the lifetime of the magnetic field is controversial[126, 127, 173], the constant magnetic field in our model could overestimate the flow. According to [126], the magnetic field decreases by a factor of 100 between the initial (0.1 fm/c) and final (5 fm/c) times in the presence of nonzero conductivity. As a simple approximation, we may assume that the magnetic field is described by a power-law drop-off, which results in  $B(t) \sim 1/t^{1.2}$ . By taking the initial and freeze-out temperature as  $T_i = 430$  MeV and  $T_f = 150$  MeV, we find the

freeze-out time  $\tau_f \sim 7$  fm as we set the thermalization time  $\tau_{th} = 0.3$  fm and average temperature  $T_{avg} \sim 200$  MeV with the Bjorken hydrodynamics  $T/T_i = (\tau_{th}/\tau)^{1/3}$ . We then obtain the average magnetic field  $B_{avg} \sim 0.1B_0$  with the setup above, where  $B_0$  is the initial magnetic field. By utilizing the average magnetic field with the same t'Hooft coupling and average temperature, we find that the  $v_2$  drop about 100 times as shown in Fig.5.18.

Although the photon  $v_2$  here can only be evaluated numerically, it is approximately proportional to  $B_z^2$  for small  $B_z$ . As a result, we may as well consider the result with average  $(eB)^2$ . With the above approximation, we find  $B_{avg}^2 \sim 0.031B_0^2$  corresponding to  $B_{avg} \sim 0.18B_0$ . As shown in Fig.5.19, the  $v_2$  with  $B_{avg}^2 \sim 0.031B_0^2$  is 25 times smaller. However, as the nonlinear effect with large  $B_z$  becomes more pronounced, the computation with average magnetic field may underestimate the contribution from such a strong magnetic field in early times. It is thus desirable to incorporate a time-dependent magnetic field in the setup as future work. On the other hand, it is also worthwhile to notice that the  $v_2$  in our model is enhanced as we turn down the coupling with fixed magnetic field and temperature through the relation  $eB = B_z\pi^{-1}\sqrt{\lambda/2}$ .

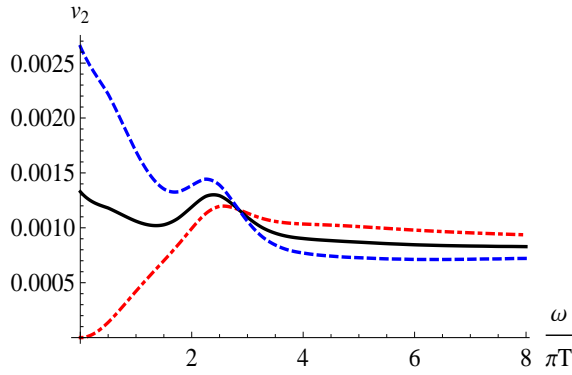


FIGURE 5.18: The colors correspond to the same cases as in Fig.5.15. Here we consider the contributions from both massless quarks and massive quarks with  $m = 1.307$  at  $B_z = 0.1(\pi T)^2$ .

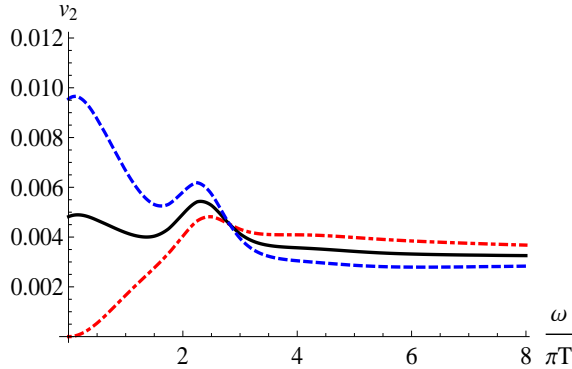


FIGURE 5.19: The colors correspond to the same cases as in Fig.5.15. Here we consider the contributions from both massless quarks and massive quarks with  $m = 1.3$  at  $B_z = 0.2(\pi T)^2$ .

Since we choose the maximum magnetic field from its initial value, the  $v_2$  obtained in our model should be regarded as the upper bound generated by solely magnetic field in the strongly coupled scenario. In reality, such a mechanism only yields a partial contribution to the measured  $v_2$ . As shown in [183], the viscous hydrodynamics also results in a substantial contribution to thermal-photon  $v_2$ . To construct full  $v_2$  for thermal photons, both contributions from the magnetic field and from viscous hydrodynamics should be taken into account. Furthermore, in the alternative scheme, the intermediate t'Hooft coupling is taken, where the corrections from finite t'Hooft coupling in the gravity dual have to be considered. More explicitly, the next leading order correction is of  $\mathcal{O}(\lambda^{-3/2})$ . It is found in [184] that the photoemission rate increases as the coupling decreases in the absence of magnetic fields when the  $\mathcal{O}(\lambda^{-3/2})$  correction is included.

## 5.4 Concluding Remarks

In this chapter, we have evaluated the thermal photon spectra originating from massive quarks in the anisotropic plasma with moderate pressure anisotropy and a constant yet strong magnetic field through the holographic approach. At large frequency,

we found that the amplitudes of spectra with different quark masses are increased by the magnetic field when the photons move perpendicular to it. The spectra for photons moving parallel to the magnetic field saturate the results in the absence of magnetic fields. At moderate frequency, the magnetic field triggers a resonance for the spectrum with heavy quarks when the photons move perpendicular to the magnetic field. The resonance becomes more robust when the photons are polarized along the magnetic field. However, the pressure anisotropy leads to a competing effect and suppresses the resonance. However, we conclude that the suppression may not be applicable to the QGP produced in heavy ion collisions since the direction of pressure anisotropy in the MT geometry is distinct from that in heavy ion collisions. On the other hand, we have computed the elliptic flow  $v_2$  of thermal photons in a strongly coupled plasma with a constant magnetic field. Our result is qualitatively consistent with the direct-photon  $v_2$  measured in RHIC at intermediate energy. Nevertheless, due to the simplified setup, the thermal-photon  $v_2$  in our model should be regarded as the upper bound for the  $v_2$  generated by solely the magnetic field in the strongly coupled scenario.

## Holographic Chiral Electric Separation Effect

The work in this chapter was first published in [133]. As discussed in Section 1.4, the anomalous effects led by electromagnetic fields in heavy ion collisions have been emphasized in recent years. There have been extensive studies in holography to address the issues related to magnetic fields in strongly coupled plasmas. The CME has been investigated in distinct thermalized backgrounds[185, 186, 187, 188, 189, 190, 191]. In the original paper of CMW[110], the propagating dispersion relation was studied in the Sakai-Sugimoto(SS) model[15, 192]. In a recent study in [193], the CME and CMW have been further investigated in out-of-equilibrium conditions. Nevertheless, the existence of CME in SS model is somewhat controversial[186, 185, 188, 194]. The Chern-Simons(CS) term therein is crucial to generate an axial current caused by a magnetic field, while it gives rise to an anomalous vector current. In order to make the theory invariant under electromagnetic gauge transformations, the Bardeen counterterm has to be introduced on the boundary, which turns out to cancel the vector current and wipe out CME in the system[186]. It was argued that the recipe to preserve both the gauge invariance and vector current is to allow

the non-regular bulk solutions, where the background gauge fields responsible for chemical potentials become non-vanishing on the horizon[188, 194]. Unlike many effects led by magnetic fields, CESE has not been analyzed in the strongly coupled scenario. As a result, we investigate the CESE in the framework of SS model in the presence of both vector and axial chemical potentials. Since axial anomaly is irrelevant to CESE, the problem with the CS term for CME does not exist in our approach.

This chapter is organized in the following order. In Section 6.1, we discuss the axial electric conductivity, where we make a simple estimate for it based on the power counting with small chemical potentials. In Section 6.2, we briefly review the SS model. In order to compute both the normal and axial conductivities in the SS model in the presence of small vector and axial chemical potentials we will perform the background-field expansion to identify the origin of CESE in the effective action in Section 6.3 and present the results in Section 6.4. In Section 6.5, we then solve the full DBI action to evaluate both conductivities for arbitrary chemical potentials. Finally, we make discussions in the last section.

## 6.1 Interpretation of Chiral Electric Conductivity

In a hot and dense system with massless chiral fermions, we can define two currents,  $\mathbf{J}_R$  and  $\mathbf{J}_L$  with respect to left and right handed fermions. For simplicity, we neglect the chiral anomaly in our discussion. In the presence of an external electric field  $\mathbf{E}$ , the left and right handed fermions will be dragged by the electric force and two charge currents will be induced,

$$\mathbf{J}_R = \sigma_R e \mathbf{E}, \quad \mathbf{J}_L = \sigma_L e \mathbf{E}, \quad (6.1)$$

where  $e$  is the charge of fermions,  $\sigma_{R/L}$  denotes the left/right handed conductivity as a function of  $\mu_{R/L}$  and temperature  $T$ , with

$$\mu_{R/L} = \mu_V \pm \mu_A, \quad (6.2)$$

the chemical potential of right/left handed fermions. On the other hand, it is straightforward to describe this system by two other currents, the vector and axial vector currents,

$$\mathbf{J}_V = \frac{1}{2}(\mathbf{J}_R + \mathbf{J}_L) = \sigma_V e \mathbf{E}, \quad (6.3)$$

$$\mathbf{J}_a = \frac{1}{2}(\mathbf{J}_R - \mathbf{J}_L) = \sigma_5 e \mathbf{E}, \quad (6.4)$$

where we can read from (6.1) that the normal and chiral electric conductivities are given by,

$$\begin{aligned} \sigma_V &= \frac{1}{2}(\sigma_R + \sigma_L), \\ \sigma_5 &= \frac{1}{2}(\sigma_R - \sigma_L). \end{aligned} \quad (6.5)$$

Here we find the chiral electric conductivity  $\sigma_5$  is induced by the interactions of fermions and can exist without chiral anomaly. Also, given that  $\mu_R \neq \mu_L$  corresponding to  $\sigma_R \neq \sigma_L$ , the CESE should exist for arbitrary values of the chemical potentials.

Now let us discuss the property of this new transport coefficient. Taking the parity transform to (6.4), since left and right handed fermions will exchange with each other, we get,

$$\sigma_5(\mathbf{x}) = -\sigma_5(-\mathbf{x}), \quad (6.6)$$

which implies it is a pseudo scalar. In the macroscopic scaling, there is only a pseudo scalar in our system,  $\mu_A$ . Therefore, in a small  $\mu_A$  case, we can assume,  $\sigma_5 \propto \mu_A$ .

Since we neglect the chiral anomaly, the system has a  $U(1)_L \times U(1)_R$  symmetry. We can take the charge conjugate transformation  $e \rightarrow -e$ ,  $\mu_{R/L} \rightarrow -\mu_{R/L}$  to the left and right handed currents (6.1) independently. Because  $\mathbf{E}$  as an external field does not change the sign, and the  $\mathbf{J}_{R/L}$  as charge currents will give minus signs, finally we find  $\sigma_{R/L}(\mu_{R/L}) = \sigma_{R/L}(-\mu_{R/L})$ . In the small  $\mu_{R/L}$  limit, we can get  $\sigma_{R/L} = C_{1,R/L} + C_{2,R/L}\mu_R^2 + C_{3,R/L}\mu_L^2$ , with  $C_i$  as functions of  $T$ . On the other hand, because the system is invariant under the chiral transformation, we get  $C_{1,R} = C_{1,L}$ ,  $C_{2,R} = C_{3,L}$ , and  $C_{2,L} = C_{3,R}$ . Inserting these relations into (6.5) yields

$$\sigma_5 = \chi_e \mu_A \mu_V, \quad (6.7)$$

where  $\chi_e$  is a function of  $T$ . This relation is also assumed in Ref. [124].

Next, we discuss a special system where different chirality particles will not interact with each other, i.e. right handed particles will only interact with right handed particles, so do the left handed particles. Therefore, we can assume  $\sigma_{R/L} = \sigma_{R/L}(T; \mu_{R/L})$ . On the other hand, for chiral fermions without chiral anomaly, the system will be invariant under the chiral transformation, i.e. one can exchange the left and right handed fermions and the system is invariant. In this case, we can rewrite  $\sigma_{R/L}$  as,

$$\sigma_{R/L} = \sigma(T; \mu_{R/L}), \quad (6.8)$$

where  $\sigma$  is just a normal conductivity. Then, we get, in small  $\mu_A$  cases,

$$\begin{aligned} \sigma_V &= \frac{1}{2}(\sigma_R + \sigma_L) = \sigma(T, \mu_V) + \frac{1}{2} \frac{\partial^2 \sigma(T, \mu_V)}{\partial \mu_V^2} \mu_A^2 + O(\mu_A^3), \\ \sigma_5 &= \frac{1}{2}(\sigma_R + \sigma_L) = \frac{\partial \sigma(T, \mu_V)}{\partial \mu_V} \mu_A + O(\mu_A^3), \end{aligned}$$

or

$$\sigma_5(T, \mu_V, \mu_A) = \mu_A \partial_{\mu_V} \sigma_V(T, \mu_V), \quad \mu_A \rightarrow 0. \quad (6.9)$$

Later, we will show this behavior in our framework.

Besides [124], this effect is also suggested in other weakly coupled systems. Roughly speaking, different chiralities are quite similar to different flavors in a weakly coupled hot QCD plasma. The flavor non-singlet currents correspond to the axial currents here. It is shown that the conductivities of such flavor non-singlet currents is nonzero and can be quite large in the case of large  $\mu/T$  [195].

## 6.2 Basics of Sakai-Sugimoto model

In order to describe a strongly coupled chiral plasma, we have to introduce the chiral symmetry in the gravity theory, while the chiral symmetry is not manifest in the D3/D7 system. We thus introduce an alternative system incorporating fundamental matter with chiral symmetry in the gauge/gravity duality proposed by Sakai and Sugimoto(SS)[15, 192]. The SS model stems from the embeddings of  $N_f$   $D8$  branes and  $N_f$   $\overline{D8}$  branes in the background dictated by  $N_c$   $D4$  branes. The schematic description of the embeddings is illustrated in Fig.6.1, where the  $x^4$  direction is compactified on an  $S^1$ . The compactification yields a Kaluza-Klein mass  $M_{KK}$  and breaks supersymmetry. In vacuum, the solution of the D4 branes in Poincare coordinates reads

$$ds^2 = \left(\frac{U}{L}\right)^{3/2} \left(- (dx^0)^2 + (dx^i)^2 + f(U) dx_4^2\right) + \left(\frac{L}{U}\right)^{3/2} \left(\frac{dU^2}{f(U)} + U^2 d\Omega_4^2\right),$$

$$f(U) = 1 - \frac{U_{KK}^3}{U^3}, \quad U_{KK} = \frac{4}{9} L^3 M_{KK}^2, \quad (6.10)$$

where  $L$  is the AdS radius. Note that the periodic boundary condition is imposed along  $x^4$ , which results in  $M_{KK}$  to avoid the conical singularity at  $U = U_{KK}$ . The IR wall at  $U = U_{KK}$  implies that the dual gauge theory is confining. The embedded  $D8$  branes and  $\overline{D8}$  branes are separated along the  $x^4$  direction on the boundary, while they should coincide with each other in the bulk at  $U = U_0 \geq U_{KK}$  as depicted in Fig.6.2a. In this scenario, the chiral symmetry is spontaneously broken. At finite

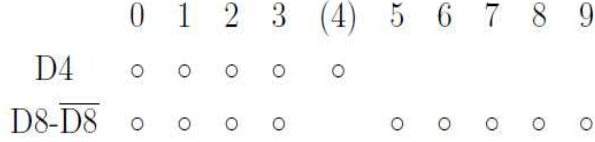


FIGURE 6.1: The schematic description of the embeddings in the SS model[15].

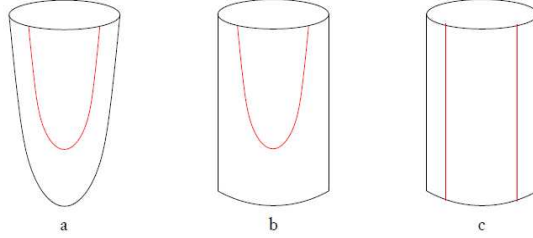


FIGURE 6.2: D8-brane embeddings in the Sakai-Sugimoto model[16]:(a)chiral symmetry breaking in vacuum (b)chiral symmetry breaking in the plasma (c)chiral symmetry restored in the plasma. Here the black circles on top represent the compactified  $x^4$  on  $S^1$  and the red curves represent the  $D8$  branes and  $\overline{D8}$  branes in the bulk.

temperature, an alternative solution becomes dominant, where the metric is given by[196]

$$ds^2 = \left(\frac{U}{L}\right)^{3/2} \left(-f(U)(dx^0)^2 + (dx^i)^2 + dx_4^2\right) + \left(\frac{L}{U}\right)^{3/2} \left(\frac{dU^2}{f(U)} + U^2 d\Omega_4^2\right),$$

$$f(U) = 1 - \frac{U_T^3}{U^3}, \tag{6.11}$$

where  $U_T$  is the position of the event horizon of a black hole in the bulk. Now, the embedded  $D8$  branes and  $\overline{D8}$  branes can be either connected as shown in Fig.6.2b or disconnected as shown in Fig.6.2c. In the connected case, the chiral symmetry is still broken, whereas the chiral symmetry is restored in the disconnected case.

For our purpose, we consider the SS model with an  $U(1)_L$  symmetry assigned to  $D8$  and an  $U(1)_R$  symmetry assigned to  $\overline{D8}$ ,

$$S_{tot} = S_{D8}(A_L) + S_{\overline{D8}}(A_R), \tag{6.12}$$

where  $A_{L/R}$  represent the background gauge fields contributing to the chemical potentials in  $L/R$  sectors. The background geometry in Eddington-Finkelstein(EF) coordinates with a black hole solution reads

$$ds^2 = \left(\frac{U}{L}\right)^{3/2} (-f(U)dt^2 + (dx^i)^2) + 2dUdt + \left(\frac{L}{U}\right)^{3/2} U^2 d\Omega_4^2 + \left(\frac{U}{L}\right)^{3/2} \frac{dx_4^2}{(M_{KK}l_s)^2}, \quad L^3 = \pi g_s N_c l_s^3, \quad f(U) = 1 - \left(\frac{U_T}{U}\right)^3, \quad (6.13)$$

where  $g_s = g_{YM}^2 (2\pi M_{KK} l_s)^{-1}$  is the string coupling and  $l_s$  is the typical string length. The  $D8/\overline{D8}$  branes now span the coordinates  $(U, t, x^i, \Omega_4)$ . Note that we use  $t$  to denote the EF time in this chapter. We will only consider the deconfined phase, where the temperature is determined by  $U_T$  via

$$T = \frac{3}{4\pi} \left(\frac{U_T}{L^3}\right)^{1/2}. \quad (6.14)$$

Note we also work in the chiral symmetry restored phase, where  $\partial_U x_4 = 0$ . The reduced 5-dimensional action of  $D8/\overline{D8}$  branes is given by[185]

$$S_{D8/\overline{D8}} = -CL^{9/4} \int d^4x dU U^{1/4} \sqrt{\det(g_{5d} + 2\pi l_s^2 F_{L/R})} \mp \frac{N_c}{96\pi^2} \int d^4x dU \epsilon^{MNPQR} (A_{L/R})_M (F_{L/R})_{NP} (F_{L/R})_{QR}, \quad (6.15)$$

where

$$C = N_c^{1/2} / (96\pi^{11/2} g_s^{1/2} l_s^{15/2}), \quad \sqrt{\det(g_{5d})} = (U/L)^{9/4}. \quad (6.16)$$

Here  $-(+)$  sign in front of the CS term corresponds to  $D8(\overline{D8})$  branes, while the CS term does not affect CESE and will be discarded in our computations. The chemical potentials dual to the boundary values of the time components of the background gauge fields are

$$\mu_{L/R} = \lim_{U \rightarrow \infty} (A_{L/R})_t. \quad (6.17)$$

Now, our strategy to compute the normal and axial conductivities will be the following: We firstly solve for the background gauge fields from the actions in (6.15) to acquire the chemical potentials in the  $R/L$  bases. Then we perturb the actions with electric fields to generate the  $R/L$  currents. Finally, by extracting the electric conductivities in the  $R/L$  sectors, we can evaluate the normal and axial conductivities directly from (6.5).

Since both the normal conductivity  $\sigma_V$  and the axial conductivity  $\sigma_5$  have to be evaluated numerically, we list the numerical values for all fixed parameters here for reference. By following the convention in [185], where the numerical values are chosen to fit the pion decay constant and  $\rho$  meson mass[192], we take

$$2\pi l_s^2 = 1\text{GeV}^{-2}, \quad \lambda = g_{YM}^2 N_c = 17, \quad M_{KK} = 0.94\text{GeV}, \quad (6.18)$$

which gives

$$L^3 = (2M_{KK})^{-1}(g_{YM}^2 N_c l_s^2) = 1.44\text{GeV}^3. \quad (6.19)$$

We further choose the temperature as the average temperature in RHIC,

$$T = 200\text{MeV} = 0.2\text{GeV}, \quad (6.20)$$

which yields, via (6.14),

$$U_T = 1.02\text{GeV}^{-1}. \quad (6.21)$$

### 6.3 Background-Field Expansion

In comparison with the weakly-coupled approach in [124], we should consider the case with small chemical potentials ( $\mu_{V(A)} \ll T$ ). The statement will be justified later in this section. Thus, we have to treat the background gauge fields responsible for the chemical potentials in the Dirac-Born-Infeld(DBI) actions in (6.15) perturbatively.

Now, by expanding the DBI actions up to quartic terms of the background gauge fields, we find

$$\begin{aligned}
S_{D8/\bar{D}8} &= -C \int d^4x dU U^{5/2} \left( 1 + \frac{1}{4} \tilde{F}_{MN} \tilde{F}^{MN} - \frac{1}{32} (\tilde{F}_{MN} \tilde{F}^{MN})^2 \right) \\
&\mp \frac{N_c}{96\pi^2} \int d^4x dU \epsilon^{MNPQK} A_M F_{NP} F_{QK},
\end{aligned} \tag{6.22}$$

where  $\tilde{F} = 2\pi l_s^2 F$  and we omit the  $L/R$  symbols above for simplicity. We then define the axial and vector gauge fields,

$$A_a = \frac{1}{2}(-A_L + A_R), \quad A_V = \frac{1}{2}(A_L + A_R). \tag{6.23}$$

By combining the contributions from  $D8$  and  $\bar{D}8$  branes together, the full action yields

$$\begin{aligned}
S_{tot} &= -C \int d^4x dU U^{5/2} \left( 1 + \frac{1}{2} (\tilde{F}_{aMN} \tilde{F}_a^{MN} + \tilde{F}_{VMN} \tilde{F}_V^{MN}) \right. \\
&\quad - \frac{1}{16} \left( (\tilde{F}_{aMN} \tilde{F}_a^{MN})^2 + (\tilde{F}_{VMN} \tilde{F}_V^{MN})^2 \right) - \frac{1}{8} \tilde{F}_{aMN} \tilde{F}_a^{MN} \tilde{F}_{VPQ} \tilde{F}_V^{PQ} \\
&\quad \left. - \frac{1}{4} (\tilde{F}_{aMN} \tilde{F}_V^{MN})^2 \right) \\
&\quad + \frac{N_c}{48} \int d^4x dU (A_a \wedge F_a \wedge F_a + A_a \wedge F_V \wedge F_V + 2A_V \wedge F_a \wedge F_V).
\end{aligned} \tag{6.24}$$

The action then leads to the field equations,

$$\begin{aligned}
\partial_M \left( U^{5/2} \left( 2F_V^{MN} - \frac{1}{2} F_V^{MN} F_{VPQ} F_V^{PQ} - \frac{1}{2} F_V^{MN} F_{aPQ} F_a^{PQ} - F_a^{MN} F_{aPQ} F_V^{PQ} \right) \right) &= 0, \\
\partial_M \left( U^{5/2} \left( 2F_a^{MN} - \frac{1}{2} F_a^{MN} F_{aPQ} F_a^{PQ} - \frac{1}{2} F_a^{MN} F_{VPQ} F_V^{PQ} - F_V^{MN} F_{VPQ} F_a^{PQ} \right) \right) &= 0.
\end{aligned}$$

Recall that the time components of the background gauge fields should contribute to chemical potentials. We may set other components of the background gauge fields

to zero. In practice, it is more convenient to solve the field equations above by reshuffling them into the  $L/R$  bases or directly minimize the  $D8$  and  $\overline{D8}$  actions, where the right-handed and left-handed fields are decoupled. In the  $L/R$  bases, the equations of motions then become

$$\partial_M \left( U^{5/2} \left( \tilde{F}_{(L/R)}^{MN} - \frac{1}{4} \tilde{F}_{(L/R)}^{MN} \tilde{F}_{(L/R)PQ} \tilde{F}_{(L/R)}^{PQ} \right) \right) = 0. \quad (6.25)$$

Since we only have to solve  $A_t(U)$ , the equations of motion reduce to just one equation,

$$\partial_U \left( U^{5/2} \left( \tilde{F}_{(L/R)Ut} + \frac{1}{2} \tilde{F}_{(L/R)Ut}^3 \right) \right) = 0, \quad (6.26)$$

The equation of motion now yields three solutions,

$$\begin{aligned} \tilde{F}_{(L/R)Ut} = & \frac{-2 \times 3^{2/3} + 3^{1/3} \left( 9y + \sqrt{24 + 81y^2} \right)^{2/3}}{3 \left( 9y + \sqrt{24 + 81y^2} \right)^{1/3}}, \\ & \frac{1 \pm i\sqrt{3}}{3^{1/3} \left( 9y + \sqrt{24 + 81y^2} \right)^{1/3}} + \frac{i \left( i \pm \sqrt{3} \right) \left( 9y + \sqrt{24 + 81y^2} \right)^{1/3}}{2 \times 3^{2/3}}, \end{aligned} \quad (6.27)$$

where

$$y = \gamma_{L/R} U^{-5/2} \quad (6.28)$$

is a dimensionless parameter for  $\gamma_{L/R}$  being the integration constants. Near the boundary  $y \rightarrow 0$ , the three solutions reduce to  $y$ ,  $\pm i\sqrt{2}$ . Given that the first solution is normalizable on the boundary, we may choose it as the physical solution. Also, the first solution is always real with an arbitrary value of  $y$ . As we make the transformation  $\gamma_{L/R} \rightarrow -\gamma_{L/R}$ , we find  $\tilde{F}_{(L/R)Ut} \rightarrow -\tilde{F}_{(L/R)Ut}$ , where the negative  $\gamma_{L/R}$  will contribute to negative chemical potentials. Notice that the validity of the

background-field expansion from the DBI action requires  $\tilde{F}_{(L/R)Ut} \ll 1$  at arbitrary  $U$ . Since the region below the horizon  $U = U_T$  is causally disconnected and the physical solution monotonic increases with respect to  $y$ , the maximum of  $\tilde{F}_{(L/R)Ut}$  locates on the horizon. From (6.27), we find a critical value  $y_c = 1.5$  such that  $\tilde{F}_{(L/R)Ut}(y = y_c) = 1$ , which implies the valid integration constants  $\gamma_{L/R}$  should satisfy  $\gamma_{L/R} \ll y_c U_T^{5/2}$ . After obtaining the background-field strength, we subsequently compute the chemical potentials by choosing the radial gauge  $A_{(L/R)U} = 0$  without loss of generality. The chemical potentials in the  $L/R$  bases are given by

$$\begin{aligned} \mu_{(L/R)} &= A_{(L/R)t}(U = \infty) = \frac{1}{5\pi l_s^2} \gamma_{(L/R)}^{\frac{2}{5}} \tilde{\mu}(y_{(R/L)T}), \\ \tilde{\mu}(y_{(L/R)T}) &= \int_0^{y_{(L/R)T}} \frac{dy}{y^{7/5}} \left( \frac{-2 \times 3^{2/3} + 3^{1/3} \left(9y + \sqrt{24 + 81y^2}\right)^{2/3}}{3 \left(9y + \sqrt{24 + 81y^2}\right)^{1/3}} \right), \end{aligned} \quad (6.29)$$

where  $y_{(L/R)T} = \gamma_{L/R} U_T^{-5/2}$ . We may now input the numerical values for relevant coefficients to examine the validity of the background-field expansion in the limit of small chemical potentials ( $\mu_{(L/R)} \ll T$ ). We firstly rescale the chemical potentials by temperature as

$$\frac{\mu_{(L/R)}}{T} = \frac{TR^3}{5\pi l_s^2} \left(\frac{4\pi}{3}\right)^2 y_{(L/R)T}^{\frac{2}{5}} \tilde{\mu}(y_{(L/R)T}). \quad (6.30)$$

By taking  $y_{(L/R)T} = y_c = 1.5$  with the numerical values of all parameters from (6.18) to (6.21), we obtain the ratio to the critical chemical potential and temperature, which reads

$$\frac{\mu_c}{T} = \frac{\mu_{(L/R)}(y_{(L/R)T} = y_c)}{T} \approx 4.51. \quad (6.31)$$

In our setup, it turns out that the small chemical potentials ( $\mu_{(L/R)} \ll T$ ) correspond to  $\tilde{F}_{(R/L)Ut} \ll 1$ , which supports the background-field expansion. Moreover, the

expansion is even valid for intermediate chemical potentials ( $\mu_{L/R} \sim T$ ). Recall that the constraint for the integration constants  $\gamma_{L/R}$  now becomes  $\gamma_{L/R} \ll y_c U_T^{5/2} \approx 4.51 \text{ GeV}^{-5/2}$ .

## 6.4 DC and AC Conductivities for Small Chemical Potentials

Subsequently, by further fluctuating the full action in (6.24) with gauge fields,

$$(A_{L(R)})_\mu \rightarrow (A_{L(R)})_\mu + (a_{L(R)})_\mu, \quad (6.32)$$

the expansion up to the quadratic terms of the fluctuations can be written as

$$\begin{aligned} S_{tot}^{(2)} = & -C \int d^4x dU U^{5/2} \left[ \frac{1}{2}(\tilde{f}_V^2 + \tilde{f}_a^2) - \frac{1}{8}(\tilde{f}_V^2 \tilde{F}_V^2 + \tilde{f}_a^2 \tilde{F}_a^2 + \tilde{F}_V^2 \tilde{f}_a^2 + \tilde{F}_a^2 \tilde{f}_V^2) \right. \\ & - \frac{1}{2}(\tilde{f}_V \cdot \tilde{F}_V)(\tilde{f}_a \cdot \tilde{F}_a) - \frac{1}{2}(\tilde{f}_V \cdot \tilde{f}_a)(\tilde{F}_V \cdot \tilde{F}_a) - \frac{1}{2}(\tilde{f}_V \cdot \tilde{F}_a)(\tilde{f}_a \cdot \tilde{F}_V) \\ & \left. - \frac{1}{4} \left( (\tilde{f}_V \cdot \tilde{F}_V)^2 + (\tilde{f}_a \cdot \tilde{F}_a)^2 + (\tilde{f}_V \cdot \tilde{F}_a)^2 + (\tilde{f}_a \cdot \tilde{F}_V)^2 \right) \right] \\ & + \frac{N_c}{16} \int d^4x dU (A_a \wedge f_a \wedge f_a + A_a \wedge f_V \wedge f_V + 2A_V \wedge f_a \wedge f_V), \end{aligned}$$

where

$$\begin{aligned} \tilde{F}^2(\tilde{f}^2) &= \tilde{F}_{MN} \tilde{F}^{MN} (\tilde{f}_{MN} \tilde{f}^{MN}), \\ \tilde{f} \cdot \tilde{F}(\tilde{f} \cdot \tilde{f} \text{ or } \tilde{F} \cdot \tilde{F}) &= \tilde{f}_{MN} \tilde{F}^{MN} (\tilde{f}_{MN} \tilde{f}^{MN} \text{ or } \tilde{F}_{MN} \tilde{F}^{MN}), \\ f_{ij} &= \partial_i a_j - \partial_j a_i, \quad \tilde{F}(\tilde{f}) = 2\pi l_s^2 F(f). \end{aligned} \quad (6.33)$$

Since only the time components of the gauge fields  $A_{V(a)t}(U)$  are nonzero, we have

$$F_{V(a)}^2 = -2(\partial_U A_{V(a)t})^2, \quad F_{VMN} F_a^{MN} = -2\partial_U A_{Vt} \partial_U A_{at}. \quad (6.34)$$

We see that the cross terms of the vector and axial fluctuations may generate an axial current proportional to the product of a vector chemical potential and an axial

chemical potential in the presence of an electric field similar to the case in [124]. Nevertheless, since  $\tilde{F}_{V(a)} \sim U^{-5/2}$  on the boundary as shown in (6.28), all these cross terms actually vanish on the boundary. On the other hand, the cross terms still give rise to the modifications of equations of motion in the bulk. It turns out that the derivatives of the vector fluctuation  $a_V$  with respect to  $U$  can depend on the axial fluctuation  $a_a$  and vice versa due to the mixing of the vector and axial gauge fields in the equations of motion in the presence of both the vector and axial chemical potentials. It is thus more convenient to work out conductivities of the vector and axial currents in the  $L/R$  bases, where the left handed and right handed sectors are decoupled.

Now, we should compute  $\sigma_{R(L)}$  in the  $L/R$  bases. The relevant terms in the  $D8/\overline{D8}$  actions in the  $L/R$  bases read

$$S_{D8/\overline{D8}}^{(2)} = -C \int d^4x dU U^{5/2} \left( \frac{1}{4} \tilde{f}^2 - \frac{1}{8} (\tilde{f} \cdot \tilde{F})^2 - \frac{1}{16} \tilde{f}^2 \tilde{F}^2 \right)_{L/R}, \quad (6.35)$$

where we drop the CS term here since it is irrelevant to CESE. The actions then lead to decoupled equations of motion,

$$\partial_M \left( U^{5/2} \left( \tilde{f}^{MN} - \frac{1}{2} \tilde{F}^{MN} \tilde{F} \cdot \tilde{f} - \frac{1}{4} \tilde{f}^{MN} \tilde{F}^2 \right) \right)_{L/R} = 0. \quad (6.36)$$

Although we start in EF coordinates, it is more convenient to work in Poincare coordinates to handle the holographic renormalization as we evaluate the currents. In Poincare coordinates, the  $AdS_5$  part of the metric is rewritten as

$$ds_{5d}^2 = \left( \frac{U}{L} \right)^{3/2} (-f(U)(dx^0)^2 + (dx^i)^2) + \left( \frac{L}{U} \right)^{3/2} \frac{dU^2}{f(U)}, \quad (6.37)$$

where  $x^0$  denotes the Poincare time. In fact, all equations previously shown in this section without explicitly specifying the spacetime indices can be applied to both

EF coordinates and Poincare coordinates, which relies on the same  $\sqrt{\det(g_{5d})} = (U/R)^{9/4}$  in two coordinates. One can actually show that  $A_t(U) = A_0(U)$  for  $A_U = 0$ . We will consider only the electric fluctuation  $eE_3 = f_{03}$  along the  $x^3$  direction and further choose the temporal gauge  $a_0 = 0$  without loss of generality. By choosing such a gauge, the  $\tilde{f} \cdot \tilde{F}$  terms in the actions and equations of motion above should vanish. We then make an ansatz for the fluctuation as

$$a_3(U, x^0) = e^{-i\omega x^0} a_3(U, \omega). \quad (6.38)$$

Hereafter the shorthand notation  $a_3$  denotes  $a_3(U, \omega)$ . The  $D8/\overline{D8}$  actions now become

$$S_{D8/\overline{D8}}^{(2)} = -\frac{C}{2}(2\pi l_s^2)^2 \int d^4x dU U^{5/2} \left( \left( f(U) |\partial_U a_3|^2 - \left(\frac{L}{U}\right)^3 \frac{\omega^2}{f(U)} |a_3|^2 \right) \left( 1 + \frac{1}{2} \tilde{F}_{U0}^2 \right)_{L/R} \right). \quad (6.39)$$

Also, we obtain a single equation of motion,

$$\begin{aligned} C(U) \partial_U^2 a_3 + B(U) \partial_U a_3 + D(U) a_3(U) &= 0, \quad \text{for} \\ C(U) &= f(U) U^{5/2} \left( 1 + \frac{1}{2} \tilde{F}_{U0}^2 \right), \\ B(U) &= \partial_U \left( U^{5/2} f(U) \left( 1 + \frac{1}{2} \tilde{F}_{U0}^2 \right) \right), \\ D(U) &= U^{5/2} \left(\frac{L}{U}\right)^3 \frac{\omega^2}{f(U)} \left( 1 + \frac{1}{2} \tilde{F}_{U0}^2 \right). \end{aligned} \quad (6.40)$$

The near-boundary solution then takes the form

$$a_3(U)|_{U \rightarrow \infty} = a_3^{(0)} + \frac{a_3^{(1)}}{U} + \frac{b_3^{(0)}}{U^{3/2}} + \frac{a_3^{(2)}}{U^2} + \frac{b_3^{(1)}}{U^{5/2}} \dots, \quad (6.41)$$

where all higher-order coefficients  $a_3^{(n)}$  and  $b_3^{(n)}$  depend on  $a_3^{(0)}$  and  $b_3^{(0)}$ , respectively. The two independent coefficients  $a_3^{(0)}$  and  $b_3^{(0)}$  will be determined by the incoming-wave boundary conditions near the horizon as we numerically solve the equations of motion in (6.40).

Before proceeding to the evaluation of (6.40), we should handle the UV divergence for the  $D8/\overline{D8}$  actions on the boundary at  $U_0 \rightarrow \infty$ . After removing the divergence by subtracting proper counterterms, the renormalized actions become

$$\left(S_{D8/\overline{D8}}^{(2)}\right)_{\text{ren}} = C(2\pi l_s^2)^2 \int d^4x \left( \frac{3}{2} a_3^{(0)*} b_3^{(0)} + \mathcal{O}(U_0^{-1/2}) \right)_{L/R}, \quad (6.42)$$

which give rise to the  $L/R$  currents

$$(j_3)_{L/R} = \frac{3C}{2} (2\pi l_s^2)^2 b_3^{(0)}|_{L/R} = 2C(2\pi l_s^2)^2 \lim_{U \rightarrow \infty} \left( U^{\frac{3}{2}} (U^2 \partial_U^2 a_3 + 2U \partial_U a_3) \right)_{L/R}. \quad (6.43)$$

The similar treatment to the divergence at the boundary can be found in [171]. Now, to solve (6.40) numerically, we have to impose the incoming-wave boundary conditions at the horizon by setting

$$a(U)_{L/R} = \left( 1 - \left( \frac{U_T}{U} \right) \right)^{-i\frac{\hat{\omega}}{4}} a_T(U)_{L/R} \quad (6.44)$$

for  $\hat{\omega} = \omega/(\pi T)$ . One can show that  $\partial_U a_T(U)|_{U \rightarrow U_h} = a'_T(U_h)$  linearly depends on  $a_T(U_h)$  by expanding the equation of motion with the expression in (6.44) near the horizon, while the value of  $a_T(U_h)$  will not affect the computation of conductivities. The values of  $a_T(U_h)$  and  $a'_T(U_h)$  from the expression in (6.44) then provide the proper boundary conditions for the equation of motion. By using the AdS/CFT

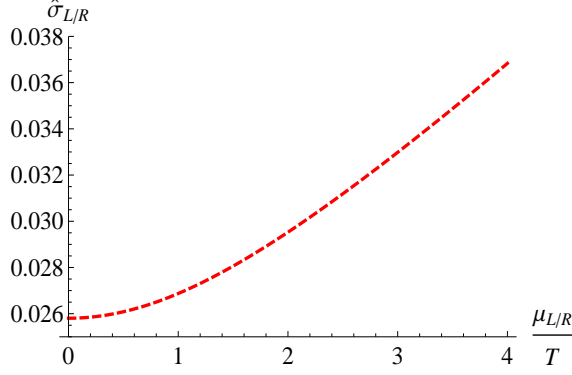


FIGURE 6.3: The DC conductivities in the  $L/R$  bases versus the chemical potentials scaled by temperature.

prescription, the spectral densities from (6.43) are

$$\begin{aligned}
\chi_{L/R}(\omega) &= \text{Im} \frac{3C}{2} (2\pi l_s^2)^2 \left( \frac{b_3^{(0)}}{a_3^{(0)}} \right)_{L/R} \\
&= 2C(2\pi l_s^2)^2 U_T^{\frac{3}{2}} \text{Im} \lim_{\hat{U} \rightarrow \infty} \left( \hat{U}^{\frac{3}{2}} \frac{\hat{U}^2 \partial_{\hat{U}}^2 a_3 + 2\hat{U} \partial_{\hat{U}} a_3}{a_3} \right)_{L/R}, \quad (6.45)
\end{aligned}$$

where  $\hat{U} = U/U_T$  and  $8C\pi^2 l_s^4 U_T^{3/2} = 8N_c \lambda T^3 / (81M_{KK})$ . The zero-frequency limit of the spectral functions contribute to the DC conductivities as

$$\sigma_{L/R} = \lim_{\omega \rightarrow 0} \frac{\chi(\omega)_{L/R}}{\omega}. \quad (6.46)$$

Since the equations of motion and the currents for left handed and right handed sectors take the same form, we only have to compute one of them. By solving the equations of motion in (6.40) and employing the relation in (6.46), we obtain the DC conductivities in the  $L/R$  bases as shown in Fig.6.3, where the increase of chemical potentials leads to mild enhancement for the conductivities. Here we define a dimensionless quantity

$$\hat{\sigma}_i = 81\sigma_i / (8N_c \lambda T), \quad (6.47)$$

where  $i = R/L, V, 5$  and we will hereafter use this convention in the paper. Next, by converting the conductivities in the  $L/R$  bases into the  $V/a$  bases through (6.5), we derive both the normal conductivity  $\sigma_V$  and the axial one  $\sigma_5$ . Whereas the overall amplitudes of  $a_{3(L/R)}$  do not affect the conductivity, we will choose proper amplitudes such that  $E_{3L} = E_{3R} = E_3$  is the net electric field on the boundary. As shown in Fig.6.4, where we fix the vector chemical potential and vary the axial one, the normal conductivity and axial conductivity are slightly enhanced by the axial chemical potential. Similarly, as shown in Fig.6.5, both the normal and axial conductivities also temperately increase as we fix the axial chemical potential and increase the vector one.

In Fig.6.8, we plot the ratios to the axial conductivity and the product of the axial and vector chemical potentials. As shown in Fig.6.8 with the fixed vector chemical potentials, we find that the axial conductivity is approximately linear to  $\mu_A$  for small chemical potentials. One may further conclude that  $\sigma_5 \propto \mu_V \mu_A$  provided all curves in Fig.6.8 coincide. As we gradually reduce  $\mu_V$ , the ratios will converge to a single value, where the small deviations may come from higher-order corrections in powers of  $\mu_V \mu_A / T^2$  along with the errors stemming from the background-field expansions when  $\mu_{V/A}$  become larger. The ratios in Fig.6.8 as well correspond to the results by exchanging the values of  $\mu_V$  and of  $\mu_A$ , where the reason will be explained later. Thus, from Fig.6.8, we conclude that the axial conductivity is approximately proportional to the product of  $\mu_V$  and  $\mu_A$  for small chemical potentials as pointed out in [124]. Since only the  $\tilde{F}_{U0}^2$  terms are involved in the computations above, the  $L/R$  conductivities are independent of the signs of  $L/R$  chemical potentials. We may observe interesting symmetries for both  $\sigma_V$  and  $\sigma_5$ . Under the transformations ( $\mu_R \rightarrow \mu_R, \mu_L \rightarrow -\mu_L$ ) and ( $\mu_R \rightarrow -\mu_R, \mu_L \rightarrow \mu_L$ ), which correspond to the exchanges ( $\mu_V \rightarrow \mu_A, \mu_A \rightarrow \mu_V$ ) and ( $\mu_V \rightarrow -\mu_A, \mu_A \rightarrow -\mu_V$ ) respectively, both  $\sigma_V$  and  $\sigma_5$  remain unchanged; they are as well invariant under the transformation ( $\mu_R \rightarrow$

$-\mu_R, \mu_L \rightarrow -\mu_L$ ) corresponding to  $(\mu_V \rightarrow -\mu_V, \mu_A \rightarrow -\mu_A)$ . As proposed in [124], the leading-log order correction of the normal conductivity due to small chemical potentials is proportional to  $\mu_V^2 + \mu_A^2$  and the axial conductivity is proportional to  $\mu_V \mu_A$ , which preserve the symmetries above. In Fig.6.6 and Fig.6.7, we also show the agreement of the power-counting estimations in (6.9) and the numerical results with small chemical potentials.

We can further evaluate the AC conductivities for  $\omega \neq 0$  as the responses to a frequency-dependent electric field. The real part and imaginary part of the  $L/R$  conductivities should be obtained from

$$\begin{aligned} \text{Re}[\hat{\sigma}_{L/R}(\omega)] &= T^2 M_{KK}^{-1} \text{Im} \lim_{\hat{U} \rightarrow \infty} \left( \hat{U}^{\frac{3}{2}} \frac{\hat{U}^2 \partial_{\hat{U}}^2 a_3 + 2\hat{U} \partial_{\hat{U}} a_3}{\omega a_3} \right)_{L/R}, \\ \text{Im}[\hat{\sigma}_{L/R}(\omega)] &= -T^2 M_{KK}^{-1} \text{Re} \lim_{\hat{U} \rightarrow \infty} \left( \hat{U}^{\frac{3}{2}} \frac{\hat{U}^2 \partial_{\hat{U}}^2 a_3 + 2\hat{U} \partial_{\hat{U}} a_3}{\omega a_3} \right)_{L/R}. \end{aligned} \quad (6.48)$$

Their combinations then give rise to the normal and axial AC conductivities. In Fig.6.9, we illustrate the real part of the normal AC conductivity with different chemical potentials. It turns out that the corrections from small chemical potentials are almost negligible. Our primary interest will be the axial AC conductivity as shown in Fig.6.10 and Fig.6.11, where different values of the axial chemical potentials give rise to distinct amplitudes in oscillations. We find that the  $Re(\sigma_5)$  will be negative in some frequencies. This does not break the second law of thermodynamics as shown in Appendix C.1.

## 6.5 Arbitrary Chemical Potentials

For large chemical potentials, the expansion of background fields becomes invalid. We thus have to solve the full DBI action. By considering only the time component of the background gauge fields, the  $D8/\overline{D8}$  actions in Poincare coordinates take the

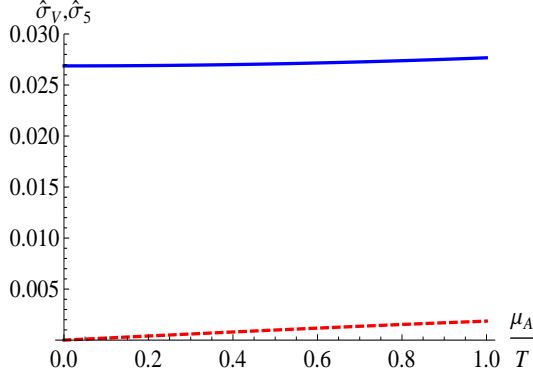


FIGURE 6.4: The blue and red(dashed) curves correspond to the normal DC conductivity and the axial one with  $\mu_V = T$ , respectively.

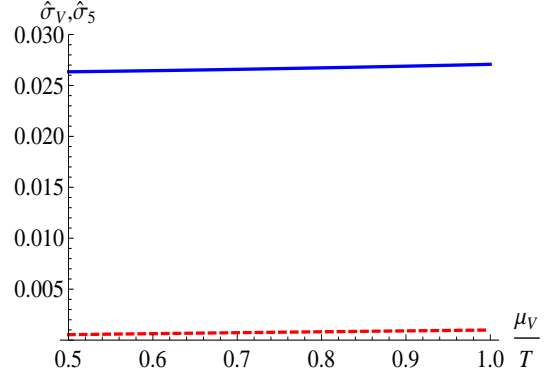


FIGURE 6.5: The blue and red(dashed) curves correspond to the normal DC conductivity and the axial one with  $\mu_A = 0.5T$ , respectively.

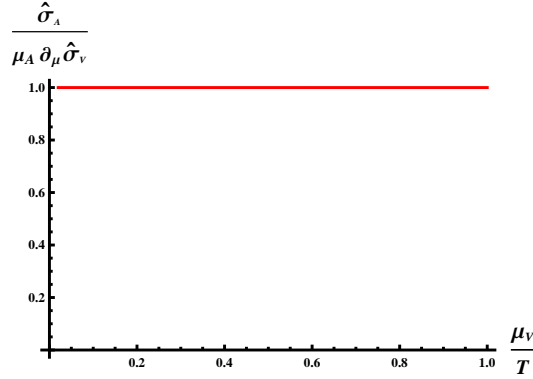


FIGURE 6.6: Power-counting estimation in (6.9) with  $\mu_A = 0.01T$ .

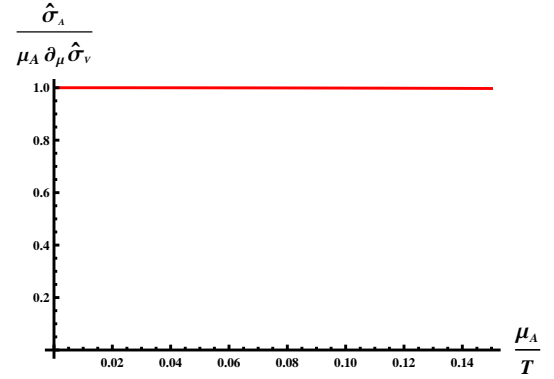


FIGURE 6.7: Power-counting estimation in (6.9) with  $\mu_V = 0.2T$ .

form

$$S_{D8/\overline{D8}} = -CL^{9/4} \int d^4x dU U^{5/2} \sqrt{1 - (2\pi l_s^2)^2 (F_{L/R})_{0U}^2}, \quad (6.49)$$

where the solutions read

$$(F_{R/L})_{0U} = \frac{\alpha_{R/L}}{\sqrt{U^5 + (2\pi l_s^2)^2 \alpha_{R/L}^2}} \quad (6.50)$$

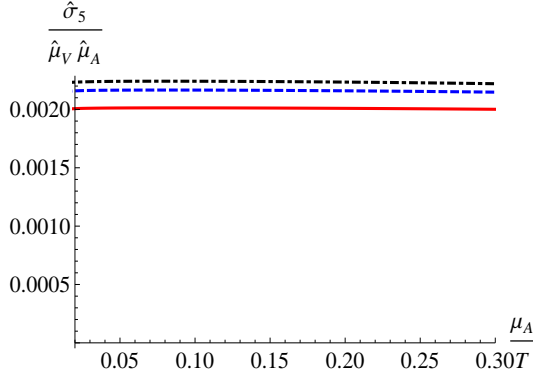


FIGURE 6.8: The red, blue(dashed), and black(dot-dashed) curves correspond to the cases with  $\mu_V = T$ ,  $0.6T$ , and  $0.3T$ . Here  $\hat{\mu}_{V/A} = \mu_{V/A}/T$ .

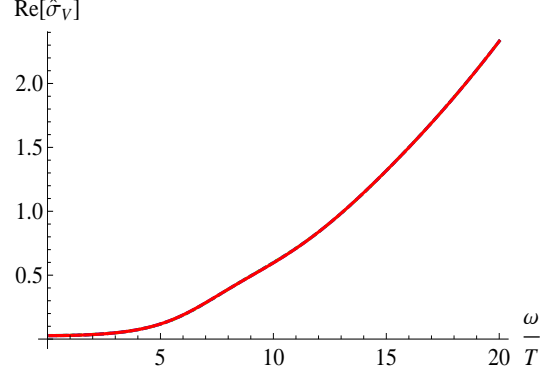


FIGURE 6.9: The red(solid), blue(dashed), and green(dotted) curves correspond to the real part of the normal AC conductivity with  $\mu_A = 0.2T$ ,  $0.5T$ , and  $0.9T$ , respectively. Here  $\mu_V = T$ .

with integration constants  $\alpha_{R/L}$ . In the absence of a vector chemical potential, we have  $\alpha_R = -\alpha_L$ . By requiring regularity at the horizon, we obtain

$$(A_{R/L})_0(U) = \int_{U_T}^U dU' \frac{\alpha_{R/L}}{2\sqrt{(U')^5 + (2\pi l_s^2)^2 \alpha_{R/L}^2}} \quad (6.51)$$

which result in the chemical potentials on the boundary

$$\mu_{R/L} = (A_{R/L})_0(U = \infty) = \frac{\alpha_{R/L}}{3U_T^{\frac{3}{2}}} {}_2F_1\left(\frac{3}{10}, \frac{1}{2}, \frac{13}{10}, -\frac{(2\pi l_s^2)^2 \alpha_{R/L}^2}{U_T^5}\right). \quad (6.52)$$

The result is the same as that found in EF coordinates[185].

Next, we should introduce the electric perturbation. By considering only the fluctuation  $a_3(U, x^0)$ , the computation is considerably simplified. Following the same setup in section III, one can show that the quadratic terms in the probe-brane actions in Poincare coordinates now become

$$S_{D8/\overline{D8}}^{(2)} = -C(2\pi l_s^2)^2 \int \frac{d^4 x dU U^{5/2}}{\sqrt{1 - \tilde{F}_{0U}^2}} \left( f(U) |\partial_U a_3|^2 - \left(\frac{L}{U}\right)^3 \frac{\omega^2}{f(U)} |a_3|^2 \right). \quad (6.53)$$

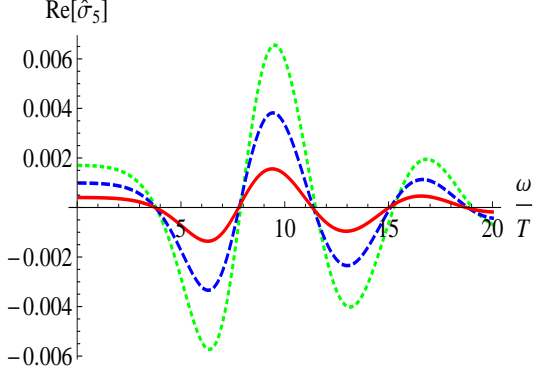


FIGURE 6.10: The red(solid), blue(dashed), and green(dotted) curves correspond to the real part of the axial AC conductivity with  $\mu_A = 0.2T$ ,  $0.5T$ , and  $0.9T$ , respectively. Here  $\mu_V = T$ .

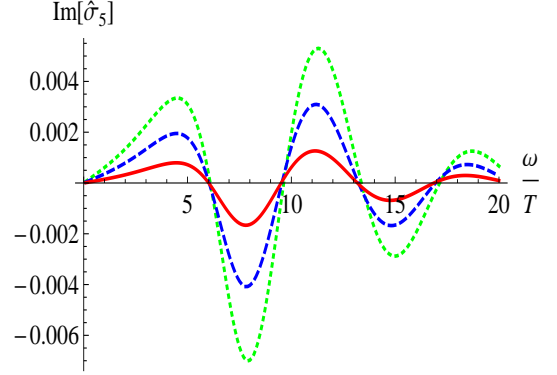


FIGURE 6.11: The red(solid), blue(dashed), and green(dotted) curves correspond to the imaginary part of the axial AC conductivity with  $\mu_A = 0.2T$ ,  $0.5T$ , and  $0.9T$ , respectively. Here  $\mu_V = T$ .

The equation of motion is given by

$$\begin{aligned}
 C_f(U)\partial_U^2 a_3 + B_f(U)\partial_U a_3 + D_f(U)a_3(U) &= 0, \quad \text{for} \\
 C_f(U) &= f(U)U^{5/2} \left(1 - \tilde{F}_{0U}^2\right)^{-1/2}, \\
 B_f(U) &= \partial_U \left( U^{5/2} f(U) \left(1 - \tilde{F}_{0U}^2\right)^{-1/2} \right), \\
 D_f(U) &= U^{5/2} \left( \frac{L}{U} \right)^3 \frac{\omega^2}{f(U)} \left(1 - \tilde{F}_{0U}^2\right)^{-1/2}, \tag{6.54}
 \end{aligned}$$

where the near-boundary solution takes the same form as (6.41). From (6.50), we find that  $(F_{R/L})_{0U} \rightarrow U^{-5/2}$  for  $U \rightarrow \infty$ , which do not contribute to the on-shell actions on the boundary. In fact, since  $(1 - \tilde{F}_{0U}^2)^{-1/2} \rightarrow 1 + \tilde{F}_{0U}^2/2$  on the boundary, the boundary action in (6.53) will be exactly the same as that in (6.39). We can then follow the same procedure to carry out the holographic renormalization and evaluate the conductivities, where the results are shown in Fig.6.12-Fig.6.18.

As shown in Fig.6.12, the result derived from solving the full DBI action and from the background-field expansion deviate when the chemical potentials are increased.

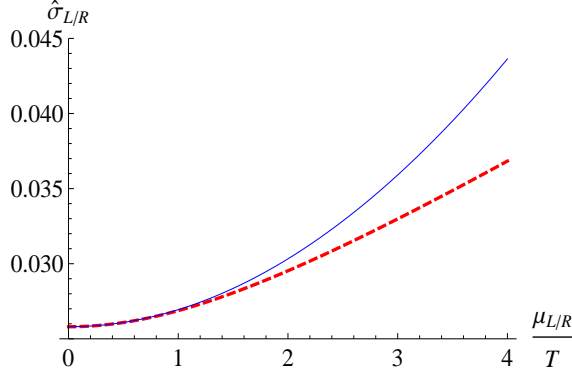


FIGURE 6.12: The DC conductivities in the  $L/R$  bases versus the chemical potentials scaled by temperature. The dashed red curve and solid blue curve correspond to the result from the background-field expansion and from solving the full DBI action, respectively.

Although we derive a critical chemical potential  $(\mu_c)_{L/R} \approx 4.51T$  in (6.31), the comparison of numerical results in Fig.6.12 may suggest that the background-field expansion is approximately valid for  $\mu_{L/R} < T$ . In Fig.6.13 and Fig.6.14, we present the DC normal and axial conductivities with a fixed vector chemical potential and with a fixed axial chemical potential, respectively. Compared to Fig.6.4 and Fig.6.5, the increase of conductivities with respect to the increase of chemical potentials become more pronounced for large chemical potentials.

Surprisingly, as shown in Fig.6.15, the relation  $\hat{\sigma}_5 \propto \mu_V \mu_A$  still holds even for the cases with large chemical potentials, where the expected higher-order corrections only result in negligible contributions. By comparing Fig.6.15 with Fig.6.8, we also find a small correction for the case with  $\mu = T$ . In Fig.6.16-Fig.6.18, we further illustrate the AC conductivities. As shown in Fig.6.16, the mild oscillatory behavior appears as we turn up the chemical potentials. From Fig.6.17 and Fig.6.18, we find that the increase of chemical potentials not only increases the amplitudes but also leads to phase shifts.

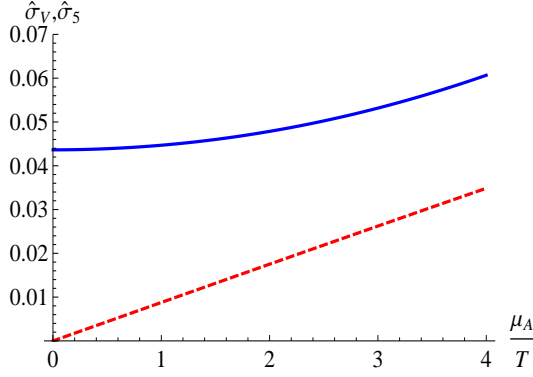


FIGURE 6.13: The blue and red(dashed) curves correspond to the normal DC conductivity and the axial one with  $\mu_V = 4T$ , respectively.

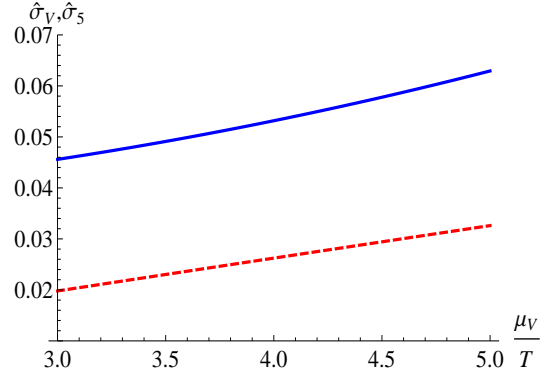


FIGURE 6.14: The blue and red(dashed) curves correspond to the normal DC conductivity and the axial one with  $\mu_A = 3T$ , respectively.

## 6.6 Discussions

In this chapter, we have shown that the CESE exists in the presence of both vector and axial chemical potentials for arbitrary magnitudes. In the framework of the SS model characterizing a strongly coupled chiral plasma, we have evaluated both the normal and axial DC conductivities induced by an electric field. Both conductivities are enhanced by the increase of chemical potentials. In addition, we have found that the axial conductivity is approximately proportional to the product of the vector and axial chemical potentials for arbitrary magnitudes. We have computed the AC conductivities led by a frequency-dependent electric field as well. The axial conductivity oscillates with respect to the frequency of the electric field, where the amplitude is increased and the phase is shifted when the chemical potentials are increased.

The observation in section 6.3 that the cross terms of the background gauge fields and fluctuating gauge fields result in an axial current from the equation of motion in the bulk may imply that CESE is due to the medium effect in a thermal background. In this paper, we only consider the case for  $\mu_V > \mu_A > 0$ , which corresponds to the

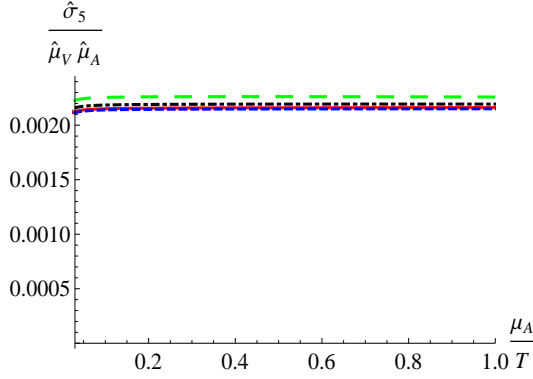


FIGURE 6.15: The red, blue(dashed), black(dot-dashed), and green(long-dashed) curves correspond to the cases with  $\mu_V = 10T, 8T, 4T$ , and  $T$ . Here  $\hat{\mu}_{V/A} = \mu_{V/A}/T$ .

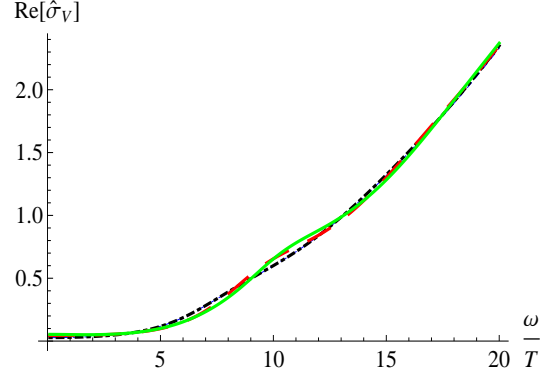


FIGURE 6.16: The Green(solid), red(long-dashed), and black(dot-dashed) curves correspond to the real part of the normal AC conductivity with  $(\mu_V, \mu_A) = (4T, 3T), (4T, T)$  and  $(T, 0.9T)$ . The blue(dashed) curve corresponds to the one with  $(\mu_V, \mu_A) = (T, 0.9T)$  from the background-field expansions.

system with more positive charged fermions than negative charged fermions and with more right handed fermions than left handed fermions. The axial current is generated parallel to the electric field, which is manifested by a positive axial conductivity. As discussed in the end of section 6.4, all results remain unchanged for the cases with  $\mu_A > \mu_V > 0$  or with  $\mu_V < 0$  and  $\mu_A < 0$  based on the symmetries under the transformations between  $\mu_V$  and  $\mu_A$ . Our approach can be easily applied to the cases for  $\mu_V > 0 > \mu_A$  or  $\mu_V < 0 < \mu_A$ . The most significant change is that the axial conductivities will become negative in such cases, which suggests that the axial currents will be engendered anti-parallel to the electric fields as mentioned in [124]. Given that  $\mu_V \mu_A < 0$  corresponding to  $\mu_L^2 > \mu_R^2$  along with the monotonic increase of  $\sigma_{R/L}$  by turning up  $\mu_{R/L}$ , we directly obtain  $\sigma_5 < 0$  by definitions in the cases with  $\mu_V > 0 > \mu_A$  or  $\mu_V < 0 < \mu_A$ . Notice that the normal conductivities will be always positive in all the cases since  $\sigma_{R/L} > 0$  for arbitrary values of the chemical potentials. The entropy principle for CESE is further discussed in the appendix.

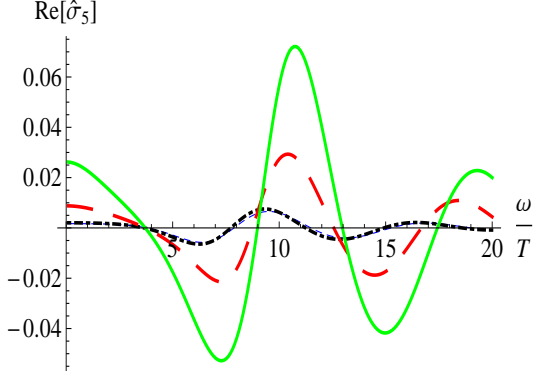


FIGURE 6.17: The real part of the axial AC conductivity with the colors corresponding to the same cases as Fig.6.16.

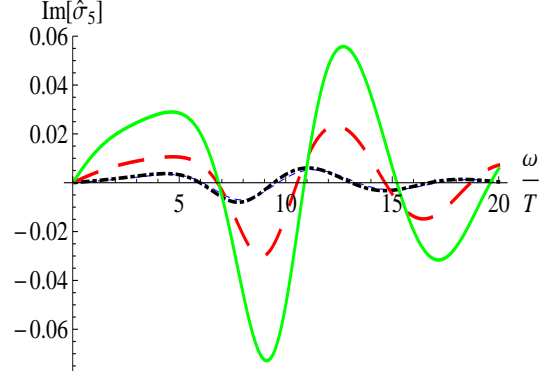


FIGURE 6.18: The imaginary part of the axial AC conductivity with the colors corresponding to the same cases as Fig.6.16.

Moreover, the most intriguing finding in our work is the relation  $\sigma_5 \propto \mu_V \mu_A$  for arbitrary chemical potentials. From the weakly coupled approach in [124], it is natural to anticipate such a relation as the leading-log order contribution for small chemical potentials. Nevertheless, with large chemical potentials, one may expect the relation would breakdown due to the higher-order corrections of  $\mu_V/T$  and  $\mu_A/T$ . It turns out that the influence from the higher-order corrections are negligible in the strongly coupled scenario at least in the setup of SS model. Since the axial conductivity here can only be computed numerically, it is difficult to find the origin of the suppression of the higher-order corrections. It would be thus interesting to study CESE in different holographic models such as the  $D3/D7$  system, where the axial chemical potential is incorporated via rotating flavor branes as discussed in [190], to explore the universality of this relation. On the other hand, we may as well conjecture that there exists nontrivial resummation which leads to the cancellation of higher-order corrections in the weakly coupled computations in QED(or QCD) for the axial conductivity. Also, the coupling dependence of the axial conductivity in the strongly coupled scenario is distinct from that derived in the weakly coupled approaches. In our model, we find  $\sigma_5 \propto g_{YM}^2 N_c^2$  from (6.28), while it is found in [124]

that  $\sigma_5 \propto 1/(e^3 \ln(1/e))$  in thermal QED.

From the phenomenological perspective as proposed in [124], the CESE along with CME can be possibly observed through the charge azimuthal asymmetry in heavy ion collisions. Whereas the chemical potential is small compared to the temperature in high-energy collisions[197], the CESE may be suppressed in such a case. However, since CESE could exist for arbitrary chemical potentials as shown in our model, the RHIC beam energy scan with lower collision energy[198], which can produce the plasma with the chemical potential comparable to the temperature, could be promising to measure such an effect. Although the chemical potentials can be drastically increased in the low-energy collisions, the collision energy can not be too low such that QGP in the deconfined phase is not formed after the collisions. Furthermore, due to the rapid depletion of the electric field with respect to time in heavy ion collisions[123], the CESE should be more robust in the pre-equilibrium phase. It is thus desirable to investigate CESE in the out-of-equilibrium conditions.

## Conclusions and Outlook

In this dissertation, we have addressed many important issues in heavy ion collisions through different models in the AdS/CFT correspondence. For jet quenching, we found that the thermalization of the medium is more influential for the probes with lower energy. On the other hand, despite the model dependence, our results for jet quenching and thermalization with nonzero chemical potentials could shed some light on the upcoming RHIC beam energy scan. In particular, the small thermalization times with larger chemical potentials found in our study may be tested by the hydrodynamical simulations for low-energy collisions. For pressure anisotropy, we found the competing effects on the critical mass between the magnetic field and pressure anisotropy close to the transition point, which is rather intriguing in theory. For the thermal-photon  $v_2$  enhanced by a magnetic field, our study was unable to confirm that the strong magnetic field is the dominant source for large elliptic flow of direct photons, while it has shown that the magnetic field can lead to sizable results in ideal conditions in the strongly coupled scenario. For CESE, it is striking that the axial conductivity for CESE is approximately proportional to the product of the vector chemical potential and the axial chemical potential for arbitrary magnitudes of

chemical potentials. Further studies of CESE in distinct holographic models will be thus worthwhile. To conclude this dissertation, we will discuss the future directions especially focused on the electromagnetic-field induced effects in strongly coupled gauge theories.

We may continue our study in CESE in Chapter 6. In order to further analyze the universality of the relation between the axial conductivity and chemical potentials, we will evaluate the axial conductivity in different holographic models. Although we mention that the D3/D7 system could be an intuitive choice, chiral symmetry is not manifest in the D3/D7 embeddings. Recently, the  $D3 - D7 - \overline{D7}$  embeddings in the  $AdS_5 \times T^{1,1}$  background have been developed by Kuperstein and Sonnenschein(KS)[199]. The KS model also possesses a chiral symmetry characterized by the  $D7$  and  $\overline{D7}$  branes, which provides an alternative choice for investigating anomalous effects in chiral systems via holography. In the framework of the KS model, we can introduce different chemical potentials in the right-handed and left-handed sectors on the  $D7$  and  $\overline{D7}$  branes and evaluate the axial conductivity in CESE by following the same approach in SS model. Furthermore, by considering the leading-order backreacted metric as reported in [200], we can compute the corrections to the transport coefficients in terms of the  $\lambda N_f/N_c$  expansion with  $\lambda$  being the t'Hooft coupling, which allows us to study CESE beyond the quenched approximation. On the other hand, since the 5-dimensional background geometry in KS model is asymptotic  $AdS_5$ . We may apply the MT geometry to KS model to further investigate the anisotropic effect upon CESE.

In addition, similar to CMW mentioned in Section 1.4, an electric field may induce an chiral electric wave (CEW) from the density fluctuations in a chiral plasma[124]. We will thus continue the study in Chapter 6 to further explore CEW. We will invoke both the SS model and KS model to evaluate the dispersion relation of CEW and extract the wave velocity and diffusion constant by following the similar approach

for CMW[110]. In the previous studies of CMW, only small chemical potentials are considered. Such a setup may characterize the energetic collisions in RHIC and LHC, which result in small chemical potentials as mentioned in Chapter 1. However, we will investigate CMW and CEW with a large vector chemical potential based on the enhancement of CESE led by the increase of the vector chemical potential, which is imperative for the collisions with lower energy in the RHIC beam energy scan[197, 198]. In particular, we anticipate that the density fluctuations will be more prominent near the critical point of the chiral phase transition in the QCD phase diagram. Therefore, the inclusion of a large vector chemical potential is essential to further probe the QCD phase diagram with anomalous effects. In this case, we have to firstly reformulate the wave equations and subsequently analyze the dispersion relation in holography. To be more pragmatic in comparison with asymmetric collisions in experiments, we have to consider the presence of both electric and magnetic fields, where the interplay between CMW and CEW should result in nontrivial physics.

As briefly referred in Section 5.1, the presence of a strong magnetic field may favor the chiral symmetry breaking and the formation of fermionic condensates. The competing effects on the critical mass between the magnetic field and pressure anisotropy close to the transition point may imply that the anisotropy disfavors the chiral symmetry breaking as opposed to the magnetic field. To confirm our speculation, it is desirable to calculate the quark condensate near the transition point between the confined and deconfined phases, for which we have to study the Minkowski embedding in the MT background. Moreover, we may also include a finite chemical potential in such a model. We can then study the phase diagram with respect to the temperature, chemical potential, magnetic field, and anisotropy in a strongly interacting gauge theory. On the other hand, since the chiral symmetry breaking is not manifest in the D3/D7 systems, we should also analyze the magnetic catalysis in the KS model with the MT background. Alternatively, we can consider

the anisotropy induced by the presence of a magnetic field in an originally isotropic background. Practically, one should study the backreaction from the magnetic field coupling to the flavor branes in the KS model by making a  $\lambda N_f/N_c$  expansion. Such a computation will be sophisticated. However, it is indispensable for understanding the influence from a magnetic field and the induced anisotropy in the unquenched limit.

Although the studies in static conditions could bring about profound results, it is desirable to generalize the studied to time-dependent conditions more analogous to heavy ion experiments. We may investigate CME and CESE in the SS and KS models in the presence of time-dependent electromagnetic fields in the quenched approximation. Given that the time-dependent backreactions to the background geometries are neglected, the conventional AdS/CFT prescriptions for the computations of transport coefficients in static conditions may not be applied. A new formalism for the computations of time-dependent correlation functions to tackle the problems is needed. Tentatively, we may take the Wigner transform to replace Fourier transform when evaluating the time-dependent correlation functions.

Similarly, we may investigate the anomalous transport in the AdS-Vaidya type geometry to mimic the non-equilibrium phase in heavy ion collisions. We may implement the AdS-Vaidya metric as the background geometry and incorporate the gauge fluctuations contributing to the chemical potentials. Such a setup corresponds to the case with small chemical potentials. For finite chemical potentials, we could utilize the AdS-RN-Vaidya geometry by assigning the time-dependent charge to a finite axial chemical potential emerging from a thermalizing medium. Nonetheless, to involve both the vector and axial chemical potentials, the AdS-RN-Vaidya geometry has to be modified to include two charges. The studies involving time-dependent electromagnetic fields or non-equilibrium geometries not only provide us significant information in heavy-ion phenomenology, but also introduce potential recipes for

analyzing quantum quench and other problems related to the non-equilibrium and strongly interacting systems in condensed matter and cold atom physics.

# Appendix A

## Appendices for Chapter 3

### A.1 Perturbative Expansions of the Dilaton Field

In [63], it is showed that the AdS-vaitya metric is the leading-order solution in the expansion of a weak dilaton field as a non-normalizable excitation with respect to time. At late times, the higher-order terms in the weak-field expansion may dominate and thus undermine the perturbation. However, the dilaton field on the boundary is time-varying only within a period which is approximately equivalent to the thickness of the falling shell on the boundary in AdS-Vaidya spacetime. At late times, the dual geometry should be governed by AdS-Schwarzschild metric; the dilaton field on the boundary vanishes, while it diffuses near the future horizon, which corresponds to the quasi-normal mode led by the scattering between the dilaton field and the backreaction of the spacetime metric. If the time period for the time-varying dilaton filed on the boundary were short, the perturbative expansion would be the exact solution within that time period. The non-vanishing higher-order terms near the future horizon should match the quasi-normal mode outside that time period. In the following, we will show that the quasi-normal mode would be negligible by choosing a

Gaussian profile of the dilaton field on the boundary with the appropriate amplitude and width.

Recall the expansion of the dilaton field and the mass function in [63],

$$\phi(r, v) = \phi_0(v) + \frac{\partial_v \phi_0}{r} + \frac{\phi_3}{r^3} + \mathcal{O}\left(\frac{1}{r^4}\right) \text{ for } r = z^{-1}, \quad (\text{A.1})$$

$$m(v) = \frac{1}{2} \int_{-\infty}^v dt \left( (\partial_t^2 \phi_0)^2 + \frac{3}{4} (\partial_t \phi_0)^4 - 3(\partial_t \phi_0) \phi_3 \right), \quad (\text{A.2})$$

where  $\phi_3 = \frac{1}{4r^3} \int_{-\infty}^v dt (-\partial_t \phi_0) m(t) + (\partial_t \phi_0)^2 \partial_t^2 \phi_0$  is at  $\mathcal{O}(\epsilon^3)$  for  $\epsilon$  denoting the field amplitude on the boundary. Then we take  $\phi_0(v) = \epsilon e^{-v^2/v_0^2}$  for  $v_0 = 0.1$  and  $\epsilon = 0.02306$ , which leads to  $m(v \rightarrow \infty) = M \approx 1$ . Since the future horizon  $r_h = M^{1/3} \approx 1$ , this choice satisfies the required condition for AdS-Vaidya metric that  $r \delta t \gg \epsilon$  at large  $r$  by approximating  $\delta t \sim v_0$ , where  $\delta t$  denotes the time period for the time-varying dilaton field on the boundary. The mass functions up to the leading order  $\mathcal{O}(\epsilon^2)$  and to the next leading order  $\mathcal{O}(\epsilon^4)$  are illustrated in Fig.A.1, whereas two functions almost coincide due to the  $\mathcal{O}(\epsilon^2)$  suppression of the correction from the next leading order. The mass function may degenerate to a step function at the thin-shell limit when  $v_0 \rightarrow 0$ . Here the two turning points appearing in Fig.A.1 come from the second derivatives of the dilaton field with the Gaussian profile encoded in the leading-order contribution of the mass function.

Subsequently, we will match the perturbative solution and the quasi-normal mode at  $v = \delta t/2$ , where the dilaton field on the boundary is time-varying within  $-\delta t/2 < v < \delta t/2$ . As showed in Fig.A.2, the  $\mathcal{O}(\epsilon^3)$  terms may dominate  $\phi(v, r)$  as  $v \sim \delta t$ . Although the dilaton field with the Gaussian profile should decay to zero at  $v \rightarrow \infty$ , the perturbation would breakdown at large  $v > \delta t/2$  and the dilaton field has to match the quasi-normal mode in the AdS-Schwarzschild spacetime. Here we take  $\delta t/2 = 3v_0$ . It is showed in [63] that the quasi-normal mode  $\phi_q(r, (v - \delta t/2))$  as the solution of the dilaton equation in the AdS-Schwarzschild spacetime is determined

by the initial condition  $\phi_q(r, 0) = \phi_3(r, 0)/r^3$  and the boundary condition  $\phi_q(\infty, v - \delta t/2) = 0$ . Since the maximum amplitude of the lowest quasi-normal mode is small compared with the leading order terms of  $\phi(r, v)$  for  $-3v_0 < v < 3v_0$ , the broadening of the dilaton field by the higher order perturbation and the quasi-normal mode may be ignored. In [63], this quasi-normal mode is interpreted as the resummed perturbation at the third order.

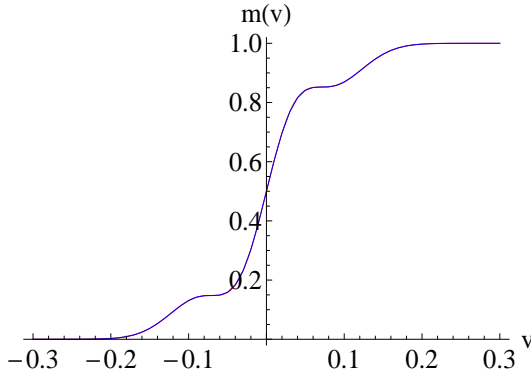


FIGURE A.1: The comparison between the leading-order mass function to  $\mathcal{O}(\epsilon^2)$  and the next leading-order one to  $\mathcal{O}(\epsilon^4)$  in terms of  $v$ . Two results coincide and cannot be distinguished in the figure.

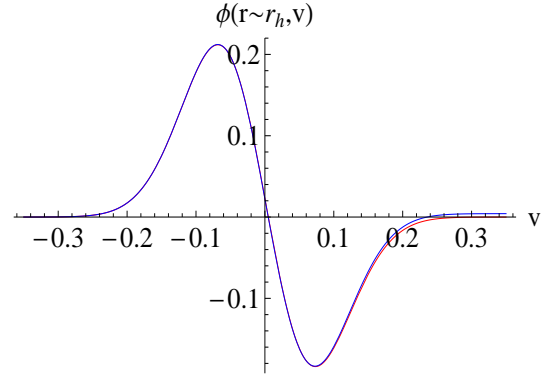


FIGURE A.2: The red curve and blue curve illustrate the  $\phi(z = 0.99, v)$  up to  $\mathcal{O}(\epsilon)$  and  $\mathcal{O}(\epsilon^3)$ , respectively. When  $v \approx 3v_0$ , the contribution from the higher order terms starts to increase, while its amplitude is rather small as  $v$  is still within  $(-3v_0, 3v_0)$ .

## A.2 Quasi-Static Approximation and the Thin-Shell Limit

In this subsection, we will discuss about the validity of the quasi-static approximation and the thin-shell limit by investigating the mass shell generated by the dilaton field with the Gaussian profile in  $AdS_4$  background. By taking  $\phi_0(v) = \epsilon e^{-v^2/v_0^2}$ , the leading-order mass function is given by

$$m(v) = \frac{1}{2} \int_{-\infty}^v dt (\partial_t^2 \phi_0(t))^2 = M \frac{k e^{-k^2}}{3\sqrt{\pi}} (1 - 2k^2) + \frac{M}{2} (1 + \text{erf}(k)), \quad (\text{A.3})$$

where  $k = \frac{\sqrt{2}v}{v_0}$ ,  $M = \frac{3\sqrt{2\pi}}{4v_0^3}\epsilon^2$ , and  $erf(k)$  is the error function. By applying the quasi-static approximation, the redshift factor can be computed from the integral of (3.8) along with the linear approximation in (A.5) at  $d = 3$ , while we will not restrict the computation in the thin-shell limit. Since the mass function in (A.3) now is more complex than the hyperbolic tangent-like function in the Section.II, we have to solve the integral in (3.8) numerically. The positions of the center of the shells with different setups obtained from the numerical solutions of the redshift factors are shown in Fig.A.3. These setups have different  $\epsilon$  and  $v_0$  but all lead to  $M = 1$ .

On the other hand, we can numerically solve  $v(t, z)$  by using (3.7),

$$\begin{aligned} \frac{\partial}{\partial z} \left( \frac{\partial v(t, z)}{\partial t} \right) &= \left( \frac{\partial f(v, z)}{\partial v} \right)_z \frac{1}{f(v, z)^2} \left( \frac{\partial v(t, z)}{\partial t} \right) \\ &= \frac{-z^3}{(1 - m(v)z^3)^2} \left( \frac{\partial m(v)}{\partial v} \right) \left( \frac{\partial v(t, z)}{\partial t} \right), \end{aligned} \quad (\text{A.4})$$

with the following boundary and initial conditions,  $v(t, 0) = t$  and  $v(0, z) = -z$ . Given that the thickness of the shell is not too large, the initial condition  $v(0, z)$  should be approximately valid since the spacetime in the early time is governed by the pure AdS metric. The mass function  $m(v)$  as a function of  $t$  and  $z$  from this full numerical computation is shown in Fig.A.5. Compared to Fig.A.3, the falling shells obtained from the quasi-static approximation and from the numerical solution match qualitatively. To have a closer comparison, we may track the centers of the shells from the numerical solutions, which are as well illustrated in Fig.A.3 in comparison with the result from the quasi-static approximation. It turns out that the quasi-static approximation with the linear approximation qualitatively describes the scenario of the falling shell even beyond the thin-shell limit.

In addition, the qualitative behavior of the falling shell is independent of the spacetime dimensions. In the early time, the shell with distinct thickness all fall with the speed of light. Since the spacetime is still analogous to the pure vacuum,

the profiles of the shell or the distributions of the injected energy will be irrelevant. While in the later time, the shell with larger thickness falls faster. At the late stage of the thermalization, the shell with larger thickness covers larger range of the virtuality scale, which may facilitate the thermalization process. The small deviations based on the different thickness of the shells can be observed in Fig.A.4. We see that the deviation between the quasi-static approximation and the full numerical computation only emerges in late times.

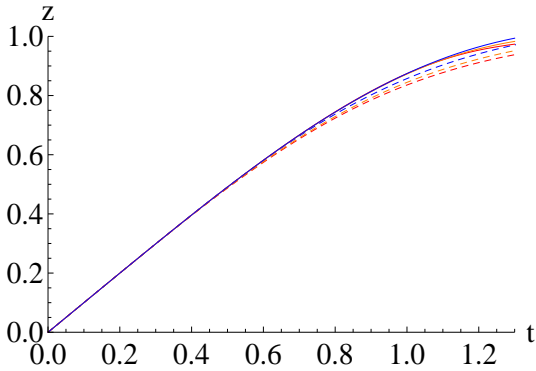


FIGURE A.3: The solid red, orange, and blue curves represent the position of the center of the shell using the linear approximation for  $(v_0, \epsilon) = (0.1, 0.02306)$ ,  $(0.2, 0.06523)$ , and  $(0.4, 0.18451)$ , respectively. The dashed curves are the result of numerically computing  $v(t, z)$ .

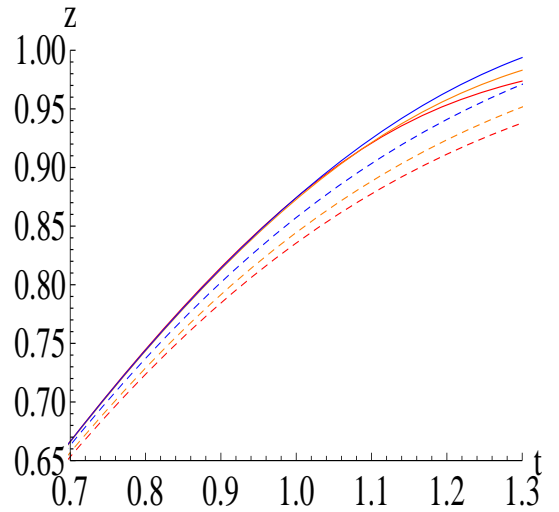


FIGURE A.4: Same plot as in Fig.A.3, but zooming onto late time evolution.

In Appendix A.1, we discuss the broadening of the dilaton field along the  $v$  direction based on the scattering between the dilaton field and the backreaction of the spacetime metric, whereas the amplitude of the broadening is negligible. Along the  $z$  direction, the upper portion of the shell may receive stronger gravitational force and thus falls faster than the lower portion of the shell. The scenario should be more manifest when the shell approaches the future horizon. Therefore, we may expect the compression of the shell near the future horizon. As illustrated in Fig.A.6, where

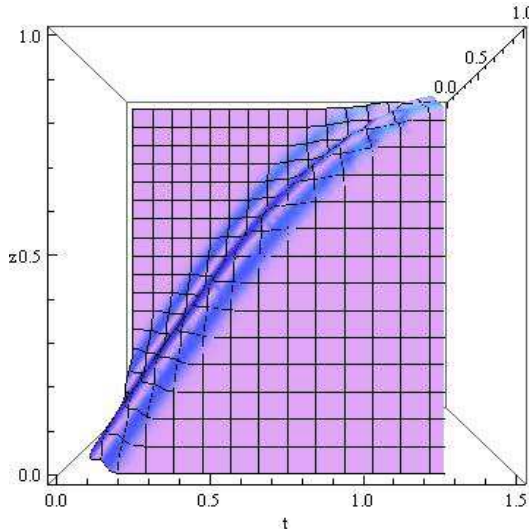


FIGURE A.5: The full numerical computation for  $m(v)$  at  $v_0 = 0.1$  and  $\epsilon = 0.02306$ .

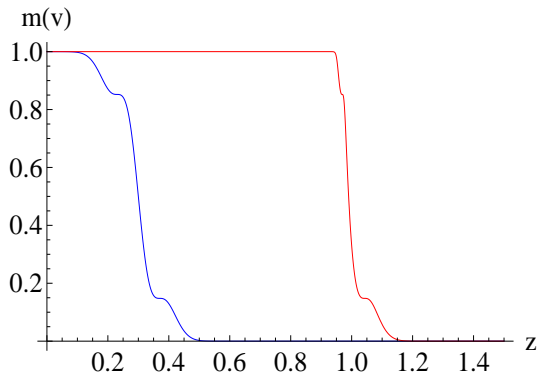


FIGURE A.6: The red and blue curves represent the leading order mass function to  $\mathcal{O}(\epsilon^2)$  for  $v_0 = 0.1$  and  $\epsilon = 0.02306$  at  $z_0 = 0.99$  and  $z_0 = 0.3$ , respectively.

we evaluate the mass function in terms of  $z$  from the solution of  $v(t(z_0), z)$  by solving (A.4) numerically, the upper portion of the shell shrinks when approaching the future horizon and the profile of the shell becomes asymmetric. Since the thickness of the shell along the  $z$  direction may be compressed and the broadening along the  $v$  direction can be discarded, we conclude that the thin-shell limit should be appropriate in the framework of the AdS-Vaidya spacetime.

### A.3 The Redshift Factor and Thermalization times

In this appendix, we will introduce further approximations to compute the redshift factor and thermalization time of the medium. To solve the integral in (3.9), we have to write  $v(t, z)$  in terms of  $z$  at fixed  $t(z_0)$ . In principle, we can employ the numerical solution of  $v(t, z)$  from (A.4), while we may make further approximations to obtain an analytical solution without losing the generality. Given that the integrand in (3.9) is non-vanishing only in the vicinity of  $z_0$  when the thickness of the shell is small, we

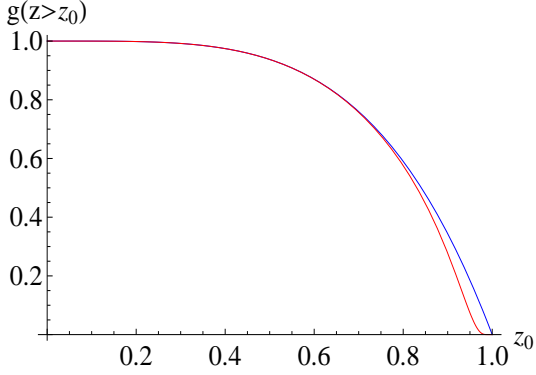


FIGURE A.7: The red curve represents the redshift factor  $c(z_0)$  as a function of the position of the shell, while the blue curve represents  $F(z_0)$ , where the future horizon is at  $z_h = 1$ .

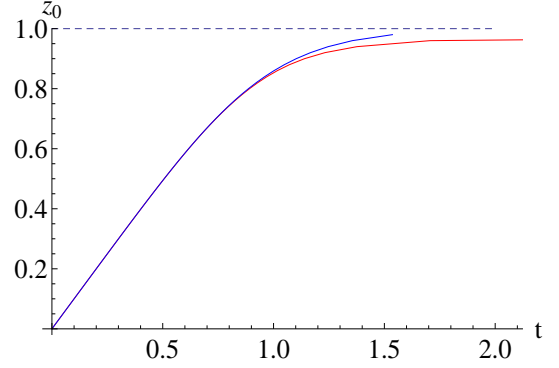


FIGURE A.8: The blue and red curves represent the positions of the shell obtained from (3.18) and (A.8), respectively. Here the blue dashed line denotes the future horizon at  $z_h = 1$ .

may approximate it by a linear function,

$$v(t(z_0), z) \approx \frac{\partial v(t(z_0), z)}{\partial z} (z - z_0) = -\frac{z - z_0}{1 - Mz_0^4/2}, \quad (\text{A.5})$$

to solve for  $g(t(z_0), z_p)$ . Now the integral in the exponent of (3.8) can be simplified as

$$\log g(t(z_0), z_p) = \int_{-\infty}^{a_p} da \frac{-(2 - Mz_0^4) \text{sech}^2 a}{Mz_0^4 \left( \tanh a + \frac{2 - Mz_0^4}{Mz_0^4} \right)^2}, \quad (\text{A.6})$$

where  $a = \frac{z - z_0}{v_0(1 - Mz_0^4/2)}$ . When  $v_0$  is small,  $a \rightarrow +(-)\infty$  for  $z_p$  being inside(outside) the shell and  $a = 0$  for  $z = z_0$ . Since we take the integration from the boundary to the bulk, the lower bound of the integral should be at  $a \rightarrow -\infty$ . Solving the integral in (A.6) analytically, we obtain the redshift factor,

$$g(z_0, z_p) = \begin{cases} 1 & \text{if } v > 0 (z_p < z_0), \\ \exp \left[ -\frac{Mz_0^4}{2(1 - Mz_0^4)} \right] & \text{if } v = 0 (z_p = z_0), \\ c(z_0) = \exp \left[ -\frac{Mz_0^4(1 - \frac{M}{2}z_0^4)}{(1 - Mz_0^4)} \right] & \text{if } v < 0 (z_p > z_0). \end{cases} \quad (\text{A.7})$$

The redshift factor inside the shell  $c(z_0)$  only depends on the position of the shell. As shown in Fig.A.7, the redshift effect pronounces only when the shell is away the boundary. It also deviates from  $F(z_0)$  in the region close to the horizon. Now, by combining (3.5) and (A.7), we can track the position of the shell,

$$t_0 = \int_0^{z_0} dz_s \frac{\exp\left[\frac{Mz_s^4}{2(1-Mz_s^4)}\right]}{1 - \frac{M}{2}z_s^4}, \quad (\text{A.8})$$

which is illustrated in Fig.A.8 for  $M = z_h^{-4} = 1$ . Compared to the trajectory obtained from (3.18), the position of the shell shown in (A.8) falls much slower.

From the redshift factor in (A.7), we can compute the falling velocities of the different portions of the shell even though the thickness of the shell is small. We find

$$\begin{aligned} v_t(z_0) &= F(z_0) = 1 - \frac{z_0^4}{z_h^4}, \\ v_c(z_0) &= \left(1 - \frac{z_0^4}{2z_h^4}\right) \exp\left[-\frac{z_0^4/z_h^4}{2(1 - z_0^4/z_h^4)}\right], \\ v_b(z_0) &= c(z_0) = \exp\left[-\frac{z_0^4/z_h^4 \left(1 - \frac{z_0^4}{2z_h^4}\right)}{(1 - z_0^4/z_h^4)}\right], \end{aligned} \quad (\text{A.9})$$

where  $v_t$ ,  $v_c$ , and  $v_b$  represent the falling velocities of the top, center, and the bottom of the shell, respectively. When the shell is away from the horizon,  $v_t(z_0) \approx v_c(z_0) \approx v_b(z_0)$  up to the order of  $z_0^4/z_h^4$ , which implies the thickness of the shell remains unchanged. When the shell approaches the horizon, the expansion of  $z_0^4/z_h^4$  becomes invalid and  $v_c(z_0) \lesssim v_b(z_0) < v_t(z_0)$ , where  $v_b(z_0) < v_t(z_0)$  suggests the compression of the shell as discussed in Appendix A.2. Counter-intuitively,  $v_c(z_0) \lesssim v_b(z_0)$  may suggest that the bottom of the shell will be pulled back by the center of the shell when approaching the horizon. This effect comes from an error of the linear approximation around the center of the shell in our computation. In fact, the linear approximation

breakdowns when the shell is deformed when approaching the horizon as shown in the later paragraph by considering the next leading order correction.

Given that the center and the bottom of the shell fall much slower than the top of the shell, we may define the thermalization time at  $t_{th} = t_0|_{z_0=0.98z_h}$ . We find  $t_{th}T=0.49, 1.52,$  and  $1.36$  for solving  $t_0$  from the top, the center, and the bottom of the shell, respectively. Recall that  $0.15 \leq t_{th}T \leq 1.52$  for the QGP generated in RHIC, the thermalization time of the center of the shell roughly matches the upper bound. However, to fix the counter-intuitive result that  $v_c(z_0) \lesssim v_b(z_0)$ , we have to compute the falling velocities to the next leading order; we will find that the bottom of the shell falls slower than the center of the shell as expected.

Before proceeding to the next leading order computation, we may recall that we not only make the linear approximation of  $v(t(z_0), z)$  in the integral of (A.6) but also approximate  $z$  as  $z_0$  to obtain the analytic result. To verify that this further approximation does not affect the falling velocities qualitatively, we should carry out the integral in (3.9) numerically by only substituting the  $v(t(z_0), z)$  with the expression in (A.5). Now, we have to define the upper bound  $z_p$  in the integral to characterize the top and the bottom of the shell. We may define  $|z - z_0| = 3v_0$  as the edges of the shell based on  $m(v = 3v_0) \approx M$  and  $z - z_0 \approx -v$  at the leading order expansion. In other words, by taking the numerical integral with respect to  $z$  from 0 to  $z_p = z_0 + 3v_0$ , we can obtain the redshift factor  $c(z_0)$  in the quasi-AdS spacetime and compute the falling velocity of the bottom of the shell. In this condition, we find the falling velocities,  $v_t(z_0) = 1 - z_0^4 = 0.078$ ,  $v_c(z_0) = (1 - z_0^4/2)g(z_0, z_p = z_0) = 0.0019$ , and  $v_b(z_0) = g(z_0, z_p = z_0 + 3v_0) = 0.0022$  by taking  $M = 1$  and  $z_0 = 0.98$ . By using (A.9), we obtain  $v_t(z_0) = 0.078$ ,  $v_c(z_0) = 0.0014$ , and  $v_b(z_0) = 0.0017$  with the same  $M$  and  $z_0$ . It turns out that  $v_c < v_b$  in both cases with and without approximating  $z$  as  $z_0$  in the integrand when computing the redshift factor, which suggests that the primary error should stem from the linear

approximation of  $v(t(z_0), z)$ .

To the next leading order, we have

$$\begin{aligned}
v(t(z_0), z) &\approx \partial_z v(t(z_0), z)|_{z=z_0}(z - z_0) + \frac{1}{2} \partial_z^2 v(t(z_0), z)|_{z=z_0}(z - z_0)^2 \quad (\text{A.10}) \\
&= -\frac{z - z_0}{1 - \frac{Mz_0^4}{2}} - \frac{(z - z_0)^2}{\left(1 - \frac{Mz_0^4}{2}\right)^2} \left( Mz_0^3 - \frac{z_0^4}{2 \left(1 - \frac{Mz_0^4}{2}\right)} \frac{dm(v)}{dv} \Big|_{z=z_0} \right),
\end{aligned}$$

where we use the chain rule  $\left(\frac{\partial f(v, z)}{\partial z}\right)_t = \left(\frac{\partial f(v, z)}{\partial z}\right)_v + \left(\frac{\partial f(v, z)}{\partial v}\right)_z \left(\frac{\partial v(t, z)}{\partial z}\right)_t$  for deriving the second equality. Here the derivative of the mass function

$$\frac{dm(v)}{dv} = \frac{M}{2v_0} \operatorname{sech}^2\left(\frac{v}{v_0}\right) = \frac{2m(v)}{v_0} \left(1 - \frac{m(v)}{M}\right) \quad (\text{A.11})$$

is highly localized at  $z_0$ ; we may thus substitute  $\frac{dm(v)}{dv}|_{z=z_0}$  with  $\frac{M}{2v_0} \theta(v_0 - |z - z_0|)$  in (A.10), where  $\theta$  denotes the unit step function. When  $|z - z_0| \approx v_0$ , this term leads to comparative contribution compared to the leading order term. By computing the falling velocities with the redshift factor obtained from the numerical integral of (3.9) up to the next leading order, we find  $v_t(z_0) = 1 - z_0^4 = 0.078$ ,  $v_c(z_0) = (1 - z_0^4/2)g(z_0, z_p = z_0) = 0.020$ , and  $v_b(z_0) = g(z_0, z_p = z_0 + 3v_0) = 0.017$  by taking  $M = 1$  and  $z_0 = 0.98$ . Now, we acquire the plausible relation  $v_t > v_c > v_b$ , while the values of  $v_c$  and  $v_b$  are much larger than those derived from the leading order approximation. To extract the accurate falling velocities of different portions of the shell when approaching the future horizon, it is necessary to compute the redshift factor up to the higher order. Nevertheless, the velocity of the top of the shell is not affected by the higher order correction and it may provide an upper limit for the thermalization time of the medium.

## A.4 The String Profile in the Quasi-AdS Spacetime

In this appendix, we will analyze more details about the string profile in the quasi-AdS spacetime and reproduce the ratio of the energy to momentum of the massless particle in (3.25) by following the approach in [103]. We require that the initial trajectory of the particle coincide with the direction of a lightlike signal traveling down the string worldsheet, where the later leads to the minimum stopping distance of the falling string. By taking  $h_{\alpha\beta}l^\alpha l^\beta = 0$ , we obtain the basis of the lightlike vectors to be

$$l^\alpha = (1/\sqrt{1-\tilde{v}^2}, 1) \quad \text{or} \quad (1, -\sqrt{1-\tilde{v}^2}) . \quad (\text{A.12})$$

By taking the first basis in (A.12), we can form the spacetime vector

$$l_\mu = l^\alpha \frac{\partial X_\mu}{\partial \sigma^\alpha} = \frac{1}{\sqrt{1-\tilde{v}^2}}(-1, \tilde{v}, 0, 0, 0) , \quad (\text{A.13})$$

which transmits the lightlike signal on the string worldsheet and falls into the future horizon. Now the 4-momentum of the massless particle should be proportional to the spacetime direction:  $q_\mu \propto l_\mu$ . Thus we can write down the momentum ratio

$$\frac{\tilde{q}_i}{\tilde{q}_0} = \frac{l_i}{l_0} = -\tilde{v}. \quad (\text{A.14})$$

It turns out that the spacetime vector  $l_\mu$  is independent of  $z$  in the quasi-AdS spacetime. By approximating the small pieces of the string as massless particles and matching their initial momenta with  $l_\mu$ , all pieces of the string will carry the same initial momentum. Thus the initial trajectories of all pieces of the string should be parallel. Furthermore, since  $\tilde{q}_\mu$  is conserved in the quasi-AdS spacetime, they continually move along the null geodesic and the string thus remains straight, which supports our argument in the context.

## A.5 The Dangling String and Wave velocity in the Quasi-AdS Spacetime

In this appendix, we compute the wave velocity by investigating a dangling string in the quasi-AdS spacetime. We firstly write down the Nambu-Goto action in the quasi-AdS spacetime. By choosing  $\tilde{t}$  and  $z$  as the worldsheet coordinates and setting  $x^1(\tilde{t}, z)$  we get

$$S = \frac{-1}{2\pi\alpha'} \int d\tilde{t}dz \frac{1}{z^2} \sqrt{1 - \left(\frac{dx^1}{d\tilde{t}}\right)^2 + \left(\frac{dx^1}{dz}\right)^2}. \quad (\text{A.15})$$

As mentioned in the context, the profile of the string in the quasi-AdS spacetime should remain straight. We thus set

$$x^1(\tilde{t}, z) = \tilde{v}\tilde{t} + \delta x^1(\tilde{t}, z). \quad (\text{A.16})$$

After taking the expansion of the Lagrangian in (A.15) with respect to the derivatives of  $\delta x^1$ , we write down the equation of motion by extremizing the deviation of the Lagrangian. We find

$$\frac{d^2\delta x^1(\tilde{t}, z)}{dz^2} - 2z^{-1}\frac{d\delta x^1(\tilde{t}, z)}{dz} = (1 - \tilde{v}^2)^{-1}\frac{d^2\delta x^1(\tilde{t}, z)}{d\tilde{t}^2}. \quad (\text{A.17})$$

From the equation above and  $d\tilde{t} = F(z_0)dt$ , we derive the wave velocity

$$v_w = \sqrt{1 - \tilde{v}^2}F(z_0). \quad (\text{A.18})$$

On the other hand, the velocity of the falling shell in the thin-shell limit can be derived from (3.18),

$$v_0 = \frac{dz_0}{dt} = F(z_0). \quad (\text{A.19})$$

At the collision point,  $z_0 = z_c$ , the wave velocity in the quasi-AdS spacetime is always smaller than the velocity of the falling shell unless the string is static. Thus

the information may not be transmitted to the lower part of the string inside the shell from the collision point.

## A.6 Finding the Stopping Distance in Eddington-Finkelstein Coordinates

It is technically difficult to track the null geodesic of the massless particle beyond the thin shell limit in Poincare coordinates, since the trajectory of the particle is continuously deflected by interactions with the shell. However, irrespective of the details of the interaction, it is easier to compute the stopping distance of the probe in EF coordinates. Similar computations have been performed in section 3.2. By using the metric in (3.35) or (3.36) and setting the momentum component of the massless particle non-zero only along  $v$ ,  $z$ , and  $x^1$  directions, we can write down the geodesic equations in terms of the affine parameter  $\lambda$ ,

$$\begin{aligned}
\frac{d^2 v}{d\lambda^2} + \Gamma_{vv}^v \left( \frac{dv}{d\lambda} \right)^2 + \Gamma_{11}^v \left( \frac{dx^1}{d\lambda} \right)^2 &= 0 \\
\frac{d^2 z}{d\lambda^2} + \Gamma_{vv}^z \left( \frac{dv}{d\lambda} \right)^2 + 2\Gamma_{vz}^z \left( \frac{dv}{d\lambda} \right) \left( \frac{dz}{d\lambda} \right) + \Gamma_{11}^z \left( \frac{dx^1}{d\lambda} \right)^2 + \Gamma_{zz}^z \left( \frac{dz}{d\lambda} \right)^2 &= 0, \\
\frac{d^2 x^1}{d\lambda^2} + 2\Gamma_{z1}^1 \left( \frac{dz}{d\lambda} \right) \left( \frac{dx^1}{d\lambda} \right) &= 0.
\end{aligned} \tag{A.20}$$

For  $d = 3$ , the relevant Christoffel symbols are given by

$$\begin{aligned}
\Gamma_{vv}^v &= \frac{1}{z} \left( 1 + m(v)z^3 - \frac{1}{2}Q^2m(v)^{4/3}z^4 \right), \quad \Gamma_{11}^v = -\frac{1}{z}, \\
\Gamma_{vv}^z &= \frac{1}{z} \left( -1 + \frac{1}{2}m(v)z^3 + \frac{1}{2}m(v)^2z^6 - \frac{3}{4}Q^2m(v)^{7/3}z^7 + \frac{1}{4}z^8Q^4m(v)^{8/3} \right) \\
&\quad - \frac{1}{z} \left( \frac{1}{2}z^4 - \frac{1}{3}Q^2m(v)^{1/3}z^5 \right) \frac{dm(v)}{dv}, \quad (\text{A.21}) \\
\Gamma_{vz}^z &= -\frac{1}{z} \left( 1 + m(v)z^3 - \frac{1}{2}Q^2m(v)^{4/3}z^4 \right), \quad \Gamma_{zz}^z = -\frac{2}{z}, \\
\Gamma_{11}^z &= \frac{1}{z} \left( 1 - m(v)z^3 - \frac{1}{2}Q^2m(v)^{4/3}z^4 \right), \quad \Gamma_{z1}^1 = -\frac{1}{z}.
\end{aligned}$$

For  $d = 4$ ,

$$\begin{aligned}
\Gamma_{vv}^v &= \frac{1}{z} \left( 1 + m(v)z^4 - \frac{4}{3}Q^2m(v)^{3/2}z^6 \right), \quad \Gamma_{11}^v = -\frac{1}{z}, \\
\Gamma_{vv}^z &= \frac{1}{z} \left( -1 + m(v)^2z^8 + \frac{2}{3}Q^2m(v)^{3/2}z^6 - 2Q^2m(v)^{5/2}z^{10} + \frac{8}{9}Q^4m(v)^3z^{12} \right) \\
&\quad - \frac{1}{2z} \left( z^5 - Q^2z^7m(v)^{1/2} \right) \frac{dm(v)}{dv}, \quad (\text{A.22}) \\
\Gamma_{vz}^z &= -\frac{1}{z} \left( 1 + m(v)z^4 - \frac{4}{3}Q^2m(v)^{3/2}z^6 \right), \quad \Gamma_{zz}^z = -\frac{2}{z}, \\
\Gamma_{11}^z &= \frac{1}{z} \left( 1 - m(v)z^4 + \frac{2}{3}Q^2m(v)^{3/2}z^6 \right), \quad \Gamma_{z1}^1 = -\frac{1}{z}.
\end{aligned}$$

In addition to these, the mass function is defined as

$$m(v) = \frac{M}{2} \left( 1 + \tanh \left( \frac{v}{v_0} - \frac{1}{2} \right) \right), \quad (\text{A.23})$$

where the shift in the hyperbolic-tangent function is to fit the setup illustrated in Fig.A.9. In the thin-shell limit, the mass function defined here will degenerate to the

expression in (3.38). The momentum along the  $x^1$  direction  $q_1 = |\vec{q}| = z^{-2} \frac{dx^1}{d\lambda}$  from the definition  $q_\mu = g_{\mu\nu} \frac{dx^\nu}{d\lambda}$  is conserved in EF coordinates. Thus, we may rewrite the geodesic equations in terms of the derivative with respect to  $x^1$ ,

$$\begin{aligned} \frac{dx^\mu}{d\lambda} &= \frac{dx^\mu}{dx^1} \frac{dx^1}{d\lambda} = z^2 |\vec{q}| x'^\mu, \\ \frac{d^2 x^\mu}{d\lambda^2} &= |\vec{q}|^2 z^2 (x''^\mu z^2 + 2zz' x'^\mu), \end{aligned} \quad (\text{A.24})$$

where the prime denotes the derivative with respect to  $x^1$ . By inserting (A.24) into the geodesic equations, we find the last equation in (A.20) is automatically satisfied due to the conservation of momentum along  $x^1$ . We then have to introduce proper initial conditions to solve other two geodesic equations in (A.20). Even though the energy of the particle is not conserved in the AdS-RN-Vaidya spacetime, initially the gravitational effect led by the falling shell is negligible. Therefore, we may write down the initial conditions as a massless particle falling in the pure AdS metric. For a particle ejected from  $z_I$ , we have

$$\begin{aligned} z|_{x^1=0} &= z_I, \quad v|_{x^1=0} = t|_{x^1=0} - z|_{x^1=0} = -z_I, \\ v'|_{x^1=0} &= (t' - z')|_{x^1=0} = \frac{\omega_0}{|\vec{q}|} - \frac{\sqrt{\omega_0^2 - |\vec{q}|^2}}{|\vec{q}|}, \\ z'|_{x^1=0} &= \frac{\sqrt{\omega_0^2 - |\vec{q}|^2}}{|\vec{q}|}, \end{aligned} \quad (\text{A.25})$$

where  $\omega_0$  and  $\vec{q}$  represent the initial energy and momentum of the massless particle in Poincare coordinates. The stopping distance obtained in EF coordinates is shown in Fig.A.10 for  $d = 4$  in the thin-shell limit, where we also make a comparison with the result illustrated in Fig.3.17 with the same initial conditions. The results match and cannot be distinguished from the plot. This holds for  $d = 3$  as well. We can also evaluate the stopping distance with the thick shell in EF coordinates, it turns out that the deviation from the thin shell is negligible.

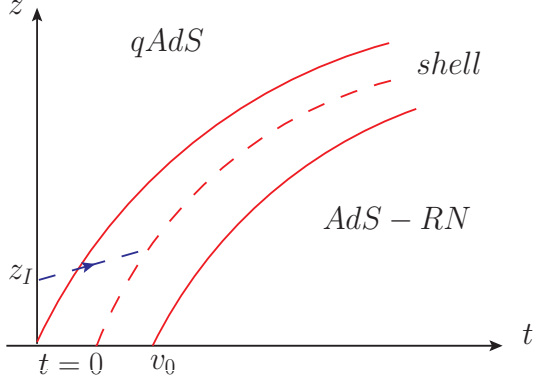


FIGURE A.9: The scenario of a massless particle ejecting from the boundary as the shell starts to fall, where  $v_0$  denotes the thickness of the shell and the solid red curves and the dashed red curve represent the surfaces and the center of the shell, respectively. Here the blue dashed line represents the massless particle ejected from  $z_I$ .

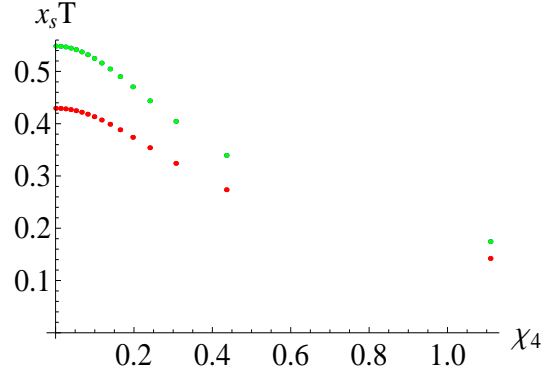


FIGURE A.10: The green points represent the stopping distances in AdS-RN-Vaidya spacetime in EF coordinates, which match those derived in Poincare coordinates as shown by the blue points. Here the initial conditions are the same as those in Fig.3.17 and we take  $v_0 = 0.0001$ .

## A.7 The Dyonic Black Hole

Here we will summarize some properties of the dyonic black hole in  $d = 3$ . The action we consider is the following

$$S_0 = \frac{1}{8\pi G_N} \left( \frac{1}{2} \int d^4x \sqrt{-g} (R - 2\Lambda) - \frac{1}{4} \int d^4x F^2 \right), \quad (\text{A.26})$$

which results in the following eom

$$R_{\mu\nu} - \frac{1}{2} (R - 2\Lambda) g_{\mu\nu} = g^{\alpha\rho} F_{\rho\mu} F_{\alpha\nu} - \frac{1}{4} g_{\mu\nu} F^2, \quad (\text{A.27})$$

$$\partial_\rho [\sqrt{-g} F^{\rho\sigma}] = 0, \quad \partial_\rho [\sqrt{-g} (\star F)^{\rho\sigma}] = 0, \quad (\text{A.28})$$

where  $(\star F)$  is the Hodge dual of  $F$ . In  $(3 + 1)$ -bulk dimensions, the Hodge dual of the bulk electro-magnetic field is another two form. Thus it is possible for a black hole to possess both electric and magnetic charges. Such a dyonic black hole is given

by

$$ds^2 = \frac{L^2}{z^2} \left( -f dt^2 + \frac{dz^2}{f} + d\vec{x}^2 \right), \quad \Lambda = -\frac{3}{L^2}, \quad (\text{A.29})$$

$$f(z) = 1 - Mz^3 + \frac{1}{2L^2} (Q_e^2 + Q_m^2) z^4, \quad (\text{A.30})$$

$$F = Q_e dz \wedge dt + Q_m dx \wedge dy, \quad (\text{A.31})$$

where  $Q_e$  and  $Q_m$  denote the electric and the magnetic charges respectively.

In the extremal case, the function  $f$  can be written as

$$f(z) = 1 - 4 \left( \frac{z}{z_H} \right)^3 + 3 \left( \frac{z}{z_H} \right)^4, \quad (\text{A.32})$$

where  $z_H$  is the location of the event-horizon. It is easy to check that the temperature is given by

$$4\pi T = - \left. \frac{df}{dz} \right|_{z_H} = 0. \quad (\text{A.33})$$

Therefore for the extremal case, we can write

$$z_H^3 = \frac{4}{M}, \quad Q_e^2 + Q_m^2 = \frac{6}{L^2} \frac{1}{z_H^4}. \quad (\text{A.34})$$

We can now find the corresponding Vaidya-type background sourced by appropriate matter field

$$S = S_0 + \kappa S_{\text{ext}}. \quad (\text{A.35})$$

This will give the following equations of motion

$$R_{\mu\nu} - \frac{1}{2} (R - 2\Lambda) g_{\mu\nu} - g^{\alpha\rho} F_{\rho\mu} F_{\alpha\nu} + \frac{1}{4} g_{\mu\nu} F^2 = (16\pi G_N \kappa) T_{\mu\nu}^{\text{ext}}, \quad (\text{A.36})$$

$$\partial_\rho [\sqrt{-g} F^{\rho\sigma}] = (8\pi G_N \kappa) J_e^\sigma, \quad (\text{A.37})$$

$$\partial_\rho [\sqrt{-g} (\star F)^{\rho\sigma}] = (8\pi G_N \kappa) J_m^\sigma. \quad (\text{A.38})$$

Here  $J_e$  denotes the electric current and  $J_m$  denotes the magnetic current. The dyonic-Vaidya background takes the following form

$$\begin{aligned}
ds^2 &= \frac{L^2}{z^2} (-f dv^2 - 2dv dz + d\vec{x}^2), \\
f(z, v) &= 1 - m(v)z^3 + \frac{1}{2L^2} (q_e(v)^2 + q_m(v)^2) z^4,
\end{aligned} \tag{A.39}$$

with the following vector fields

$$F_{zv} = q_e(v), \quad F_{xy} = q_m(v). \tag{A.40}$$

The above background is sourced by the following stress-energy tensor

$$2\kappa T_{\mu\nu}^{\text{ext}} = \frac{z^2}{L^2} \left( L^2 \frac{dm}{dv} - z \left( q_e \frac{dq_e}{dv} + q_m \frac{dq_m}{dv} \right) \right) \delta_{\mu\nu} \delta_{\nu\nu}. \tag{A.41}$$

The electric and magnetic sources are given by

$$\kappa J_e^\mu = \frac{dq_e}{dv} \delta^{\mu\nu}, \quad \kappa J_m^\mu = \frac{dq_m}{dv} \delta^{\mu\nu}. \tag{A.42}$$

The extremal limit is now obtained by considering

$$z_H(v)^3 = \frac{4}{m(v)}, \quad q_e(v)^2 + q_m(v)^2 = \frac{6}{L^2} \frac{1}{z_H(v)^4}. \tag{A.43}$$

Once  $m(v)$  is chosen, we can pick the electric and magnetic charge functions according to the above formula. An obvious such choice is given by

$$q_e(v)^2 = \frac{3}{4L^2} \left( \frac{m(v)}{\sqrt{2}} \right)^{4/3} = q_m(v)^2. \tag{A.44}$$

# Appendix B

## Appendices for Chapter 4 and Chapter 5

### B.1 General Expressions for Field Equations

In this appendix, we demonstrate the derivation of general expressions of field equations in the string frame in gauge invariant forms. From the quadratic term of the field strength in the DBI action, we have the field equations in the Maxwell form as shown in (5.8). By taking Fourier transform of the gauge field as shown in (4.20), the field equations in the gauge of  $A_u = 0$  now read

$$\begin{aligned}(MG^{uu}G^{jj}A'_j)' - MG^{jj}(G^{tt}\omega^2 + G^{ii}q^2)A_j &= 0, \\(MG^{uu}G^{tt}A'_t)' - MG^{tt}G^{ii}(q^2A_t + q\omega A_i) &= 0, \\(MG^{uu}G^{tt}A'_i)' - MG^{tt}G^{ii}(\omega^2A_i + q\omega A_t) &= 0, \\ \omega G^{tt}A'_t - qG^{ii}A'_i &= 0,\end{aligned}\tag{B.1}$$

where  $M = e^{-\phi}\sqrt{-\det G_{\mu\nu}}$  and  $i$  denotes the propagating direction and  $j$  denotes the polarization of the gauge field. The first equation here represents the transverse mode and the rest three contribute to the longitudinal modes. To rewrite the field

equations into the gauge invariant form, we define

$$E_i = qA_t + \omega A_i, \quad E_j = \omega A_j, \quad (\text{B.2})$$

where we set  $k_0 = -\omega$  and  $k_i = q$ . By using the first equation of (B.1) and (B.2), we obtain the gauge invariant form for the transverse modes,

$$E_j'' + (\log(MG^{uu}G^{jj}))' E_j' - \frac{1}{G^{uu}}(G^{tt}\omega^2 + G^{ii}q^2)E_j = 0. \quad (\text{B.3})$$

By combining the rest three equations in (B.1) and (B.2) and doing some algebras, we then derive the gauge invariant form for the longitudinal modes,

$$E_i'' + \left[ (\log(MG^{uu}G^{ii}))' + \left( \log\left(\frac{G^{tt}}{G^{ii}}\right) \right)' \frac{G^{ii}q^2}{k^2} \right] E_i' - \frac{k^2}{G^{uu}}E_i = 0, \quad (\text{B.4})$$

where  $k^2 = G^{tt}\omega^2 + G^{ii}q^2$ . Furthermore, by using the last equation in (B.1), we can also rewrite the near-boundary action into the gauge invariant form as

$$\begin{aligned} S_\epsilon &= -2K_{D7} \int \frac{d^4k}{(2\pi)^4} G^{uu} M (G^{tt} A_t^* A_t' + G^{jj} A_j^* A_j' + G^{ii} A_i^* A_i') \\ &= -2K_{D7} \int \frac{d^4k}{(2\pi)^4} G^{uu} M \left( \frac{G^{ii}G^{tt}}{q^2G^{ii} + \omega^2G^{tt}} E_i^* E_i' + \frac{G^{jj}}{\omega^2} E_j^* E_j' \right). \end{aligned} \quad (\text{B.5})$$

Finally, by implementing (4.26), we obtain the photon spectral density

$$\chi_{\epsilon_j}(\omega) = 8K_{D7} \text{Im} \lim_{u \rightarrow 0} \frac{G^{uu} M G^{jj} E_j'(u, \omega)}{E_j(u, \omega)}. \quad (\text{B.6})$$

## B.2 Near-Boundary Expansion

To analyze the asymptotic behavior of  $\psi(u)$  with black-hole embedding near the boundary in MT metric, we may consider the situation with small anisotropy since the leading-order expansion of the MT geometry in terms of  $a/T$  can be solved

analytically. In this limit for  $a/T \ll 1$ , the leading-order solution of MT geometry reads [14],

$$\begin{aligned}
\mathcal{F}(u) &= 1 - \frac{u^4}{u_h^4} + a^2 \mathcal{F}_2(u) + \mathcal{O}(a^4), \\
\mathcal{B}(u) &= 1 + a^2 \mathcal{B}_2(u) + \mathcal{O}(a^4), \\
\mathcal{H}(u) &= e^{-\phi(u)}, \phi(u) = a^2 \phi_2(u) + \mathcal{O}(a^4),
\end{aligned} \tag{B.7}$$

where the coefficients for the anisotropic contributions are given by

$$\begin{aligned}
\mathcal{F}_2(u) &= \frac{1}{24u_h^2} \left[ 8u^2(u_h^2 - u^2) - 10u^4 \log 2 + (3u_h^4 + 7u^4) \log \left( 1 + \frac{u^2}{u_h^2} \right) \right], \\
\mathcal{B}_2(u) &= -\frac{u_h^2}{24} \left[ \frac{10u^2}{u_h^2 + u^2} + \log \left( 1 + \frac{u^2}{u_h^2} \right) \right], \\
\phi_2(u) &= -\frac{u_h^2}{4} \log \left( 1 + \frac{u^2}{u_h^2} \right).
\end{aligned} \tag{B.8}$$

We then insert the analytic expression of the background metric above into (4.34) and solve for  $\psi(u)$  near the boundary. We may assume that the asymptotic expansion of  $\psi(u)$  takes form,

$$\psi(u) = \psi_1 \frac{u}{u_h} + \psi_3 \frac{u^3}{u_h^3} + \psi_5 \frac{u^5}{u_h^5} + a^2 \log \left( \frac{u}{u_h} \right) \left( \rho_3 \frac{u^3}{u_h^3} + \rho_5 \frac{u^5}{u_h^5} \right) + \dots, \tag{B.9}$$

where the logarithmic terms come from anisotropy and have to vanish as  $a \rightarrow 0$ . Up to the  $\mathcal{O}(a^2)$  and  $\mathcal{O}(u^6)$  of (4.34), we find

$$\begin{aligned}
\psi_5 &= \frac{1}{8} \psi_1 (1 + 8\psi_1 \psi_3) + \frac{a^2}{96} (8\psi_1^3 - 9\psi_3 + \psi_1(-2 + \log 32)), \\
\rho_3 &= \frac{5}{24} \psi_1, \quad \rho_5 = \psi_1^2 \rho_3,
\end{aligned} \tag{B.10}$$

where the coefficients of higher-order terms are determined by  $\psi_1$  and  $\psi_3$  associated with the quark mass and condensate, respectively. Since the leading-order logarithmic term dominates the  $\mathcal{O}(u^3)$  term near the boundary, it is awkward to extract

$\psi_3$  in terms of the expansion in the  $u$  coordinate when the background geometry is anisotropic.

# Appendix C

## Appendices for Chapter 6

### C.1 Entropy Principle for CESE

As shown in Eq. (6.5),  $\sigma_5$  can be negative if  $\sigma_R < \sigma_L$ . However, as known, the normal transport coefficients should be always positive definite according to the second law of thermodynamics. So in the section, we will prove that negative  $\sigma_5$  will also obey the entropy principle.

Let us start from the relativistic hydrodynamics with chiral fermions. The energy-momentum and charge conservation equations read,

$$\begin{aligned}\partial_\mu T^{\mu\nu} &= eF^{\nu\lambda}(J_{R,\lambda} + J_{L,\lambda}), \\ \partial_\mu J_R^\mu &= 0, \\ \partial_\mu J_L^\mu &= 0,\end{aligned}\tag{C.1}$$

where  $J_R^\mu$  and  $J_L^\mu$  are four vector form of right and left handed currents,  $F^{\mu\nu}$  is the field strength tensor. Here we neglect the chiral anomaly in this discussion for simplicity. Those quantities can be decomposed as,

$$T^{\mu\nu} = (\epsilon + P + \Pi)u^\mu u^\nu - (P + \Pi)g^{\mu\nu} + \pi^{\mu\nu},\tag{C.2}$$

and

$$J_{R/L}^\mu = n_{R/L}u^\mu + \nu_{R/L}^\mu, \quad (\text{C.3})$$

where  $\epsilon$ ,  $P$ ,  $n_{R/L}$  and  $u^\mu$  are the energy density, the pressure, the number density of right (left) handed fermions and fluid velocity, respectively.  $g^{\mu\nu}$  is the metric and we choose it as  $\text{diag}\{+, -, -, -\}$ . The dissipative terms  $\Pi$ ,  $\pi^{\mu\nu}$  and  $\nu_{R/L}^\mu$  denote the bulk viscous pressure, the shear viscous tensor and the diffusion currents, respectively. Note that we have chosen the Landau frame where the heat flux current in  $T^{\mu\nu}$  does not appear.

For simplicity, we neglect the viscosities in the following discussion and only concentrate on the diffusion currents. The complete discussion can be found in the Sec II. of [195]. With the help of Gibbs-Duhem relation  $d\epsilon = Tds + \mu_R dn_R + \mu_L dn_L$ , with  $s$  the entropy density, from  $u_\nu \partial_\mu T^{\mu\nu} + \mu_R \partial_\mu J_R^\mu + \mu_L \partial_\mu J_L^\mu = u_\nu e F^{\nu\lambda} (J_{R,\lambda} + J_{L,\lambda})$ , we get,

$$\partial_\mu S^\mu = - \sum_{i=R,L} \nu_i^\mu \left[ \partial_\mu \frac{\mu_i}{T} + \frac{eE_\mu}{T} \right], \quad (\text{C.4})$$

where the electric field is defined in a comoving frame,  $E^\mu = F^{\mu\nu} u_\nu$ ,  $S^\mu$  is the covariant entropy flow defined as [76, 201],

$$S^\mu = \frac{1}{T} [P u^\mu + T^{\mu\nu} u_\nu - \mu_R J_R^\mu - \mu_L J_L^\mu] = s u^\mu - \frac{\mu_R}{T} \nu_R^\mu - \frac{\mu_L}{T} \nu_L^\mu.$$

The second law of thermodynamics requires,  $\partial_\mu S^\mu \geq 0$ . It can be satisfied if  $\nu_V^\mu$  have the following forms,

$$\nu_i^\mu = \sum_{j=R,L} \lambda_{ij} (g^{\mu\nu} - u^\mu u^\nu) \left[ \partial_\nu \frac{\mu_j}{T} + \frac{eE_\nu}{T} \right], \quad (\text{C.5})$$

and

$$\lambda_{RR} \lambda_{LL} - \frac{1}{4} (\lambda_{RL} + \lambda_{LR})^2 \geq 0, \quad \lambda_{RR} \geq 0, \quad \lambda_{LL} \geq 0, \quad (\text{C.6})$$

where the factor  $g^{\mu\nu} - u^\mu u^\nu$  guaranteed  $u_\mu \nu_V^\mu = 0$ . We find the heat and electric conductivities form a unique combination and share the same transport coefficient [195]. If the system has a time reversal symmetry, then we get

$$\lambda_{RL} = \lambda_{LR}, \tag{C.7}$$

which is called Onsager relation and has been proved in various of approaches, e.g. from kinetic theory [195].

Now we turn to the vector and axial vector currents,  $J_V^\mu$  and  $J_a^\mu$ . Inserting the constrains (C.6) and Onsager relation (C.7), yields,

$$\begin{aligned} \sigma_V &= (\lambda_{RR} + \lambda_{LR} + \lambda_{RL} + \lambda_{LL})T \geq 0, \\ \sigma_5 &= (\lambda_{RR} + \lambda_{RL} - \lambda_{LR} - \lambda_{LL})T = (\lambda_{RR} - \lambda_{LL})T, \end{aligned} \tag{C.8}$$

where  $\sigma_V$  as a normal conductivity is found to be positive, but  $\sigma_5$  can be negative.

We find the entropy principle does not constrain  $\sigma_5$  directly and does also not require a positive definite  $\sigma_5$ . The similar conclusion is also obtained for a fluid with the multi-flavor case [195].

# Bibliography

- [1] B. Back, M. Baker, M. Ballintijn, D. Barton, B. Becker, et al., Nucl.Phys. **A757**, 28 (2005), [nucl-ex/0410022](#).
- [2] P. Huovinen, P. Kolb, U. W. Heinz, P. Ruuskanen, and S. Voloshin, Phys.Lett. **B503**, 58 (2001), [hep-ph/0101136](#).
- [3] K. Ackermann et al. (STAR Collaboration), Phys.Rev.Lett. **86**, 402 (2001), [nucl-ex/0009011](#).
- [4] S. Adler et al. (PHENIX Collaboration), Phys.Rev.Lett. **91**, 182301 (2003), [nucl-ex/0305013](#).
- [5] J. Adams et al. (STAR Collaboration), Phys.Rev.Lett. **92**, 052302 (2004), [nucl-ex/0306007](#).
- [6] U. W. Heinz, pp. 3–12 (2005), [nucl-th/0512051](#).
- [7] W. Florkowski, R. Ryblewski, and M. Strickland, Nucl.Phys. **A916**, 249 (2013), [1304.0665](#).
- [8] D. d’Enterria (2009), [0902.2011](#).
- [9] S. Bass et al., *Hot and Dense QCD Matter: Unraveling the Mysteries of the Strongly Interacting Quark-Gluon-Plasma. A Community White Paper on the Future of Relativistic Heavy-Ion Physics in the US* (2012).
- [10] A. Adare et al. (PHENIX Collaboration), Phys.Rev.Lett. **109**, 122302 (2012), [1105.4126](#).
- [11] J. Erdmenger, N. Evans, I. Kirsch, and E. Threlfall, Eur.Phys.J. **A35**, 81 (2008), [0711.4467](#).
- [12] J. Casalderrey-Solana, H. Liu, D. Mateos, K. Rajagopal, and U. A. Wiedemann (2011), [1101.0618](#).
- [13] D. Mateos and L. Patino, JHEP **0711**, 025 (2007), [0709.2168](#).
- [14] D. Mateos and D. Trancanelli, JHEP **1107**, 054 (2011), [1106.1637](#).

- [15] T. Sakai and S. Sugimoto, *Prog.Theor.Phys.* **113**, 843 (2005), [hep-th/0412141](#).
- [16] O. Bergman, J. Erdmenger, and G. Lifschytz, *Lect.Notes Phys.* **871**, 591 (2013), [1207.5953](#).
- [17] D. J. Gross and F. Wilczek, *Phys.Rev.Lett.* **30**, 1343 (1973).
- [18] H. D. Politzer, *Phys.Rev.Lett.* **30**, 1346 (1973).
- [19] R. Baier, A. H. Mueller, D. Schiff, and D. Son, *Phys.Lett.* **B502**, 51 (2001), [hep-ph/0009237](#).
- [20] T. Hirano and K. Tsuda, *Phys.Rev.* **C66**, 054905 (2002), [nucl-th/0205043](#).
- [21] P. F. Kolb and U. W. Heinz (2003), [nucl-th/0305084](#).
- [22] M. Tannenbaum, *Rept.Prog.Phys.* **69**, 2005 (2006), [nucl-ex/0603003](#).
- [23] P. M. Chesler and L. G. Yaffe, *Phys.Rev.Lett.* **102**, 211601 (2009), [0812.2053](#).
- [24] P. M. Chesler and L. G. Yaffe, *Phys.Rev.* **D82**, 026006 (2010), [0906.4426](#).
- [25] V. Balasubramanian, A. Bernamonti, J. de Boer, N. Copland, B. Craps, et al., *Phys.Rev.Lett.* **106**, 191601 (2011), [1012.4753](#).
- [26] V. Balasubramanian, A. Bernamonti, J. de Boer, N. Copland, B. Craps, et al., *Phys.Rev.* **D84**, 026010 (2011), [1103.2683](#).
- [27] M. P. Heller, R. A. Janik, and P. Witaszczyk, *Phys.Rev.Lett.* **108**, 201602 (2012), [1103.3452](#).
- [28] M. P. Heller, R. A. Janik, and P. Witaszczyk, *Phys.Rev.* **D85**, 126002 (2012), [1203.0755](#).
- [29] M. P. Heller, D. Mateos, W. van der Schee, and D. Trancanelli, *Phys.Rev.Lett.* **108**, 191601 (2012), [1202.0981](#).
- [30] P. Kovtun, D. Son, and A. Starinets, *Phys.Rev.Lett.* **94**, 111601 (2005), [hep-th/0405231](#).
- [31] B. Andersson, G. Gustafson, G. Ingelman, and T. Sjostrand, *Phys.Rept.* **97**, 31 (1983).
- [32] B. Webber, *Nucl.Phys.* **B238**, 492 (1984).
- [33] J. C. Collins, *Nucl.Phys.* **B396**, 161 (1993), [hep-ph/9208213](#).

- [34] D. Molnar and S. A. Voloshin, Phys.Rev.Lett. **91**, 092301 (2003), [nucl-th/0302014](#).
- [35] R. Fries, B. Muller, C. Nonaka, and S. Bass, Phys.Rev.Lett. **90**, 202303 (2003), [nucl-th/0301087](#).
- [36] R. Fries, B. Muller, C. Nonaka, and S. Bass, Phys.Rev. **C68**, 044902 (2003), [nucl-th/0306027](#).
- [37] V. Greco, C. Ko, and P. Levai, Phys.Rev.Lett. **90**, 202302 (2003), [nucl-th/0301093](#).
- [38] F. Karsch, E. Laermann, and A. Peikert, Phys.Lett. **B478**, 447 (2000), [hep-lat/0002003](#).
- [39] Y. Aoki, Z. Fodor, S. Katz, and K. Szabo, Phys.Lett. **B643**, 46 (2006), [hep-lat/0609068](#).
- [40] A. Mocsy and P. Petreczky, Phys.Rev.Lett. **99**, 211602 (2007), [0706.2183](#).
- [41] J. M. Maldacena, Adv.Theor.Math.Phys. **2**, 231 (1998), [hep-th/9711200](#).
- [42] S. Gubser, I. R. Klebanov, and A. M. Polyakov, Phys.Lett. **B428**, 105 (1998), [hep-th/9802109](#).
- [43] E. Witten, Adv.Theor.Math.Phys. **2**, 253 (1998), [hep-th/9802150](#).
- [44] E. Witten, Adv.Theor.Math.Phys. **2**, 505 (1998), [hep-th/9803131](#).
- [45] O. Aharony, S. S. Gubser, J. M. Maldacena, H. Ooguri, and Y. Oz, Phys.Rept. **323**, 183 (2000), [hep-th/9905111](#).
- [46] G. Policastro, D. Son, and A. Starinets, Phys.Rev.Lett. **87**, 081601 (2001), [hep-th/0104066](#).
- [47] A. Buchel and J. T. Liu, Phys.Rev.Lett. **93**, 090602 (2004), [hep-th/0311175](#).
- [48] D. Mateos, Class.Quant.Grav. **24**, S713 (2007), [0709.1523](#).
- [49] L. D. McLerran and R. Venugopalan, Phys.Rev. **D49**, 3352 (1994), [hep-ph/9311205](#).
- [50] L. D. McLerran and R. Venugopalan, Phys.Rev. **D49**, 2233 (1994), [hep-ph/9309289](#).
- [51] E. Iancu, A. Leonidov, and L. D. McLerran, Nucl.Phys. **A692**, 583 (2001), [hep-ph/0011241](#).

- [52] E. Ferreiro, E. Iancu, A. Leonidov, and L. McLerran, Nucl.Phys. **A703**, 489 (2002), [hep-ph/0109115](#).
- [53] D. Kharzeev and M. Nardi, Phys.Lett. **B507**, 121 (2001), [nucl-th/0012025](#).
- [54] D. Kharzeev, E. Levin, and M. Nardi, Nucl.Phys. **A747**, 609 (2005), [hep-ph/0408050](#).
- [55] T. Hirano, U. W. Heinz, D. Kharzeev, R. Lacey, and Y. Nara, Phys.Lett. **B636**, 299 (2006), [nucl-th/0511046](#).
- [56] H.-J. Drescher, A. Dumitru, A. Hayashigaki, and Y. Nara, Phys.Rev. **C74**, 044905 (2006), [nucl-th/0605012](#).
- [57] H.-J. Drescher and Y. Nara, Phys.Rev. **C76**, 041903 (2007), [0707.0249](#).
- [58] B. Schenke, P. Tribedy, and R. Venugopalan, Phys.Rev.Lett. **108**, 252301 (2012), [1202.6646](#).
- [59] D. Grumiller and P. Romatschke, JHEP **0808**, 027 (2008), [0803.3226](#).
- [60] S. S. Gubser, S. S. Pufu, and A. Yarom, Phys.Rev. **D78**, 066014 (2008), [0805.1551](#).
- [61] J. L. Albacete, Y. V. Kovchegov, and A. Taliotis, JHEP **0807**, 100 (2008), [0805.2927](#).
- [62] L. Alvarez-Gaume, C. Gomez, A. Sabio Vera, A. Tavanfar, and M. A. Vazquez-Mozo, JHEP **0902**, 009 (2009), [0811.3969](#).
- [63] S. Bhattacharyya and S. Minwalla, JHEP **09**, 034 (2009), [0904.0464](#).
- [64] S. Lin and E. Shuryak, Phys.Rev. **D79**, 124015 (2009), [0902.1508](#).
- [65] J. L. Albacete, Y. V. Kovchegov, and A. Taliotis, JHEP **0905**, 060 (2009), [0902.3046](#).
- [66] S. S. Gubser, S. S. Pufu, and A. Yarom, JHEP **0911**, 050 (2009), [0902.4062](#).
- [67] J. Casalderrey-Solana, M. P. Heller, D. Mateos, and W. van der Schee (2013), [1305.4919](#).
- [68] J. Bjorken, Phys.Rev. **D27**, 140 (1983).
- [69] A. Bialas, M. Bleszynski, and W. Czyz, Nucl.Phys. **B111**, 461 (1976).
- [70] M. L. Miller, K. Reygers, S. J. Sanders, and P. Steinberg, Ann.Rev.Nucl.Part.Sci. **57**, 205 (2007), [nucl-ex/0701025](#).

- [71] D. Kharzeev and E. Levin, Phys.Lett. **B523**, 79 (2001), [nucl-th/0108006](#).
- [72] D. Kharzeev, E. Levin, and M. Nardi, Phys.Rev. **C71**, 054903 (2005), [hep-ph/0111315](#).
- [73] H.-J. Drescher and Y. Nara, Phys.Rev. **C75**, 034905 (2007), [nucl-th/0611017](#).
- [74] P. Huovinen, Int.J.Mod.Phys. **E22**, 1330029 (2013), [1311.1849](#).
- [75] K. Aamodt et al. (ALICE Collaboration), Phys.Rev.Lett. **105**, 252302 (2010), [1011.3914](#).
- [76] W. Israel and J. Stewart, Annals Phys. **118**, 341 (1979).
- [77] A. Muronga, Phys.Rev.Lett. **88**, 062302 (2002), [nucl-th/0104064](#).
- [78] H. Song and U. W. Heinz, Phys.Rev. **C77**, 064901 (2008), [0712.3715](#).
- [79] M. Luzum and P. Romatschke, Phys.Rev. **C78**, 034915 (2008), [0804.4015](#).
- [80] P. Bozek and W. Broniowski, Phys.Rev. **C85**, 044910 (2012), [1203.1810](#).
- [81] P. Romatschke and M. Strickland, Phys.Rev. **D68**, 036004 (2003), [hep-ph/0304092](#).
- [82] M. Martinez and M. Strickland, Nucl.Phys. **A848**, 183 (2010), [1007.0889](#).
- [83] M. Martinez and M. Strickland, Nucl.Phys. **A856**, 68 (2011), [1011.3056](#).
- [84] M. Martinez, R. Ryblewski, and M. Strickland, Phys.Rev. **C85**, 064913 (2012), [1204.1473](#).
- [85] R. Ryblewski and W. Florkowski, Phys.Rev. **C85**, 064901 (2012), [1204.2624](#).
- [86] D. Bazow, U. W. Heinz, and M. Strickland (2013), [1311.6720](#).
- [87] R. Ryblewski, J.Phys. **G40**, 093101 (2013).
- [88] A. Adare et al. (PHENIX Collaboration), Phys.Rev.Lett. **101**, 232301 (2008), [0801.4020](#).
- [89] J. Adams et al. (STAR Collaboration), Phys.Rev.Lett. **91**, 072304 (2003), [nucl-ex/0306024](#).
- [90] S. Adler et al. (PHENIX Collaboration), Phys.Rev.Lett. **91**, 072303 (2003), [nucl-ex/0306021](#).
- [91] M. Gyulassy and X.-n. Wang, Nucl.Phys. **B420**, 583 (1994), [nucl-th/9306003](#).

- [92] R. Baier, Y. L. Dokshitzer, A. H. Mueller, S. Peigne, and D. Schiff, Nucl.Phys. **B484**, 265 (1997), [hep-ph/9608322](#).
- [93] B. Zakharov, JETP Lett. **65**, 615 (1997), [hep-ph/9704255](#).
- [94] U. A. Wiedemann, Nucl.Phys. **B588**, 303 (2000), [hep-ph/0005129](#).
- [95] M. Gyulassy, P. Levai, and I. Vitev, Nucl.Phys. **B594**, 371 (2001), [nucl-th/0006010](#).
- [96] X.-f. Guo and X.-N. Wang, Phys.Rev.Lett. **85**, 3591 (2000), [hep-ph/0005044](#).
- [97] H. Liu, K. Rajagopal, and U. A. Wiedemann, Phys.Rev.Lett. **97**, 182301 (2006), [hep-ph/0605178](#).
- [98] H. Liu, K. Rajagopal, and U. A. Wiedemann, JHEP **0703**, 066 (2007), [hep-ph/0612168](#).
- [99] S. S. Gubser, Phys.Rev. **D74**, 126005 (2006), [hep-th/0605182](#).
- [100] C. Herzog, A. Karch, P. Kovtun, C. Kozcaz, and L. Yaffe, JHEP **0607**, 013 (2006), [hep-th/0605158](#).
- [101] W. Horowitz, Nucl.Phys. **A904-905**, 186c (2013), [1210.8330](#).
- [102] P. M. Chesler, K. Jensen, A. Karch, and L. G. Yaffe, Phys. Rev. **D79**, 125015 (2009), [0810.1985](#).
- [103] S. S. Gubser, D. R. Gulotta, S. S. Pufu, and F. D. Rocha, JHEP **10**, 052 (2008), [0803.1470](#).
- [104] P. Arnold and D. Vaman, JHEP **10**, 099 (2010), [1008.4023](#).
- [105] P. Arnold and D. Vaman, JHEP **1104**, 027 (2011), [1101.2689](#).
- [106] B. Betz and M. Gyulassy, Phys.Rev. **C86**, 024903 (2012), [1201.0281](#).
- [107] J. S. Schwinger, Phys.Rev. **82**, 664 (1951).
- [108] D. Kharzeev and A. Zhitnitsky, Nucl.Phys. **A797**, 67 (2007), [0706.1026](#).
- [109] D. E. Kharzeev, L. D. McLerran, and H. J. Warringa, Nucl.Phys. **A803**, 227 (2008), [0711.0950](#).
- [110] D. E. Kharzeev and H.-U. Yee, Phys.Rev. **D83**, 085007 (2011), [1012.6026](#).
- [111] D. Son and A. R. Zhitnitsky, Phys.Rev. **D70**, 074018 (2004), [hep-ph/0405216](#).
- [112] K. Fukushima, D. E. Kharzeev, and H. J. Warringa, Phys.Rev. **D78**, 074033 (2008), [0808.3382](#).

- [113] Y. Burnier, D. E. Kharzeev, J. Liao, and H.-U. Yee, Phys.Rev.Lett. **107**, 052303 (2011), 1103.1307.
- [114] G. Wang (STAR Collaboration), Nucl.Phys.A904-905 **2013**, 248c (2013), 1210.5498.
- [115] H. Ke (STAR Collaboration), J.Phys.Conf.Ser. **389**, 012035 (2012), 1211.3216.
- [116] K. Tuchin, Phys.Rev. **C83**, 017901 (2011), 1008.1604.
- [117] K. Tuchin (2012), 1206.0485.
- [118] G. Basar, D. Kharzeev, D. Kharzeev, and V. Skokov, Phys.Rev.Lett. **109**, 202303 (2012), 1206.1334.
- [119] K. Fukushima and K. Mameda, Phys.Rev. **D86**, 071501 (2012), 1206.3128.
- [120] A. Bzdak and V. Skokov, Phys.Rev.Lett. **110**, 192301 (2013), 1208.5502.
- [121] D. Lohner (ALICE Collaboration) (2012), 1212.3995.
- [122] A. Bzdak and V. Skokov, Phys.Lett. **B710**, 171 (2012), 1111.1949.
- [123] Y. Hirono, M. Hongo, and T. Hirano (2012), 1211.1114.
- [124] X.-G. Huang and J. Liao, Phys.Rev.Lett. **110**, 232302 (2013), 1303.7192.
- [125] H.-T. Ding, A. Francis, O. Kaczmarek, F. Karsch, E. Laermann, et al., Phys.Rev. **D83**, 034504 (2011), 1012.4963.
- [126] K. Tuchin (2013), 1301.0099.
- [127] L. McLerran and V. Skokov (2013), 1305.0774.
- [128] E. Caceres, A. Kundu, B. Muller, D. Vaman, and D.-L. Yang (2012), 1208.6368.
- [129] E. Caceres, A. Kundu, and D.-L. Yang, JHEP **1403**, 073 (2014), 1212.5728.
- [130] B. Muller and D.-L. Yang, Phys.Rev. **D87**, 046004 (2013), 1210.2095.
- [131] S.-Y. Wu and D.-L. Yang, JHEP **1308**, 032 (2013), 1305.5509.
- [132] B. Muller, S.-Y. Wu, and D.-L. Yang, Phys.Rev. **D89**, 026013 (2014), 1308.6568.
- [133] S. Pu, S.-Y. Wu, and D.-L. Yang (2014), 1401.6972.
- [134] H. Nastase (2007), 0712.0689.

- [135] A. V. Ramallo (2013), 1310.4319.
- [136] G. T. Horowitz and A. Strominger, Nucl.Phys. **B360**, 197 (1991).
- [137] I. R. Klebanov, Nucl.Phys. **B496**, 231 (1997), hep-th/9702076.
- [138] J. Polchinski, Phys.Rev.Lett. **75**, 4724 (1995), hep-th/9510017.
- [139] W. Mueck and K. Viswanathan, Phys.Rev. **D58**, 106006 (1998), hep-th/9805145.
- [140] A. Karch and L. Randall, JHEP **0106**, 063 (2001), hep-th/0105132.
- [141] A. Karch and E. Katz, JHEP **0206**, 043 (2002), hep-th/0205236.
- [142] J. Babington, J. Erdmenger, N. J. Evans, Z. Guralnik, and I. Kirsch, Phys.Rev. **D69**, 066007 (2004), hep-th/0306018.
- [143] D. Mateos, R. C. Myers, and R. M. Thomson, Phys.Rev.Lett. **97**, 091601 (2006), hep-th/0605046.
- [144] C. Hoyos-Badajoz, K. Landsteiner, and S. Montero, JHEP **0704**, 031 (2007), hep-th/0612169.
- [145] D. Mateos, R. C. Myers, and R. M. Thomson, JHEP **0705**, 067 (2007), hep-th/0701132.
- [146] E. Caceres and A. Kundu, JHEP **1209**, 055 (2012), 1205.2354.
- [147] Y. Hatta, E. Iancu, and A. H. Mueller, JHEP **05**, 037 (2008), 0803.2481.
- [148] S. B. Giddings and A. Nudelman, JHEP **0202**, 003 (2002), hep-th/0112099.
- [149] F. Dominguez, C. Marquet, A. Mueller, B. Wu, and B.-W. Xiao, Nucl.Phys. **A811**, 197 (2008), 0803.3234.
- [150] D. Galante and M. Schvellinger, JHEP **1207**, 096 (2012), 1205.1548.
- [151] E. Caceres and A. Guijosa, JHEP **0612**, 068 (2006), hep-th/0606134.
- [152] E. Caceres and A. Guijosa, JHEP **0611**, 077 (2006), hep-th/0605235.
- [153] P. M. Chesler and L. G. Yaffe, Phys.Rev.Lett. **106**, 021601 (2011), 1011.3562.
- [154] R. A. Janik and P. Witaszczyk, JHEP **0809**, 026 (2008), 0806.2141.
- [155] D. Mateos and D. Trancanelli, Phys.Rev.Lett. **107**, 101601 (2011), 1105.3472.
- [156] D. Giataganas, JHEP **1207**, 031 (2012), 1202.4436.

- [157] A. Rebhan and D. Steineder, JHEP **1208**, 020 (2012), 1205.4684.
- [158] M. Chernicoff, D. Fernandez, D. Mateos, and D. Trancanelli, JHEP **1208**, 041 (2012), 1203.0561.
- [159] M. Chernicoff, D. Fernandez, D. Mateos, and D. Trancanelli, JHEP **1208**, 100 (2012), 1202.3696.
- [160] K. B. Fadafan and H. Soltanpanahi (2012), 1206.2271.
- [161] M. Chernicoff, D. Fernandez, D. Mateos, and D. Trancanelli (2012), 1208.2672.
- [162] L. Patino and D. Trancanelli, JHEP **1302**, 154 (2013), 1211.2199.
- [163] P. Romatschke and M. Strickland, Phys.Rev. **D70**, 116006 (2004), hep-ph/0406188.
- [164] M. Panero, Phys.Rev.Lett. **103**, 232001 (2009), 0907.3719.
- [165] R. Baier, Nucl.Phys. **A715**, 209 (2003), hep-ph/0209038.
- [166] S. Caron-Huot, P. Kovtun, G. D. Moore, A. Starinets, and L. G. Yaffe, JHEP **0612**, 015 (2006), hep-th/0607237.
- [167] D. T. Son and A. O. Starinets, JHEP **0209**, 042 (2002), hep-th/0205051.
- [168] P. K. Kovtun and A. O. Starinets, Phys.Rev. **D72**, 086009 (2005), hep-th/0506184.
- [169] K. A. Mamo, JHEP **1308**, 083 (2013), 1210.7428.
- [170] Y. Bu, Phys. Rev. D **87**, 026005 (2013), URL <http://link.aps.org/doi/10.1103/PhysRevD.87.026005>.
- [171] H.-U. Yee, Phys.Rev. **D88**, 026001 (2013), 1303.3571.
- [172] T. Albash, V. G. Filev, C. V. Johnson, and A. Kundu, JHEP **0808**, 092 (2008), 0709.1554.
- [173] K. Tuchin (2013), 1305.5806.
- [174] J. Casalderrey-Solana and D. Mateos, Phys.Rev.Lett. **102**, 192302 (2009), 0806.4172.
- [175] S. Chakraborty and N. Haque, Nucl.Phys. **B874**, 821 (2013), 1212.2769.
- [176] A. Dumitru, Y. Guo, and M. Strickland, Phys.Lett. **B662**, 37 (2008), 0711.4722.

- [177] A. Dumitru, Y. Guo, and M. Strickland, Phys.Rev. **D79**, 114003 (2009), 0903.4703.
- [178] M. Strickland and D. Bazow, Nucl.Phys. **A879**, 25 (2012), 1112.2761.
- [179] M. Strickland, Phys.Rev.Lett. **107**, 132301 (2011), 1106.2571.
- [180] A. Mocsy, P. Petreczky, and M. Strickland, Int.J.Mod.Phys. **A28**, 1340012 (2013), 1302.2180.
- [181] A. Rebhan and D. Steineder, Phys.Rev.Lett. **108**, 021601 (2012), 1110.6825.
- [182] S. S. Gubser, Phys.Rev. **D76**, 126003 (2007), hep-th/0611272.
- [183] C. Shen, U. W. Heinz, J.-F. Paquet, I. Kozlov, and C. Gale (2013), 1308.2111.
- [184] B. Hassanain and M. Schvellinger, Phys.Rev. **D85**, 086007 (2012), 1110.0526.
- [185] H.-U. Yee, JHEP **0911**, 085 (2009), 0908.4189.
- [186] A. Rebhan, A. Schmitt, and S. A. Stricker, JHEP **1001**, 026 (2010), 0909.4782.
- [187] A. Gorsky, P. Kopnin, and A. Zayakin, Phys.Rev. **D83**, 014023 (2011), 1003.2293.
- [188] A. Gynther, K. Landsteiner, F. Pena-Benitez, and A. Rebhan, JHEP **1102**, 110 (2011), 1005.2587.
- [189] T. Kalaydzhyan and I. Kirsch, Phys.Rev.Lett. **106**, 211601 (2011), 1102.4334.
- [190] C. Hoyos, T. Nishioka, and A. O'Bannon, JHEP **1110**, 084 (2011), 1106.4030.
- [191] I. Gahramanov, T. Kalaydzhyan, and I. Kirsch, Phys.Rev. **D85**, 126013 (2012), 1203.4259.
- [192] T. Sakai and S. Sugimoto, Prog.Theor.Phys. **114**, 1083 (2005), hep-th/0507073.
- [193] S. Lin and H.-U. Yee, Phys.Rev. **D88**, 025030 (2013), 1305.3949.
- [194] V. Rubakov (2010), 1005.1888.
- [195] J.-W. Chen, Y.-F. Liu, S. Pu, Y.-K. Song, and Q. Wang, Phys.Rev. **D88**, 085039 (2013), 1308.2945.
- [196] K. Peeters, J. Sonnenschein, and M. Zamaklar, Phys.Rev. **D74**, 106008 (2006), hep-th/0606195.
- [197] A. Andronic, P. Braun-Munzinger, and J. Stachel, Nucl.Phys. **A772**, 167 (2006), nucl-th/0511071.

- [198] L. Kumar (STAR Collaboration), Nucl.Phys. **A904-905**, 256c (2013), 1211.1350.
- [199] S. Kuperstein and J. Sonnenschein, JHEP **0809**, 012 (2008), 0807.2897.
- [200] M. Ihl, A. Kundu, and S. Kundu, JHEP **1212**, 070 (2012), 1208.2663.
- [201] S. Pu (2011), 1108.5828.
- [202] D.-L. Yang and B. Muller, J.Phys. **G39**, 015007 (2012), 1108.2525.
- [203] T. Mehen and D.-L. Yang, Phys.Rev. **D85**, 014002 (2012), 1111.3884.

# Biography

Di-Lun Yang was born in Kaohsiung, Taiwan on January 23, 1985. He received his bachelor degree of science from Department of Physics, National Taiwan University in June, 2007. In Fall 2009, he entered the Physics Graduate Program at Duke University. He will get Doctor of Philosophy in May 2014 from Department of Physics at Duke University. He passed the preliminary exam and became the doctoral candidate in February 2012. As a graduate student at Duke University, he has written the articles listed in [202, 203, 128, 129, 130, 131, 132, 133].